Hydrogen Storage Technologies

Scrivener Publishing
100 Cummings Center, Suite 541J
Beverly, MA 01915-6106

Advances in Hydrogen Production and Storage

Series Editors: Mehmet Sankir and Nurdan Demirci Sankir

Scope: Energy is one of the most important issues for humankind. Increasing energy demand, regional limitations, and serious environmental effects of the conventional energy sources provide the urgent need for new, clean, and sustainable energy. **Advances in Hydrogen Production and Storage** emphasizes the basics of renewable energy and storage as well as the cutting edge technologies employed for these applications. The series focuses mainly on hydrogen generation, photoelectrochemical solar cells, fuel cells and flow batteries.

Submission to the series: Please send book proposals to Mehmet Sankir at mehmetsankir@yahoo.com

Publishers at Scrivener
Martin Scrivener (martin@scrivenerpublishing.com)
Phillip Carmical (pcarmical@scrivenerpublishing.com)

Hydrogen Storage Technologies

Edited by
Mehmet Sankir and
Nurdan Demirci Sankir

WILEY

This edition first published 2018 by John Wiley & Sons, Inc., 111 River Street, Hoboken, NJ 07030, USA and Scrivener Publishing LLC, 100 Cummings Center, Suite 541J, Beverly, MA 01915, USA

For more information about Scrivener publications please visit www.scrivenerpublishing.com.

Wiley Global Headquarters
111 River Street, Hoboken, NJ 07030, USA

For details of our global editorial offices, customer services, and more information about Wiley products visit us at www.wiley.com.

Library of Congress Cataloging-in-Publication Data

ISBN 978-1-119-45988-0

Cover image: Mehmet Sankir and Russell Richardson
Cover design by Russell Richardson

Set in size of 11pt and Minion Pro by Exeter Premedia Services Private Ltd., Chennai, India

Printed in the USA

10 9 8 7 6 5 4 3 2 1

Contents

Preface

Our heavy dependence on fossil fuel resources, which is the cause of worldwide problems, has to be reduced in order to improve the environment and, in turn, the impact it has on human health. Hydrogen has drawn great attention as a nonpolluting energy carrier due to its diverse methods of production and storage. In the first volume of our series, *Advances in Hydrogen Production and Storage*, we thoroughly introduced hydrogen production technologies. However, since hydrogen storage is considered a key technology for stationary and portable power generation, especially for transportation, the second volume of the series is devoted to hydrogen storage technologies. This volume covers the novel technologies used to efficiently store and distribute hydrogen. Discussed are the underlying basics, as well as advanced details, of hydrogen storage technologies, which is highly beneficial for science and engineering students as well as experienced engineers and researchers. Additionally, the book was written to provide a comprehensive approach to the area of hydrogen storage for readers from a wide variety of backgrounds. The intent of the book is to satisfy the need for a broad coverage of the hydrogen storage technologies. Therefore, it was written by distinguished authors with knowledge and expertise in areas of hydrogen storage, whose contributions can benefit readers from universities and industries. The editors wish to thank the authors for their efforts in writing their chapters.

We have separated the book into two major parts: Chemical and Electrochemical Hydrogen Storage and Carbon-Based Materials for Hydrogen Storage. In Part I, hydrogen storage technologies within the context of chemical and electrochemical methods are clearly discussed in five chapters. Chapter 1 focuses on a multistage compression system based on metal hydrides for hydrogen storage. It also includes the development of a validated numerical analysis of a three-stage compression system. Chapter 2 discusses metal-N-H systems and their physicochemical properties for hydrogen storage. Mg-based nanomaterials with enhanced sorption kinetics for hydrogen storage are thoroughly introduced in Chapter 3. Next, in Chapter 4, evaluation of gaseous and electrochemical hydrogen

storage performances of Ti-Zr-Ni alloys are analyzed. The final chapter of Part I, Chapter 5, deals with the electrochemical methods for hydrogenation/dehydrogenation of metal hydrides. The five chapters in Part II are devoted to carbon-based materials for hydrogen storage. Chapter 6 covers the activated carbon obtained from agro-industrial waste for use in hydrogen storage. Chapter 7 introduces the concept of hydrogen storage with carbonaceous materials. Next, Chapter 8 provides a fairly comprehensive introduction to hydrogen storage characteristics of graphene addition in hydrogen storage materials. Part II concludes with a discussion in Chapter 9 of the crucial features of hydrogen adsorption of nanotextured carbon-based materials.

Series Editors
Mehmet Sankır, PhD. and Nurdan Demirci Sankır, PhD.
Department of Materials Science and Nanotechnology Engineering,
TOBB University of Economics and Technology

PART I

CHEMICAL AND ELECTROCHEMICAL HYDROGEN STORAGE

Mehmet Sankir and Nurdan Demirci Sankir (eds.) Hydrogen Storage Technologies,
(1–38) © 2018 Scrivener Publishing LLC

1

Metal Hydride Hydrogen Compression Systems – Materials, Applications and Numerical Analysis

Evangelos I. Gkanas* **and Martin Khzouz**

Hydrogen for Mobility Lab, Institute for Future Transport and Cities, School of Mechanical, Automotive and Aerospace Engineering, Coventry University, Coventry, UK

Abstract

In this chapter, an analysis of the usage of hydrogen storage technologies for the design and construction of effective thermally driven hydrogen compressors is presented. A discussion on the available technologies for compressing hydrogen is presented; followed by an analysis of the combination of metal hydrides to design a metal hydride hydrogen compression (MHHC) system. The physicochemical and thermodynamic aspects of the metal hydride formation is introduced and the most suitable materials for compression processes are considered and analyzed. The necessity for the development of an accurate numerical analysis to describe a multistage MHHC system is explained, analyzed and discussed.

Keywords: Hydrogen storage, metal hydrides, hydrogen compression, thermally driven compressor, intermetallic compounds, numerical analysis, renewable energy

1.1 Introduction

In the current chapter, the topic of hydrogen compression by utilization of metal hydrides will be discussed and analyzed. Initially, the importance of using hydrogen technologies will be introduced, followed by an analysis

**Corresponding author*: evangelos.gkanas@coventry.ac.uk/egkanas@gmail.com

Mehmet Sankir and Nurdan Demirci Sankir (eds.) Hydrogen Storage Technologies, (3–38) © 2018 Scrivener Publishing LLC

and comparison between the most dominant ways to compress hydrogen such as mechanical compression, electrochemical compression and metal hydride hydrogen compression. The case of operating metal hydrides connected in series to compress hydrogen will be further analyzed in terms of the available metal hydride families, the physicochemical nature of hydrogen sorption by metallic materials, the thermodynamic aspects of metal hydride formation and the heat management of metal hydride tanks during the compression. The challenges for the proper material selection will be identified and analyzed, followed by a detailed analysis of the most promising materials for such application. The final part of the chapter will present a detailed mathematical analysis during the operation of a multistage MHHC system by introducing the necessary assumptions for the study. Furthermore, the heat, mass and momentum conservation equations for the needed numerical analysis will be introduced for the hydrogen-metal system in a step-by-step analysis, whereas a detailed case of a three-stage compression system will also be considered and analyzed.

1.2 Adoption of a Hydrogen-Based Economy

1.2.1 Climate Change and Pollution

The uncontrolled emissions of carbon dioxide (CO_2) through human activities are subject to global concern regarding energy sustainability, global climate and quality of human life [1]. Carbon dioxide is an essential component for life; thus, the CO_2 concentration in the atmosphere in either low or elevated levels can lead to global climate change, including all the side effects of this process [2, 3]. To achieve reduction in energy-related greenhouse gas emissions, several improvements must be achieved in terms of the energy supply sectors; conversion towards different energy sources is mandatory [4].

1.2.2 Toward a Hydrogen-Based Future

For the establishment of a globally hydrogen-based economy, safe and efficient ways of producing, storing and compressing hydrogen are mandatory for both stationary and mobile applications; small and/or large scale [5, 6]. Theoretically, hydrogen and electricity are enough to satisfy global energy needs, and can form an energy system that would be independent of energy sources [7]. Hydrogen does not normally exist naturally; it can be used as an energy vector to store/extract energy from fossil fuels and/or renewable energy sources (RES) and then convert to electricity and heat by using fuel

cells or combustion engines [8, 9]. Thus, hydrogen will play a key role in integrating future energy systems and bridging the transition from a fossil-based to a more RES-based energy economy. Furthermore, there are other certain technological obstacles for the full implementation of the hydrogen economy in the next years; effective, green and economically viable hydrogen production [10], further development of the PEM fuel cells in terms of reliability, efficiency and cost [11] and the effective storage of hydrogen [12].

1.2.3 Hydrogen Storage

For successful application of hydrogen as an energy carrier, hydrogen needs to be stored safely for variable periods of time as efficiently as gasoline [13], while simple handling and low costs should also be ensured. Under normal temperature and pressure conditions, 1 kg of hydrogen will occupy a volume of 12.15 m^3 and an energy content of 33.5 kWh, whereas for the same energy content, the volume that gasoline occupies is 0.0038 m^3. Thus, for hydrogen to become a competitive energy carrier, its volume density must be increased [14]. As a result, three separate ways for hydrogen storage are identified: *Compressed hydrogen storage*, *hydrogen storage in liquid form*, and *solid-state hydrogen storage*.

1.2.3.1 Compressed Hydrogen Storage

The storage of hydrogen at high pressure cylinders is probably the most common way for storing hydrogen; however, for both transportation and stationary applications the amount of hydrogen that can be stored in a reasonable volume is small [15]. Even at really high pressures (700–800 bar), such technology suffers from low volumetric density and the energy content is lower than that of the gasoline energy content under the same conditions. Furthermore, safety issues are also a drawback due to the possible embrittlement of the cylinders. Finally, the large cost of the (mechanical) compression and the large pressure drop inside the gas cylinder which is necessary when hydrogen is released (e.g., during the charging of the tank within a hydrogen fuel cell vehicle), are other factors that need to be considered.

1.2.3.2 Hydrogen Storage in Liquid Form

The storage of hydrogen in liquid form offers double capacity comparing to the high-pressure hydrogen storage. However, the volumetric storage capacity is still low; half of the capacity required by the Department of Energy (DOE) [16]. The high cost of liquefication is an issue that must be

Table 1.1 Comparison between the most common technologies for hydrogen storage in terms of volumetric capacity and technological drawbacks [15].

Storage technology	Volumetric capacity ($kgH^2\ m^{-3}$)	Technological drawbacks
High-Pressure Gas (800 bar)	40	Safety, Cost, Pressure drop during use, Embrittlement
Liquid Hydrogen (21 K)	71	Safety, Cost, Thermal Losses
Solid-State Storage	80–160	–

taken into account and also the safety regarding the handling of cryogenic tanks and the loss due to evaporation must be considered.

1.2.3.3 Solid-State Hydrogen Storage

The storage of hydrogen in solid-state form with the formation of metal hydrides (intermetallics and complex hydrides) is a very attractive technology to store hydrogen in an efficient and safe way. This technology is characterized by large volumetric capacities which do not suffer from the drawbacks of pressurized and liquid hydrogen. The storage of hydrogen in solid form is based on the specific properties of several metals that can adsorb hydrogen due to their capability to accept hydrogen atoms in their metal lattice [17]. Also, due to the relative low pressures of operation, the hydrogen storage in solid form is considered a relatively safe technique. Table 1.1 presents a comparison of the above-mentioned technologies in terms of the volumetric capacity and the technological drawbacks.

1.3 Hydrogen Compression Technologies

The first step towards the understanding of hydrogen compression is the detailed analysis of the pressure-density diagram for hydrogen, as presented in Figure 1.1 at six temperatures [18]. At lower pressures (up to 15 bar) the pressure is almost proportional to the density (straight line). For high pressures, the hydrogen density does not increase linearly with the pressure. A hydrogen density of almost 20 kgm^{-3} is reached at 300 bar (30 MPa) for the temperature of 30 °C. At a pressure of 800 bar (80 MPa) the density

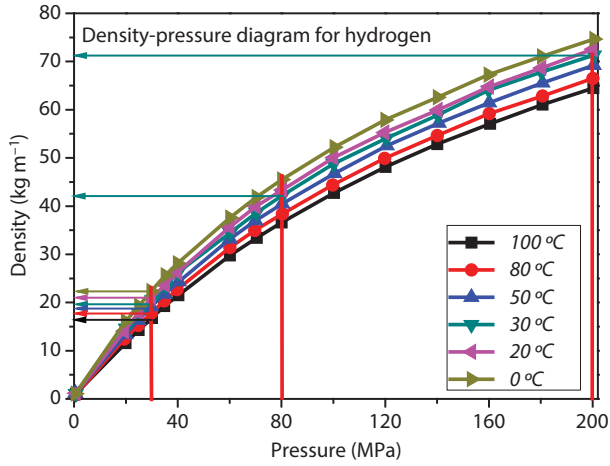

Figure 1.1 Density of the compressed hydrogen as pressure function at six different temperatures [18].

can be increased to around 41 kgm^{-3} and at very high pressures (2000 bar) the density can reach 70 kgm^{-3}. However, the later pressure is technically not feasible. When operating a hydrogen refuelling station, the pressure of hydrogen does not exceed 700 bar. High-pressure storage of hydrogen allows volume reduction of 5 kg to 0.125 m^3 at 700 bar [19]. There are several types of hydrogen compressors available; reciprocating piston compressor, ionic liquid piston compressor, electrochemical compressor, metal hydride hydrogen compressor and piston-metal diaphragm compressor.

1.3.1 Reciprocating Piston Compressor

The reciprocating piston compressor is based on two principles; the high-pressure cylinders with small area piston(s) and the hydraulic drive cylinder with large area piston(s) [20]. The hydrogen compression is achieved by using hydraulic power to deliver low-pressure hydrogen to the low-pressure hydraulic cylinder. The cylinder has a piston of a relatively large area. Thus, the pressurized hydrogen will initiate a force on the large piston surface, that will result in a balanced force against the smaller surface piston in a high-pressure cylinder. The pressure at high-pressure cylinder will be increased due to the difference between the surfaces of the two pistons. The movement of the hydraulic piston during the stroke is the major parameter that affects the discharge rate; furthermore, the cycle can be self-maintained by reversing the direction of the piston movement. One

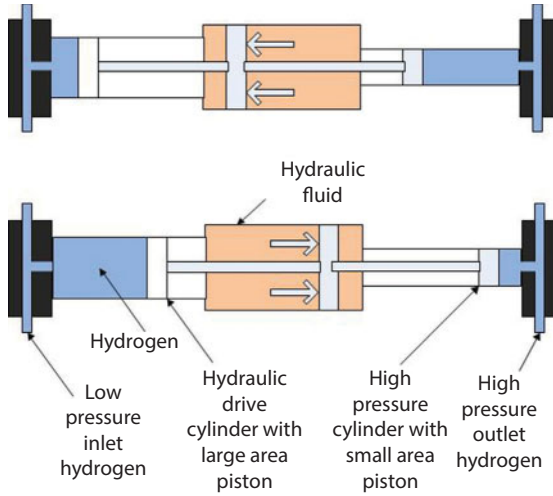

Figure 1.2 Schematic of a two-stage mechanical compressor.

of the major issues in mechanical compressors is that the working fluid should be moisture free to avoid any damage or corrosion of the piston surface. Another drawback is the cooling of the hydraulic drive to prevent any unexpected heat increase during compression and to achieve high compression efficiency. Figure 1.2 illustrates the compression cycle during a two-stage mechanical compression system.

The mechanical compressors should be installed in vibration free areas, on solid supports and using isolation pads. An integrated control system is essential to be installed when hydrogen is compressed. The control system will monitor the inlet hydrogen temperature, the outlet hydrogen temperature, the cooling fluid flow and the temperature. The most important safety feature with hydrogen compressors is to install hydrogen leak vent ports which are used during maintenance and purging of the entire compressor system during maintenance [21].

1.3.2 Ionic Liquid Piston Compressor

The ionic liquid compressor is an alternative approach to the solid piston compressors. The advantage of this technology over the piston approach is the lack of issues that are related to mechanical moving parts. The liquid can extract the heat from the gas during the compression process [22]. Thus, the cost of liquid compressor is reduced due to simplicity of the components and the sealing system. The entire system has longer life operations with significant improvement in efficiency. However, the type of the

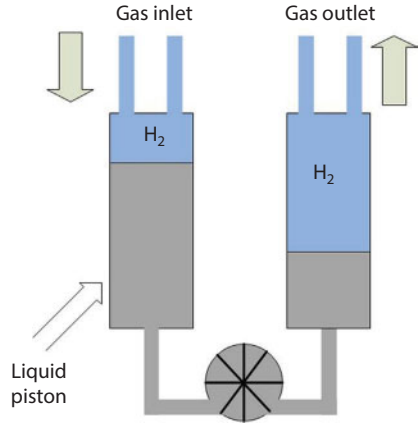

Figure 1.3 Schematic of a hydraulic liquid ionic compressor (LINDE) [26].

ionic liquid is crucial for the operation of such compressors, as the liquids can decompose at elevated temperatures [23]. The ionic liquid also plays a major role in reducing the mechanical losses, and as a consequence, the efficiency improvement. The liquid has low compressibility and low solubility of gases [24]. The most important aspect of designing such compressors is the correct selection of ionic liquid and construction materials with which to overcome possible corrosion issues, by including materials with high corrosion resistivity [25]. Figure 1.3 shows an example of a hydraulic liquid ionic compression system [26].

1.3.3 Piston-Metal Diaphragm Compressor

Piston-metal diaphragm compressors are also known as metal diaphragm compressors, where the compression is achieved by using a metal diaphragm. The operation of such devices is based on the reciprocating motion of a piston inside the cylinder. The diaphragm is usually a thin metal membrane which isolates the gas from the hydraulic fluid [27]. Figure 1.4 illustrates the schematics of a diaphragm compression system, where the piston motion causes pull (piston moves downwards) and push (piston moves upwards) for hydraulic fluid leading to the hydrogen inlet and the outlet at high pressures [28].

1.3.4 Electrochemical Hydrogen Compressor

The working principle of an electrochemical compressor is based on an electrochemical cell, consisting of an anode, a membrane electrode assembly

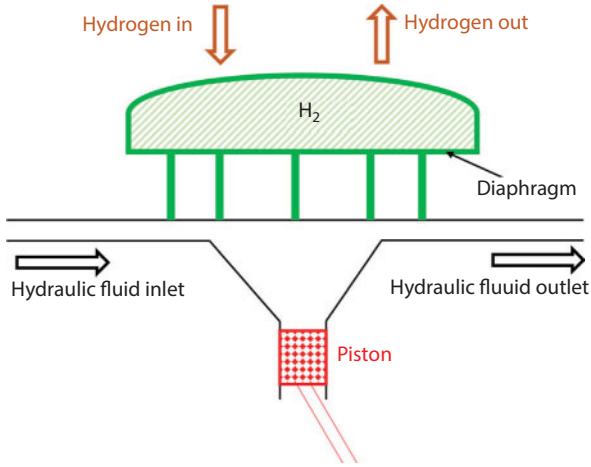

Figure 1.4 Schematic of a diaphragm compression system [28].

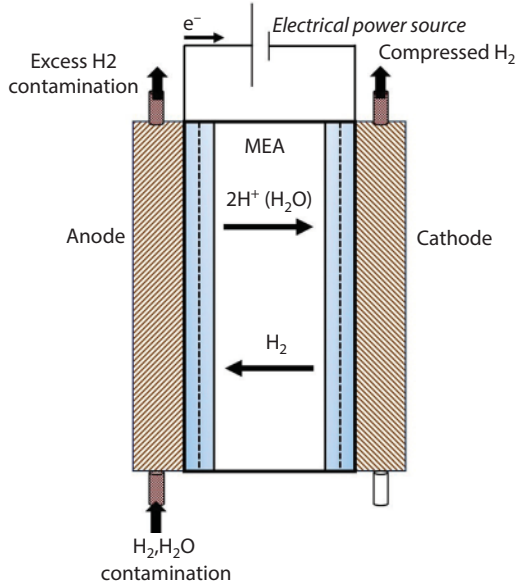

Figure 1.5 Basic components and the operational principle of the electrochemical compressor.

(MEA) and the cathode [29]. The basic components and the principle of operation of the electrochemical compressor are presented in Figure 1.5.

The compression process is simple and no moving parts are necessary. Furthermore, such compression systems are used when a small quantity of

hydrogen needs to be compressed, insofar as that regime is more efficient. When a potential difference is applied, the hydrogen is oxidized on the anode side. The ions are transported through the membrane to the cathode side where the proton is reduced at a higher pressure [30]. To achieve such performance, the cathode compartment must be hermetically sealed. To achieve higher compression ratios, a cascade must be installed (a series of membrane electrode assemblies). The electrochemical compression is very efficient [31, 32]. By using this technology, hydrogen can be compressed from ambient pressure to 16 MPa [33]. Also, the power demand follows the isothermal compression. For compression to 700 bar, almost 10 $MWkg^{-1}$ is expected [34]. A main parameter that affects the efficiency of the electrochemical compressor is the humidification of the membrane; the membrane has to be saturated with water to present excellent ionic conductivity. In the past years, several endeavours for commercialization of such technology have been reported [35–37], claiming the development of both a single-stage compressor that reaches 800 bar [37] and 200 bar [36], and a three-cell stack compressor reaching 170 bar [35].

1.4 Metal Hydride Hydrogen Compressors (MHHC)

The operation of a metal hydride hydrogen compressor can be simply explained as follows: Hydrogen is first stored in the metal hydride at a low supply pressure and temperature; the hydrogen remains in the hydride until it is exposed due to an increase in temperature or pressure drop; then, the stored hydrogen exits the hydride. If the temperature increase is sufficient and the final storage volume is smaller than the supply volume, the hydrogen exits the metal hydride at pressures that range from approximately 3–10 times the original supply pressure [38]. A multistage metal hydride hydrogen compression (MHHC) system uses a combination of different metal hydrides to increase the final compression ratio while maximizing the hydrogenation process from the supply pressure of each stage [39].

1.4.1 Operation of a Two-Stage MHHC

A simplified two-stage MHHC system is illustrated in Figure 1.6. The compression cycle can be summarized as follows:

Step 1: Valve No.1 opens and the low-pressure electrolyzer is attached to the first-stage reactor. When Valve No.1 opens, the first stage absorbs hydrogen in low pressure from the

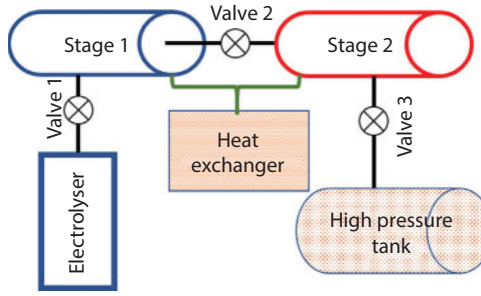

Figure 1.6 A simplified scheme of a two-stage metal hydride hydrogen compression system.

supplier until the hydrogenation process ends. Then Valve No.1 closes and the first-stage reactor is in equilibrium.

Step 2: A sensible heating process of the first stage reactor occurs at a predefined high temperature (T_H) in order to increase the pressure inside the tank and prepare the system for the upcoming coupling.

Step 3: Valve No.2 opens between the tanks of the first stage and the second stage, where the temperature of the first-stage reactor is high (T_H) and the temperature of the second stage is low (T_L); thus, the released hydrogen from the first stage enters the second stage and is absorbed by the second-stage alloy. At the end of this process, Valve No. 2 closes.

Step 4: Another sensible heating process takes place at a predefined high temperature (T_H) to increase the pressure inside the second-stage reactor.

Step 5: Valve No.3 opens and pressure hydrogen is stored in a high-pressure tank, while reactor 1 is prepared for the next compression cycle.

The above steps can also be described by the van't Hoff diagrams for the first- and second-stage materials, as depicted in Figure 1.7a. The red lines correspond to the sensible heating process for each reactor, the black dashed line to the hydrogenation process for both stages and the black solid line to the dehydrogenation process respectively. It is essential that the material selection should fulfill certain criteria in order to ensure that the operation of the compression system will be safe and efficient. According to Figure 1.7b, the plateau pressure for the hydrogenation process of the first-stage material should be sufficiently low in order for the material to be able to absorb the hydrogen from the low-pressure hydrogen supplier.

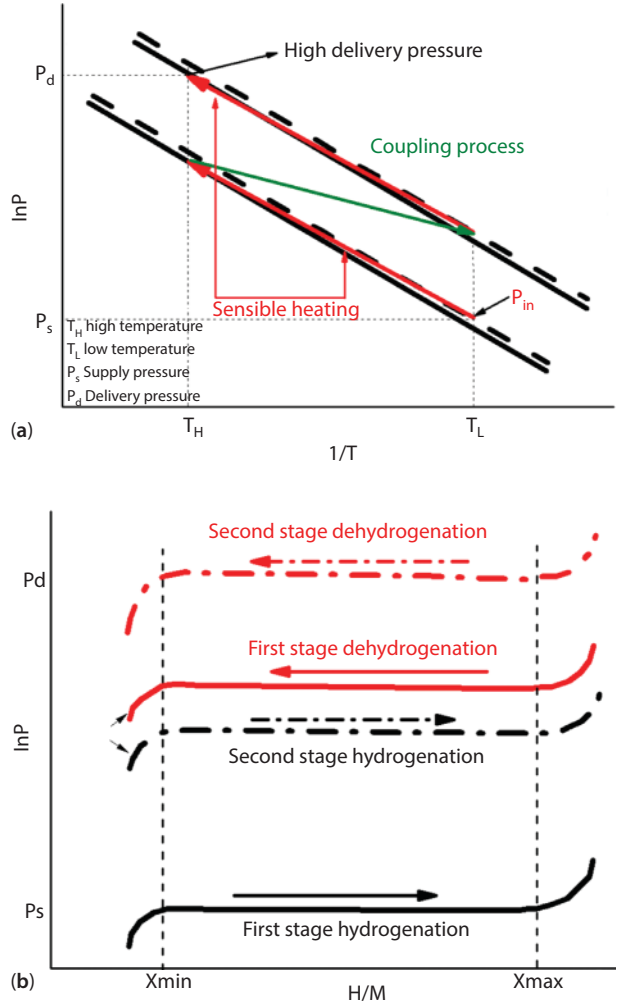

Figure 1.7 The van't Hoff diagram describing the operation steps of a two-stage metal hydride hydrogen compressor (a) and P-c-T plot describing the operation steps of a two-stage metal hydride hydrogen compressor (b).

Furthermore, it is important that the plateau pressure of the dehydrogenation process for the first-stage material should be higher than the plateau pressure for the hydrogenation of the second-stage material in order to ensure the presence of the pressure difference between the two reactors, which is going to act as the driving force to lead hydrogen from the first tank to the other. Finally, to achieve the highest compression ratio, the plateau pressure of the final stage must be as high as possible.

Table 1.2 Overview of solid hydrogen storage options.

Carbon and high surface area materials	**Chemical hydrides**	**Rechargeable hydrides**	**Chemical hydrides**
Activated charcoals	Encapsulated NaH	Alloys – Intermetallics	Ammonia Borozane
Nanotubes – Graphene	LiH and MgH_2 Slurries	Nanocrystalline	Aluminum Hydride
Graphite Nanofibers	CaH_2, $LiAlH_4$, etc.	Complex	

1.4.2 Metal Hydrides

The first step for the understanding of the operation of a multistage MHHC system is the detailed analysis on the background of the metal hydrides. The storage of hydrogen in solid materials has the potential to become a safe and efficient way to store energy for stationary, mobile and portable applications. There are four main groups of suitable materials for solid-state hydrogen storage applications: carbon and other high surface area materials; H_2O-reactive chemical hydrides; thermo-chemical hydrides; and rechargeable hydrides. Table 1.2 summarizes the potential materials of these groups.

Special attention has been given to the rechargeable hydride family of materials [40]. Metal hydrides can store atomic hydrogen in the metallic crystal structure. In the case of interstitial metal hydrides, the molecular hydrogen in the gas phase splits into atomic hydrogen on the surface of the material and then it diffuses into the atomic structure of the host metal [41]. Many different metallic compounds exist that can absorb hydrogen in this manner. In most cases, however, the storage does not occur at moderate temperature and pressure for practical storage purposes and the mass of the absorbed hydrogen is only a small fraction of the mass of the host metal [42].

1.4.3 Thermodynamic Analysis of the Metal Hydride Formation

1.4.3.1 Pressure-Composition-Temperature (P-c-T) Properties

The thermodynamic aspects of the hydride formation and information related to the thermodynamic properties of solid hydrides can be

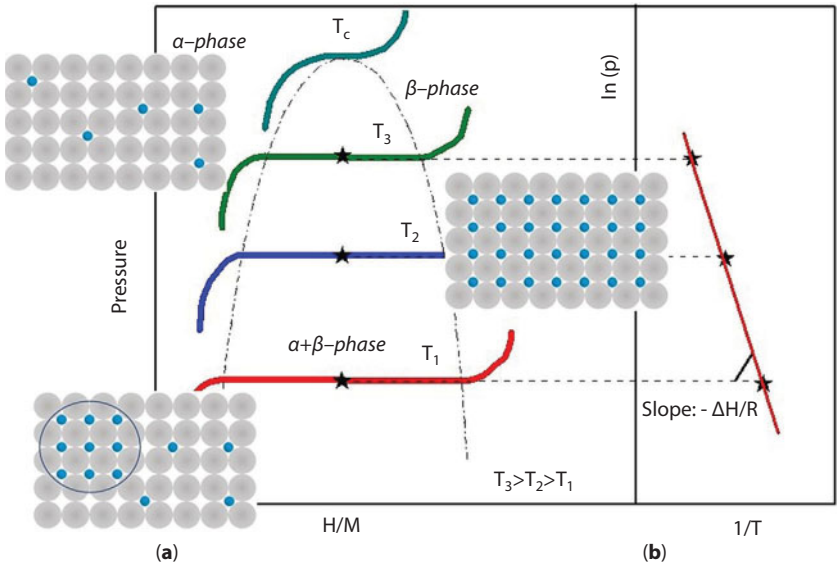

Figure 1.8 P-c-T curves at different temperatures (a) and van't Hoff plot (b). The upper left lattice represents the solid solution phase (α-phase), the lower left lattice represents the co-existence of the solid solution and the hydride phase (in the cycle) and finally the middle right lattice represents the hydride phase (β-phase).

extracted from the pressure-composition-temperature curve (P-c-T) [43]. Figure 1.8a illustrates typical isotherm curves of a reversible hydride. By measuring the changes in the hydrogen pressure and the corresponding changes of the hydrogen concentration in the metal at a predefined temperature, the P-c-T curve is constructed. Ideally, the P-c-T curves should present a flat plateau. The plateau results from the co-existence of a solid solution (α-phase) and the hydride phase (β-phase). The effect of temperature on the behavior of the isotherm curves is also depicted in Figure 1.8a. When the temperature increases, the plateau pressure also increases to higher levels until a critical temperature T_c. At temperatures higher than T_c, the plateau region disappears and the α-phase coverts to the β-phase continuously.

Initially, the metal dissolves only a small amount of hydrogen (<0.25 wt%), which creates a solid solution of hydrogen in the metal matrix and is called "α-phase" [44]. As the hydrogen pressure increases, the interactions between the atomic hydrogen and the metal atoms dominate locally and the nucleation of a new phase is initiated (β-phase). In the plateau region, the solid solution (α-phase) and the β-phase co-exist [45]. The length of

the plateau region determines the amount of hydrogen that can be stored reversibly with a small pressure variation. This phenomenon is explained from the Gibbs phase rule [46]:

$$F = 2 - \pi + N \tag{1.1}$$

where F is the degree of freedom, π is the number of phases and N is the number of chemical species. Thus, existence of one additional phase leads to the loss of a degree of freedom. When the stoichiometric hydride has formed, completely depleting the α-phase, one additional degree of freedom is regained and the additional absorption of hydrogen will now require a large pressure increase.

The equilibrium pressure, defined as the mid-plateau pressure P_{eq}, is related to the changes in enthalpy (ΔH) and entropy (ΔS) of the hydride formation/deformation as a function of temperature and is described by the van't Hoff law:

$$\ln P_{eq} = \frac{\Delta \mathrm{H}}{R_g \cdot T} - \frac{\Delta S}{R_g} \tag{1.2}$$

where P is the pressure *(Pa)*, *R (J/molK)* is the universal gas constant, and *T(K)* is the temperature. The value of enthalpy is an index of the metal hydride stability. The higher the absolute value of the enthalpy shows a high degree of stability of the hydride, low dissociation pressure and the requirement of rather elevated temperatures decomposition for hydrogen release [47]. By plotting the van't Hoff diagram lnP vs 1/T (Figure 1.8b) the enthalpy can be calculated from the slope (−ΔH/R) and the entropy from the intersection with y-axis. The entropy term corresponds mostly to the dissociation from molecular hydrogen to atomic during the sorption.

1.4.3.2 Slope and Hysteresis

The hysteresis between the hydrogenation and the dehydrogenation process is a phenomenon where the plateau corresponds to the hydrogenation is at a higher pressure than the plateau for the dehydrogenation, forming a hysteresis loop, as shown in Figure 1.9.

One explanation for the hysteresis is that the accommodation of the elastic and plastic energies is not equal for the hydrogenation and dehydrogenation [48]. Another aspect explains the hysteresis in terms of coherent

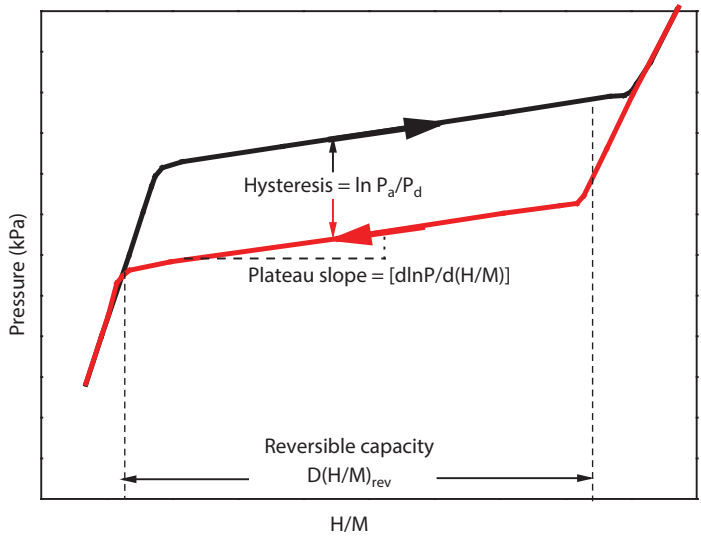

Figure 1.9 Representation of the hysteresis between the hydrogenation process (black isotherm) and the dehydrogenation process (red isotherm) and the slope of the plateau region.

strain [49]. Quantitatively, hysteresis is represented by the free energy difference:

$$\Delta G_{H_2} = R \cdot T \cdot \ln\left(\frac{P_A}{P_D}\right) \tag{1.3}$$

where P_A and P_D are the hydrogenation and dehydrogenation pressures respectively. For practical applications, hysteresis is an important feature because it has a critical impact at the service pressure of the hydride tank. For most applications, hysteresis should be as low as possible and this can be achieved by element substitution and heat treatment.

Another important characteristic of an experimental P-c-T curve is the plateau slope, which is represented by the following relation:

$$Slope = \frac{d(\ln P)}{d(H/M)} \tag{1.4}$$

1.4.4 Material Challenges for MHHCs

The usage of metal hydrides to compress hydrogen introduces several requirements regarding the material selection. The multistage operation

introduces strict requirements into the tuneability of the P-c-T characteristics, because during the coupling of the first stage (dehydrogenation process) and the second stage (hydrogenation) the isotherms of both stages must be synchronized [50]. One of the main drawbacks of the MHHC application is the proper selection of the materials for the first and the second stage to achieve high compression ratio while minimizing the operation temperature range [51]. Furthermore, some additional requirements are that the materials should present fast kinetics to ensure a fast compression cycle. The hydrides should also present relatively high reversible hydrogenation/dehydrogenation capacities to eliminate the total amount of the material. Low plateau slope for the isotherms of the materials, low hysteresis and cycle stability are also required. Finally, the cost of the compression process should be affordable, and the hydrides should present tolerance to the impurities [52]. There are several types of materials that meet the above requirements and will be analyzed in the following sections.

1.4.4.1 AB_5 Intermetallics

The AB_5 intermetallics consist of the element A (rare earth metal) and B (d-transition metal). A wide range of AB_5 intermetallics can be synthesized because it is relatively easy to substitute elements on the A or B sites. Element A is usually one of the lanthanide family such as La, Y or Zr. For industrial-based applications, mischmetal (Mm) is commonly used. Mm is a generic name used for an alloy or rare earth elements mixed in several proportions. The composition of the Mm normally includes up to 50% Ce and 45% La, with the rest being lesser amounts of Nd and Pr. The B site is mainly Ni, but substitution with other transition elements, such as Sn, Si, Ti and/or Al, is common to optimize the operation of the AB_5 intermetallics. When a partial substitution on the A or B sites with several elements takes place, the storage properties, such as the plateau pressure and slope, hysteresis, and degradation resistance to contamination, can be improved [53]. A very important aspect in the research and development of AB_5 intermetallics is the degradation of capacity over long-term cycling. This can result in reduction of the capacity and increased plateau slopes. For example, $LaNi_5$ can experience a reduction in capacity of 56% after 520 cycles at 500 K [54]. Improvements can be made by substituting Al or Sn [55]. For example, $LaNi_{4.8}Sn_{0.2}$ only experiences capacity loss of 10% after 1330 cycles at 500 K. The gravimetric storage capacity of the AB_5 intermetallics is substantially lower than the current U.S. DOE targets for mobile hydrogen storage applications. On the other hand, the AB_5-based intermetallics have remarkable cycling properties, including resistance to gaseous impurity contamination, long-term stability and high volumetric storage density.

1.4.4.2 AB_2 Intermetallics

The AB_2-type intermetallics, also known as Laves phase intermetallics, present mainly three major types of crystal structures of the Laves phase materials; the hexagonal C14, the cubic C15 and the hexagonal C36, where their main difference is the layer structure [56]. Laves phase forms the largest group of intermetallics and, thus, they present a wide range of properties. The stability of the hydrides depends on several factors such as geometry, packing density, valence electron concentration and/or the difference in electronegativity [57]. Laves phase intermetallics have been recognized to be attractive hydrogen storage materials, particularly the Zr-based intermetallics [58]. Such materials present relatively large hydrogen storage capacity, long cycling life and low cost, thus they are usually too stable at room temperature and sensitive to gas impurities. Normally, they require a high energy activation process which implies several hydrogenation/dehydrogenation cycles at low temperature and high pressure (hydrogenation process) and high temperature (dehydrogenation process) [59].

1.4.4.3 TiFe-Based AB-Type Intermetallics

Hydrogen storage using the AB-type alloys (TiFe based) can reach storage capacities close to 2 wt% under ambient conditions after the activation process and present excellent cyclic lifetime. They normally present an ordered body-centered cubic (BCC) structure and two distinct plateaus in the hydrogenation isotherm [60]. Partial substitutions of elements can also be used to modify the hydrogen sorption behavior, with the most dominant being the substitution of Fe with Mn and Ni, which can lower the pressure of the first plateau and stabilize the hydride.

1.4.4.4 Vanadium-Based BCC Solid Solution Alloys

Solid solution alloys formed by dissolving one or more hydrogen-absorbing metallic elements are another option for solid-state hydrogen storage [61]. Such materials do not necessarily present stoichiometric or near-stoichiometric compositions. They can be formed from several host solvents such as Pd, Ti, Zr and V. Out of the hydrogen storage point of view, the Pd-based alloys suffer from low gravimetric capacities and high cost. In addition, the Ti- and Zr-based solid solutions are too stable. V-based alloys have been found to present favorable hydrogenation properties and advantages in terms of gravimetric capacities. Although V is an expensive raw material, the substitution with the low-cost ferrovanadium has shown

promising results; thus, the Fe-containing V-based solid solutions can make feasible hydrogen storage materials [62].

1.5 Numerical Analysis of a Multistage MHHC System

A numerical model based on the coupled heat, mass and momentum conservation equations for the full description of the hydrogen compression using metal hydrides, is very useful for the understanding of the coupled reaction kinetics, the design of an effective compression system and the effective heat management of the compressor. The numerical description of a metal hydride hydrogen compressor is a challenging procedure, as it involves the coupling dehydrogenation/hydrogenation process between the two metal hydride beds with the reaction kinetics and the heat transfer phenomena. The following analysis is a step-by-step approach to the numerical description of a multistage metal hydride hydrogen compression system.

1.5.1 Assumptions

To simplify the problem of hydrogen storage in the interstitial sites of the metal lattice, which is a complex process containing chemical reactions, diffusion and heat transfer, it is essential to make some assumptions for modeling purposes. The following assumptions are the most common ones used for the numerical analysis of the hydrogenation/dehydrogenation process:

a) Initially uniform temperature and pressure profiles.
b) Hydrides thermal conductivity and specific heat capacity are assumed constant during the hydrogenation process. The specific heat capacity is very difficult to measure experimentally, particularly near the phase change conditions, and therefore a large error is introduced. The thermal conductivity of the hydride depends on the hydrogen concentration, the pressure and the temperature. However, when an effective heat management is being applied (addition of high thermal conductivity materials such as aluminum foams, internal heat management, etc.), the hydride thermal conductivity becomes irrelevant and the overall effective conductivity can be considered as constant [63].
c) The medium is in local thermal equilibrium, which implies that there is no heat transfer between solid and gas phases

d) Hydrogen is treated as an ideal gas from a thermodynamic point of view.
e) The bed void fraction remains constant and uniform throughout the reaction.
f) The characteristics (the kinetics and thermal properties) of the bed are unaffected by the number of loading and unloading cycles. Thus, the bed aging is neglected.
g) The metal hydride bed fills the entire space between the cooling tubes (perfect packing condition).

1.5.2 Physical Model and Geometries

The most common geometry that is used for solid-state hydrogen storage and compression is of cylindrical shape. The cylindrical metal hydride beds can be designed to allow both axial and/or radial hydrogen supply [70]. Furthermore, due to the large amount of internal stresses that the compression will introduce, the selection of cylindrical geometries is crucial, as they allow uniform distribution of the stresses. Figure 1.10 illustrates the cross section of the cylindrical reactor(s) that will be considered in the current analysis.

For the description needed for the numerical model and the simulation of the multistage hydrogen compression, the initial volume that the hydride powder occupies within the metal hydride tank is 50% of the tank's maximum theoretical volume. During the hydrogenation process, the volume of the hydride can increase up to 30% due to the lattice expansion, so it is necessary to have enough space available to avoid the stresses and eventually possible damage to the tank. The reactor properties are selected to be similar to the properties of commercially available stainless-steel reactors (usually stainless steel).

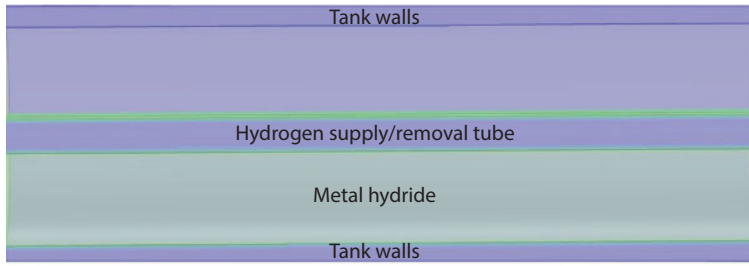

Figure 1.10 Schematic of a cylindrical metal hydride tank. The tank is filled up to 50% of the total volume of the tank due to the expansion of the metal hydride lattice during the hydrogen sorption.

1.5.3 Heat Equation

Assuming thermal equilibrium between the hydride powder and hydrogen gas, a single heat equation is solved instead of separate equations for solid and gas phases:

$$(\rho \cdot Cp)_{eff} \cdot \frac{\partial T}{\partial t} + (\rho_g \cdot C_{p_g} \cdot \overline{v}_g) \cdot \nabla T + \nabla \cdot (\mathrm{k}_{\mathrm{eff}} \cdot \nabla T) = \mathrm{Q}_H \quad (1.5)$$

The term Q_H (Wm^{-3}) in Equation 1.5 represents the heat that has been generated during the hydrogenation process or the amount of heat that is necessary for the dehydrogenation process. The amount of heat that is been produced during the hydrogenation process depends on several thermophysical properties, such as the enthalpy of formation ΔH (J/mol), the porosity of the material ε, the density changes during the reaction ($kg\ m^{-3}$), the reaction rate (s^{-1}) and the molecular mass of the stored gas ($kg\ mol^{-1}$) [64, 65].

The effective heat capacity is given by:

$$(\rho \cdot Cp)_{\mathrm{e}} = \varepsilon \cdot \rho_g \cdot C_{pg} + (1-\varepsilon) \cdot \rho_s \cdot C_{ps} \quad (1.6)$$

and the effective thermal conductivity is given by:

$$k_e = \varepsilon \cdot k_g + (1-\varepsilon) \cdot k_s \quad (1.7)$$

The terms ρ_g, C_{pg}, C_{ps} and m refer to the density of the gas phase ($kg\ m^{-3}$), the specific heat capacity of the gas phase ($J\ kg^{-1}K^{-1}$), the heat capacity of the solid phase and the kinetic term for the reaction respectively. The parameter that represents the void fraction is symbolized with ε. M_{H2} represents the molecular mass of hydrogen ($kg\ mol^{-1}$) and T represents the temperature (K).

1.5.4 Hydrogen Mass Balance

The equation that describes the diffusion of hydrogen inside the metal matrix is given by:

$$\varepsilon \cdot \frac{\partial(\rho_g)}{\partial t} + div(\rho_g \cdot \vec{v}_g) = \pm Q \quad (1.8)$$

where (−) refers to the hydrogenation process and (+) to the dehydrogenation process, v_g is the velocity of gas during diffusion within the metal

lattice and Q is the mass source term describing the amount of hydrogen mass diffused per unit time and unit volume in the metal lattice.

1.5.5 Momentum Equation

The velocity of a gas during diffusion through a porous medium can be described by Darcy's law. By neglecting the gravitational effect, the equation which describes the velocity of gas inside the metal matrix is given by:

$$\vec{v}_g = -\frac{K}{\mu_g} \cdot grad(\vec{P}_g) \tag{1.9}$$

where $K\ (m^2)$ is the permeability of the solid and $\mu_g\ (Pa\ s)$ is the dynamic viscosity of gas and $P_g\ (Pa)$ is the pressure of gas within the metal matrix.

1.5.6 Kinetic Expressions for the Hydrogenation and Dehydrogenation

The kinetic description for the hydrogenation process per unit time and volume is described by the following equation:

$$m_a = C_a \cdot \exp\left[-\frac{E_a}{R_g \cdot T}\right] \cdot \ln\left[\frac{p_g}{P_{eq}}\right] \cdot (\rho_{ss} - \rho_s) \tag{1.10}$$

The amount of hydrogen released from the hydride bed is given by:

$$m_d = C_d \cdot \exp\left[-\frac{E_d}{R_g \cdot T}\right] \cdot \left(\frac{P_{eq} - p_g}{P_{eq}}\right) \cdot \rho_s \tag{1.11}$$

where ρ_s and ρ_{ss} are the density of the hydride at any time and at saturation state respectively $(kg\ m^{-3})$; $C_a(s^{-1})$ and $C_d(s^{-1})$ refer to the pre-exponential constants for the hydrogenation and dehydrogenation process and the E_a $(J\ mol^{-1})$ and E_d $(J\ mol^{-1})$ are the activation energy for hydrogenation and dehydrogenation process respectively.

The constants C_a and C_d as well as the activation energies for both the hydrogenation process and the dehydrogenation E_a and E_d can be extracted from the experimental results. The first step is to obtain the kinetics of the

hydrogenation and dehydrogenation process at several temperatures, and the next step is the design of the van't Hoff plot (lnP *vs* 1/T). From the slope of the plot the activation energy can be extracted and from the intersect of the plot with the y-axis the constant can also be calculated [66, 67]. The saturation density is determined by calculating the hydride concentration ($mol\ m^{-3}$) after the storage process and the volume of the hydride after the expansion process that occurs during the hydrogenation.

1.5.7 Equilibrium Pressure

To incorporate and consider the effect of hysteresis and the plateau slope on the equilibrium pressure P_{eq}, the following equation can be used [68, 69]:

$$\ln\frac{P_{eq}}{10^5} = \left\{\left[\frac{\Delta H}{RT} - \frac{\Delta S}{R}\right] + (\varphi_s \pm \varphi_0)\cdot\tan\left[\pi\cdot\left(\frac{x}{x_{sat}} - \frac{1}{2}\right)\right] \pm \frac{S}{2}\right\} \quad (1.12)$$

The plateau slope is given by the flatness factors φ_s and φ_0; S represents the hysteresis effect which is given by ($\ln P_{abs}/P_{des}$), designated '+' for hydrogenation and '–' for dehydrogenation. The terms x and x_{sat} represent the local hydride concentration ($mol\ m^{-3}$) at any given time and at saturation respectively. The flatness factors and the hysteresis effects can be extracted experimentally by using the data collected from the hydrogenation kinetics and isotherms.

1.5.8 Coupled Mass and Energy Balance

The situation of the system during the coupling between the first and the second stage after opening the valve between them, has an important impact on the compression cycle and the numerical description of such process is very challenging. The number of hydrogen moles inside the interconnector between the two reactors is updated from the following equation:

$$n_t = n_{in} + n_{des} - n_{abs} \quad (1.13)$$

The pressure of hydrogen inside the interconnector is updated by:

$$p_t = \frac{n_t \cdot R_g \cdot T}{V_1 + V_2} \quad (1.14)$$

where V_1 and V_2 are the volumes of the first- and second-stage tanks respectively. The term T represents the temperature of the gas inside the interconnector. By considering the pressure of hydrogen in the interconnector, we can use it as the driving force to lead hydrogen from the first stage to the second, therefore the kinetic equations for both hydrogenation and dehydrogenation process during the coupling are provided by the following equations:

$$m_{abs} = C_{abs} \cdot \exp\left(\frac{-E_a}{R_g \cdot T}\right) \cdot \ln\left(\frac{p_t}{P_{eq}}\right) \cdot (\rho_{ss} - \rho_s) \tag{1.15}$$

for hydrogenation and

$$m_{des} = C_{des} \cdot \exp\left(\frac{-E_d}{R_g \cdot T}\right) \cdot \left(\frac{P_{eq} - p_t}{P_{eq}}\right) \cdot (\rho_s) \tag{1.16}$$

for the dehydrogenation process.

1.5.9 Validation of the Numerical Model

A very important process that is necessary after the proposal of a mathematical model is the investigation of its validity. Thus, the comparison of the numerical data with solid experimental results is a reliable method of validation. A very reliable way to validate the predicted numerical data with the real-life experimental, is the comparison of the hydrogenation/dehydrogenation kinetics and the temperature behavior during the hydrogen storage/release. For the purposes of the current analysis, $MmNi_{4.6}Al_{0.4}$ was used for the validation process. The experimental results were collected by operating a commercial Sievert-type apparatus. The amount of powder inserted in the bed was 0.58 g. Figure 1.11 shows the tank geometry used for the validation process. The hydrogen supplied had an initial pressure of 15 bar.

Figure 1.12 presents the comparison between the experimental data and the simulation results for the temperature profile (red line and red dots respectively) and the hydrogen storage capacity (black line and black dots respectively). The results of the numerical work compared to the experimental data present good agreement with a maximum deviation of less than 5%.

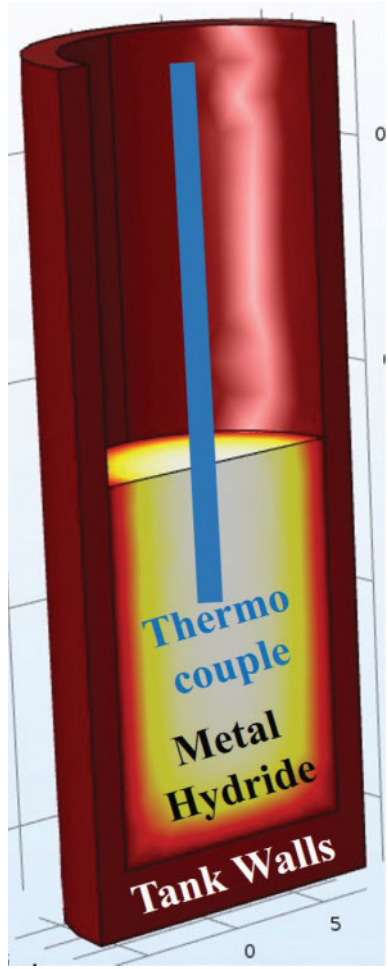

Figure 1.11 Schematic of a cylindrical metal hydride tank used for the validation process. The tank is filled up to 50% of the total volume of the tank due to the expansion of the metal hydride lattice during the hydrogen sorption. A thermocouple was installed to measure the temperature of the hydride during the hydrogenation/dehydrogenation.

1.5.10 Material Selection for a Three-Stage MHHC

The importance of the proper material selection for a multistage MHHC system has been analyzed in detail. In the current analysis, a detailed example of a three-stage MHHC system will be introduced. Three different materials were considered for the different stages of the compression. For the first stage, $LaNi_5$ was considered, while for the second stage, another

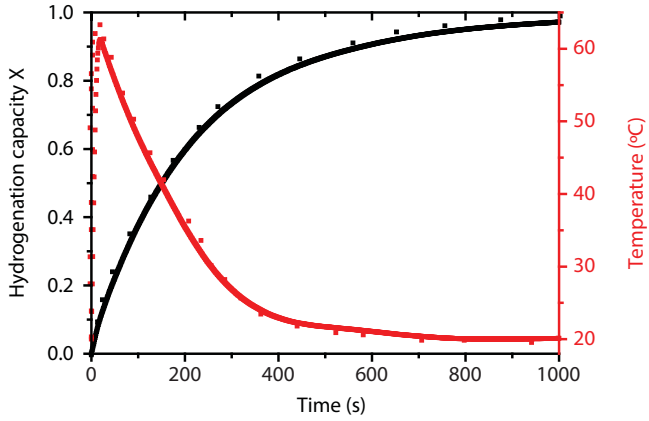

Figure 1.12 Validation of the predicted temperature profile (red) and the hydrogen storage capacity (black) for $MmNi_{4.6}Al_{0.4}$.

AB_5-Intermetallic ($MmNi_{4.6}Al_{0.4}$) was used. Finally, for the third stage, an AB_2-Laves phase intermetallic has been introduced. The hydrogenation process was selected to take place at 20 °C and the dehydrogenation at 130 °C. Table 1.3 presents the equilibrium pressures for the selected materials at the correspondent temperatures for the hydrogenation and the dehydrogenation.

1.5.11 Temperature Evolution of the Complete Three-Stage Compression Cycle

Figure 1.13 depicts the bed average temperature evolution for the complete compression cycle with time, when utilizing $LaNi_5$, $MmNi_{4.6}Al_{0.4}$ and an *AB_2-Laves phase intermetallic* for the compression stages. The sensible heating processes are not included in the figure, but they are described by the vertical black dashed line. During the initial stage of the hydrogenation process for the first stage, due to the exothermic nature of the storage reaction, a sudden increase of the bed's temperature is observed; then, due to the heat management, the temperature gradually decreases. The sudden temperature increase is explained from the poor thermodynamic properties of the hydride powders and especially the poor thermal conductivity, which does not allow the generated amount of heat to be transferred from the hydride bed to the external cooling sink; thus, the amount of heat is stored in the metal hydride bed, resulting in a sudden rise of the temperature during the first step of the storage. After the end of the hydrogenation

Table 1.3 Values of the equilibrium pressures for the selected materials at the desired storage/release temperatures.

First stage	**Hydrogenation (20 °C) Dehydrogenation (130 °C)**	**Second stage**	**Hydrogenation (20 °C) Dehydrogenation (130 °C)**	**Third stage**	**Hydrogenation (20 °C) Dehydrogenation (130 °C)**
$LaNi_5$	P_{eq} = 1.94 bar P_{eq} = 41.39 bar	$MmNi_{4.6}Al_{0.4}$	P_{eq} = 2.69 bar P_{eq} = 111.89 bar	AB_2	P_{eq} = 33.03 bar P_{eq} = 325.75 bar

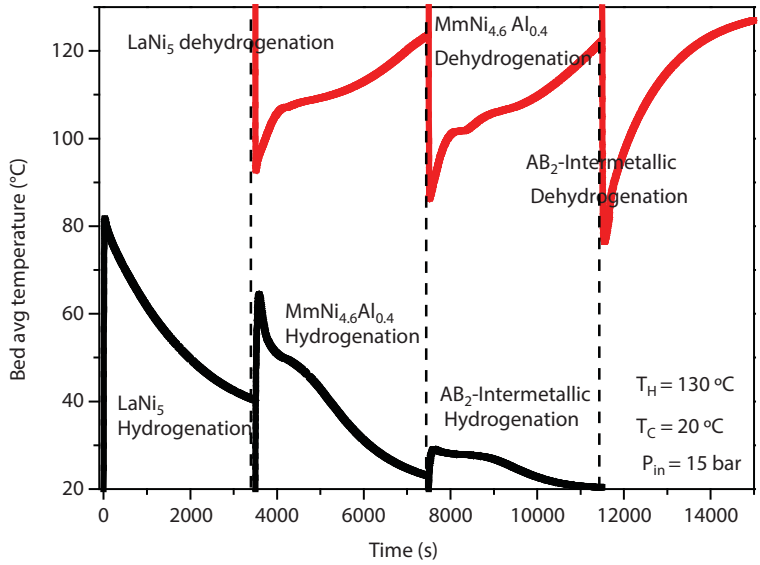

Figure 1.13 Bed average temperature evolution during the complete three-stage compression process when using $LaNi_5$, $MmNi_{4.6}Al_{0.4}$ and AB_2 Laves phase Intermetallic as the stages of the compression.

process, a sensible heating of the hydride bed takes place, where the equilibrium pressure of the material increases as per van't Hoff's law. When the dehydrogenation process begins, the necessary amount of heat has not been transferred from the external heater (130 °C) to the hydride bed due to the poor thermal conductivity, and initially the necessary amount of heat is provided by the hydride itself, resulting in a sudden decrease of the bed's temperature, as illustrated in Figure 1.13. Therefore, an effective heat management scenario is essential for the dehydrogenation.

1.5.12 Pressure and Storage Capacity Evolution During the Complete Three-Stage Compression Cycle

The average pressure of the operating metal hydride beds during the three-stage compression cycle is presented in Figure 1.14.

Initially, a low-pressure hydrogen supplier (a commercial electrolyzer) is attached to the first stage and provides hydrogen at pressure 15 bar; due to the pressure difference, hydrogen enters the bed. By maintaining a low temperature of the first stage, hydrogen is stored at the lattice of the material, indicating a gradual reduction of the hydrogen pressure during the first

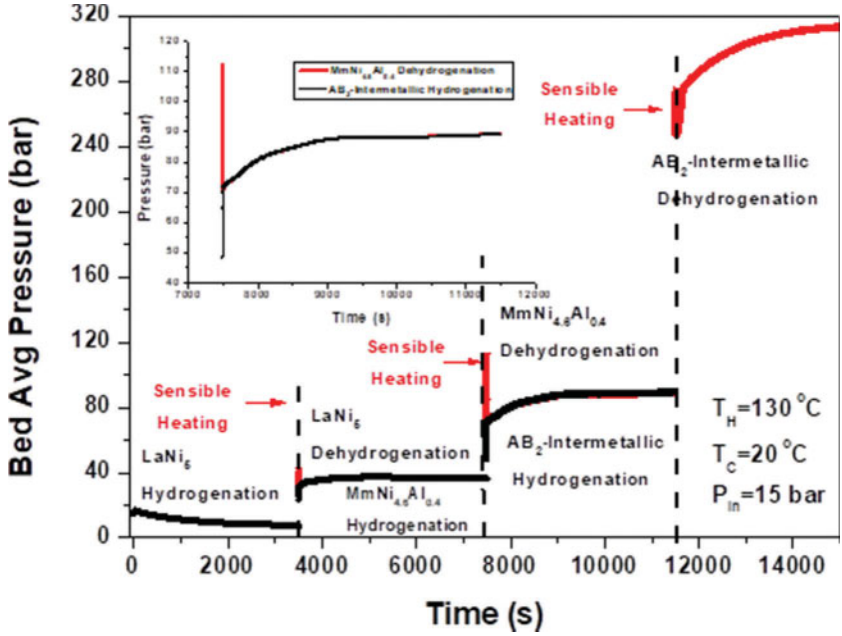

Figure 1.14 Bed average pressure evolution during the complete three-stage compression process when using $LaNi_5$, $MmNi_{4.6}Al_{0.4}$ and AB_2-Intermetallic as the stages of the compression.

step of the pressure evolution. The pressure of hydrogen at the end of the hydrogenation process is almost 7 bar. After the hydrogenation, a sensible heating of the reactor occurs. During this process, there is a sharp increase in the bed's pressure, due to the increase of the equilibrium pressure as per van't Hoff's law. After the sensible heating process, the coupled dehydrogenation-hydrogenation procedure takes place. During the initial step of the coupling, the equilibrium pressure of the first reactor decreases while the equilibrium pressure of the second reactor increases sharply due to the very fast kinetics between the two reactors. After this rapid initial stage of the coupling process, the pressure inside of both reactors increases due to the presence of a driving potential. This process is accurately described in the inlaid graph in Figure 1.14. At the end of the first coupled process the pressure reaches 38–39 bar at the second reactor. A subsequent sensible heating process occurs where the pressure increases up to 110 bar. Then, the second coupling between the second (dehydrogenation) and third (hydrogenation) stage is initiated, where the pressure Trent is similar to the behavior described for the first coupling; the difference is that the second

coupling takes place at a higher pressure range. The pressure of hydrogen after the second coupling is almost 89 bar. Finally, during the last dehydrogenation process in the high-pressure hydrogen tank the final hydrogen delivery pressure is almost 320 bar, indicating a pressure ratio of 22:1 when the compressor operates between 20–130 °C.

1.5.13 Importance of the Number of Stages and Proper Selection

Both two-stage and three-stage compression systems operate under the same principle; by utilizing metal hydrides connected in series to pressurize hydrogen. The major difference is the number of stages (and consequently the number of materials) used during the operation. It is preferable to use more stages for a compression system when strict requirements for the temperature and pressure arise. For example, if the heat management is based on cold/hot water respectively, the operational temperatures will be 90–95 °C during the dehydrogenation; thus, the compression ratio when using a two-stage compressor will be relatively small according to previous analysis [54], as at lower temperatures the maximum theoretical pressure will also be lower than the target pressure. A possible solution to that engineering problem is the addition of an extra stage (material) suitable for the applicable conditions. As already mentioned, the proper selection of materials is crucial for the effective operation of the compressor in order to achieve the maximum driving force during the coupling between the stages. Thus, the operation of a three-stage system can provide flexibility in the use of material compared to a two-stage compressor. For example, by comparing the results when operating the three-stage compressor presented in the current chapter between 20–130 °C to compress 60 g of hydrogen, where the compression ratio was found to be 22:1, to the results of a two-stage compression system [54], where an almost similar compression ratio was found, it is obvious that for the selection of a two- or three-stage (or even larger number of stages) system, someone needs to decide which parameters need to be sacrificed in order for the final pressure to be achieved. For a three-stage system, the duration of the compression cycle is higher, as is the energy consumption (as more modules need to be thermodynamically and mechanically treated). On the other hand, since the pressure doesn't have to be increased directly (in one-step process), but can involve an intermediate stage, a three-stage compressor offers more flexibility and choices on the material selection, while for the two-stage compression the material selection has to be very strict and the choices might not be plentiful. Thus, it is obvious that the selection of the proper

compression system depends on many parameters such as the compression ratio, the cycle time, the operation conditions, the size and the energy consumption.

1.6 Conclusions

In the current chapter, the use of metal hydrides for the establishment of a multistage compression system was analyzed. The importance of the hydrogen economy for the future generations was discussed and the use of hydrogen-based applications, both portable and stationary, was highlighted. A detailed comparison of the available systems for hydrogen compression was introduced. The importance of the proper selection of metal hydrides was discussed and an analysis of the advantages and disadvantages of available materials for metal hydride compression were presented. A detailed discussion on the development of a validated numerical analysis regarding a three-stage compression system was performed; the importance of the proper material selection and the number of stages was highlighted.

Acknowledgments

Dr. Evangelos Gkanas would like to express his gratitude to Dr. Sofoklis Makridis, Dr. Athanasios Stubos, Dr. Alastair Stuart, Professor David Grant and Professor Gavin Walker for their support and mentoring during his research endeavour in metal hydride hydrogen compression systems.

Nomenclature

		Subscripts	
C_a	Absorption Reaction Constant, s^{-1}	a	Absorption
C_d	Desorption Reaction Constant, s^{-1}	d	Desorption
C_p	Specific Heat, J/kg^{-K}	e	Effective
E_a	Activation Energy for Absorption $J/molH_2$	eq	Equilibrium
h	Heat Transfer Coefficient, W/m^2K	f	External Cooler
k	Thermal Conductivity, W/m^{-K}	g	Gas
K	Permeability, m^2	i	Initial

M	Molecular Weight, kg/mol	s	Solid
m	Kinetic Expression	ss	Saturation
n	Number of Hydrogen Moles	Greek Letters	
P	Pressure, bar	ε	Porosity
R	Gas Global Constant, J/mol^{-K}	μ	Dynamic Viscosity, kg/ms
t	Time (s)	ρ	Density, kg/m^3
T	Temperature (K)	ΔH	Reaction Enthalpy, J/mol
v	Gas Velocity, m/s	ΔS	Reaction Entropy, J/mol-K
V	Volume, m^3		

References

1. The European Commission. Towards a European strategy for the security of energy supply. EUR-Lex 1–111, 2000.
2. Gkanas, E.I., Steriotis, T.A., Stubos, A.K., Myler, P. & Makridis, S.S., A complete transport validated model on a zeolite membrane for carbon dioxide permeance and capture. *Appl. Therm. Eng*. 74, 36–46, 2015.
3. Ipcc. IPCC Special Report on Emissions Scenarios. *Change* 599, 2000.
4. Züttel, A. *et al.*, Hydrogen Storage, in: *Hydrogen as a Future Energy Carrier*. Wiley-VCH Verlag GmbH & Co. KGaA, pp. 165–263, 2008.
5. Bossel, U., Does a hydrogen economy make sense?. *Proceedings of the IEEE*, 94(10), pp. 1826–1836, 2006.
6. Bockris, J.O., Smith, D. and Veziroğlu, T.N., *Solar Hydrogen Energy: The Power to Save the Earth*. London: Macdonald Optima, p. 147, 1991. file://catalog.hathitrust.org/Record/007993195.
7. Bockris, J., Veziroglu, T., A solar-hydrogen energy system for environmental compatibility. *Environmental Conservation*, 12(2), 105–118, 1985.
8. Conte, M., Iacobazzi, A., Ronchetti, M., Vellone, R., Hydrogen economy for a sustainable development: State-of-the-art and technological perspectives. *J. Power Sources* 100, 171–187, 2001.
9. Steinberg, M., Cheng, H.C., Modern and prospective technologies for hydrogen production from fossil fuels. *Int. J. Hydrogen Energy* 14, 797–820, 1989.
10. Ewan, B.C.R., Allen, R.W.K., A figure of merit assessment of the routes to hydrogen. *Int. J. Hydrogen Energy* 30, 809–819, 2005.
11. United States. Dept. of Energy. Office of Science. Basic research needs for the hydrogen economy. Report of the Basic Energy Sciences Workshop on Hydrogen Production, Storage and Use, May 13–15, 2003, *Basic Research Needs for the Hydrogen Economy*, 2004.

12. Sandrock, G., Panoramic overview of hydrogen storage alloys from a gas reaction point of view. *J. Alloys Compd*. 293, 877–888, 1999.
13. da Rosa, A., *Fundamentals of Renewable Energy Processes*, Academic Press, 2009.
14. Gkanas, E.I., Khzouz, M., Numerical analysis of candidate materials for multistage metal hydride hydrogen compression processes. *Renew. Energy* 111, 484–493, 2017.
15. Sandí, G., Hydrogen storage and its limitations. *Electrochem. Soc. Interface Fall*, 40–44, 2004.
16. Satyapal, S., Petrovic, J., Read, C., Thomas, G., Ordaz, G., The U.S. Department of Energy's National Hydrogen Storage Project: Progress towards meeting hydrogen-powered vehicle requirements. *Catal. Today* 120, 246–256, 2007.
17. Gkanas, E.I., *et al.*, Hydrogenation behavior in rectangular metal hydride tanks under effective heat management processes for green building applications. *Energy* 142, 518–530, 2018.
18. Niaz, S., Manzoor, T., Pandith, A.H., Hydrogen storage: Materials, methods and perspectives. *Renew. Sust. Energ. Rev.* 50**,** 457–469, 2015.
19. Léon, A. (Ed.), Hydrogen technology. mobile and portable applications. *J. Chem. Inf. Model.* 53, 2013.
20. LX-Series™, Low pressure gas compressors, http://www.hydropac.com/how-intensifiers-work.html, 2017.
21. LX-Series™, Low pressure gas compressors, Literature, Compressor Capacity, http://www.hydropac.com/literature/LX%20Capacity%20Chart%20Hydrogen%20scfm%2010–2008.pdf, 2017.
22. Arjomand Kermani, N., Rokni, M., Heat transfer analysis of liquid piston compressor for hydrogen applications. *Int. J. Hydrog. Energy* 40, 11522–11529, 2015.
23. Predel, T., Schlücker, E., Ionic liquids in oxygen compression. *Chem. Eng. Technol.* 32, 1183–1188, 2009.
24. The Linde Group, Report. http://www.the-linde-group.com. 2017.
25. Kermani, N.A., Petrushina, I., Nikiforov, A., Rokni, M., Metal alloys for the new generation of compressors at hydrogen stations: Parametric study of corrosion behavior. *Renew. Energy* 116, 805–814, 2018.
26. BASF, Ionic liquids as engineering fluids, http://www.intermediates.basf.com/chemicals/web/en/function/conversions:/publish/content/news-and-publications/brochures/download/BASF_Ionic_Liquids_Engineering_Fluids.pdf, 2017.
27. Bloch, H.P., *A Practical Guide to Compressor Technology*, 2nd ed. Wiley, 2005.
28. How diaphragm reciprocating compressor works, http://www.sundyne.com/Products/Compressors/Legacy-Brands/PPI-Pressure-Products-Industries/How Diaphragm-Reciprocating-Compressors-Work, 2017.
29. Grigoriev, S.A., Djous, K.A., Millet, P., Kalinikov, A.A., Porembskiy, V.I., Fateev, V.N., *et al.*, Characterization of PEM electrochemical hydrogen compressors. Fundamentals and Developments of Fuel Cells Conference FDFC, Nancy, France, 10–12 December, 2008.

30. STORHY, Publishable Final Activity Report. Hydrogen Storage Systems for Automotive Application, http://www.storhy.net/pdf/StorHy_FinalPublActivityReport_FV.pdf, 2008.
31. Casati, C., Longhi, P., Zanderighi, L., Bianchi, F., Some fundamental aspects in electrochemical hydrogen purification/compression. *J. Power Sources* 180, 103–113, 2008.
32. Ströbel, R., *et al.*, The compression of hydrogen in an electrochemical cell based on a PE fuel cell design. *J. Power Sources* 105, 208–215, 2002.
33. Barbir, F., PEM electrolysis for production of hydrogen from renewable energy sources. *Sol. Energy* 78, 661–669, 2005.
34. Rohland, B., Eberle, K., Strobel, R., Scholta, J., Garche. J., Electrochemical hydrogen compressor. *Electrochim. Acta* 43, 3841–3846, 1998.
35. Bouwman, P., Electrochemical hydrogen compression (EHC) solutions for hydrogen infrastructure. *Fuel Cells Bull.* 2014, 12–16, 2014.
36. FCE to demo hydrogen co-production, high-pressure compressor. *Fuel Cells Bull.*, 2010(11), 8–9, 2010.
37. HyET electrochemical hydrogen compressor reaches 800 bar rating. *Fuel Cells Bull.* 2011, 8, 2011.
38. Gkanas, E.I., Makridis, S.S., Stubos, A.K., Modeling and simulation for absorption-desorption cyclic process on a three-stage metal hydride hydrogen compressor. *Comput. Aided Chem. Eng.* 32, 379–384, 2013.
39. Gkanas, E.I., *et al.*, Efficient hydrogen storage in up-scale metal hydride tanks as possible metal hydride compression agents equipped with aluminium extended surfaces. *Int. J. Hydrogen Energy* 41, 10795–10810, 2016.
40. Makridis, S.S., *et al.*, Polymer-stable magnesium nanocomposites prepared by laser ablation for efficient hydrogen storage. *Int. J. Hydrogen Energy* 38, 11530–11535, 2013.
41. Koultoukis, E.D., *et al.*, High-temperature activated AB2 nanopowders for metal hydride hydrogen compression. *Int. J. Energy Res.* 38, 477–486, 2014.
42. Corbo, P., Migliardini, F., Veneri, O., Hydrogen fuel cells for road vehicles. *Media* 245, 2011.
43. Chandra, D., Reilly, J.J., and Chellappa, R., Metal hydrides for vehicular applications: The state of the art. *JOM* 58, 26–32, 2006.
44. Edwards, P.P., Kuznetsov, V.L., David, W.I.F., and Brandon, N.P. Hydrogen and fuel cells: Towards a sustainable energy future. *Energy Policy* 36, 4356–4362, 2008.
45. Walker, G. (Ed.), *Solid-State Hydrogen Storage: Materials and Chemistry*, Woodhead Publishing, 2008.
46. Smith, J.M., Van Ness, H.C., Abbott, M.M., *Introduction to Chemical Engineering Thermodynamics*. Chemical Engineering Series, 27, McGraw Hill, 2005.
47. Klebanoff, L., *Hydrogen Storage Technology: Materials and Applications*. p. 91, CRC Press, 2012.
48. Balasubramaniam, R. Hysteresis in metal hydrogen systems. *J. Alloys Compd.* 253, 203–206, 1997.

49. Hirscher, M., Borgschulte, A., *Handbook of Hydrogen Storage: New Materials for Future Energy Storage*. *Ceramic*, Wiley-VCH, 2010.
50. Bedbak, S.S., Gopal, M.R., Performance analysis of a compressor driven metal hydride cooling system. *Int. J. Hydrogen Energy* 30, 1127–1137, 2005.
51. Bowman, R.C., Fultz, B., Metallic hydrides I: Hydrogen storage and other gas-phase applications. *MRS Bull.* 27, 688–693, 2002.
52. Førde, T., Maehlen, J.P., Yartys, V.A., Lototsky, M.V., Uchida, H., Influence of intrinsic hydrogenation/dehydrogenation kinetics on the dynamic behaviour of metal hydrides: A semi-empirical model and its verification. *Int. J. Hydrogen Energy* 32, 1041–1049, 2007.
53. Liang, G., Huot, J., Schulz, R., Hydrogen storage properties of the mechanically alloyed LaNi5-based materials. *J. Alloys Compd.* 320, 133–139, 2001.
54. Gkanas, E.I., *et al.*, Numerical study on a two-stage metal hydride hydrogen compression system. *J. Alloys Compd.* 645, S18–S22, 2015.
55. Bowman, R.C., Luo, C.H., Ahn, C.C., Witham, C.K., Fultz, B., The effect of tin on the degradation of LaNi5-ySny metal hydrides during thermal cycling. *J. Alloys Compd.* 217, 185–192, 1995.
56. Shaltiel, D., Jacob, I., Davidov, D., Hydrogen absorption and desorption properties of AB2 Laves-phase pseudobinary compounds. *J. Less-Common Met.* 53, 117–131, 1977.
57. Shoemaker, D.P., Shoemaker, C.B., Concerning atomic sites and capacities for hydrogen absorption in the AB2 Friauf-Laves phases. *J. Less-Common Met.* 68, 43–58, 1979.
58. Feng, F., Geng, M., Northwood, D.O., Electrochemical behaviour of intermetallic-based metal hydrides used in Ni/metal hydride (MH) batteries: A review. *Int. J. Hydrogen Energy* 26, 725–734, 2001.
59. Gkanas, E.I., Makridis, S.S., Effective thermal management of a cylindrical MgH2 tank including thermal coupling with an operating SOFC and the usage of extended surfaces during the dehydrogenation process. *Int. J. Hydrogen Energy* 41, 5693–5708, 2016.
60. Psoma, A., Sattler, G., Fuel cell systems for submarines: From the first idea to serial production. *J. Power Sources* 106, 381–383, 2002.
61. Iba, H., Akiba, E., Hydrogen absorption and modulated structure in Ti–V–Mn alloys. *J. Alloys Compd.* 253–254, 21–24, 1997.
62. Tamura, T., Kazumi, T., Kamegawa, A., Takamura, H., Okada, M., Protium absorption properties and protide formations of Ti-Cr-V alloys. *J. Alloys Compd.* 356–357, 505–509, 2003.
63. Melnichuk, M., Silin, N., Guidelines for thermal management design of hydride containers. *Int. J. Hydrogen Energy* 37, 18080–18094, 2012.
64. Gambini, M., Stilo, T., Vellini, M., Montanari, R., High temperature metal hydrides for energy systems Part A: Numerical model validation and calibration. *Int. J. Hydrogen Energy* 42, 3–10, 2017.
65. Busqué, R., Torres, R., Grau, J., Roda, V., Husar, A., Effect of metal hydride properties in hydrogen absorption through 2D-axisymmetric modeling and

experimental testing in storage canisters. *Int. J. Hydrogen Energy* 42, 19114–19125, 2017.
66. Mohammadshahi, S.S., Gray, E.MacA., Webb, C.J., A review of mathematical modelling of metal-hydride systems for hydrogen storage applications. *Int. J. Hydrogen Energy* 41, 3470–3484, 2016.
67. Muthukumar, P., Linder, M., Mertz, R., Laurien, E., Measurement of thermodynamic properties of some hydrogen absorbing alloys. *Int. J. Hydrogen Energy* 34, 1873–1879, 2009.
68. Muthukumar, P., Singh Patel, K., Sachan, P., Singhal, N., Computational study on metal hydride based three-stage hydrogen compressor. *Int. J. Hydrogen Energy* 37, 3797–3806, 2012.
69. Nishizaki, T., Miyamoto, K., Yoshida, K., Coefficients of performance of hydride heat pumps. *J. Less-Common Met.* 89, 559–566, 1983.
70. Mazzucco, A., *et al.*, Bed geometries, fueling strategies and optimization of heat exchanger designs in metal hydride storage systems for automotive applications: A review. *Int. J. Hydrogen Energy* 39, 17054–17074, 2014.

2

Nitrogen-Based Hydrogen Storage Systems: A Detailed Overview

Ankur Jain[1,*], Takayuki Ichikawa[1,2] and Shivani Agarwal[3,*]

[1]Natural Science Centre for Basic Research and Development, Hiroshima University, Kagamiyama, Higashi-Hiroshima, Japan
[2]Graduate School of Engineering, Hiroshima University, Kagamiyama, Higashi-Hiroshima, Japan
[3]Department of Physics, JECRC University, Jaipur, India

Abstract

Hydrogen as an energy carrier has been proposed as an efficient alternative to the current energy infrastructure due to its cleanliness, unlimited supply and higher energy content per unit mass. The solid-state hydrogen storage offers a potential and safe solution compared to compressed gas as it requires no essential pressure. The search for a material having suitable properties with high gravimetric and volumetric capacities is a crucial material challenge for moving towards an energy economy based on hydrogen. Properties of H_2 storing materials are required to be lightweight, low cost, excellent kinetics of adsorption and desorption, and recyclability. Nitrogen-containing systems have emerged as promising materials for hydrogen storage. The discovery of the interaction between nitrides and hydrogen more than a decade before, opened up a new class of metal-N-H systems. Since the preliminary studies on lithium amide, several double-cation complex amide systems have been developed. The research field of these amide-imide systems has matured enough for their fundamental understanding, and several new and promising combinations are being currently explored, with particular interest in sodium amide. These systems are ready to be implemented for practical applications. In addition to these metal-N-H systems, ammonia has also been considered as an attractive energy carrier in recent years owing to its high hydrogen content, i.e., 17.7 wt%. Despite its high hydrogen content, ammonia as hydrogen storage material is still far from being used for practical applications because of its efficient

**Corresponding authors*: ankur.j.ankur@gmail.com; shivaniphy@gmail.com

Mehmet Sankir and Nurdan Demirci Sankir (eds.) Hydrogen Storage Technologies, (39–88) © 2018 Scrivener Publishing LLC

production, storage, and dissociation. The present chapter presents an overview of the developments of metal-N-H systems in terms of their crystal structure, thermodynamics, sorption properties and future aspects, as well as progress related to ammonia production, storage, and dissociation.

Keywords: Amide-imide system, lithium amide, sodium amide, double-cation amide, NH_3 synthesis, NH_3 storage, NH_3 decomposition, NH_3 fuel cell

2.1 Introduction

Hydrogen storage material has been a subject of intensive research during the last few decades. To establish hydrogen economy, a suitable and safe hydrogen storage media is needed, which has been offered by solid-state hydrogen storage materials. During the exploration for suitable material for solid-state hydrogen storage [1, 2], a breakthrough arose with the introduction of a new family based on nitride material. Although the materials of this family have been known for more than a century, the exposure of nitride with hydrogen was opened up in 2002 in a two-step reaction [1]. The first member of this family, i.e., $LiNH_2$, can absorb 11 wt% H_2 via the following reaction [3]:

$$Li_3N + 2H_2 \rightarrow Li_2NH + LiH + H_2 \rightarrow LiNH_2 + 2LiH \qquad (2.1)$$

Amides can be considered analogous to NH_3, where N atom bonds with H atoms; however, significant structural and electronic properties are varied due to the co-presence of metal to N bond [4, 5]. During the last one and a half decades, numerous amide/hydride systems have been explored and/or (re)invented with high H content, especially when the metal is Li or Mg [6].

The next contender in this family is NH_3, which contains 17.7 wt% hydrogen. The use of ammonia as a hydrogen carrier has been attracting the attention of the scientific community since the early 1980s [7]. Apart from amide/imide and ammonia, hydrazine (N_2H_4) is another potential candidate belonging to nitrogen-based hydrogen storage systems [8, 9]; however, it is very unstable, toxic and easily explodes in the presence of oxygen. Hydrazine contains 12.6 wt% hydrogen and is reported to decompose via the following two competing reactions as supported by different catalysts [8]:

$$3N_2H_4 \rightarrow 4NH_3 + N_2 \qquad (2.2)$$

$$N_2H_4 \rightarrow N_2 + 2H_2 \qquad (2.3)$$

Some researchers keep ammonia borane also in this category of N_2-based systems for hydrogen storage; however, the chemistry involved with these systems is entirely different and more complex. So, in this chapter, we will limit ourselves to amide/imide and ammonia systems.

2.2 Amide/Imide Systems

As mentioned above, amides $M(NH_2)_x$ and imides $M(NH)_x$ are formed when M and H are both bonded with N. In general, direct decomposition of amide produces imides and evolved ammonia rather than H_2. However, when combined with metal hydrides, they desorb H_2 gas. In this section, first, single metal amides/imides will be described in terms of their structural and sorption properties, which will be followed by double-cation amide/imide systems.

2.2.1 Single-Cation Amide/Imide Systems

2.2.1.1 Lithium Amide/Imide

2.2.1.1.1 Synthesis

Lithium amide can be prepared by the direct reaction of lithium metal and ammonia gas at 400 °C, as reported by Titherley [10]. A low-temperature method of lithium amide preparation was claimed in a US patent in 1980 [11], according to which, first a mixture of lithium metal with catalyst (Co) and inert liquid aromatic hydrocarbon (toluene) was formed at around 0 to –60 °C followed by the addition of liquid ammonia. This turns into $Li(NH_3)_4$, which transforms into $LiNH_2$ by heating it up to 70 °C, resulting in the excess NH_3 or H_2 being exhausted. Recently, nanoparticles of pure lithium amide were obtained by deprotonation of ammonia with n-butyl lithium [12]. Even though several approaches have been proposed, the reaction between LiH and NH_3 gas has been widely accepted for the preparation of lithium amide, as the formation enthalpy of this reaction (~42 kJ/mol) suggests the formation of $LiNH_2$ even at room temperature [13]. On the other hand, Li_2NH can be synthesized simply by overnight heating of $LiNH_2$ at 350 °C [3].

2.2.1.1.2 Crystal Structure

Lithium amide was reported to have a tetragonal structure with space group I-4 (No.82) [14–17]. Figure 2.1 shows the unit cell of $LiNH_2$, where H_1 and H_2 are nonequivalent H atoms, which occupy 8g Wyckoff site. Lithium atoms denoted by Li1, Li2, and Li3 prefer to occupy 2a, 2c, and 4f position, whereas, the nitrogen atom is placed at the 8g site. Whereas the

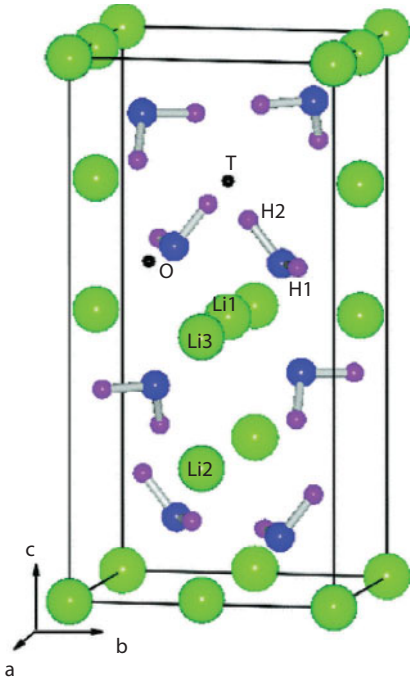

Figure 2.1 The conventional unit cell of $LiNH_2$, with Li, N, and H represented by green (large), blue (medium), and purple (small) spheres, respectively. T and O (small black spheres) denote one of the tetrahedral and octahedral sites of the N sublattice, respectively. (Reproduced from [16] with permission of American Physical Society)

crystal structure of $LiNH_2$ is well known and widely accepted, the Li_2NH structure is still under debate and controversial [18–24].

On the basis of XRD results, Juza and Opp [18] suggested antifluorite structure with Fm3m symmetry without discussing the position of H atom. Some of the following studies suggested that hydrogen prefers one of the sites around the nitrogen atom [19, 20]. Several models have been proposed to identify the low energy ordered structure, e.g., orthorhombic structure with Pbca symmetry by Mueller and Ceder [21], orthorhombic Ima2 structure by Balogh *et al.* [23]. The electronic structure analysis by Miwa *et al.* [24] suggested an ionic feature between Li^+ and NH_2^-, whereas the existence of covalency was found in the internal bonding of NH_2^-.

2.2.1.1.3 Sorption Mechanism and Thermodynamics

Chen *et al.* [3] proposed the sorption reaction at first according to Equation 2.1 with a total gravimetric capacity of 11.5 wt% (Figure 2.2). However, the

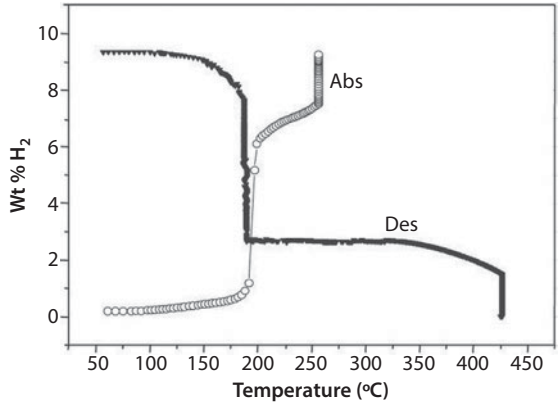

Figure 2.2 Weight variations during hydrogen absorption and desorption processes over Li_3N samples. (Reproduced from [3] with permission of Nature Publishing Group)

enthalpy change of the first reaction of nitride to imide conversion is too high (−148 kJ mol), thus making it unsuitable for the application. The second reaction of imide-amide conversion can accommodate 7 wt% H_2 with a quite nice value of enthalpy, i.e., −44.5 kJ/mol, thus allowing the reversible reaction to proceed well below 300 °C.

To understand the H_2 evolution at around 150 °C, opposite charge attraction theory was proposed by Chen *et al.* [25], which suggests the direct combination of $H^{\delta+}$ from $LiNH_2$ and $H^{\delta-}$ from LiH as well as $N^{\delta-}$ and $Li^{\delta+}$ to form Li_2NH, thus evolving H_2 at such a low temperature. However, a contemporary study by Hu and Ruckenstein [26] suggested a two-fold reaction as follows:

$$2LiNH_2 \rightarrow Li_2NH + NH_3 \tag{2.4}$$

$$NH_3 + LiH \rightarrow LiNH_2 + H_2 \tag{2.5}$$

Since the reaction (2.5) occurs ultrafast, it results in a direct evolution of H_2 from $LiNH_2$ and LiH mixture. The above mechanism was confirmed by Ichikawa *et al.* [13] using a TDMS experiment performed on two-layered material consisting of $LiNH_2$ and LiH. Later, Hu *et al.* [27] also investigated the reaction mechanism of $LiNH_2$+LiH mixture by *in-situ* ^1H NMR and revealed the release of NH_3 at a temperature as low as 30 °C and rapid capture of NH_3 by LiH at 150 °C. More recently, both of the above mechanisms were reviewed again by Cao *et al.* [28]. They suggested the occurrence of an ion-migration-based mechanism for the amide-hydride system in close

contact, while the second mechanism based on NH_3 mediated reaction occurs when $–NH_2$ group and hydride are not in direct contact. In addition to the above mechanisms, a heterogeneous solid-state reaction between $LiNH_2$ and LiH has been proposed by Aguey-Zinsou *et al.* [29], which is believed to be controlled by Li^+ diffusion from LiH to $LiNH_2$ across the interface.

2.2.1.2 Sodium Amide/Imide

2.2.1.2.1 Synthesis

Sodium amide can be produced by a direct reaction of sodium metal with dry NH_3 gas, as reported by Titherley in 1894 [10], which has been widely accepted as an industrial process also. For a complete conversion of Na metal into $NaNH_2$, a temperature of 300–450 °C is needed [30]. The use of different catalysts, e.g., iron oxide and transition metal chlorides, was recommended to perform the above reaction. However, these catalysts remain in the final product and are difficult to separate. To overcome this problem, recently a catalyst-free synthesis of $NaNH_2$ nanoparticles has been proposed by ammoniation of metallic sodium particulated in the pores of silica gel at 100 °C [31]. Room temperature synthesis has also been reported by ball milling of sodium hydride with gaseous NH_3 [32].

2.2.1.2.2 Crystal Structure

The structure of sodium amide was first derived in two contemporary reports by Juza *et al.* [33] and Zalkin and Templeton [34] by XRD. The D position in $NaND_2$ was determined by a neutron diffraction study performed by Nagib *et al.* [35]. According to the above results, $NaNH_2$ crystallize in an orthorhombic structure with Fddd space group, as shown in Figure 2.3 [36]. The lattice parameters were obtained as a = 8.964 Å, b = 10.456 Å, and c = 8.073 Å [36]. The Na, N and H atoms occupy 16f, 16g, and 32f sites respectively, thus forming NaN_4 tetrahedra.

Later in 1972, Raman spectra for $NaNH_2$ was recorded, which shows the existence of simple C_{2v} point symmetry of NH_2^- with 3 bands assigned at 3267, 3218 and 1531 cm^{-1}, corresponding to symmetric, asymmetric stretch and bending modes [37].

2.2.1.2.3 Sorption Mechanism and Thermodynamics

Whereas lithium amide has been extensively studied for its sorption properties, sodium amide system has been only modestly explored until a recent application of $NaNH_2$ to crack NH_3 to produce H_2 [38]. Its relatively

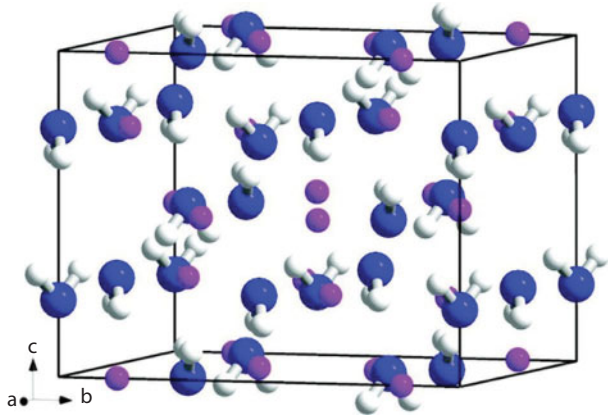

Figure 2.3 Ambient-pressure crystal structure of $NaNH_2$ in space group Fddd. The coordinate system is indicated to show the orientations of the unit cell. The color codes for atoms are pink (sodium), blue (nitrogen), and white (hydrogen). (Reproduced from [36] with permission of American Chemical Society)

low H_2 content (5.9 wt%), high decomposition enthalpy (−123.8 kJ mol^{-1}), high reactivity in molten state and complexity involved with this system limits its exploration. The first decomposition of $NaNH_2$ was reported by Titherley in 1894 [10], and was later confirmed by Sakurazawa *et al.* [39] in 1937. It was suggested that $NaNH_2$ decomposes into NaH/Na, N_2, and H_2 gases according to the following reaction:

$$NaNH_2 \rightarrow NaH + 0.5N_2 + 0.5H_2 \quad (2.6)$$

$$NaNH_2 \rightarrow Na + 0.5N_2 + H_2 \quad (2.7)$$

The formation of two gases induces a large entropy change of 200.9 J/K mol, which results in a decomposition temperature of 343 °C [38]. The decomposition mechanism has recently been investigated in detail by Jain *et al.* [40, 41] and Jepsen *et al.* [42]. All these reports, on the basis of TG-TDMS results, suggested the decomposition of $NaNH_2$ into Na metal and NH_3 as major products with a small amount of N_2 and H_2, as shown in Figure 2.4 [41]. As mentioned earlier, no imide-like structure has been reported for Na-N-H system. However, very recently, Yamaguchi *et al.* [43] reported an imide-like structure as an intermediate state during decomposition under vacuum, as shown in Figure 2.4. The presence of a broad peak at around 3150–3200 cm^{-1} suggests the presence of –NH group similar to Li_2NH. The authors claimed that the decomposition pathway of $NaNH_2$

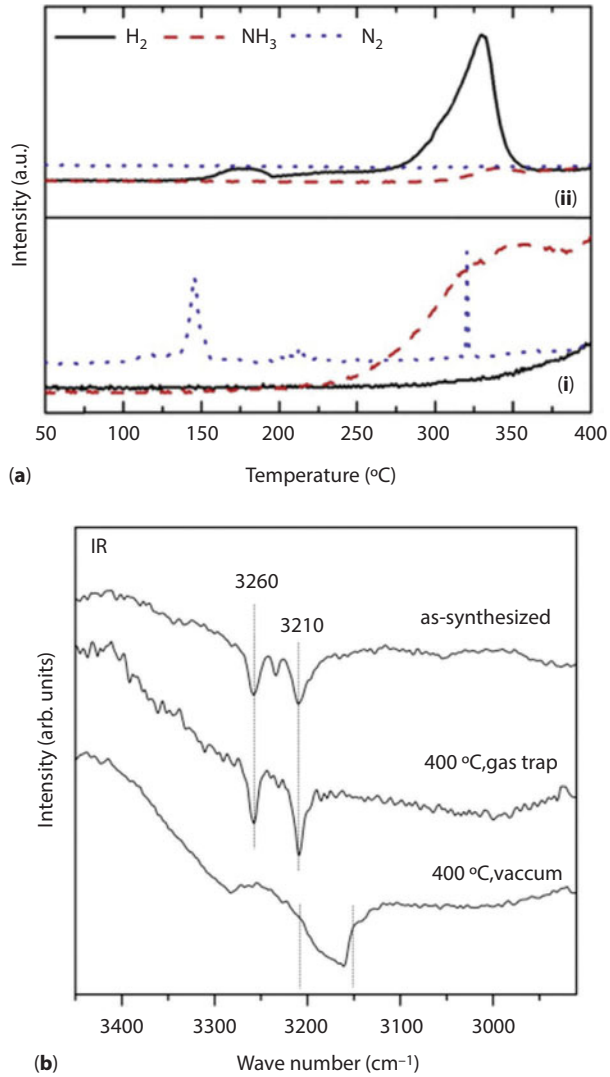

Figure 2.4 (a) H_2, N_2 and NH_3 MS profile for (i) $NaNH_2$ and (ii) $NaNH_2$–NaH decomposition (Reproduced from [41] with permission of Elsevier). (b) IR spectra of the as-synthesized $NaNH_2$, the reaction products after heating at 400 °C under the gas trap, and the vacuum condition (Reproduced from [43] with permission of Elsevier).

can strongly be affected by the presence of gaseous species in the reaction field. Similar to its analogous $LiNH_2$, sodium amide also evolves NH_3 as a major product rather than H_2. Thus, the addition of metal hydride seems necessary to react with this NH_3 and desorb H_2, thus making it applicable

as hydrogen storage material. Employing this idea, NaH was added to $NaNH_2$ and was found to be effective in suppressing the NH_3 evolution completely, as shown in Figure 2.4.

2.2.1.3 Magnesium Amide/Imide

2.2.1.3.1 Synthesis

Magnesium amide, $Mg(NH_2)_2$, was synthesized by the reaction of Mg or Mg_3N_2 with gaseous or liquid NH_3; however, the preparation time needed for this conversion was a matter of years [44, 45]. After a long time, Nakamori *et al.* [46] prepared $Mg(NH_2)_2$ by a gas-solid reaction of MgH_2 and ammonia at 603–653 K for 1 week as per the following reaction:

$$MgH_2 + 2NH_3 \rightarrow Mg(NH_2)_2 + 2H_2 \tag{2.8}$$

$$Mg + 2NH_3 \rightarrow Mg(NH_2)_2 + H_2 \tag{2.9}$$

A faster method of synthesizing $Mg(NH_2)_2$ has been proposed by Leng *et al.* [32]. They prepared $Mg(NH_2)_2$ using rocking milling of MgH_2 under NH_3 atmosphere (0.4 MPa) for 13 h followed by annealing at 300 °C for 13 h. The formation of MgNH usually proceeded from the decomposition of $Mg(NH_2)_2$ according to the following reaction:

$$Mg(NH_2)_2 \rightarrow MgNH + NH_3 \text{ (300–400 °C)} \tag{2.10}$$

2.2.1.3.2 Crystal Structure

The structure of $Mg(NH_2)_2$ was first unfolded by Jacobs and Juza [44] in 1969, which suggested the tetragonal structure of this compound with space group I41/acd. However, the H positions could not be determined without uncertainty. Thus, a detailed investigation using neutron powder diffraction was conducted on $Mg(ND_2)_2$ by Sørby *et al.* [15]. The cation is tetrahedrally coordinated by amide ions with the Mg-N distance between 2.00(1) to 2.17(1) Å. The three different amide ions are arranged with N-D separations in the range of 0.95(1)–1.07(1) Å. As shown in Figure 2.5, Mg atoms are arranged at (0.3734, 0.3612, 0.0631) position, whereas N1, N2 and N3 atoms of three different NH2 ions are placed at (0.2867, 0, 0.25), (0, 0.25, 0.2574) and (0.0128, 0.0229, 0.3757) positions. The position of four H atoms, H1, H2, H3 and H4, are at (0.236, 0.061, 0.271), (0.058, 0.201, 0.239), (0.229, 0.177, 0.104) and (0.209, 0.285, 0.148) [47].

The structure of MgNH was first confirmed by Jacobs and Juza [44]. It is found to be crystallized in hexagonal structure with space group P6/m

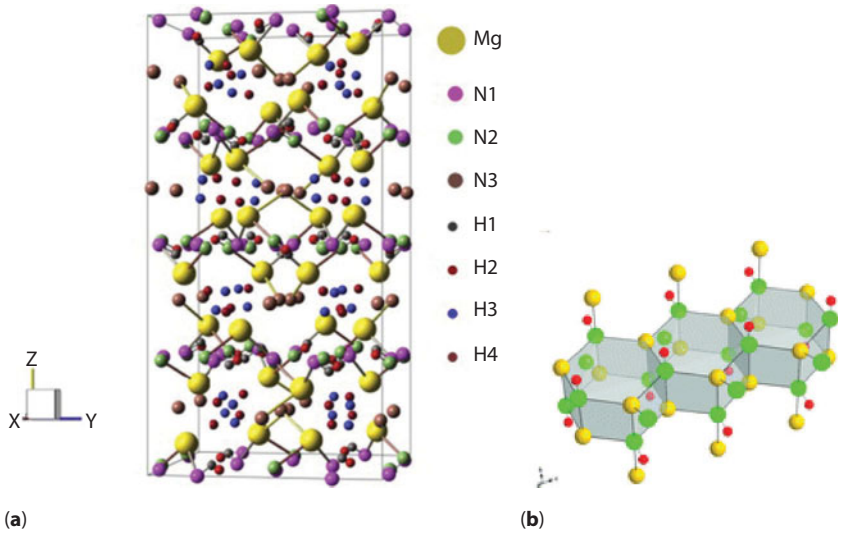

Figure 2.5 (a) Unit cell of $Mg(NH_2)_2$. The big yellow balls denote the Mg atom, the medium pink, green, and dark brown balls denote the N1, N2, and N3 atoms, respectively, and the small grey, red, blue, and light brown balls denote the H1, H2, H3, and H4 atoms, respectively (Reproduced from [47] with permission of Elsevier). (b) Structure representation of a small part (three units) of the infinite sequence of face sharing Mg_6N_6 units in magnesium imide. Mg_6N_6 hexagonal prisms are highlighted in gray; Magnesium atoms are in yellow; Nitrogen atoms are in green; Deuterium atoms are in red. (Reproduced from [48] with permission of American Chemical Society).

with lattice parameter a = 11.574 Å and c = 3.681 Å. In a later study by Dolci *et al.* [48], the structure was found to be the same, however, with a different space group, i.e., P6 322. A total of 12 MgNH formula units form a unit cell with Mg, N and H atoms placed at 6j and 6k Wyckoff sites. The structure was suggested to have a sequence of linked linear chains of Mg_6N_6 hexagonal prism clusters (Figure 2.5) [48].

2.2.1.3.3 Sorption Mechanism and Thermodynamics

Magnesium amide decomposes to Mg_3N_2 and NH_3 via an intermediate step of MgNH formation, as shown in reaction 2.10 and 2.11.

$$MgNH \rightarrow 1/3Mg_3N_2 + 1/3\ NH_3\ (>350\ °C) \qquad (2.11)$$

The reaction proceeds in a similar way to Li-N-H system. The reaction enthalpies for the reactions 2.10 and 2.11 were found to be 120 ± 11 kJ mol^{-1}

and 112 kJ mol^{-1} respectively, as measured by NH_3 pressure-composition isotherms [49]. A small amount of H_2 and N_2 were also observed by gas chromatography, which was suggested due to NH_3 decomposition [49]. In order to get H_2 out of this amide, Nakamori *et al.* [46] tried to make a mixture of $Mg(NH_2)_2$ with MgH_2 in 1:1 and 1:2 molar ratio; however, they observed more weight loss than the speculated value as of H_2 desorption only. And so they concluded that the NH_3 desorption took place during the reaction. Later, Hu *et al.* [50, 51] found that ball milled $Mg(NH_2)_2$ and MgH_2 in 1:1 and 1:2 molar ration desorb hydrogen as per the following reactions:

$$Mg(NH_2)_2 + MgH_2 \rightarrow 2MgNH + 2H_2 \tag{2.12}$$

$$Mg(NH_2)_2 + 2MgH_2 \rightarrow Mg_3N_2 + 4H_2 \tag{2.13}$$

The reaction enthalpy of reaction 2.13 has been calculated as 3.5 kJ/molH_2, which shows the mild endothermic nature of this reaction, thus making it very slow to proceed. Since the reaction rate is too slow for this reaction, this could be the reason that earlier reports [46] didn't observe this reaction.

2.2.1.4 Calcium Amide/Imide

2.2.1.4.1 Synthesis

$Ca(NH_2)_2$ was first prepared by the reaction of Ca metal and liquid NH_3 at room temperature [52]. Similar to other amides, Leng *et al.* [32] prepared $Ca(NH_2)_2$ starting from CaH_2 and milled it with 0.4MPa gaseous NH_3 for 8 h. The synthesis of calcium imide was carried out by the reaction of $Ca(NH_2)_2$ with $NaNH_2$ at 850 °C in an autoclave [53]. Apart from amide and imide, Ca also forms another N-H compound, i.e., Ca_2NH, which is synthesized by the reaction of Ca_3N_2 with CaH_2 [54, 55] at around 900–1000 °C:

$$Ca_3N_2 + CaH_2 \rightarrow 2Ca_2NH \tag{2.14}$$

2.2.1.4.2 Crystal Structure

Calcium amide crystallized in C-5 anatase-type tetragonal structure with space group D_{19}^{4th} as predicted by Juza and Schumacher [52], where NH_2 ions occupy ideal atomic positions. The actual atomic position of all the atoms including H atom were determined by Senker *et al.* [56] using a

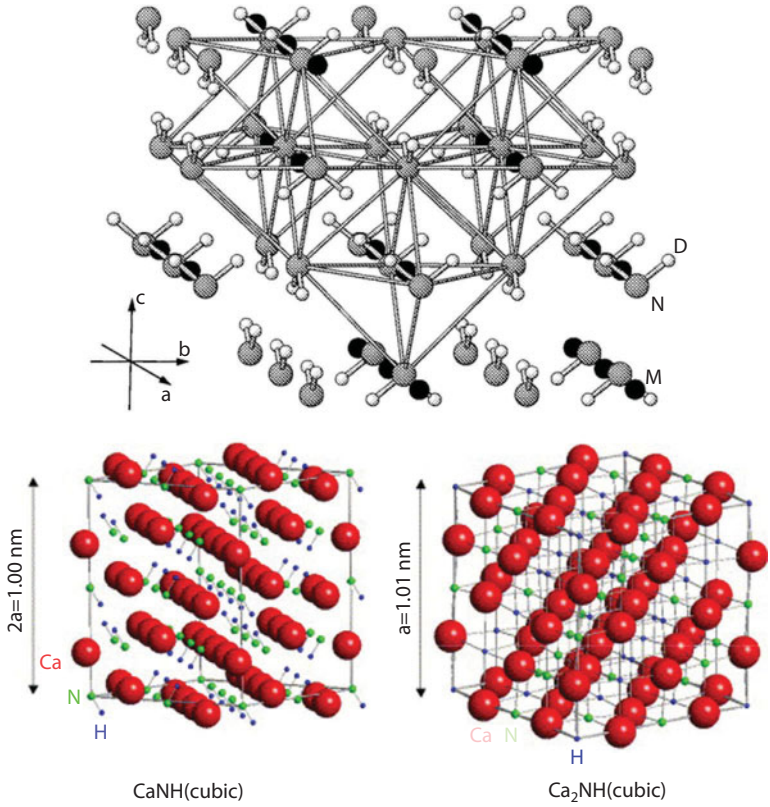

Figure 2.6 (Top) Part of the structure of $Ca(ND_2)_2$ including the amide ion orientation (Reproduced from [56] with permission of American Chemical Society). (Bottom Left) Structure of CaNH and (Bottom Right) Structure of Ca_2NH (Reproduced from [57] with permission of Elsevier).

neutron diffraction experiment. The structure was described by a disordered cubic close packing of amide ions with cations occupying half of the octahedral sites. Ca, N and D atoms occupy 4a, 8e and 16h sites respectively (Figure 2.6).

Calcium imide crystallizes in cubic structure with Fm3m space group. Ca and N atoms are arranged in the motif of NaCl-type structure, whereas H atoms of the imide groups are disordered within a Ca octahedral and occupy a six-fold split position [53]. Although Ca_2NH consists of Ca, N, and H, in contrast to $Ca(NH_2)_2$ and CaNH, it doesn't have an N-H bond. The structure of calcium hydride nitride is an NaCl-type cubic structure with space group Fd3m with lattice parameter a = 10.13 Å. The structures of CaNH and Ca_2NH are shown in Figure 2.6.

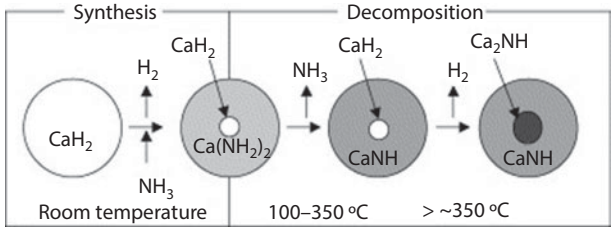

Figure 2.7 Schematic diagram of the synthesis and decomposition processes of $Ca(NH_2)_2$. Synthesis: CaH_2 reacts with ammonia to produce $Ca(NH_2)_2$ during milling, but still exists in a core part. Decomposition: $Ca(NH_2)_2$ decomposes to CaNH by heating, then CaNH reacts with CaH_2 in the core part at high temperatures and desorbs H_2. (Reproduced from [58] with permission of Elsevier)

2.2.1.4.3 Sorption Mechanism and Thermodynamics

Calcium amide itself decomposes into calcium imide and NH_3, similar to other amides [52]:

$$Ca(NH_2)_2 \rightarrow CaNH + NH_3 \tag{2.15}$$

Upon addition of a similar cation hydride, i.e., CaH_2, the NH_3 evolution can be suppressed, as it is absorbed by CaH_2. Hino *et al.* [58] reported the mechanism of H_2 desorption from a mixture of $Ca(NH_2)_2$ and CaH_2 (Figure 2.7) as follows:

$$Ca(NH_2)_2 + CaH_2 \rightarrow 2CaNH + 2H_2\ (3.5\ wt\%) \tag{2.16}$$

A further addition of CaH_2 continues this reaction with the formation of Ca_2NH and addition of 2.1 wt% H_2 evolution according to the following reaction:

$$CaNH + CaH_2 \rightarrow Ca_2NH + H_2 \tag{2.17}$$

2.2.2 Double-Cation Amide/Imide Systems

Inspired by effective H_2 desorption instead of NH_3 evolution from $LiNH_2$–LiH system, several complex double-cation amide systems M-M′-N-H were developed and studied for their structural and hydrogenation properties. This section will describe some of these important systems in detail.

2.2.2.1 Li-Na-N-H

2.2.2.1.1 Synthesis

The first synthesis of Li-Na-N-H was reported by Jacobs and Harbrecht through direct reaction of Li and Na metals with supercritical ammonia [59]. Two different phases were formed using Li:Na ratios of 1:2 and 3:1. Later, another approach was proposed by Lowton *et al.* [60] that used a solid-state synthesis route using the parent amides, i.e., $LiNH_2$ and $NaNH_2$, thus eliminating the use of supercritical ammonia. They prepared these phases by heating the mixture of parent amides at 200 °C for 12–24 hours under vacuum/Ar flow. In a more recent report, these Li-Na-N-H systems were obtained by milling a mixture of $LiNH_2$ and $NaNH_2$ in 3:1 ratio in a high-energy Spex ball mill for 90 min followed by 6 h annealing at 150 °C [61].

2.2.2.1.2 Crystal Structure

The structure of the above two phases was determined by Jacobs and Harbrecht [59], who suggested a tetragonal structure for both of the above. A detailed structural analysis was performed in 2008 using synchrotron X-ray diffraction. It is suggested that $Li_3Na(NH_2)_4$ crystallizes in I4-tetragonal structure with Li at 2a (0,0,0) and 4f (0,1/2,z) sites, Na at 2c (0,1/2,1/4) site and N at 8g (x,y,z) sites, whereas H atoms occupy 8g sites. The lattice parameters were found to be a = 5.081(1) Å and c = 11.511 Å. Another phase, i.e., $LiNa_2(NH_2)_3$ crystallizes in the same structure but different space group, i.e., $P4_2/m$. This structure is composed of Na atoms located at 4i (1/2,0,z), 2a (0,0,0) and 2f (1/2,1/2,1/4) sites, Li at 4j (x,y,0) site and N at 8k (x,y,z) and 4j (x,y,0) sites, whereas H atoms occupy 8k sites. The structures of both the phases are shown in Figure 2.8.

2.2.2.1.3 Sorption Mechanism

The sorption properties of this mixed cation amide were studied in 2016 [40, 61]. Jepsen *et al.* [61] suggested the decomposition of $Li_3Na(NH_2)_4$ into $LiNH_2$ and NH_3 at around 230 °C followed by further decomposition into Li_2NH. However, the results shown by Jain *et al.* [40] suggest the existence of two endothermic events during the decomposition of $Li_3Na(NH_2)_4$ without any gaseous evolution, which was suggested to be melting/phase transformation according to the following reaction:

$$2Li_3Na(NH_2)_4 \rightarrow LiNa_2(NH_2)_3 + 5LiNH_2 \qquad (2.18)$$

The hydrogenation of both the product or the starting material leads to the formation of a mixture of $LiNH_2$, NaH, and NH_3 as follows:

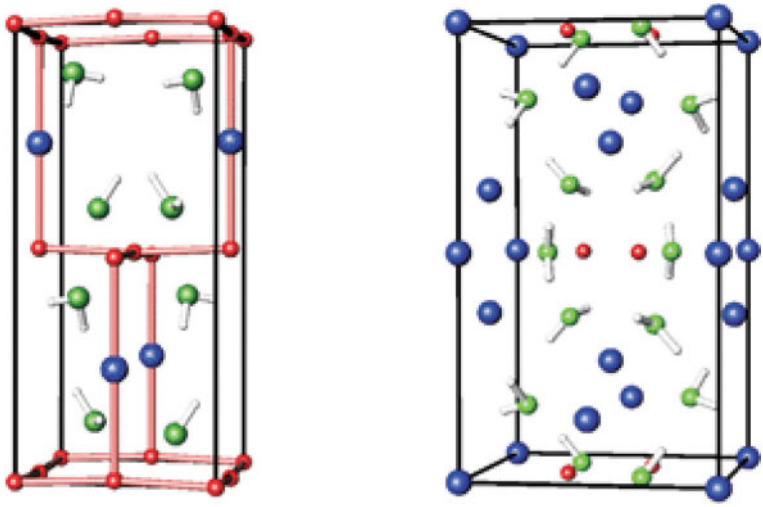

Figure 2.8 Crystal structures of $Li_3Na(NH_2)_4$ (left), and $LiNa_2(NH_2)_3$ (right); with Li represented as red spheres, Na as blue spheres, N as green spheres and H as white spheres. (Reproduced from [60] with permission of Royal Society of Chemistry)

$$Li_3Na(NH_2)_4 + H_2 \rightarrow 3LiNH_2 + NaH + NH_3 \qquad (2.19)$$

During this investigation, Jain *et al.* [40] solved a long-awaited two peak mystery of $LiNH_2$-NaH system that was observed by Ichikawa *et al.* in 2004 [13]. It is found that $LiNH_2$-NaH system is analogous to $NaNH_2$-LiH system and desorbs about 4 wt% H_2 through cation exchange in the temperature range of 200–400 °C, followed by NH_3 mediated reaction in the temperature range of 200–400 °C with a reversible H_2 absorption at 2 MPa H_2 according to the following reaction:

$$10NaNH_2 + 10\ LiH\ (10LiNH_2 + 10NaH) \rightarrow 2Li_3Na(NH_2)_4 + 2\ Li_2NH + 8Na + 6H_2 \qquad (2.20)$$

The mechanism shown in Figure 2.9 suggests that the first peak originated from the reaction of $LiNH_2$ and NaH, while the second peak was due to the reaction of $NaNH_2$-NaH.

A composite of $Li_3Na(NH_2)_4$ and LiH in the molar ratio 1:4 has also been reported by Jepsen *et al.* [61] and suggested slightly lower H_2 desorption temperature (216 °C) in comparison to the $LiNH_2$-LiH system (242 °C) with the additional peaks at 296, 316 and 392 °C. It seems that the composite of $Li_3Na(NH_2)_4$ and LiH behave quite similar to the $LiNH_2$-NaH/$NaNH_2$-LiH composites, as shown by Jain *et al.* [40].

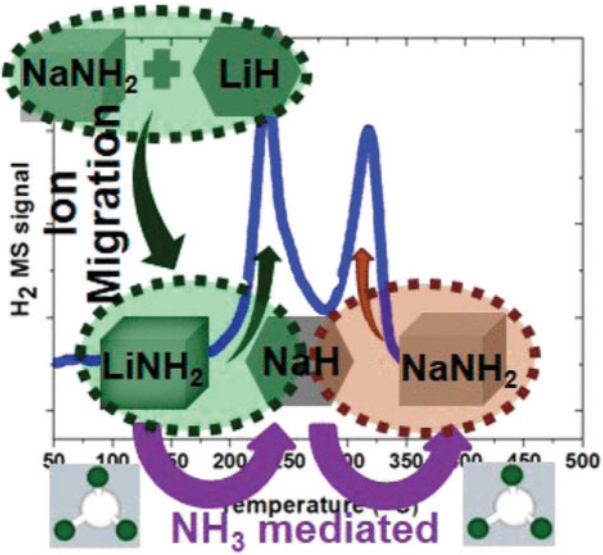

Figure 2.9 The sorption mechanism of $LiNH_2$-NaH system. (Reproduced from [40] with permission of American Chemical Society)

2.2.2.2 Li-Mg-N-H

Among all the double-cation amide/imide systems, Li-Mg-N-H is the most studied system owing to its much smaller enthalpy of dehydrogenation according to the following reaction [62]:

$$2LiNH_2 + MgH_2 \rightarrow Mg(NH_2)_2 + 2\,LiH \rightarrow Li_2Mg(NH)_2 + 2H_2 \quad (2.21)$$

This double-cation imide has quite interesting properties, thus has attracted the attention of the hydrogen community over the last decade.

2.2.2.2.1 Synthesis

The most acceptable method to synthesize this novel ternary imide is according to reaction 2.21. However, there are many other routes available for this fascinating structure. Liu *et al.* [63] prepared this imide by sintering a mixture of $Mg(NH_2)_2$ and $2LiNH_2$ at a temperature of 150–315 °C after 36 h milling as follows:

$$Mg(NH_2)_2 + 2LiNH_2 \rightarrow Li_2Mg(NH)_2 + 2NH_3 \quad (2.22)$$

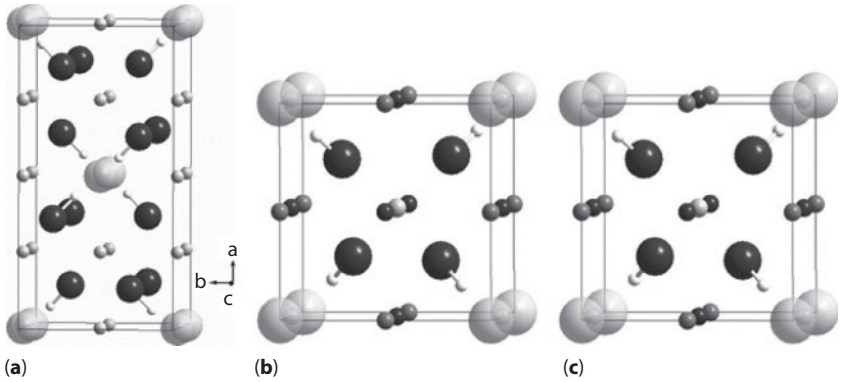

Figure 2.10 (a) Structure of α-$Li_2Mg(NH)_2$. Nitrogen atoms (dark grey), protons (white), mixed lithium and magnesium sites (small light grey) and vacancies (large transparent grey) are shown; (b) Structure of β-$Li_2Mg(NH)_2$. Nitrogen atoms (dark grey), protons (white), lithium (light grey bcc site), two distinct mixed lithium and magnesium sites (small dark grey) and vacancies (large translucent grey) are shown; (c) Structure of γ-$Li_2Mg(NH)_2$. Nitrogen atoms (dark grey), protons (white), and mixed lithium, magnesium, and vacancy sites (small grey) are shown. (Reproduced from [65] with permission of Elsevier)

Another route starting from a mixture of $Mg(NH_2)_2$ and Li_3N was proposed by Ma *et al.* [64] by heating it at 240 °C under dynamic vacuum:

$$3Mg(NH_2)_2 + 2\,Li_3N \rightarrow 3Li_2Mg(NH)_2 + 2NH_3 \qquad (2.23)$$

2.2.2.2.2 Crystal Structure

The structure of $Li_2Mg(NH)_2$ was unfolded by Rijssenbeek *et al.* [65] in 2008 using XRD and neutron diffraction experiments. As can be seen from Figure 2.10, $Li_2Mg(NH)_2$ crystallized in orthorhombic structure with space group lba2, which can be considered as a supercell of the high-temperature cubic form of Li_2NH [19, 20]. In the structure, Li and Mg atoms occupy 4b and 8c sites, whereas N and H atoms are arranged at the 8c site. The IR bands corresponding to $Li_2Mg(NH)_2$ appear at 3180 and 3163 cm^{-1}, as shown by Markmaitree *et al.* [66, 67]. It is observed that the disordering of cations and cation vacancies occurred in the structure of $Li_2Mg(NH)_2$ upon increasing the temperature. As the temperature increased above 350 °C, α-orthorhombic phase converts to β-cubic phase $Li_2Mg(NH)_2$ with P43m space group, where some of the tetrahedral sites (3c) are occupied by Li and Mg and some other 3d sites are partially occupied by Li. The N and H atoms occupy 4e sites, as shown in Figure 2.10b. A further increase in temperature above 530 °C transforms this phase to γ phase, which crystallized

into Fm3m cubic cell. It is observed that Li and Mg atoms are randomly distributed over the tetrahedral site. The cubic $Li_2Mg(NH)_2$ shows a broad IR absorption peak at 3174 cm^{-1} [68].

2.2.2.2.3 Sorption Mechanism

As shown in reaction 2.21, Li-Mg-N-H can store 5.6 wt% with desorption enthalpy and entropy values ~ 38.9 kJ/mol and 112 J/K mol H_2, which allow H_2 release at 1 atm pressure at below 90 °C [69]. As can be seen from Figure 2.11, most of the hydrogen can be absorbed and desorbed from this system in a temperature range of 100–200 °C. Luo and Rönnebro [70] have shown the viability of this system through a PCT diagram (Figure 2.11). It is observed that MgH_2 substituted $LiNH_2$ + LiH system can provide 41

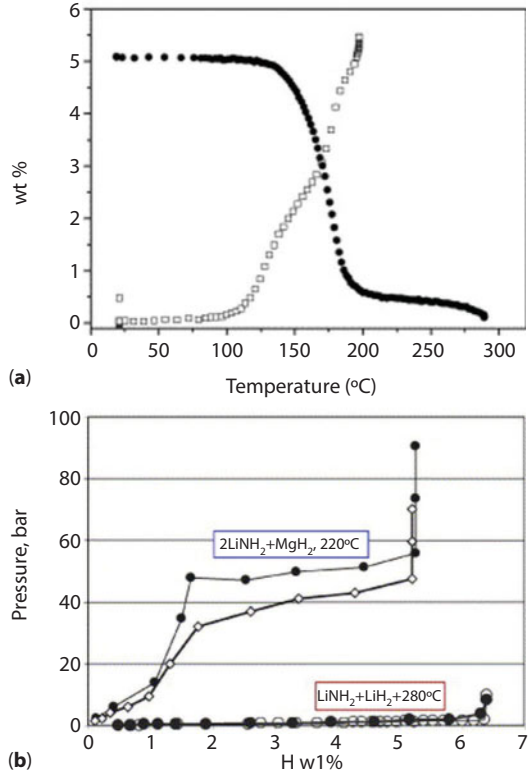

Figure 2.11 (a) Hydrogen absorption in a $Li_2Mg(NH)_2$ sample and desorption from $Mg(NH_2)_2$ + 2LiH sample (Reproduced from [69] with permission of Elsevier); (b) Pressure-composition isotherms at 220 °C for ($2LiNH_2$ + MgH_2). Isotherms at 285 °C for ($LiNH_2$ + LiH) are included for comparison (Reproduced from [70] with permission of Elsevier).

bar of hydrogen at 220 °C, i.e., the substitution of LiH by 1/2 MgH_2 can dramatically destabilize this system.

Inspired by the exiting performance of this system, several groups studied different $Mg(NH_2)_2$/LiH composites with different molar ratios in order to get higher H_2 content. Leng *et al.* [71] prepared $Mg(NH_2)_2$/LiH composite in a molar ratio of 3:8 and achieved a reversible capacity of 6.9 wt%. A further increase in molar ratio to 1:4 brings the H_2 capacity up to 9.1 wt% [72]. The reactions for the above two molar ratios were initially proposed as follows:

$$3Mg(NH_2)_2 + 8LiH \leftrightarrow Mg_3N_2 + 4Li_2NH + 8H_2 \quad (2.24)$$

$$3Mg(NH_2)_2 + 12LiH \leftrightarrow 4Li_3N + Mg_3N_2 + 12H_2 \quad (2.25)$$

However, later an *in-situ* synchrotron X-ray diffraction and powder neutron diffraction experiments [73] show the existence of single-phase $Li_{2+x}MgN_2H_{2-x}$ rather than the presence of $Mg_3N_2/Li_3N/Li_2NH$ in the final product. Xiong *et al.* [74] prepared a series of $Mg(NH_2)_2$/LiH systems with different molar ratios and concluded that lowering the amount of LiH in composite enhances the NH_3 evolution, whereas an increase of LiH content pulls the H_2 desorption temperature to the higher side.

Although the thermodynamics of $Mg(NH_2)_2$–LiH system suggest H_2 sorption occurs at 90 °C, it shows the sorption only in the range of 100–200 °C, which must be associated with the huge kinetic barrier. Several efforts have been carried out to enhance the kinetics using metal oxides [75], halides [76, 77], metal nitrides [78], Ti additives [79], LaH_2 [80], C-nanostructures [81], Na-based additives [82], etc., but most of them don't have a significant effect on the kinetics of Li-Mg-N-H system. A significant improvement was achieved by KH additive in a small amount [83], which drastically reduced the operating temperature by 50 °C, as shown in Figure 2.12. After this discovery, several potassium compounds were tested and found effective for kinetic enhancement [84–87].

The improvement in the kinetics can be understood on the basis of NH_3 mediated reaction [88]. KH reacts with NH_3 faster than LiH, which is evolved from $Mg(NH_2)_2$, thus convert into KNH_2 and release H_2 simultaneously:

$$KH + NH_3 \rightarrow KNH_2 + H_2 \quad (2.26)$$

This KNH_2 then reacts with LiH to regenerate KH as follows:

$$KNH_2 + LiH \rightarrow LiNH_2 + KH \quad (2.27)$$

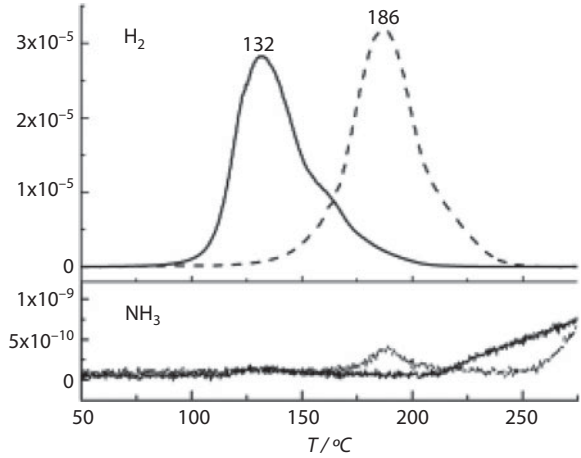

Figure 2.12 Temperature dependences of H_2 and NH_3 release from the potassium-modified (—) and the pristine (- - - -) samples. (Reproduced from [83] with permission of John Wiley and Sons)

This cycle continues until the consumption of LiH. Thus, the presence of KH acts as a pseudo-catalytic agent and accelerates the decomposition of $Mg(NH_2)_2$–LiH system.

Another mechanism has been proposed by Wang *et al.* [89, 90], according to which the formation of an intermediate kinetic stable product, such as $K_2Mg(NH_2)_4$ or $Li_3K(NH_2)_4$, is very important and plays a key role in weakening N-H bonds, which enhance the kinetics of the overall process. Another approach to enhance the kinetics is particle reduction; a 36 h milled $Li_2Mg(NH)_2$ system was found to start absorbing hydrogen at 80 °C in comparison to onset temperature of 150 °C for normally prepared $Li_2Mg(NH)_2$ [91].

2.2.2.3 Other Double-Cation Amides/Imides

2.2.2.3.1 Li-Ca-N-H System

The synthesis of a Li-Ca-N-H system was first attempted by Xiong *et al.* [92] without describing its composition or structure in detail. They prepared this new ternary imide by heat treatment of a mixture of $LiNH_2$ and CaH_2 in 2:1 molar ratio at 300 °C, which has shown a different structure from those of starting material. Later, in 2007, Wu [93] defined the structure of this new compound as a trigonal-La_2O_3-type structure with space group (P3m1) using XRD, NMR and X-ray absorption fine structure

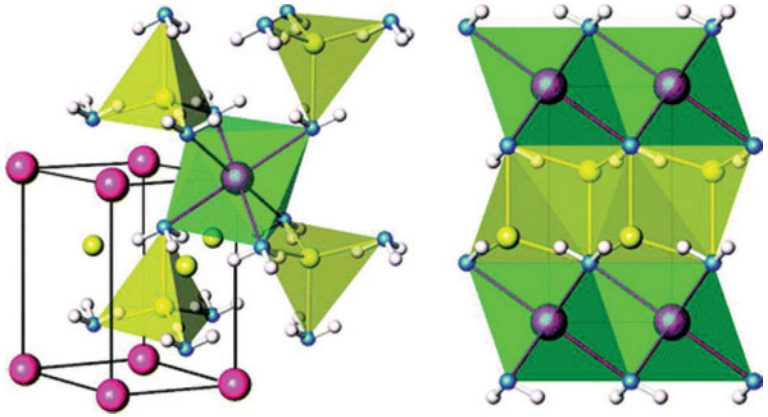

Figure 2.13 (Left) Off-[110] view of the refined trigonal structure of $Li_2Ca(NH)_2$. $Ca(NH)_6$ octahedra are in green; $Li(NH)_4$ tetrahedra are in yellow. Ca, Li, and N atoms are represented by large pink, yellow, and blue spheres, respectively. H atoms are randomly distributed at one of the three white sites around each N atom. (Right) The layered structure of $Li_2Ca(NH)_2$ viewed as a "combined imide" consisting of ordered CaNH layer and Li_2NH layer. (Reproduced from [94] with permission of American Chemical Society)

analysis. From the Rietveld refinement, it was found that Ca atoms occupy 1b site (0,0,1/2), Li occupy 2d site (1/3,2/3,0.8841) and N atoms occupy 2d sites (1/3,2/3,0.2565). The location of hydrogen could not be known in this study because of the small scattering factor of hydrogen, which was later solved using neutron powder diffraction by Wu *et al.* [94]. It was observed from the fitting of NPD data that D atom is equally distributed on 6i sites around each N atom, which is in good agreement with that predicted from DFT calculations [95]. On the basis of these results, the structure of $Li_2Ca(NH)_2$ was defined as shown in Figure 2.13.

After the initial investigation by Xiong *et al.* [92], the hydrogen desorption/absorption properties were investigated by Tokoyoda *et al.* [96] and they suggested the formation of an unknown imide phase (it was later identified as $Li_2Ca(NH)_2$).

$$2LiNH_2 + CaH_2 \xrightarrow{200C} CaNH + Li_2NH + 2H_2 \xrightarrow{400C} Li_2Ca(NH)_{2+2H2} \tag{2.28}$$

It was suggested that rehydrogenation of final product does not lead to the formation of initial mixture, but change to a mixture of CaNH, $LiNH_2$, and LiH [94] according to the following reaction:

$$Li_2Ca(NH)_2 + H_2 \rightarrow CaNH + LiNH_2 + LiH \tag{2.29}$$

Later, in 2010, the sorption properties of $LiNH_2/CaH_2$ system with different molar ratio was examined and the formation of a new compound with composition $Li_4CaN_4H_6$ [97] was reported as follows:

$$4LiNH_2 + CaH_2 \rightarrow Li_4CaN_4H_6 + 2H_2 \quad (2.30)$$

Whereas, hydrogenation of final product leads to a mixture of $LiNH_2$, LiH and a solid solution of $2CaNH\text{-}Ca(NH_2)_2$.

2.2.2.3.2 Na-Mg-N-H System

Similar to its parent amide, i.e., $NaNH_2$, Na-Mg-N-H system has been relatively less explored. The first report came into the picture from a mixture of $Mg(NH_2)_2$–NaH system [98]. This system was explored with the different molar ratio. It was revealed that the higher content of NaH in this system reduces N_2 and NH_3 evolution in comparison to that for 1:1 molar ratio. However, it costs less H_2 capacity at the same time with an increase in temperature for H_2 absorption. An unknown phase was observed in the dehydrogenated state, which can reabsorb H_2 to obtain the starting material. Several other investigations with different molar ratios have been carried out and different reactions were observed [99–102], but the unknown mixed-cation imide/nitride phase composition as well as structure is still unknown, which would be interesting to explore in the future in order to identify the real reaction mechanism.

2.2.2.3.3 Mg-Ca-N-H System

Mg-Ca-N-H system was explored as a low-cost amide hydride system [103], which can release 4.9 wt% H_2 in two steps up to 510 °C as follows:

$$2Mg(NH_2)_2 + 4CaH_2 \rightarrow CaMg_2N_2 + Ca_2NH + CaNH + 7H_2 \quad (2.31)$$

The system was found partially reversible in low-temperature range, i.e., up to 260 °C. A novel ternary imide, i.e., $MgCa(NH)_2$, has been claimed to be synthesized by 72 h milling of $Mg(NH_2)_2$–CaH_2 in 1:1 molar ratio. This novel imide was suggested to crystallize in cubic CaNH-like structure [104, 105].

$$Mg(NH_2)_2 + CaH_2 \rightarrow MgCa(NH)_2 + 2H_2\ (4\ wt\%) \quad (2.32)$$

2.2.2.3.4 M-Al-N-H and M-B-N-H System

Apart from these relatively simpler amide-hydride systems, more complex amide systems have also been tested by adding alanates and borohydrides

to the amides [106–124]. Whereas a significant alteration could be possible in the sorption thermodynamics, the kinetic barrier still is a serious issue. Several combinations for these alanate-amide systems were examined, e.g., $LiAlH_4$–$LiNH_2$ in 2:1 and 1:2 molar ratio with 8.1 and 9.5 wt% H_2 release according to following reactions [106, 107]:

$$2LiAlH_4 + LiNH_2 \rightarrow 2Al + Li_2NH + LiH + 4H_2 \quad (2.33)$$

$$LiAlH_4 + 2LiNH_2 \rightarrow Li_3AlN_2H_4 + 2H_2 \rightarrow Li_3AlN_2 + 4H_2 \quad (2.34)$$

Significant improvement in the kinetic performance could be achieved by adding hexamethylphosphoramide (HMPA) solvent, which reduced the desorption temperature of 1:1 $LiAlH_4$/$LiNH_2$ system to 50 °C from 200 °C for the solvent-free $LiAlH_4$/$LiNH_2$ system [108]. The reaction was proposed as follows:

$$LiAlH_4 + LiNH_2 \xrightarrow{HMPA} Li_2NH + Al + \frac{5}{2}H_2 \quad (2.35)$$

The reaction mechanism was proposed to proceed through the formation of AlH species and simultaneous H_2 evolution (Figure 2.14).

More complex systems having two cations also show promise, e.g., $NaAlH_4$/$LiNH_2$ system in 1:1 ratio has been proposed to react as follows with 5.2 wt% H_2 evolution [109]:

$$NaAlH_4 + LiNH_2 \rightarrow NaH + LiH + AlN + 2H_2 \quad (2.36)$$

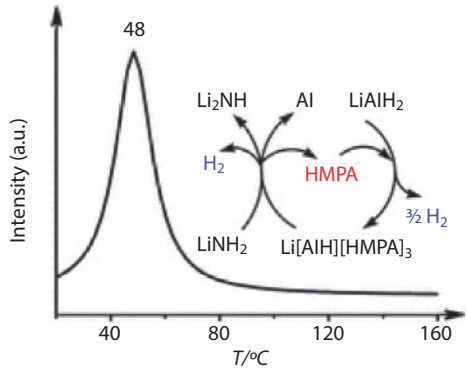

Figure 2.14 Hydrogen desorption from $LiAlH_4$-$LiNH_2$/HMPA; inset shows the schematic mechanism of dehydrogenation. (Reproduced from [108] with the permission of Royal Society of Chemistry)

This can be described as a two-fold reaction:

$$2NaAlH_4 + LiNH_2 \rightarrow Na_2LiAlH_6 + AlN + 2H_2 \quad (2.37)$$

$$Na_2LiAlH_6 + LiNH_2 \rightarrow 2LiH + 2NaH + AlN + 2H_2 \quad (2.38)$$

Whereas the desorption properties of the above systems were promising, unfortunately these were only one-way reactions or some of them can absorb H_2 partially through a different reaction route, e.g., $LiAlH_4/LiNH_2$ (1:2), i.e., Li_3AlN_2 system can reabsorb only 2 equivalents of H_2 in a different reaction instead of 4 wt% in the desorption reaction [107]:

$$Li_3AlN_2 + 2H_2 \leftrightarrow LiNH_2 + 2LiH + AlN \quad (2.39)$$

Similar to the above, the borohydride addition also suggests quite nice desorption properties; however, these also possess the same issue of reversibility. The final products are some M-B-N compounds which are even more stable than their analogous M-Al-N, so are unable to absorb hydrogen at all [114–124].

2.3 Ammonia (NH_3) as Hydrogen Storage Media

Apart from solid-state materials, hydrogen can be stored indirectly in other chemicals such as methanol, methane or ammonia. Out of these, ammonia can be considered as a much cleaner option owing to its carbon-free structure and high hydrogen content of 17.7 wt%. In terms of energy density, only ammonia and hydrides place very close to the conventional fuels, i.e., coal and oil [125]. NH_3 was first projected as an energy storage option by L. Green in 1982 [126]. There are several other advantages of ammonia which allow it to be adopted for energy needs. The first of these benefits is its technological infrastructure, which is well established and already in use on an industrial level [126]. Secondly, it is a low-cost chemical with a low boiling point of −33.5 °C. It can easily be stored in the liquid state under 8 bar pressure, which is an advantageous feature in comparison to liquid hydrogen with a boiling point of −252 °C. Thus, liquid NH_3 is much easier to handle than liquid H_2 [127]. Despite these promising features, NH_3 is still not being used as a fuel because of its high toxicity [128]; however, recent investigations on its safe solid-state storage in halides, borohydrides, etc., have solved this issue to a great extent [129]. This section will describe the essential aspects of NH_3 production, storage and its decomposition to use in energy vectors.

2.3.1 NH_3 Synthesis

The synthesis of NH_3 on an industrial scale is being carried out by the Haber-Bosch process, which was proposed at the beginning of 20th century. The synthesis of NH_3 can be performed directly from its elements at 300–500 °C under 200–350 bar pressure in the presence of suitable catalysts [130, 131]. Fritz Haber first proposed the theoretical model of ammonia production, which was realized by Bosch on an industrial scale [132–135]. Mittasch and Frankenburg [136] developed a mixed catalyst based on fused iron, which has been so effective for this process that it has been used for this industry for a long time. The development of new catalysts also uses the principle of this discovery. Haber and Bosch were awarded the Nobel Prize for this great discovery that has not only benefited science and industry, but which has also contributed a lot to society and civilization. During the last century, there have been tremendous efforts and developments which have advanced NH_3 industry greatly. The production of NH_3 was increased to 150 million tons/year in 2015, and is projected to reach 200 million tons/year in 2020. A rapid growth in world population and its energy needs warrant a further increase in ammonia production in the future. Currently, the reaction pressure has been lowered to 10–15 MPa from 100 MPa in the beginning. The required energy has also significantly decreased from 78 GJ to 27 GJ, a value nearly equal to the theoretical energy consumption of 20 GJ.

2.3.1.1 Catalytic NH_3 Synthesis Using Haber-Bosch Process

The NH_3 synthesis process from its constituent elements is as follows:

$$3H_2 + N_2 \rightarrow 2NH_3 \tag{2.40}$$

The suitable values of ΔH (−46 kJ/mol) and ΔS (−99.35 J/K mol) suggest a low-temperature reaction; however, it is not realized due to the presence of highly stable N≡N bond in nitrogen molecule. The high bond energy of 945 kJ/mol creates a significant activation barrier [132, 137, 138]. This is the reason why the reaction requires high pressure and temperature conditions. The kinetic rate of the above reaction first increases with the temperature up to a certain point then decrease with a further temperature increase due to low equilibrium NH_3 concentration which originated from its decomposition at high temperature. Thus, it is important to optimize the balance between temperature, pressure, and reaction rate to achieve high NH_3 yield with a reasonable production rate. To achieve this goal,

several catalysts have been tested and reported in the last century, which will be summarized here.

2.3.1.1.1 Iron-Based Catalyst

Ammonia synthesis could be realized as an industrial process with the development of iron-based catalyst. The invention of iron ores, e.g., a mixture of Fe_3O_4, Al_2O_3, CaO and K_2O, by Mittasch created a history. These catalysts have been proven as the most used catalyst for the NH_3 synthesis industry, maintaining their unique place even today. The magical performance of these promoted fused iron catalysts has been studied by several researchers [139–142]. Back donation process for N_2 cleavage has been suggested by Rao *et al.* [139], according to which the donation of electrons from transition metal's bonding orbitals occurs with the acceptance of electrons by their antibonding π-orbitals. A further weakening of N≡N bond can be achieved by the addition of electron donors such as K_2O [140, 141].

Until the first half of the 1980s, Fe_3O_4 was the only precursor considered for the fused iron catalyst. The invention of $Fe_{1-x}O$ based catalyst in 1986 [143] shows better performance than that of Fe_3O_4 and is now being considered as the best catalyst of this group [144–150]. It is suggested that $Fe_{1-x}O$-based (Wüstite) catalyst has the advantage of being more easily reducible with a satisfactory thermoresistance and mechanical strength [147]. It is also reported that $Fe_{1-x}O$-based catalyst has more exposing (111) and (211) planes than that of Fe_3O_4-based catalyst, which are believed to be the planes of high catalytic activity in ammonia synthesis [148]. In addition, higher lattice microstrains, i.e., more defects on the surface of Wüstite catalyst, serve as active sites for chemical reaction, thus resulting in higher catalytic activity.

2.3.1.1.2 Ruthenium-Based Catalyst

The ruthenium-based catalyst was first proposed in 1917 at the same time as the Fe-based catalyst, but it showed less catalytic activity in comparison to its rivals. After more than 50 years of this being reported, Sudo *et al.* [151] proposed a transition metal-based catalyst system with high catalytic activity for NH_3 synthesis under mild conditions, which consisted of alkali metal (Na or K) as an electron donor and transition metal (Fe, Ru, Co) as an electron acceptor. Later, in 1972, Aika *et al.* found a very high catalytic performance for NH_3 synthesis by using a system containing Ru as the active component, K as a metal promoter and carbon as catalyst carrier [152–154]. Although the addition of alkali and alkaline earth metal oxides, such as K_2O, $Cs_{2+x}O$, BaO_x, etc., enhanced the catalytic activity of Ru catalyst significantly, their ability to donate electrons is limited because

of their large work function, and thus not sufficient to facilitate NH_3 synthesis under mild conditions. The use of pure metals drastically enhances the catalytic activity [155], but at the same time, these are quite unstable because of their high reactivity with NH_3, thus converting into amides [156]. Thus, for efficient NH_3 synthesis, a stable electron donor material is required which has low work function, high melting point, and less reactivity with H_2, N_2, and NH_3. This search led to the introduction of a stable electride C12A7:e^- in 2012 by Kitano *et al.* [157]. It fulfills all the requirements of an electron donor material for Ru catalyst, i.e., it has quite a nice chemical stability because of its H_2 sorption capability, thus no H_2 poisoning on the catalyst surface.

Actually, C12A7:e^- was first synthesized in 2003 from a stable oxide $12CaO.7Al_2O_3$ and was found to be stable at room temperature in contrast to several other electrides, which usually decompose at approx. −30 °C. The unique structure of C12A7 is composed of a positively charged framework, consisting of 12 sub-nanometer sized cages (Figure 2.15). Four electrons can be injected into 4 cages by extracting 2 O^{2-} ions, which are accommodated as counteranions in sub-nanometer cages of Ca, Al and O; thus the resulting formula is $[Ca_{24}Al_{28}O_{64}]^{4+}(e^-)_4$. It was observed that the catalytic activity of Ru-loaded C12A7:e^- was an order of magnitude higher than that of only Ru-based catalyst, as shown in Figure 2.15. On the basis of several experiments and calculations [158, 159], it was revealed that the rate-limiting step in ammonia formation is the formation of $N–H_4$ species rather than N≡N bond dissociation as observed for other conventional catalysts. In addition, Ru surface is usually covered with H adatoms in the case of a conventional operation, which stops the interaction of N atoms and thus doesn't allow enhancement of NH_3 formation efficiency even with the increase in pressure. However, due to the special ability of C12A7:e^-, some of the H adatoms are allowed to move into the cages of C12A7:e^- through the reversible reaction $H^0 + e^- \leftrightarrow H^-$. This process keeps sufficient N_2 cleavage sites available on the Ru surface, which promote efficient NH_3 formation. At the same time, the H^- anions cannot be stimulated in the cages because the H release reaction can be combined with N atoms to form NH_3. This overall process (Figure 2.16) allows a persistent catalytic activity of this material.

2.3.1.1.3 Co-Mo Nitride Catalyst

Although Ru-based catalyst has shown great improvements in the NH_3 synthesis process, their high cost demands searching for cheap alternatives. On the basis of the volcano-shaped curve of catalytic activity and the nitrogen adsorption energy of metal (Figure 2.17), cheap metals, e.g., pure

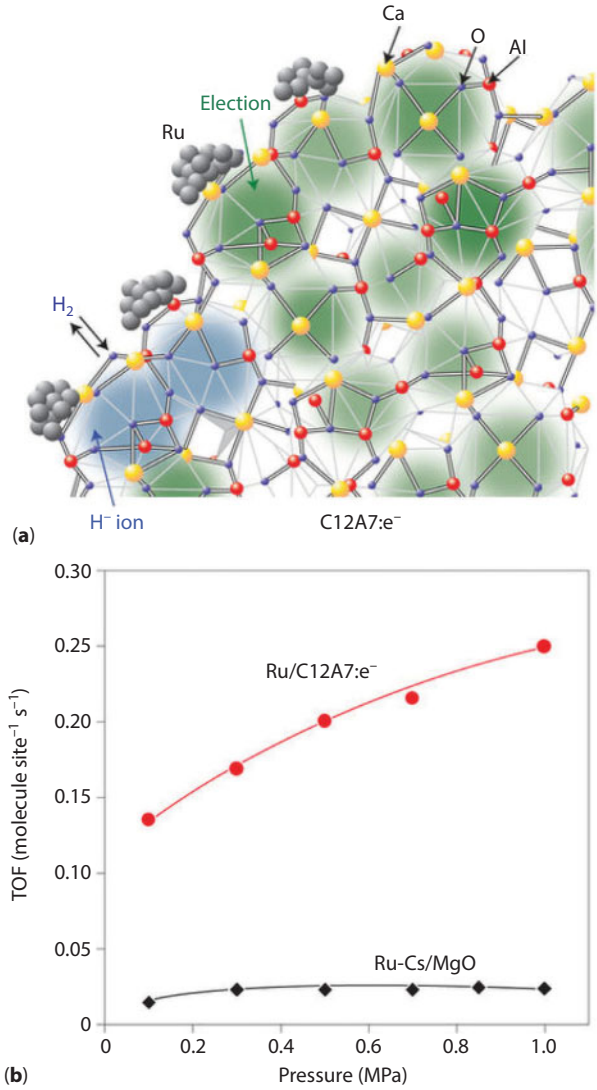

Figure 2.15 (a) Schematic model of Ru-loaded C12A7:e$^-$. High-density electrons (2.0 × 1021 cm^{-3}) are distributed statistically in the subnanometer-sized cages of C12A7 as counteranions and electrons encaged in C12A7 can be exchanged by H– ions under an H_2 atmosphere; (b) TOFs for high-pressure ammonia synthesis over 1 wt% Ru/C12A7:e$^-$ and 6 wt% Ru-Cs/MgO. (Reproduced from [157] with permission of Nature Publishing Group)

Co, Ni or Mo, have less catalytic activity than Fe or Ru catalysts. However, when Co and Mo are combined together, the alloy has a good compromise of catalytic activity and N_2 adsorption energy, thus is expected to be a suitable candidate as a catalyst.

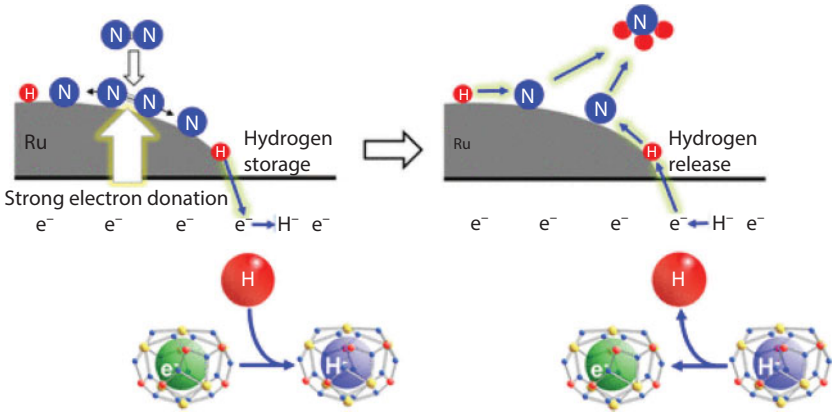

Figure 2.16 Proposed reaction mechanism of ammonia synthesis over Ru/C12A7:e⁻. (Reproduced from [159] with permission of American Chemical Society)

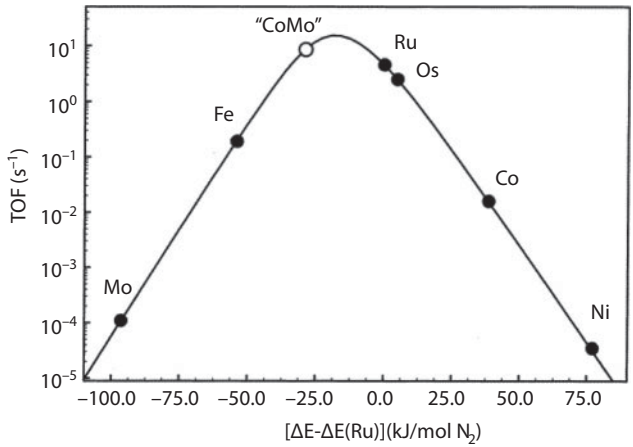

Figure 2.17 Calculated turnover frequencies for ammonia synthesis as a function of the adsorption energy of nitrogen. (Reproduced from [160] with permission of American Chemical Society)

Mittasch [161] has shown the better catalytic performance of Mo mixed with iron, cobalt or nickel. Thus, recently Kojima and Aika [162–165] developed Co-Mo bimetallic nitride and studied its detailed performance as a catalyst for NH_3 synthesis. It was observed that Co-Mo-N system has higher catalytic activity than iron/Ru-based catalyst at low NH_3 concentration. In a recent report, Co-Mo nanoparticles decorated on CeO_2 support have shown 20 times higher catalytic activity than that of the pure Co_3Mo_3N system [166].

2.3.1.2 Alternative Routes for NH_3 Synthesis

Apart from industrial production of NH_3, several alternatives have also been developed for the anticipated rapid growth in NH_3 demand in the near future. Electrochemical NH_3 production is one of the alternatives which can save almost 20% energy consumption in comparison to the commercial Haber-Bosch process [167]. Electrochemical synthesis can be divided into four categories based on the electrolytes used during the process, i.e., a liquid electrolyte-based system which can be operated near ambient temperature, a molten salt-based electrolyte which can be operated at 300–500 °C, mixed electrolyte composed of a solid electrolyte and molten salt that can operate at 300–700 °C, and finally solid electrolyte-based system capable of working at a wide range of temperatures from room temperature to 800 °C [167–170]. The electrochemical synthesis of NH_3 proceeds through the following reactions:

$$3H_2O \rightarrow 3/2O_2 + 6H^+ + 6e^- \text{ (Anode acidic condition)} \quad (2.41)$$

$$6OH^- \rightarrow 3H_2O + 3/2O_2 + 6e^- \text{ (Anode base condition)} \quad (2.42)$$

$$N_2 + 6H^+ + 6e^- \rightarrow 2NH_3 \text{ (Cathode acidic condition)} \quad (2.43)$$

$$N_2 + 6H_2O + 6e^- \rightarrow 2NH_3 + 6OH^- \text{ (Cathode base condition)} \quad (2.44)$$

Thus, overall reaction is:

$$N_2 + 3H_2O \rightarrow 3/2O_2 + 2NH_3 \quad (2.45)$$

Thus, there is no fossil fuel consumption during NH_3 synthesis.

Another approach to synthesize NH_3 is based on natural enzymes known as nitrogenases. These enzymes are a combination of two proteins. The most effective nitrogenases are FeMo nitrogenases, which have two fused iron-sulfur clusters. The carbon atom is positioned at their junction while the Mo atom is at apical position [171, 172]. The NH_3 synthesis reaction occurs as follows:

$$N_2 + 8H^+ + 8e^- + 16\ ATP \rightarrow 2NH_3 + H_2 + 16\ ADP \quad (2.46)$$

A total of 244 kJ/mol NH_3 is consumed during the reaction, which is much better than the industrial process [173].

Another alternative route for NH_3 synthesis has been recently proposed by Jain *et al.* [174] using hydrolysis of nitrides according to the following reaction:

$$Li_3N + 3H_2O \rightarrow 3\ LiOH + NH_3 \tag{2.47}$$

The reaction can be proceeded below 100 °C, thus eliminating the use of fossil fuels and can be performed using renewable energy sources-based production plants.

2.3.2 NH_3 Solid-State Storage

Currently, ammonia is being stored and transported in liquid form. Normally it is stored at 1 bar and −33 °C in insulated tanks for large quantities, i.e., up to 50000 ton, whereas it is stored under pressure in SS chambers for small quantities, i.e., up to 1500 tons [175]. However, the toxicity and vapor pressure of NH_3 are two serious issues which should be overcome to make it user-friendly for mobile applications. These problems can be solved by comparably safe solid-state storage of ammonia in the form of metal ammine salts [176] and ammine metal borohydrides [177], which will be described in this section.

2.3.2.1 Metal Ammine Salts

A large number of anhydrous metal salts (MX_m) are known to absorb NH_3 and form metal amine complexes, where M can be Mg, Ca, Cr, Ni, Zn, and X can be Cl, Br, SO_4, etc. [130]. Although the chemistry of these metal ammine complexes has been known for almost a century, they could not be used for storing ammonia due to their high working pressure [178, 179] until recent reports by Liu and Aika [176, 180]. These studies have shown NH_3 absorption for $MgCl_2$, $CaCl_2$, $CaBr_2$, and SrB_2 materials and suggest that $MgCl_2$, $CaCl_2$, and $CaBr_2$ are capable of absorbing and desorbing ammonia for temperature swing adsorption method between 298 K and 473 K, whereas $CaCl_2$–$CaBr_2$ mixed halide can reversible hold NH_3 for pressure swing adsorption method between 10 and 60 kPa NH_3 [179, 180]. Out of all the studied salts so far, $MgCl_2$ has been found to be the most studied and effective material due to its high hydrogen density (9.1 wt%) and low vapor pressure [181–185]. The sorption reaction of hexa-ammine complex of $MgCl_2$ has been proposed as follows:

$$Mg(NH_3)_6Cl_2 \rightarrow Mg(NH_3)_2Cl_2 + 4NH_3\ (440\ K) \tag{2.48}$$

$$Mg(NH_3)_2Cl_2 \rightarrow Mg(NH_3)Cl_2 + NH_3\,(575\ K) \tag{2.49}$$

$$Mg(NH_3)Cl_2 \rightarrow MgCl_2 + NH_3\,(675\ K) \tag{2.50}$$

Using pressure-composition isotherms, the thermodynamic parameters were calculated as $\Delta H = -58 \pm 6$kJ/mol, $\Delta S = -150 \pm 20$ J/K mol and $\Delta H = -64 \pm 1$ kJ/mol, $\Delta S = -97 \pm 2$ J/K mol for $Mg(NH_3)_6Cl_2$ and $Mg(NH_3)Cl_2$ formation [185] respectively. The crystal structure of $Mg(NH_3)_6Cl_2$ has been evaluated as cubic K_2PtCl_6-type structure with space group Fm3m [186]. However, no description was given for H position, so a detailed investigation using PND was carried out by Sørby *et al.* [187]. They suggested that Mg atoms are located at 4a site, Cl at 8c, N at 96j and two different sites, 96k and 96j, for D atoms. An *in-situ* structural study of $Mg(NH_3)_6Cl_2$ suggests that the skeletal aggregate structure of $Mg(NH_3)_6Cl_2$ keeps the pores even after NH_3 desorption, which accounts for the exceptionally fast reloading of NH_3 in the sample. A recent study [185] suggested that a high kinetic barrier exists for the formation of mono- or di-ammine complexes, which enables the direct formation of the hexa-ammine complex at room temperature. It is observed that the formation of $Mg(NH_3)_2Cl_2$ and $Mg(NH_3)Cl_2$ can take place only at 373 K and 573 K respectively. However, milling of $MgCl_2$ introduces some structural disordered state, thus also allowing the formation of low-coordinated ammine complex at room temperature.

Another high hydrogen density ammine complex is $Ca(NH_3)_8Cl_2$ with 9.78% H_2 and lower ammonia desorption temperature than $Mg(NH_3)_6Cl_2$, as shown in Figure 2.18. However, at the same time, the ammonia vapor pressure is around 0.7 bar at room temperature due to this lower desorption temperature, but still much lower than that of liquid ammonia [181].

2.3.2.2 Ammine Metal Borohydride

Similar to metal ammine salt complexes, borohydrides can also reversibly absorb ammonia according to following general reaction:

$$M(BH_4)_m + nNH_3 \leftrightarrow M(NH_3)_n(BH_4)_m \tag{2.51}$$

The first study on ammonia absorption by lithium borohydride appeared in 1959, in which Sullivan and Johnson [188] reported the formation of four compounds of $LiBH_4$ and NH_3 up to 4 mol of NH_3/mole of $LiBH_4$. Several amine-metal borohydride complexes have been developed since then and they have been intensively studied for their H_2 sorption properties [177]; however, no report except the early report by Sullivan and

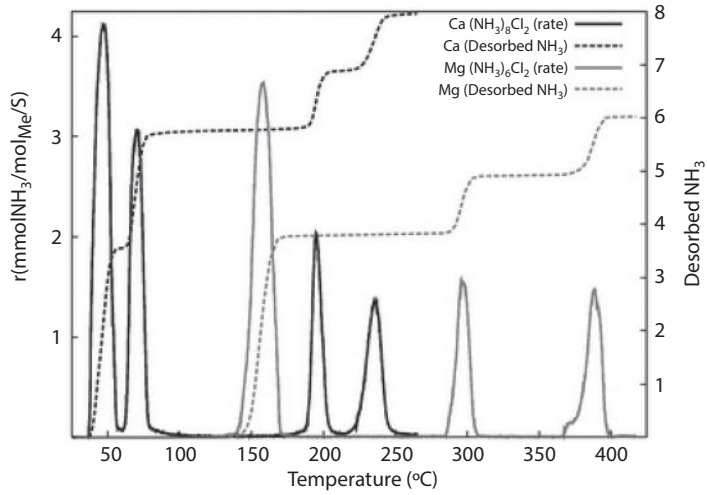

Figure 2.18 Temperature programmed desorption of ammonia from $Ca(NH_3)_8Cl_2$ and $Mg(NH_3)_6Cl_2$. (Reproduced from [130] and [181] with permission of Royal Society of Chemistry and American Chemical Society respectively)

Johnson [188] has focused on the ammonia sorption properties of borohydrides. Recently, Aoki *et al.* [189] investigated NH_3 sorption properties of alkali and alkaline metal borohydrides by means of PCI measurements (Figure 2.19) and elaborated the thermodynamics of ammonia absorption. They proposed a correlation between the plateau pressure of NH_3 sorption and the electronegativity of the cation of borohydrides. The borohydrides having high electronegative cation show lower plateau pressure of NH_3 sorption, i.e., in the order of $P_{eq}(KBH_4) > P_{eq}(NaBH_4) > P_{eq}(LiBH_4)$, $P_{eq}(Mg(BH_4)_2)$, $P_{eq}(Ca(BH_4)_2)$.

2.3.3 NH_3 Decomposition

The use of ammonia as H_2 storage media strongly depends on the efficient delivery of H_2 from it by its decomposition. It can be decomposed into its elements as the reverse reaction of the Haber-Bosch process, with ΔH = 92 kJ/mol. Being an endothermic process, it needs very high temperature, i.e., 400–500 °C, to decompose at a significant rate without catalyst [190]. However, to make it compatible with an H_2 fed PEM fuel cell, it is important to lower the decomposition temperature to the operating temperature range of PEMFC, i.e., 150–180 °C. To achieve this goal, ammonia cracking needs the use of catalysts. There have been several catalysts proposed during the past several years, out of which Ni on alumina [191] is presently

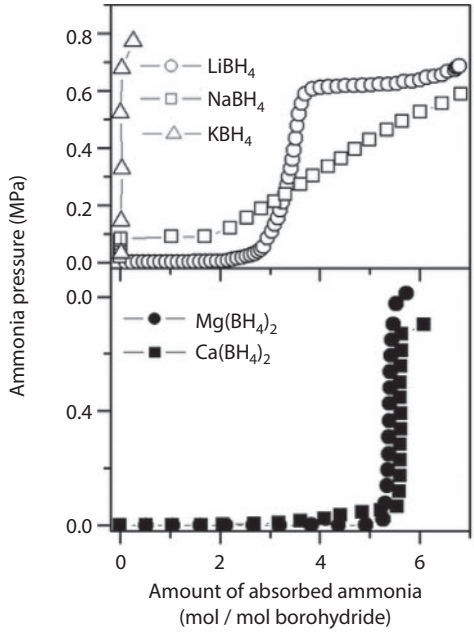

Figure 2.19 PC isotherms for NH_3 absorption of different borohydrides. (Reproduced from [189] with permission of American Chemical Society)

being used commercially owing to its high heat resistance and mechanical strength. The most effective catalyst for NH_3 decomposition is found to be Ru nanoparticles on carbon nanotubes [192, 193]. The addition of Cs as electron donating promotor further enhances the catalytic activity and reduces the operating temperature up to 300 °C [194–196]. It is important to understand the mechanism of this ammonia decomposition in order to develop suitable catalyst. Similar to H_2 absorption in metal, ammonia adsorption on the active surface is the first step of ammonia decomposition. This adsorbed ammonia molecule undergoes decomposition through N–H bond cleavage, thus forming adsorbed NH_2 and H, and then releases H_2 by combining H atoms. Then, recombination of N atoms takes place to desorb N_2 gas as a final step. The latter step is usually found to be slow [197]; however, in some cases, e.g., NiPt/Al_2O_3 catalyst, H_2 doesn't show an inhibitory effect, thus making the NH_3 decomposition reaction the first-order reaction with N_2 desorption as the rate limiting step. Thus, it has been concluded that the rate-limiting step strongly depends on the catalyst and the reaction conditions [192, 198–200]. In a study by Ganley *et al.* [201] on the number of catalysts, it was concluded that N-H bond cleavage is the rate-limiting step for Rh, Ir, Pd, Pt, and Cu, but Fe, Co, and Ni shows

N_2 desorption as the rate limiting step. In addition, it is important to note that the catalytic activity is not dependent only on the choice of metals but also on the catalytic support and potential use of promoters. This can be understood using the example of Ru catalyst, which has shown different catalytic activity for different promoters in the order of Cs > K > Na > Li > Ba > Ca [202]. On the other hand, the catalytic action of different metals was found in the order of Ru > Ni > Rh > Co > Ir > Fe > Pt > Cr > Pd > Cu > Te, Se, Pb [201] for a similar support of activated alumina. On the basis of the above, several Ru-, Fe-, Co-, and Ni-based catalysts were developed which have shown promise for NH_3 decomposition [203, 204].

Apart from the conventional catalytic decomposition of NH_3, a new approach has been proposed for H_2 generation using sodium amide [38]. It has achieved 99.2% decomposition efficiency of NH_3 by running the following reactions concurrently:

$$NaNH_2 \rightarrow Na + 1/2N_2 + H_2 \tag{2.52}$$

$$Na + NH_3 \rightarrow NaNH_2 + 1/2H_2 \tag{2.53}$$

2.3.4 Application of NH_3 to Fuel Cell

The NH_3 splits into N_2 and H_2 that can be fed into low-temperature fuel cells, such as polymer electrolyte membrane fuel cells (PEMFCs) and alkaline fuel cells (AFCs), by using a hydrogen-selective membrane [205, 206]. Using AFC with NH_3 is easier due to its tolerance towards NH_3 [207]; however, in the case of PEMFC, NH_3 is highly poisonous due to its reaction with electrode, thus limiting its long-term application [208]. Apart from H_2 fed fuel cells, NH_3 can directly be used in solid oxide fuel cell system at high temperature according to the following reaction [209]:

$$2NH_3 + 5O^{2-} \rightarrow 2NO + 3H_2O + 10e^- \tag{2.54}$$

$$2NH_3 + 3NO \rightarrow 5/2N_2 + 3H_2O \tag{2.55}$$

These are known as oxygen ion conducting electrolyte SOFCs (SOFC-O); whereas, to eliminate the formation of NO, proton conducting electrolyte-based SOFCs (SOFC-H) using doped $BaCeO_3$ and $BaZrO_3$ [210, 211] can be employed according to the following anodic reaction:

$$2NH_3 - 6e^- \rightarrow N_2 + 6H^+ \tag{2.56}$$

The theoretical maximum efficiency was found to be better for NH_3 fed SOFC-H in comparison to that of SOFC-O [212].

Another fuel cell which can work with ammonia directly is alkali and alkaline membrane fuel cell (AMFC) [213]. In contrast to the acidic proton conducting polymer electrolyte, NH_3 is compatible with an alkaline electrolyte such as KOH. NH_3-based AMFC also works on the same principle as traditional alkaline fuel cells, where hydroxide ion moves through the electrolyte as follows [214]:

$$O_2 + 2H_2O + 4e^- \rightarrow 4OH^- \tag{2.57}$$

$$2NH_3 + 6OH^- \rightarrow N_2 + 6H_2O + 6e^- \tag{2.58}$$

2.4 Future Prospects

Nitrogen-based hydrogen storage systems have rich chemistry with high hydrogen content which shows great promise for future energy systems. Double-cation amide/imide-hydride systems have matured enough in terms of the understanding of their structural and sorption properties and ready to be adopted for engineering parts. Recently, sodium amide system has emerged as a potential candidate not only as hydrogen storage media but also as a catalyst for H_2 production from NH_3. There is huge scope to develop sodium amide-based multi-cation/complex amide-hydride systems similar to their analogous $LiNH_2$. On the other hand, NH_3 has also shown great promise to be adapted as hydrogen storage media after the development of halide and borohydride to absorb it in the solid state, which overcomes the problem of toxicity and safety. The remaining challenge related to NH_3 production is to remove carbon in order to make it a cleaner option. There are several alternatives, such as electrochemical synthesis, nitrogenases-based synthesis, hydrolysis of nitrides, etc., that have been developed in recent years; however, these need to be explored in more detail. Although ammine salt complexes and recently borohydrides have been explored for the efficient solid-state storage of ammonia, borohydrides are still relatively untouched and need to be examined in the near future. Finally, the development and optimization of direct ammonia fuel cells is in the developing phase and the operating temperature is still too high for transport applications. Anyway, sooner or later the use of nitrogen-based hydrogen storage materials can establish an ammonia and hydrogen economy simultaneously and efficiently.

References

1. Jain, I.P., Lal, C., Jain, A., Hydrogen storage in Mg: A most promising material. *Int. J. Hydrogen Energy* 35, 5133–5144, 2010.
2. Jain, I.P., Jain, P., Jain, A., Novel hydrogen storage materials: A review of lightweight complex hydrides. *J. Alloys Compd.* 503, 303–309, 2010.
3. Chen, P., Xiong, Z., Luo, J., Lin, J., Tan, K.L., Interaction of hydrogen with metal nitrides and imides. *Nature* 420, 302–304, 2002.
4. Wuerthwein, E.U., Sen, K.D., Pople, J.A., Schleyer, P.V.R., Lithiated ammonia, amide anions, and ammonium ions. An ab initio study of structures, bonding, and energetic relationships. *Inorg. Chem.* 22, 496–503, 1983.
5. Chen, P., Xiong, Z., Wu, G., Liu, Y., Hu, J., Luo, W., Metal–N–H systems for the hydrogen storage. *Scripta Mater.* 56, 817–822, 2007.
6. Jain, A., Ichikawa, T., Metal amides: New hydrogen storage systems, in: *Reference Module in Materials Science and Materials Engineering*, S. Hashmi (Ed.) Elsevier, 2016, https://doi.org/10.1016/B978–0-12–803581-8.02077–4.
7. Green, L., An ammonia energy vector for the hydrogen economy. *Int. J. Hydrogen Energy* 7, 355–359, 1982.
8. Umegaki, T., Yan, J.-M., Zhang, X.-B., Shioyama, H., Kuriyama, N., Xu, Q., Boron- and nitrogen-based chemical hydrogen storage materials. *Int. J. Hydrogen Energy* 34, 2303–2311, 2009.
9. Zheng, M., Cheng, R., Chen, X., Li, N., Li, L., Wang, X., Zhang, T., A novel approach for CO-free H_2 production via catalytic decomposition of hydrazine. *Int. J. Hydrogen Energy* 30, 1081–1089, 2005.
10. Titherley, A.W., Sodium, potassium and lithium amides. *J. Chem. Soc.* 65, 504, 1894.
11. Morrison, R.C., Bach, R.O., Preparation of lithium amide. US Patent 4206191A, assigned to Lithium Corp of America Inc, 3 June 1980.
12. Baldissin, G., Boag, N.M., Tang, C.C., Bull, D.J., Synthesis of pure lithium amide nanoparticles. *Eur. J. Inorg. Chem.* 2013, 1993–1996, 2013.
13. Ichikawa, T., Hanada, N., Isobe, S., Leng, H., Fujii, H., Mechanism of novel reaction from $LiNH_2$ and LiH to Li_2NH and H_2 as a promising hydrogen storage system. *J. Phys. Chem. B* 108, 7887–7892, 2004.
14. Yang, J.B., Zhou, X.D., Cai, Q., James, W.J., Yelon, W.B., Crystal and electronic structures of $LiNH_2$. *Appl. Phys. Lett.* 88, 041914, 2006.
15. Sørby, M.H., Nakamura, Y., Brinks, H.W., Ichikawa, T., Hino, S., Fujii, H., Hauback, B.C., The crystal structure of $LiND_2$ and $Mg(ND_2)_2$, *J. Alloys Compd.* 428, 297–301, 2007.
16. Wang, J., Du, Y., Xu, H., Jiang, C., Kong, Y., Sun, L., Liu, Z.-K., Native defects in $LiNH_2$: A first-principles study. *Phys. Rev. B* 84, 024107, 2011.
17. Ning, H., Lan, Z., Bai, J., Guo, J., Density function theory investigation on the thermodynamic properties of the Li–N–H system. *Mater. Chem. Phys.* 144, 484–490, 2014.

18. Juza, R., Opp, K., Metallic amides and metallic nitrides. XXIV. The crystal structure of lithium amide. *Z. Anorg. Allg. Chem.* 266, 313–324, 1951.
19. Noritake, T., Nozaki, H., Aoki, M., Towata, S., Kitahara, G., Nakamori, Y., Orimo, S., Crystal structure and charge density analysis of Li_2NH by synchrotron X-ray diffraction. *J. Alloys Compd.* 393, 264–268, 2005.
20. Ohoyama, K., Nakamori, Y., Orimo, S.I., Yamada, K., Revised crystal structure model of Li_2NH by neutron powder diffraction. *J. Phys. Soc. Jpn.* 74, 483–487, 2005.
21. Mueller, T., Ceder, G., Effective interactions between the N–H bond orientations in lithium imide and a proposed ground-state structure. *Phys. Rev. B* 74, 134104, 2006.
22. Magyari-Köpe, B., Ozoliņš, V., Wolverton, C., Theoretical prediction of low-energy crystal structures and hydrogen storage energetics in Li_2NH. *Phys. Rev. B* 73, 220101, 2006.
23. Balogh, M.P., Jones, C.Y., Herbst, J.F., Hector, L.G., Kundrat, M., Crystal structures and phase transformation of deuterated lithium imide, Li_2ND. *J. Alloys Compd.* 420, 326–336, 2006.
24. Miwa, K., Ohba, N., Towata, S.-I., First-principles study on lithium amide for hydrogen storage. *Phys. Rev. B* 71, 195109, 2005.
25. Chen, P., Xiong, Z., Luo, J., Lin, J., Tan, K.L., Interaction between lithium amide and lithium hydride. *J. Phys. Chem. B* 107, 10967–10970, 2003.
26. Hu, Y.H., Ruckenstein, E., Ultrafast reaction between LiH and NH_3 during H_2 storage in Li_3N. *J. Phys. Chem. A* 107, 9737–9739, 2003.
27. Hu, J.Z., Kwak, J.H., Yang, Z., Osborn, W., Markmaitree, T., Shaw, L.L., Probing the reaction pathway of dehydrogenation of the $LiNH_2$ + LiH mixture using *in situ* ^1H NMR spectroscopy. *J. Power Sources* 181, 116–119, 2008.
28. Cao, H., Wang, J., Chua, Y., Wang, H., Wu, G., Xiong, Z., Qiu, J., Chen, P., NH_3 mediated or ion migration reaction: The case study on halide–amide system. *J. Phys. Chem. C* 118, 2344–2349, 2014.
29. Aguey-Zinsou, K.-F., Yao, J., Guo, Z.X., Reaction paths between $LiNH_2$ and LiH with effects of nitrides. *J. Phys. Chem. B* 111, 12531–12536, 2007.
30. Lange, L., Triebel, W., Sodium amide, in: *Ullmann's Encyclopedia of Industrial Chemistry*, Wiley-VCH Verlag GmbH & Co. KGaA, 2000.
31. Ogilvie, A.D., Makepeace, J.W., Hore, K., Ramirez-Cuesta, A.J., Apperley, D.C., Mitchels, J.M., Edwards, P.P., Sartbaeva, A., Catalyst-free synthesis of sodium amide nanoparticles encapsulated in silica gel. *Chem. Phys.* 427, 61–65, 2013.
32. Leng, H.Y., Ichikawa, T., Hino, S., Hanada, N., Isobe, S., Fujii, H., Synthesis and decomposition reactions of metal amides in metal–N–H hydrogen storage system. *J. Power Sources* 156, 166–170, 2006.
33. Juza, R., Weber, H.H., Opp, K., Kristallstruktur des natriumamids. *Z. Anorg. Allg. Chem.* 284, 73–82, 1956.

34. Zalkin, A., Templeton, D.H., The crystal structure of sodium amide. *J. Phys. Chem.* 60, 821–823, 1956.
35. Nagib, M., Kistrup, H., Jacobs, H., Neutronenbeugung am natriumdeuteroamid Na N D2. *Atomkernenergie* 26, 87–90, 1975.
36. Liu, A., Song, Y., *In situ* high-pressure study of sodium amide by Raman and infrared spectroscopies. *J. Phys. Chem. B* 115, 7–13, 2011.
37. Cunningham, P.T., Maroni, V.A., Laser Raman spectra of solid and molten $NaNH_2$: Evidence for hindered rotation of the NH_2–1 ion. *J. Chem. Phys.* 57, 1415–1418, 1972.
38. David, W.I.F., Makepeace, J.W., Callear, S.K., Hunter, H.M.A., Taylor, J.D., Wood, T.J., Jones, M.O., Hydrogen production from ammonia using sodium amide. *J. Am. Chem. Soc.* 136, 13082–13085, 2014.
39. Sakurazawa, K., Hara, R., *J. Soc. Chem. Ind. (Japan)* Suppl. 40, 10B, 1937.
40. Jain, A., Miyaoka, H., Ichikawa, T., Two-peak mystery of $LiNH_2$–NaH dehydrogenation is solved? A study of the analogous sodium amide/lithium hydride system. *J. Phys. Chem. C* 120, 27903–27909, 2016.
41. Jain, A., Kumar, S., Miyaoka, H., Zhang, T., Isobe, S., Ichikawa, T., Kojima, Y., Ammonia suppression during decomposition of sodium amide by the addition of metal hydride. *Int. J. Hydrogen Energy* 42, 22388–22394, 2017.
42. Jepsen, L.H., Wang, P., Wu, G., Xiong, Z., Besenbacher, F., Chen, P., Jensen, T.R., Thermal decomposition of sodium amide, $NaNH_2$, and sodium amide hydroxide composites, $NaNH_2$–NaOH. *Phys. Chem. Chem. Phys.* 18, 25257–25264, 2016.
43. Yamaguchi, S., Miyaoka, H., Ichikawa, T., Kojima, Y., Thermal decomposition of sodium amide. *Int. J. Hydrogen Energy* 42, 5213–5219, 2017.
44. Jacobs, H., Juza, R., Darstellung und eigenschaften von magnesiumamid und -imid. *Z. Anorg. Allg. Chem.* 370, 254–261, 1969.
45. Terentiew, A.P., Einige reaktionen des aktivierten magnesiums. *Z. Anorg. Allg. Chem.* 162, 349–352, 1927.
46. Nakamori, Y., Kitahara, G., Orimo, S., Synthesis and dehydriding studies of Mg–N–H systems. *J. Power Sources* 138, 309–312, 2004.
47. Song, Y., Yang, R., Decomposition mechanism of magnesium amide $Mg(NH_2)_2$. *Int. J. Hydrogen Energy* 34, 3778–3783, 2009.
48. Dolci, F., Napolitano, E., Weidner, E., Enzo, S., Moretto, P., Brunelli, M., Hansen, T., Fichtner, M., Lohstroh, W., Magnesium imide: Synthesis and structure determination of an unconventional alkaline earth imide from decomposition of magnesium amide. *Inorg. Chem.* 50, 1116–1122, 2011.
49. Hino, S., Ichikawa, T., Kojima, Y., Thermodynamic properties of metal amides determined by ammonia pressure-composition isotherms. *J. Chem. Thermodynamics* 42, 140–143, 2010.
50. Hu, J., Xiong, Z., Wu, G., Chen, P., Murata, K., Sakata, K., Effects of ball-milling conditions on dehydrogenation of $Mg(NH_2)_2$–MgH_2. *J. Power Sources* 159, 120–125, 2006.

51. Hu, J., Wu, G., Liu, Y., Xiong, Z., Chen, P., Hydrogen release from $Mg(NH_2)_2$–MgH_2 through mechanochemical reaction. *J. Phys. Chem. B* 110, 14688–14692, 2006.
52. Juza, R., Schumacher, H., Zur kenntnis der erdalkalimetallamide. *Z. Anorg. Allg. Chem.* 324, 278–286, 1963.
53. Sichla, Th., Jacobs, H., Darstellung und kristallstruktur von calciumimid, CaNH. *Z. Anorg. Allg. Chem.* 622, 2079–2082, 1996.
54. Brice, J.-F., Motte, J.-P., Courtois, A., Protas, J., Aubry, J., Etude structurale de Ca2NH par diffraction des rayons X, diffraction des neutrons et résonance magnétique nucléaire du proton dans le solide. *J. Solid State Chem.* 17, 135–142, 1976.
55. Reckeweg, O., DiSalvo, F.J., Alkaline earth metal nitride compounds with the composition M_2NX (M=Ca, Sr, Ba; X=□, H, Cl or Br). *Solid State Sciences* 4, 575–584, 2002.
56. Senker, J., Jacobs, H., Müller, M., Press, W., Müller, P., Mayer, H.M., Ibberson, R.M., Reorientational dynamics of amide ions in isotypic phases of strontium and calcium amide. 1. Neutron diffraction experiments. *J. Phys. Chem. B* 102, 931–940, 1998.
57. Kojima, Y., Kawai, Y., Ohba, N., Hydrogen storage of metal nitrides by a mechanochemical reaction. *J. Power Sources* 159, 81–87, 2006.
58. Hino, S., Ichikawa, T., Leng, H., Fujii, H., Hydrogen desorption properties of the Ca–N–H system. *J. Alloys Compd.* 398, 62–66, 2005.
59. Jacobs, H., Harbrecht, B., Über ein trilithiumnatriumamid, $Li_3Na(NH_2)_4$, eine verbindung mit lithiumamidverwandter struktur. *J. Less Common Metals* 85, 87–95, 1982.
60. Lowton, R.L., Jones, M.O., David, W.I.F., Johnson, S.R., Sommariva, M., Edwards, P.P., The synthesis and structural investigation of mixed lithium/sodium amides. *J. Mater. Chem.* 18, 2355–2360, 2008.
61. Jepsen, L.H., Wang, P., Wu, G., Xiong, Z., Besenbacher, F., Chen, P., Jensen, T.R., Synthesis and decomposition of $Li_3Na(NH_2)_4$ and investigations of Li–Na–N–H based systems for hydrogen storage. *Phys. Chem. Chem. Phys.* 18, 1735–1742, 2016.
62. Luo, W., *J. Alloys Compd.* ($LiNH_2$–MgH_2): A viable hydrogen storage system. 381, 284–287, 2004.
63. Liu, Y., Zhong, K., Luo, K., Gao, M., Pan, H., Wang, Q., Size-dependent kinetic enhancement in hydrogen absorption and desorption of the Li–Mg–N–H system. *J. Am. Chem. Soc.* 131, 1862–1870, 2009.
64. Ma, L.-P., Dai, H.-B., Fang, Z.-Z., Kang, X.-D., Liang, Y., Wang, P.-J., Wang, P., Cheng, H.-M., Enhanced hydrogen storage properties of Li–Mg–N–H system prepared by reacting $Mg(NH_2)_2$ with Li_3N. *J. Phys. Chem. C* 113, 9944–9949, 2009.
65. Rijssenbeek, J., Gao, Y., Hanson, J., Huang, Q., Jones, C., Toby, B., Crystal structure determination and reaction pathway of amide–hydride mixtures. *J. Alloys Compd.* 454, 233–244, 2008.

66. Markmaitree, T., Osborn, W., Shaw, L.L., Comparisons between MgH_2- and LiH-containing systems for hydrogen storage applications. *Int. J. Hydrogen Energy* 33, 3915–3924, 2008.
67. Markmaitree, T., Shaw, L.L., Synthesis and hydriding properties of $Li_2Mg(NH)_2$. *J. Power Sources* 195, 1984–1991, 2010.
68. Hu, J., Liu, Y., Wu, G., Xiong, Z., Chen, P., Structural and compositional changes during hydrogenation/dehydrogenation of the Li–Mg–N–H system. *J. Phys. Chem. C* 111, 18439–18443, 2007.
69. Xiong, Z., Hu, J., Wu, G., Chen, P., Luo, W., Gross, K., Wang, J., Thermodynamic and kinetic investigations of the hydrogen storage in the Li–Mg–N–H system. *J. Alloys Compd.* 398, 235–239, 2005.
70. Luo, W., Rönnebro, E., Towards a viable hydrogen storage system for transportation application. *J. Alloys Compd.* 404–406, 392–395, 2005.
71. Leng, H.Y., Ichikawa, T., Hino, S., Hanada, N., Isobe, S., Fujii, H., New metal–N–H system composed of $Mg(NH_2)_2$ and LiH for hydrogen storage. *J. Phys. Chem. B* 108, 8763–8765, 2004.
72. Nakamori, Y., Kitahara, G., Miwa, K., Ohba, N., Noritake, T., Towata, S., Orimo, S., Hydrogen storage properties of Li–Mg–N–H systems. *J. Alloys Compd.* 404–406, 396–398, 2005.
73. Nakamura, Y., Hino, S., Ichikawa, T., Fujii, H., Brinks, H.W., Hauback, B.C., Dehydrogenation reaction of Li–Mg–N–H systems studied by *in situ* synchrotron powder X-ray diffraction and powder neutron diffraction. *J. Alloys Compd.* 457, 362–367, 2008.
74. Xiong, Z., Wu, G., Hu, J., Chen, P., Luo, W., Wang, J., Investigations on hydrogen storage over Li–Mg–N–H complex—the effect of compositional changes. *J. Alloys Compd.* 417, 190–194, 2006.
75. Anton, D.L., Price, C.J., Gray, J., Affects of mechanical milling and metal oxide additives on sorption kinetics of 1:1 $LiNH_2/MgH_2$ mixture. *Energies* 4, 826–844, 2011.
76. Cao, H., Wu, G., Zhang, Y., Xiong, Z., Qiu, J., Chen, P., Effective thermodynamic alteration to $Mg(NH_2)_2$–LiH system: Achieving near ambient-temperature hydrogen storage. *J. Mater. Chem. A* 2, 15816–15822, 2014.
77. Price, C., Gray, J., Lascola, R., Anton, D.L., The effects of halide modifiers on the sorption kinetics of the Li–Mg–N--H system. *Int. J. Hydrogen Energy* 37, 2742–2749, 2012.
78. Ma, L.-P., Wang, P., Dai, H.-B., Cheng, H.-M., Catalytically enhanced dehydrogenation of Li–Mg–N–H hydrogen storage material by transition metal nitrides. *J. Alloys Compd.* 468, L21–L24, 2009.
79. Zhang, B., Wu, Y., Effects of additives on the microstructure and hydrogen storage properties of the Li_3N–MgH_2 mixture. *J. Alloys Compd.* 613, 199–203, 2014.
80. Zhu, X., Han, S., Zhao, X., Li, Y., Liu, B., Effect of lanthanum hydride on microstructures and hydrogen storage performances of $2LiNH_2$-MgH_2 system. *J. Rare Earths* 32, 429–433, 2014.

81. Shahi, R.R., Raghubanshi, H., Shaz, M.A., Srivastava, O.N., Improved hydrogen storage performance of $Mg(NH_2)_2$/LiH mixture by addition of carbon nanostructured materials. *Int. J. Hydrogen Energy* 38 8863–8871, 2013.
82. Liang, C., Liu, Y., Wei, Z., Jiang, Y., Wu, F., Gao, M., Pan, H., *Int. J. Hydrogen Energy* 36, 2137–2144, 2011.
83. Wang, J., Liu, T., Wu, G., Li, W., Liu, Y., Araújo, C.M., Scheicher, R.H., Blomqvist, A., Ahuja, R., Xiong, Z., Yang, P., Gao, M., Pan, H., Chen, P., Potassium-modified $Mg(NH_2)_2$/2 LiH system for hydrogen storage. *Angew. Chemie Int. Ed.* 48, 5828–5832, 2009.
84. Liang, C., Liu, Y., Gao, M., Pan, H., Understanding the role of K in the significantly improved hydrogen storage properties of a KOH-doped Li–Mg–N–H system. *J. Mater. Chem. A* 1, 5031–5036, 2013.
85. Li, C., Liu, Y., Pang, Y., Gu, Y., Gao, M., Pan, H., Compositional effects on the hydrogen storage properties of $Mg(NH_2)_2$–2LiH–*x*KH and the activity of KH during dehydrogenation reactions. *Dalton Trans.* 43, 2369–2377, 2014.
86. Li, C., Liu, Y., Yang, Y., Gao, M., Pan, H., High-temperature failure behaviour and mechanism of K-based additives in Li–Mg–N–H hydrogen storage systems. *J. Mater. Chem. A* 2, 7345–7353, 2014.
87. Durojaiye, T., Hayes, J., Goudy, A., Potassium, rubidium and cesium hydrides as dehydrogenation catalysts for the lithium amide/magnesium hydride system. *Int. J. Hydrogen Energy* 40, 2266–2273, 2015.
88. Teng, Y.-L., Ichikawa, T., Miyaoka, H., Kojima, Y., Improvement of hydrogen desorption kinetics in the LiH–NH_3 system by addition of KH. *Chem. Comm.* 47, 12227–12229, 2011.
89. Wang, J., Chen, P., Pan, H., Xiong, Z., Gao, M., Wu, G., Liang, C., Li, C., Li, B., Wang, J., Solid–solid heterogeneous catalysis: The role of potassium in promoting the dehydrogenation of the $Mg(NH_2)_2$/2 LiH composite. *ChemSusChem* 6, 2181–2189, 2013.
90. Wang, J., Wu, G., Chua, Y.S., Guo, J., Xiong, Z., Zhang, Y., Gao, M., Pan, H., Chen, P., Hydrogen sorption from the $Mg(NH_2)_2$-KH system and synthesis of an amide–imide complex of $KMg(NH)(NH_2)$. *ChemSusChem* 4, 1622–1628, 2011.
91. Liu, Y., Zhong, K., Luo, K., Gao, M., Pan, H., Wang, Q., Size-dependent kinetic enhancement in hydrogen absorption and desorption of the Li–Mg–N–H system. *J. Am. Chem. Soc.* 131, 1862–1870, 2009.
92. Xiong, Z., Wu, G., Hu, J., Chen, P., Ternary imides for hydrogen storage. *Adv. Mater.* 16, 1522–1525, 2004.
93. Wu, G., Xiong, Z., Liu, T., Liu, Y., Hu, J., Chen, P., Feng, Y., Wee, A.T.S., Synthesis and characterization of a new ternary imide–$Li_2Ca(NH)_2$. *Inorg. Chem.* 46, 517–521, 2007.
94. Wu, H., Structure of ternary imide $Li_2Ca(NH)_2$ and hydrogen storage mechanisms in amide–hydride system. *J. Am. Chem. Soc.* 130, 6515–6522, 2008.
95. Bhattacharya, S., Wu, G., Chen, P., Feng, Y.P., Das, G.P., Lithium calcium imide [$Li_2Ca(NH)_2$] for hydrogen storage: Structural and thermodynamic properties. *J. Phys. Chem. C* 112, 11381–11384, 2008.

96. Tokoyoda, K., Hino, S., Ichikawa, T., Okamoto, K., Fujii, H., Hydrogen desorption/absorption properties of Li–Ca–N–H system. *J. Alloys Compd.* 439, 337–341, 2007.
97. Chu, H., Xiong, Z., Wu, G., He, T., Wu, C., Chen, P., Hydrogen storage properties of Li–Ca–N–H system with different molar ratios of $LiNH_2/CaH_2$. *Int. J. Hydrogen Energy* 35, 8317–8321, 2010.
98. Xiong, Z., Hu, J., Wu, G., Chen, P., Hydrogen absorption and desorption in Mg–Na–N–H system. *J. Alloys Compd.* 395, 209–212, 2005.
99. Dolotko, O., Paulson, N., Pecharsky, V.K., Thermochemical transformations in $2MNH_2–3MgH_2$ systems (M = Li or Na). *Int. J. Hydrogen Energy* 35, 4562–4568, 2010.
100. Sheppard, D.A., Paskevicius, M., Buckley, C.E., Hydrogen desorption from the $NaNH_2–MgH_2$ system. *J. Phys. Chem. C* 115, 8407–8413, 2011.
101. Singh, N.K., Kobayashi, T., Dolotko, O., Wiench, J.W., Pruski, M., Pecharsky, V.K., Mechanochemical transformations in $NaNH_2$-MgH_2 mixtures. *J. Alloys Compd.* 513, 324–327, 2012.
102. Pireddu, G., Valentoni, A., Minella, C.B., Pistidda, C.,Milanese, C., Enzo, S., Mulas, G., Garroni, S., Comparison of the thermochemical and mechanochemical transformations in the $2NaNH_2–MgH_2$ system. *Int. J. Hydrogen Energy* 40, 1829–1835, 2015.
103. Hu, J., Xiong, Z., Wu, G., Chen, P., Murata, K., Sakata, K., Hydrogen releasing reaction between $Mg(NH_2)_2$ and CaH_2. *J. Power Sources* 159, 116–119, 2006.
104. Liu, Y., Liu, T., Xiong, Z., Hu, J., Wu, G., Chen, P., Wee, A.T.S., Yang, P., Murata, K., Sakata, K., Synthesis and structural characterization of a new alkaline earth imide: $MgCa(NH)_2$. *Eur. J. Inorg. Chem.* 2006, 4368–4373, 2006.
105. Liu, Y., Hu, J., Xiong, Z., Wu, G., Chen, P., Murata, K., Sakata, K., Investigations on hydrogen desorption from the mixture of $Mg(NH_2)_2$ and CaH_2. *J. Alloys Compd.* 432, 298–302, 2007.
106. Lu, J., Fang, Z.Z., Dehydrogenation of a combined $LiAlH_4/LiNH_2$ system. *J. Phys. Chem. B* 109, 20830–20834, 2005.
107. Xiong, Z., Wu, G., Liu, Y., Chen, P., Luo, W., Wang, J., Reversible hydrogen storage by a Li–Al–N–H complex. *Adv. Func. Mater.* 17, 1137–1142, 2007.
108. Zheng, X., Xu, W., Xiong, Z., Chua, Y., Wu, G., Qin, S., Chen, H., Chen, P., Ambient temperature hydrogen desorption from $LiAlH_4–LiNH_2$ mediated by HMPA. *J. Mater. Chem.* 19, 8426–8431, 2009.
109. Dolotko, O., Zhang, H., Ugurlu, O., Wiench, J.W., Pruski, M., Chumbley, L.S., Pecharsky, V., Mechanochemical transformations in $Li(Na)AlH_4–Li(Na)NH^2$ systems. *Acta Mater.* 55, 3121–3130, 2007.
110. Chua, Y.S., Wu, G., Xiong, Z., Chen, P., Investigations on the solid state interaction between $LiAlH_4$ and $NaNH_2$. *J. Solid State Chem.* 183, 2040–2044, 2010.
111. Liu, Y., Hu, J., Wu, G., Xiong, Z., Chen, P., Large amount of hydrogen desorption from the mixture of $Mg(NH_2)_2$ and $LiAlH_4$. *J. Phys. Chem. C* 111, 19161–19164, 2007.

112. Lu, J., Fang, Z.Z., Sohn, H.Y., Bowman Jr., R.C., Hwang, S.-J., Potential and reaction mechanism of Li–Mg–Al–N–H system for reversible hydrogen storage. *J. Phys. Chem. C* 111 16686–16692, 2007.
113. Pinkerton, F.E., Meisner, G.P., Meyer, M.S., Balogh, M.P., Kundrat, M.D., Hydrogen desorption exceeding ten weight percent from the new quaternary hydride $Li_3BN_2H_8$. *J. Phys. Chem. B* 109, 6–8, 2005.
114. Chater, P.A., David, W.I.F., Johnson, S.R., Edwards, P.P., Anderson, P.A., Synthesis and crystal structure of $Li_4BH_4(NH_2)_3$. *Chem. Commun.* 23, 2439–2441, 2006.
115. Noritake, T., Aoki, M., Towata, S., Ninomiya, A., Nakamori, Y., Orimo, S., Crystal structure analysis of novel complex hydrides formed by the combination of $LiBH_4$ and $LiNH_2$. *Appl. Phys. A* 83, 277–279, 2006.
116. Yang, J., Sudik, A., Siegel, D.J., Halliday, D., Drews, A., Carter III, R.O., Wolverton, C., Lewis, G.J., Sachtler, J.W.A., Low, J.J., Faheem, S.A., Lesch, D.A., Ozolins, V., Hydrogen storage properties of $2LiNH_2 + LiBH_4 + MgH_2$. *J. Alloys Compd.* 446–447, 345–349, 2007.
117. Hu, J., Fichtner, M., Chen, P., Investigation on the properties of the mixture consisting of $Mg(NH_2)_2$, LiH, and $LiBH_4$ as a hydrogen storage material. *Chem. Mater.* 20, 7089–7094, 2008.
118. Chen, X.Y., Guo, Y.H., Yu, X.B., Enhanced dehydrogenation properties of modified $Mg(NH_2)_2$–$LiBH_4$ composites. *J. Phys. Chem. C* 114, 17947–17953, 2010.
119. Zhang, Y., Tian, Q., The reactions in $LiBH_4$–$NaNH_2$ hydrogen storage system. *Int. J. Hydrogen Energy* 36, 9733–9742, 2011.
120. Chu, H., Wu, G., Zhang, Y., Xiong, Z., Guo, J., He, T., Chen, P., Improved dehydrogenation properties of calcium borohydride combined with alkaline-earth metal amides. *J. Phys. Chem. C* 115, 18035–18041, 2011.
121. Wu, C., Bai, Y., Yang, J.-H., Wu, F., Long, F., Characterizations of composite $NaNH_2$–$NaBH_4$ hydrogen storage materials synthesized via ball milling. *Int. J. Hydrogen Energy* 37, 889–893, 2012.
122. Poonyayant, N., Stavila, V., Majzoub, E.H., Klebanoff, L.E., Behrens, R., Angboonpong, N., Ulutagay-Kartin, M., Pakawatpanurut, P., Hecht, E.S., Breit, J.S., An investigation into the hydrogen storage characteristics of $Ca(BH_4)_2/LiNH_2$ and $Ca(BH_4)_2/NaNH_2$: Evidence of intramolecular destabilization. *J. Phys. Chem. C* 118, 14759–14769, 2014.
123. Pan, H., Shi, S., Liu, Y., Li, B., Yang, Y., Gao, M., Improved hydrogen storage kinetics of the Li–Mg–N–H system by addition of $Mg(BH_4)_2$. *Dalton Trans.* 42, 3802–3811, 2013.
124. Chu, H., Xiong, Z., Wu, G., Guo, J., Zheng, X., He, T., Wu, C., Chen, P., Hydrogen storage properties of Ca(BH4)2–LiNH2 system. *Chem. Asian J.* 5, 1594–1599, 2010.
125. Züttel, A., Remhof, A., Borgschulte, A., Friedrichs, O., Hydrogen: The future energy carrier. *Phil. Trans. R. Soc. A* 368, 3329–3342, 2010.
126. Green, L., An ammonia energy vector for the hydrogen economy. *Int. J. Hydrogen Energy* 7, 355–359, 1982.

127. Satyapal, S., Petrovic, J., Read, C., Thomas, G., Ordaz, G., The U.S. Department of Energy's National Hydrogen Storage Project: Progress towards meeting hydrogen-powered vehicle requirements. *Catal. Today* 120, 246–256, 2007.
128. Lan, R., Irvine, J.T.S., Tao, S., Ammonia and related chemicals as potential indirect hydrogen storage materials. *Int. J. Hydrogen Energy* 37, 1482–1494, 2012.
129. Christensen, C.H., Sørensen, R.Z., Johannessen, T., Quaade, U.J., Honkala, K., Elmøe, T.D., Køhler, R., Nørskov, J.K., Metal ammine complexes for hydrogen storage, *J. Mater. Chem.* 15, 4106–4108, 2005.
130. Klerke, A., Christensen, C.H., Nørskov, J.K., Vegge, T., Ammonia for hydrogen storage: Challenges and opportunities. *J. Mater. Chem.* 18, 2304–2310, 2008.
131. Liu, H., Ammonia synthesis catalyst 100 years: Practice, enlightenment and challenge. *Chinese J. Catalysis* 35, 1619–1640, 2014.
132. Haber, F., van Oordt, G., Über die bildung von ammoniak den elementen. *Z. Anorg. Chem.* 44, 341–378, 1905.
133. Haber, F., Untersuchungen über ammoniak: Sieben mitteilungen: I. Allgemeine übersicht des stoffes und der ergebnisse. *Z. Elektrochem.* 20, 597–604, 1914.
134. Haber, F., Taninru, S., Ponnas, H., Untersuchungen über ammoniak. Sieben mitteilungen),11. Neubestimmung des ammoniakgleichgewichts BE1 30 ATM. Druck. *Ber. Bunsenges. Phys. Chem.* 21, 89–106, 1915.
135. Haber, F., Taninru, S., Ponnas, H., Untersuchungen über ammoniak. Sieben mitteilungen): IV. Bestimmung der bildungswärme des ammoniaks bei hohen temperaturen. *Z. Elektrochem.* 21, 191–206, 1915.
136. Mittasch, A., Frankenburg, W., Early studies of multicomponent catalysts. *Adv. Catalysis* 2, 81–104, 1950.
137. Gambarotta, S., Scott, J., Multimetallic cooperative activation of N_2. *Angew. Chem. Int. Ed.* 43, 5298–5308, 2004.
138. Pool, J.A., Lobkovsky, E., Chirik, P.J., Hydrogenation and cleavage of dinitrogen to ammonia with a zirconium complex. *Nature* 427, 527–530, 2004.
139. Rao, C.N.R., Ranga Rao, G., Nature of nitrogen adsorbed on transition metal surfaces as revealed by electron spectroscopy and cognate techniques. *Surf. Sci. Rep.* 13, 223–263, 1991.
140. Tsai, M.-C., Ship, U., Bassignana, I.C., Küppers, J., Ertl, G., A vibrational spectroscopy study on the interaction of N_2 with clean and K-promoted Fe(111) surfaces: π-bonded dinitrogen as precursor for dissociation. *Surf. Sci.* 155, 387–399, 1985.
141. Hansen, T.W., Wagner, J.B., Hansen, P.L., Dahl, S., Topsoe, H., Jacobsen, C.J.H., Atomic-resolution *in situ* transmission electron microscopy of a promoter of a heterogeneous catalyst. *Science* 294, 1508–1510, 2001.
142. Spencer, N.D., Schoonmaker, R.C., Somorjai, G.A., Structure sensitivity in the iron single-crystal catalysed synthesis of ammonia. *Nature* 294, 643–644, 1981.

143. Huazhang, L., China Patent 86108528.0, 1986.
144. Liu, H.-Z., Li, X.-N., Hu, Z.-N., Development of novel low temperature and low pressure ammonia synthesis catalyst. *Appl. Catal. A* 142, 209–222, 1996.
145. Huazhang, L., Xiaonian, L., Precursor of iron catalyst for ammonia synthesis: Fe_3O_4, $Fe_{1-x}O$, Fe_2O_3 or their mixture?. *Stud. Surf. Sci. Catal.* 130, 2207–2212, 2000.
146. Huazhang, L., Caibo, L., Xiaonian, L., Yaqing, C., Effect of an iron oxide precursor on the H_2 desorption performance for an ammonia synthesis catalyst. *Ind. Eng. Chem. Res.* 42, 1347–1349, 2003.
147. Pernicone, N., Ferrero, F., Rossetti, I., Forni, L., Canton, P., Riello, P., Fagherazzi, G., Signoretto, M., Pinna, F., Wustite as a new precursor of industrial ammonia synthesis catalysts. *Appl. Catal. A: General* 251, 121–129, 2003.
148. Zheng, Y.-F., Liu, H.-Z, Liu, Z.-J., Li, X.-N., *In situ* X-ray diffraction study of reduction processes of Fe_3O_4- and $Fe_{1-x}O$-based ammonia-synthesis catalysts. *J. Solid State Chem.* 182, 2385–2391, 2009.
149. Liu, H., Han, W., Wustite-based catalyst for ammonia synthesis: Structure, property and performance. *Catal. Today* 297, 276–291, 2017.
150. Czekajło, Ł., Lendzion-Bieluń, Z., Wustite based iron-cobalt catalyst for ammonia synthesis. *Catal. Today* 286, 114–117, 2017.
151. Sudo, M., Ichikawa, M., Soma, M., Onishi, T., Tamaru, K., Catalytic synthesis of ammonia over the electron donor-acceptor complexes of alkali metals with graphite or phthalocyanines. *J. Phys. Chem.* 73, 1174–1175, 1969.
152. Aika, K.-i., Hori, H., Ozaki, A., Activation of nitrogen by alkali metal promoted transition metal I. Ammonia synthesis over ruthenium promoted by alkali metal. *J. Catal.* 27, 424–431, 1972.
153. Aika, K.-i., Yamaguchi, J., Ozaki, A., Ammonia synthesis over rhodium, iridium and platinum promoted by potassium. *Chem. Lett.* 2, 161–164, 1973.
154. Ozaki, A., Development of alkali-promoted ruthenium as a novel catalyst for ammonia synthesis. *Acc. Chem. Res.* 14, 16–21, 1981.
155. Urabe, K., Aika, K.-i., Ozaki, A., Activation of nitrogen by alkali metal-promoted transition metal: IV. Effect of potassium on the kinetics of isotopic equilibration of nitrogen on ruthenium catalysts. *J. Catal.* 38, 430–434, 1975.
156. van Ommen, J.G., Bolink, W.J., Prasad, J., Mars, P., The nature of the potassium compound acting as a promoter in iron-alumina catalysts for ammonia synthesis. *J. Catal.* 38, 120–127, 1975.
157. Kitano, M., Inoue, Y., Yamazaki, Y., Hayashi, F., Kanbara, S., Matsuishi, S., Yokoyama, T., Kim, S.-W., Hara, M., Hosono, H., Ammonia synthesis using a stable electride as an electron donor and reversible hydrogen store. *Nat. Chem.* 4, 934–940, 2012.
158. Kitano, M., Kanbara, S., Inoue, Y., Kuganathan, N., Sushko, P.V., Yokoyama, T., Hara, M., Hosono, H., Electride support boosts nitrogen dissociation over ruthenium catalyst and shifts the bottleneck in ammonia synthesis. *Nat. Commun.* 6, 6731, 2015.

159. Hara, M., Kitano, M., Hosono, H., Ru-Loaded C12A7:e^- Electride as a catalyst for ammonia synthesis. *ACS Catal.* 7, 2313–2324, 2017.
160. Jacobsen, C.J.H., Dahl, S., Clausen, B.S., Bahn, S., Logadottir, A., Nørskov, J.K., Catalyst design by interpolation in the periodic table: Bimetallic ammonia synthesis catalysts. *J. Am. Chem. Soc.* 123, 8404–8405, 2001.
161. Mittasch, A., Einiges über mehrstoffkatalysatoren. *Z. Elektrochem.* 36, 569–580, 1930.
162. Kojima, R., Aika, K.-i., Cobalt molybdenum bimetallic nitride catalysts for ammonia synthesis. *Chem. Lett.* 29, 514–515, 2000.
163. Kojima, R., Aika, K.-i., Cobalt molybdenum bimetallic nitride catalysts for ammonia synthesis: Part 1. Preparation and characterization. *Appl. Catal. A* 215, 149–160, 2001.
164. Kojima, R., Aika, K.-i., Cobalt molybdenum bimetallic nitride catalysts for ammonia synthesis: Part 2. Kinetic study. *Appl. Catal. A* 218, 121–128, 2001.
165. Kojima, R., Aika, K.-i., Cobalt molybdenum bimetallic nitride catalysts for ammonia synthesis Part 3. Reactant gas treatment. *Appl. Catal. A* 219, 157–170, 2001.
166. Tsuji, Y., Kitano, M., Kishida, K., Sasase, M., Yokoyama, T., Hara, M., Hosono, H., Ammonia synthesis over Co–Mo alloy nanoparticle catalyst prepared via sodium naphthalenide-driven reduction. *Chem. Comm.* 52, 14369–14372, 2016.
167. Giddey, S., Badwal, S.P.S., Kulkarni, A., Review of electrochemical ammonia production technologies and materials. *Int. J. Hydrogen Energy* 38, 14576–14594, 2013.
168. Amar, I.A., Lan, R., Petit, C.T.G., Tao, S., Solid-state electrochemical synthesis of ammonia: A review. *J. Solid State Electrochem.* 15, 1845–1860, 2011.
169. Kyriakou, V., Garagounis, I., Vasileiou, E., Vourros, A., Stoukides, M., Progress in the electrochemical synthesis of ammonia. *Catal. Today* 286, 2–13, 2017.
170. Shipman, M.A., Symes, M.D., Recent progress towards the electrosynthesis of ammonia from sustainable resources. *Catal. Today* 286, 57–68, 2017.
171. Spatzal, T., Aksoyoglu, M., Zhang, L., Andrade, S.L.A., Schleicher, E., Weber, S., Rees, D.C., Einsle, O., Evidence for interstitial carbon in nitrogenase FeMo cofactor. *Science* 334, 940, 2011.
172. Lancaster, K.M., Roemelt, M., Ettenhuber, P., Hu, Y., Ribbe, M.W., Neese, F., Bergmann, U., DeBeer, S., X-ray emission spectroscopy evidences a central carbon in the nitrogenase iron-molybdenum cofactor. *Science* 334, 974–977, 2011.
173. van der Ham, C.J.M., Koper, M.T.M., Hetterscheid, D.G.H., Challenges in reduction of dinitrogen by proton and electron transfer. *Chem. Soc. Rev.* 43, 5183–5191, 2014.
174. Jain, A., Miyaoka, H., Kumar, S., Ichikawa, T., Kojima, Y., A new synthesis route of ammonia production through hydrolysis of metal – Nitrides. *Int. J. Hydrogen Energy* 42, 24897–24903, 2017.

175. Appl, M., Ammonia, in: *Ullmann's Encyclopedia of Industrial Chemistry*, Wiley-VCH Verlag GmbH & Co. KGaA: Weinheim, 2007.
176. Liu, C.Y., Aika, K.-i., Absorption and desorption behavior of ammonia with alkali earth halide and mixed halide. *Chem. Lett.* 31, 798–799, 2002.
177. Paskevicius, M., Jepsen, L.H., Schouwink, P., Černý, R., Ravnsbæk, D.B., Filinchuk, Y., Dornheim, M., Besenbacher, F., Jensen, T.R., Metal borohydrides and derivatives – Synthesis, structure and properties. *Chem. Soc. Rev.* 46, 1565–1634, 2017.
178. Bougard, J., Jadot, R., Poulain, V., Proceedings of the International Absorption Heat Pump Conference, New Orleans, January 1993, 413, 1994.
179. Liu, C.Y., Aika, K.-I., Ammonia absorption on alkaline earth halides as ammonia separation and storage procedure. *Bull. Chem. Soc. Jpn.* 77, 123–131, 2004.
180. Liu, C.Y., Aika, K.-I., Ammonia absorption into alkaline earth metal halide mixtures as an ammonia storage material. *Ind. Eng. Chem. Res.* 43, 7484–7491, 2004.
181. Sørensen, R.Z., Hummelshøj, J.S., Klerke, A., Reves, J.B., Vegge, T., Nørskov, J.K., Christensen, C.H., Indirect, reversible high-density hydrogen storage in compact metal ammine salts. *J. Am. Chem. Soc.* 130, 8660–8668, 2008.
182. Elmøe, T.D., Sørensen, R.Z., Quaade, U., Christensen, C.H., Nørskov, J.K., Johannessen, T., A high-density ammonia storage/delivery system based on $Mg(NH_3)_6Cl_2$ for SCR-DeNO_x in vehicles. *Chem. Eng. Sci.* 61, 2618–2625, 2006.
183. Bevers, E.R.T., Oonk, H.A.J., Haije, W.G., van Ekeren, P.J., Investigation of thermodynamic properties of magnesium chloride amines by HPDSC and TG. *J. Thermal Anal. Calorim.* 90, 923–929, 2007.
184. Jones, M.O., Royse, D.M., Edwards, P.P., David, W.I.F., The structure and desorption properties of the ammines of the group II halides. *Chem. Phys.* 427, 38–43, 2013.
185. Aoki, T., Miyaoka, H., Inokawa, H., Ichikawa, T., Kojima, Y., Activation on ammonia absorbing reaction for magnesium chloride. *J. Phys. Chem. C* 119, 26296–26302, 2015.
186. Hwang, I.-C., Drews, T., Seppelt, K., $Mg(NH_3)_6Hg_{22}$, a Mercury Intercalation Compound. *J. Am. Chem. Soc.* 122, 8486–8489, 2000.
187. Sørby, M.H., Løvvik, O.M., Tsubota, M., Ichikawa, T., Kojima, Y., Hauback, B.C., Crystal structure and dynamics of $Mg(ND_3)_6Cl_2$. *Phys. Chem. Chem. Phys.* 13, 7644–7648, 2011.
188. Sullivan, E.A., Johnson, S., The lithium borohydride–ammonia system P–C–T relationships and densities. *J. Phys. Chem.* 63, 233–238, 1959.
189. Aoki, T., Ichikawa, T., Miyaoka, H., Kojima, Y., Thermodynamics on ammonia absorption of metal halides and borohydrides. *J. Phys. Chem. C* 118, 18412–18416, 2014.
190. Ma, Q., Peng, R., Tian, L., Meng, G., Direct utilization of ammonia in intermediate-temperature solid oxide fuel cells. *Electrochem. Commun.* 8, 1791–1795, 2006.

191. Nikki Chemical Co., http://www.nikki-chem.co.jp/eng/products/pro3_2.html.
192. Yin, S.F., Xu, B.Q., Zhou, X.P., Au, C.T., A mini-review on ammonia decomposition catalysts for on-site generation of hydrogen for fuel cell applications. *Appl. Catal. A* 277, 1–9, 2004.
193. Hill, A.K., Torrente-Murciano, L., Low temperature H_2 production from ammonia using ruthenium-based catalysts: Synergetic effect of promoter and support. *Appl. Catal. B* 172–173, 129–135, 2015.
194. Hill, A.K., Torrente-Murciano, L., *In-situ* H_2 production via low temperature decomposition of ammonia: Insights into the role of cesium as a promoter. *Int. J. Hydrogen Energy* 39, 7646–7654, 2014.
195. Li, L., Zhu, Z.H., Yan, Z.F., Lu, G.Q., Rintoul, L., Catalytic ammonia decomposition over Ru/carbon catalysts: The importance of the structure of carbon support. *Appl. Catal. A* 320, 166–172, 2007.
196. Zhang, H., Alhamed, Y.A., Al-Zahrani, A., Daous, M., Inokawa, H., Kojima, Y., Petrov, L.A., Tuning catalytic performances of cobalt catalysts for clean hydrogen generation via variation of the type of carbon support and catalyst post-treatment temperature. *Int. J. Hydrogen Energy* 39, 17573–17582, 2014.
197. García-García, F.R., Guerrero-Ruiz, A., Rodríguez-Ramos, I., Goguet, A., Shekhtman, S.O., Hardacre, C., TAP studies of ammonia decomposition over Ru and Ir catalysts. *Phys. Chem. Chem. Phys.* 13, 12892–12899, 2011.
198. Bradford, M.C.J., Fanning, P.E., Vannice, M.A., Kinetics of NH_3 decomposition over well dispersed Ru. *J. Catal.* 172, 479–484, 1997.
199. Prasad, V., Vlachos, D.G., Multiscale model and informatics-based optimal design of experiments: Application to the catalytic decomposition of ammonia on ruthenium. *Ind. Eng. Chem. Res.* 47, 6555–6567, 2008.
200. Prasad, V., Karim, A.M., Arya, A., Vlachos, D.G., Assessment of overall rate expressions and multiscale, microkinetic model uniqueness via experimental data injection: Ammonia decomposition on Ru/γ-Al_2O_3 for hydrogen production. *Ind. Eng. Chem. Res.* 48, 5255–5265, 2009.
201. Ganley, J.C., Thomas, F.S., Seebauer, E.G., Masel, R.I., A priori catalytic activity correlations: The difficult case of hydrogen production from ammonia. *Catal. Lett.* 96, 117–122, 2004.
202. Wang, S.J., Yin, S.F., Li, L., Xu, B.Q., Ng, C.F., Au, C.T., Investigation on modification of Ru/CNTs catalyst for the generation of CO_x-free hydrogen from ammonia. *Appl. Catal. B* 52, 287–299, 2004.
203. Schüth, F., Palkovits, R., Schlögl, R., Su, D.S., Ammonia as a possible element in an energy infrastructure: Catalysts for ammonia decomposition. *Energy Environ. Sci.* 5, 6278–6289, 2012.
204. Bell, T.E., Torrente-Murciano, L., H_2 production via ammonia decomposition using non-noble metal catalysts: A review. *Topics Catal.* 59, 1438–1457, 2016.
205. Metkemeijer, R., Achard, P., Comparison of ammonia and methanol applied indirectly in a hydrogen fuel cell. *Int. J. Hydrogen Energy* 19, 535–542, 1994.

206. Metkemeijer, R., Achard, P., Ammonia as a feedstock for a hydrogen fuel cell; reformer and fuel cell behavior. *J. Power Sources* 49, 271–282, 1994.
207. Kordesch, K., Hacker, V., Gsellmann, J., Cifrain, M., Faleschini, G., Enzinger, P., Fankhauser, R., Ortner, M., Muhr, M., Aronson, R.R., Alkaline fuel cells applications. *J. Power Sources* 86, 162–165, 2000.
208. Halseid, R., Vie, P.J.S., Tunold, R., Effect of ammonia on the performance of polymer electrolyte membrane fuel cells. *J. Power Sources* 154, 343–350, 2006.
209. Afif, A., Radenahmad, N., Cheok, Q., Shams, S., Kim, J.H., Azad, A.K., Ammonia-fed fuel cells: A comprehensive review. *Renew. Sust. Energ. Rev.* 60, 822–835, 2016.
210. Ni, M., Leung, D.Y.C., Leung, M.K.H., Electrochemical modeling of ammonia-fed solid oxide fuel cells based on proton conducting electrolyte. *J. Power Sources* 183, 687–692, 2008.
211. Xie, K., Yan, R., Chen, X., Wang, S., Jiang, Y., Liu, X., Meng, G., A stable and easily sintering $BaCeO_3$-based proton-conductive electrolyte. *J. Alloys Compnd.* 473, 323–329, 2009.
212. Ni, M., Leung, D.Y.C., Leung, M.K.H., Thermodynamic analysis of ammonia fed solid oxide fuel cells: Comparison between proton-conducting electrolyte and oxygen ion-conducting electrolyte. *J. Power Sources* 183, 682–686, 2008.
213. Cairns, E.J., Simons, E.L., Tevebaugh, A.D., Ammonia–oxygen fuel cell. *Nature* 217, 780–781, 1968.
214. Hejze, T., Besenhard, J.O., Kordesch, K., Cifrain, M., Aronsson, R.R., Current status of combined systems using alkaline fuel cells and ammonia as a hydrogen carrier. *J. Power Sources* 176, 490–493, 2008.

3

Nanostructured Mg-Based Hydrogen Storage Materials: Synthesis and Properties

Huaiyu Shao[1,*], Xiubo Xie[2], Jianding Li[1], Bo Li[1], Tong Liu[2,*] and Xingguo Li[3]

[1]Institute of Applied Physics and Materials Engineering (IAPME), University of Macau, Macau SAR, China
[2]Laboratory of Aerospace Materials and Performance (Ministry of Education), School of Materials Science and Engineering, Beihang University, Beijing, China
[3]Beijing National Laboratory for Molecular Sciences (BNLMS), The State Key Laboratory of Rare Earth Materials Chemistry and Applications, College of Chemistry and Molecular Engineering, Peking University, Beijing, China

Abstract

A hydrogen economy is thought to be one of the ultimate carbon-neutral energy solutions. For a future scenario, one may obtain hydrogen from renewable power, for instance, wind or solar energy; this hydrogen can be provided to fuel cell component to supply electricity and heat. For this energy storage and utilization route, one enabling technology is hydrogen storage because hydrogen as energy carrier is a gas state at normal temperature and atmosphere conditions and the energy density of hydrogen gas is low. Therefore, a critical step is to find one hydrogen storage technology with low cost and high energy density. Mg-based materials are very promising candidates for hydrogen storage due to the great abundance of Mg in earth's crust, high hydrogen storage capacity (7.7 wt% for MgH_2) and low cost (2–3 USD/kg). Mg-based materials have been investigated as possible onboard applications for decades. The challenges in Mg-based materials for onboard development are the poor kinetics and unsuitable thermodynamics.

Nanostructured materials have attracted great attention in the last decades. Downsizing from millimeter or micrometer scale to a nanometer one brings a lot of novel physical and chemical properties to the materials. Numerous nanoprocessing techniques have been adopted by researchers to fabricate Mg-based materials in nanoscale in order to enhance the sorption kinetics and alter the

**Corresponding authors*: hshao@umac.mo; tongliu@buaa.edu.cn

Mehmet Sankir and Nurdan Demirci Sankir (eds.) Hydrogen Storage Technologies, (89–116) © 2018 Scrivener Publishing LLC

thermodynamics. The author and his colleagues applied a novel nano-processing strategy—hydrogen plasma metal reaction (HPMR)—to synthesize metal nanoparticles and further produce nanostructured Mg-based hydrogen storage materials from these nanoparticles. Here in this chapter, the author will summarize the synthesis results under different conditions and morphology and microstructure information of the obtained samples, and especially focus on how downsizing could affect the sorption kinetics and the thermodynamics, including desorption enthalpy and entropy, in Mg-based hydrogen storage materials.

***Keywords*:** Hydrogen storage, nanostructure, Mg-based materials, kinetics, thermodynamics

3.1 Introduction

Currently, around 80% of the primary energy consumption is through burning fossil fuels, which has caused severe air pollution and brought energy security issues. Meanwhile, dependency on fossil fuels, such as crude oil and natural gas, has also brought a lot of energy safety issues in many countries. Development of green energy technologies with wide practicality is one of the ultimate solutions to these problems. In recent years, with advancement in technology development and cost reduction of fuel cell, hydrogen fuel cell-based technology is considered one of the promising and ultimate solutions for green energy storage and conversion. In December 2014, Toyota Motor Corporation launched real commercialization of Mirai (meaning *Future*) fuel cell vehicles (FCVs) around the world [1], which has attracted much attention. In hydrogen and fuel cell technology as green energy solution, if hydrogen is produced from renewable energy sources, then for the entire energy storage and conversion process, the final products are electricity, water and heat; and the whole process is clean and pollution free, with zero emission of carbon dioxide [2, 3].

Hydrogen energy storage also has the advantage of large gravimetrical energy density of hydrogen, great storage capacity and a large range of storage durations. Energy density for pure hydrogen is 39.4 kWh/kg (or 142 MJ/kg) for lower heating value, which is almost three times the value for gasoline (ca. 13 kWh/kg, 46 MJ/kg) or diesel (ca. 13.3 kWh/kg, 48 MJ/kg). The storage capacity of hydrogen for stationary application can be on the order of kWh to TWh; the storage time can be from a few minutes to years and there is no energy loss during this duration [4]. Hydrogen storage is a key enabling technology for realization of the hydrogen energy society for hydrogen is a gas under normal conditions and its energy density as gas is very low. In order to realize an effective

storage technology, it is crucial to develop a high-capacity and low-cost hydrogen storage technology.

Mg-based materials are very promising candidates for hydrogen storage because of the great advantages, for instance, great abundance of Mg in earth's crust (2.3%), high hydrogen storage capacity (7.7 wt% for MgH_2) and low cost for Mg metal (2–3 USD/kg) [3]. Mg-based materials have been investigated as possible onboard applications (for instance, FCVs) for decades [3, 5–15]. The technical barriers in common Mg-based materials for onboard development are the poor kinetics and unsuitable thermodynamics [3]. Kinetics properties in hydrogen storage materials mean absorption and desorption speed of hydrogen in the materials under certain working temperature and pressure conditions. Common Mg-based materials usually show poor kinetics and a temperature over 350 °C and a hydrogen pressure over 3 MPa are needed for activation. This is mainly attributed to the thick oxide layer on the surface of Mg particles, which prevents the contact between hydrogen and Mg and hampers the hydrogen penetration and diffusion reactions inside the particles. Unsuitable thermodynamics in Mg-based materials (for instance, for Mg-MgH_2 system and Mg_2Ni-Mg_2NiH_4 system) for onboard hydrogen storage is when the temperature for one atmosphere hydrogen equilibrium pressure in metal-hydride system is well above 100 °C. The enthalpy and entropy changes for the hydrogen desorption reactions in Mg-H, Mg-Ni-H systems indicate desorption temperature above 250 °C. This situation should be changed so that the working temperature in these materials can be below 100 °C to make sure that the necessary heat for hydrogen desorption in the Mg-based hydrides can be possibly supplied from the exhaust heat of fuel cell [16].

Numerous nano-processing techniques have been adopted by researchers to fabricate Mg-based materials in nanoscale in order to enhance the sorption kinetics and alter the thermodynamics. These techniques include ball milling and mechanical alloying [6, 11, 17–22], nano-confinement [23–25], thin film formation [21, 26–32], chemical vapor deposition [33], melting spinning [34–37], severe plastic formation [38–40], chemical solution synthesis [41–44], spark synthesis [45], etc. The author and his colleagues have done an intensive study on adoption of a novel nano-processing strategy—hydrogen plasma metal reaction (HPMR)—to synthesize metal nanoparticles and then to further produce nanostructured Mg-based hydrogen storage materials from these metal nanoparticles [46–54]. Here in this chapter, the author will summarize these synthesis results under different conditions and morphology and microstructure information of the obtained metal, alloy and hydride samples, and focus on how downsizing could affect the absorption kinetics and the thermodynamics,

including the desorption enthalpy and entropy, in these Mg-based hydrogen storage materials.

3.2 Experimental Details

3.2.1 Synthesis of Metal Nanoparticles

Figure 3.1 shows a schematic diagram of the hydrogen plasma metal reaction. It consists of arc melting furnace with artificial tornado system, water-cooled copper stand, tungsten electrode, heat exchanger of gas with nanoparticles, particle collector, vacuum pump and gas circulation pump and direct current (DC) power source [55]. For a typical synthesis process to produce metal nanoparticles, a metal block around 50 g was placed on the water-cooled copper anode plate or a conical graphite anode crucible. The reaction chamber was evacuated to about 100 Pa, and then gases (mixture of Ar and hydrogen) were fed into the chamber at about 0.1 MPa. When the arc plasma was generated in a current from 100 to 300 A, the sample was melted and nanoparticles were fabricated. When the arc was struck, the raw metal sample was melted rapidly. After a latent period of

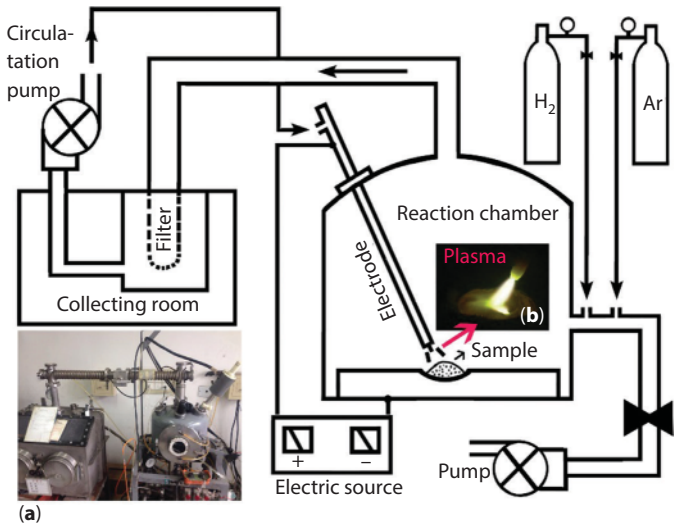

Figure 3.1 Schematic diagram of the equipment setup for synthesis of metal nanoparticles by HPMR method. It includes arc melting chamber, water-cooled copper stand, tungsten electrode, heat exchanger, nanoparticle collecting room with filter, vacuum pump and DC power source. The inserts are (a) a photo of the apparatus and (b) a real photo of the plasma during synthesis.

dozens of seconds, an intense fabrication of smoke began and the emitted metal vapors were generated. The metal vapors were taken by the circulation gas to the collecting room, where the nanoparticles were trapped on a membrane filter and collected. The metal nanoparticles were taken out from the chamber after a passivation step of filling in air slowly to prevent spontaneous ignition of the active metal nanoparticles [47].

3.2.2 Formation of the Nanostructured Hydrides and Alloys

The experimental details of the formation of the nanostructured Mg-M (M=Ni, Co, Cu) alloys and composites were presented in our previous publications [47, 48, 50, 53, 54]. Mg and M (M=Ni, Co and Cu) nanoparticles were weighed in a molar ratio of 2:1 (or 85:15 for $Mg_{85}Ni_{15}$ nanocomposite), immersed in an acetone solution and mixed by an ultrasonic homogenizer for 30 min. After being dried, the Mg-M mixture was pressed at 75 MPa into small pieces, each of which was about 10 mm in diameter, 0.3 mm in height and 0.1 g in weight. These metal mixture pieces were applied as starting samples for the fabrication of the Mg-M hydrides and alloys. Due to a very thin oxide layer on the surface of the Mg nanoparticle samples, it may help to prevent the nanostructure samples from further oxidization. Unlike other nanostructure materials, which are very sensitive to air or moisture, in our case, all the sample transfer can be conducted in air without any atmosphere protection. The mixture piece was put into an evacuated reactor system and then the system was heated up to certain temperatures (623 K for 2Mg+Ni, 673 K for 2Mg+Co, 673 K for 2Mg+Cu and 623 K for 85Mg+15Ni) in 4 MPa (3.5 MPa for 85Mg+15Ni) hydrogen atmosphere and kept for a few hours. After the heating and hydriding reaction, the system was evacuated and the alloy nanoparticle or nanocomposite samples were obtained.

3.2.3 Characterization and Measurements

X-ray diffraction (XRD) measurements of the Mg and Mg-M (M=Ni, Co or Cu) samples were carried out to obtain the structure and phase information of the samples using monochromatic Cu Kα radiation. The size distribution and the morphology of the various nanoparticle samples were observed by transmission electron microscopy (TEM). The hydrogen absorption kinetic measurements at various temperatures and the pressure-composition isotherm (PCT) measurements were conducted on a Sievert-type measurement system. A conventional pressure-volume-temperature monitoring technique was used to obtain the hydrogen absorption and

desorption capacity versus time by recording the change of gas pressure in a constant volume. The 325 mesh Mg powder sample (purity > 99.9%) from Alfa Aesar was used for comparison of the kinetic performance with nanostructured ones.

3.3 Synthesis Results of the Nanostructured Samples

Figure 3.2 shows the XRD curves and TEM images of the obtained metal nanoparticle samples prepared by HPMR method [21, 53, 56–58]. From the XRD results, we can see that all of the metal nanoparticles show almost single phase. The Mg nanoparticle sample shows hexagonal structure with a space group of $P6_3/mmc$. There is one small peak at around 42.9°, which is ascribed to a small amount of MgO impurity, which was formed during the passivation process. This thin MgO layer plays an important role in the hydrogen storage performance and it may protect the Mg nanoparticle samples from further oxidization. The obtained Ni, Co and Cu nanoparticle samples show face-centered cubic structure with a space group of $Fm3m$. The reflection peaks of all these samples are a little broadened, which indicates the nanometer scale of the samples. It is worth noting that the peak broadening of the Ni, Co and Cu samples is more obvious than that of the Mg one. This is due to the fact that Mg nanoparticles sample synthesized by HPMR method has a much larger particle size than Ni, Co and Cu samples, which can be easily observed from the TEM images of the samples (see Figure 3.2b, d, f and h). Obviously different from the Mg particles, Ni, Cu, and Co nanoparticles by HPMR methods show a granular structure and the size of these particles usually ranges from several nanometers to tens of nanometers with a mean size of 30–50 nm. However, the Mg nanoparticles are hexagonal in structure and the average particle size is about 300 nm, which is much bigger than the other metal nanoparticles. This is due to the fact that during the HPMR fabrication process, Mg has a much faster vaporization rate and higher generation rate than Ni, Co and Cu. The evaporation rate is also dependent on the vaporized metal elements relating to their melting point, boiling point and saturation vapor pressure. The evaporation rate of a metal is an essential factor affecting the generation rate and the collected particle size of the metal nanoparticles. Ohno proposed a reaction model which indicates that the initial composition in the raw material has a strong effect on the generation yield of obtained nanoparticles as well as the phase component of the prepared nanoparticles [59].

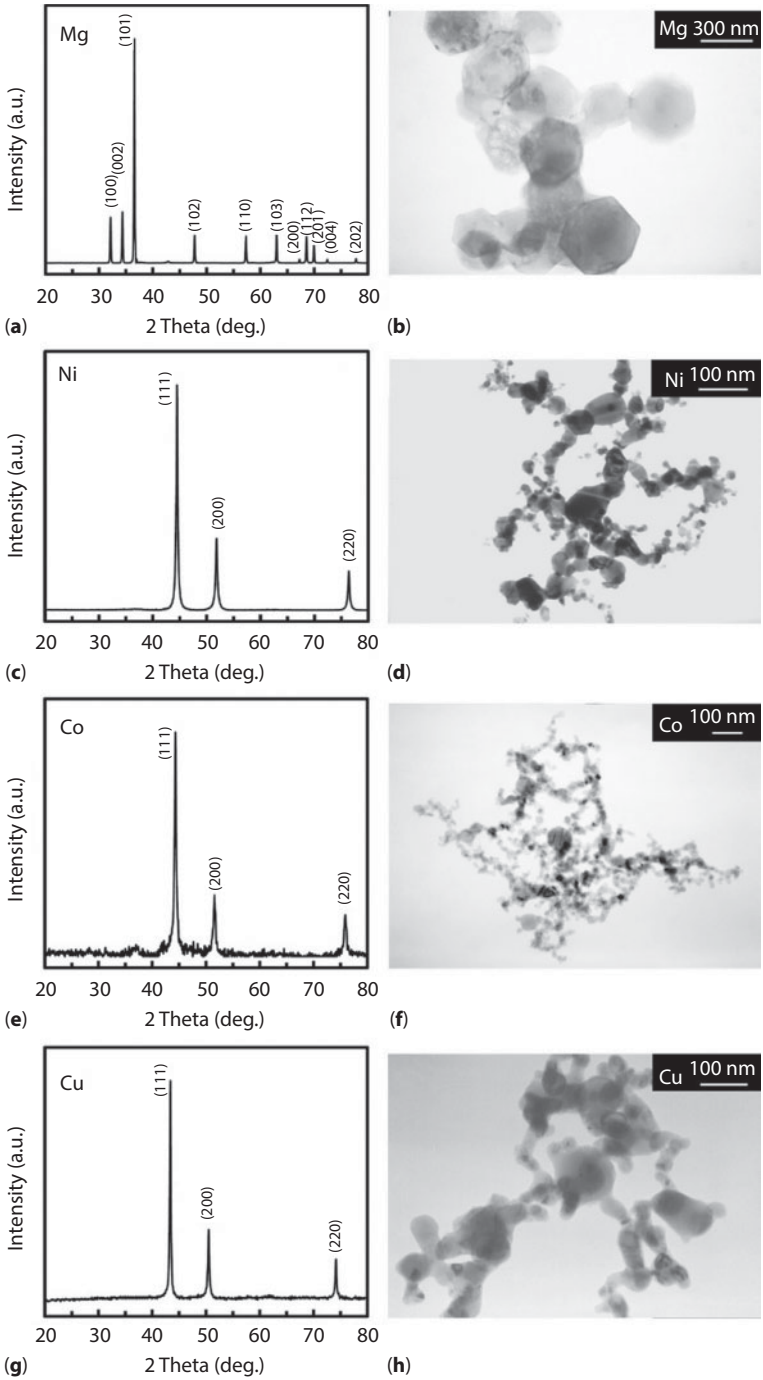

Figure 3.2 XRD curves and TEM images of the metal nanoparticle samples synthesized by HPMR method: (a, b) Mg, (c, d), Ni, (e, f) Co, and (g, h) Cu.

Figure 3.3 shows the X-ray diffraction patterns and TEM images of the synthesized Mg_2Ni, $Mg_{85}Ni_{15}$, Mg_2Co and Mg_2Cu alloys which were produced from Mg, Ni, Co and Cu metal nanoparticles by HPMR method [47, 48, 50, 53, 54]. In the Mg_2Ni, Mg_2Co and Mg_2Cu alloys, we almost obtained the single-phase intermetallic compound. For the $Mg_{85}Ni_{15}$ nanocomposite alloy, it is a mixture of Mg_2Ni and Mg particles. From the TEM images, we can see that the Mg_2Ni, Mg_2Co and Mg_2Cu particle samples have an average size of 50–200 nm, which is smaller than the original Mg particles (300 nm). This indicates that during the hydrogenation and then dehydrogenation of the Mg–M mixtures, the alloy particles will crack into smaller ones. From the TEM image of the $Mg_{85}Ni_{15}$ nanocomposite (Figure 3.3d), we can see that the transparent large particles are Mg and the small dark ones are the Mg_2Ni phase. The Mg particles have a mean size of around several hundred nm and the Mg_2Ni nanoparticles are around 30–50 nm. Small Mg_2Ni particles are dispersed on the surface of the Mg particles, which contributes some unique catalytic effect to the hydrogen storage properties.

For the mechanism of the synthesis reactions, the Mg_2Ni nano alloy is formed from hydrogenation of the Mg and Ni nanoparticles synthesized by HPMR method based on the following reactions:

$$Mg + Ni + H_2 \rightarrow Mg_2NiH_4 \tag{3.1}$$

$$Mg_2NiH_4 \rightarrow Mg_2Ni + H_2 \tag{3.2}$$

The lowest reaction temperature for the synthesis of Mg_2Ni alloy from metal nanoparticles is 553 K [46]. Sintering of Mg_2Ni alloy from Mg and Ni micrometer scale particles usually needs a temperature above 730 K [60, 61]. As we know, metal nanoparticle samples have a lower melting point because of their smaller size and larger specific surface area. Moreover, the smaller particle size of nanoparticles means a shorter diffusion distance and large contact area for the solid–solid (and gas–solid) reactions compared with micrometer scale ones. For the formation mechanism of the Mg-Co alloy system, we carefully looked at the intermediate compositions during the hydrogenation processes and concluded the reaction mechanism as follows:

$$Mg + H_2 \rightarrow MgH_2 \tag{3.3}$$

$$MgH_2 + Co + H_2 \rightarrow Mg_2CoH_5 \tag{3.4}$$

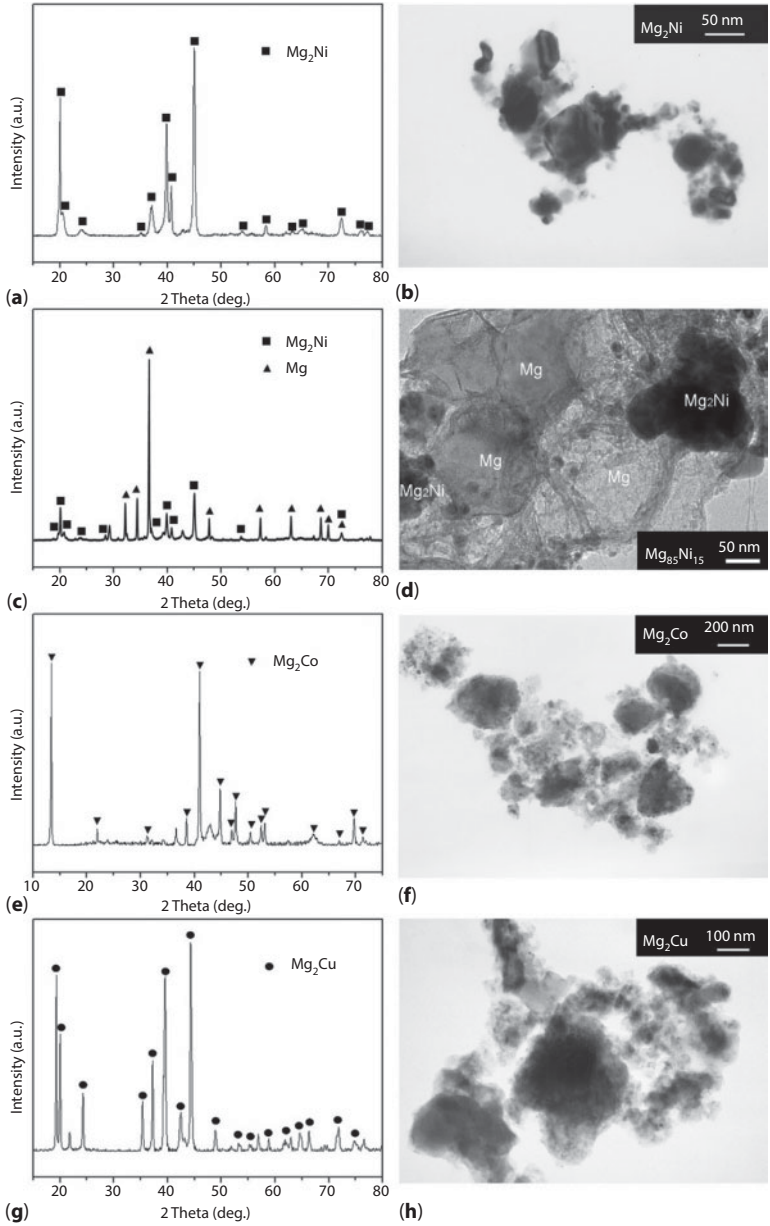

Figure 3.3 X-ray curves and TEM images of the (a, b) Mg_2Ni, (c, d) $Mg_{85}Ni_{15}$, (e, f) Mg_2Co and (g, h) Mg_2Cu alloys synthesized from Mg, Ni, Co and Cu metal nanoparticles.

After hydrogenation, the process of the evacuation of the system shows a reaction of Equation 3.5.

$$Mg_2CoH_5 \rightarrow Mg_3CoH_5 \rightarrow Mg_2Co \tag{3.5}$$

A similar case is presented in the Mg-Cu-H system. The formation mechanisms of the Mg_2Cu alloy are expressed in Equation 3.3 and Equation 3.6 in the first hydrogenation cycle.

$$MgH_2 + Cu \rightarrow Mg_2Cu + H_2 \tag{3.6}$$

The nanocomposite sample $Mg_{85}Ni_{15}$ consists of mainly Mg and Mg_2Ni phases with nanostructure. The formation mechanism of the Mg_2Ni phase is the same as Equations 3.1 and 3.2.

3.4 Hydrogen Absorption Kinetics

Figure 3.4 presents the hydrogen absorption kinetics and cycle properties of the obtained Mg-M-based nanoparticles (Mg, Mg_2Ni, Mg_2Cu, Mg_2Co and $Mg_{85}Ni_{15}$).

From Figure 3.4a, we can see that after one absorption and desorption cycle in 4 MPa hydrogen atmosphere at 673 K, the Mg nanoparticles can absorb hydrogen very quickly at 573 K. The hydrogen absorption rate becomes higher with the increase of the temperatures. The hydrogen

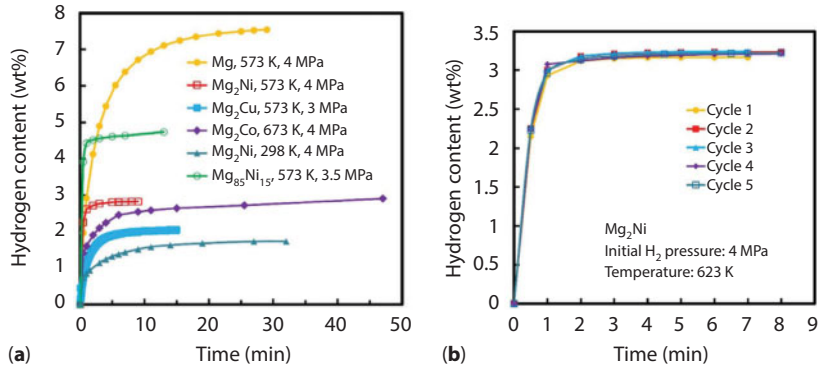

Figure 3.4 (a) Hydrogen absorption curves of various Mg-M-based nanoparticle samples (Mg, Mg_2Ni, Mg_2Cu, Mg_2Co and $Mg_{85}Ni_{15}$). (b) Absorption curves in 5 cycles of the Mg_2Ni nanoparticle sample.

content increases greatly with the time and quickly reaches a maximal value of 7.54% in 30 min at 573 K. The nanostructured Mg_2Ni sample and $Mg_{85}Ni_{15}$ samples absorb hydrogen with smaller hydrogen capacity but with a much faster speed than the Mg nanoparticle sample at the same temperature of 573 K. After 13 min absorption at 573 K under an initial hydrogen pressure of 3.5 MPa, the $Mg_{85}Ni_{15}$ nanocomposite sample shows a hydrogen capacity of 4.73%. With the existence of the nanostructured Mg_2Ni phase in the $Mg_{85}Ni_{15}$ sample, it can act as catalyst to the absorption reaction of Mg phase. We can see that the Mg_2Ni nanoparticle sample may even absorb hydrogen at room temperature; it absorbs 1.73% after 32 min absorption under 4 MPa hydrogen. From Figure 3.4b we can see that in 5 cycles at 623 K, there is no obvious delegation in the hydrogen absorption capacity and speed for the Mg_2Ni nanoparticle sample, which presents good cycle ability for the sample for hydrogen storage application. We know that normally Mg-based materials need a strict activation process before they may absorb hydrogen with a fast rate and a reasonable hydrogen capacity at temperature above 523 K. These results demonstrate superior hydrogen absorption kinetics and capacity of the Mg- and Mg-M-based nanoparticle samples.

The mechanism for nanosizing on the hydrogen absorption kinetics in Mg-based nanomaterials is illustrated in Figure 3.5 [21, 62]. The hydrogenation is one process of formation of hydrides in the Mg-based nanoparticles based on the reaction between Mg-based nanoparticle materials and hydrogen on the surface of the nanoparticles. The significant kinetics difference between the nanoparticle samples and the micrometer ones is due to the fact that the nanometer samples show a larger surface area and a smaller particle and grain size than micrometer ones. This means that the nanometer samples have a much greater contact area for the hydrogen reaction in the metals and alloys, and a much shorter distance for hydrogen diffusion in the nanometer particles during the hydrogen absorption process.

3.5 Hydrogen Storage Thermodynamics

Figure 3.6 presents the pressure-composition isotherms (PCTs) of hydrogen absorption and desorption steps of Mg-H, Mg-Ni-H, Mg-Co-H and Mg-Cu-H systems for the Mg-M nanoparticle samples [47, 48, 50, 53, 54]. It can show the absorption and desorption capacity for hydrogen storage use and the equilibrium pressure at different temperatures can be detracted for making the van't Hoff equations of different systems expressed by ln p versus $1/T$, from which thermodynamics (enthalpy and entropy change)

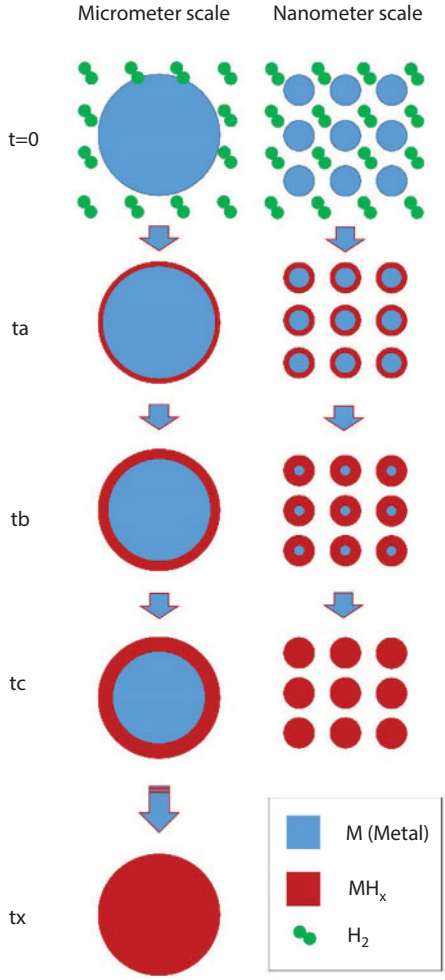

Figure 3.5 A schematic showing the effect of nanosizing on the absorption kinetics in Mg-based hydrogen storage materials. (Reproduced with permission from [62])

of the desorption reaction can be derived (see Table 3.1). One interesting point in the PCT curves for these nanostructured Mg-M-H systems (M = none, Ni, Co or Cu) is that for the absorption and desorption curves of the nanostructured Mg-H system at different temperatures (623, 648 and 673 K), the hydrogen absorption capacities are almost the same, around 7.5%. The Mg-Ni-H system shows larger hydrogen absorption capacity at higher measurement temperatures (3.0% at 623 K, 2.9% at 573 K and 2.8% at 523 K). While, in the Mg-Cu-H system, higher measurement temperature results in lower hydrogen absorption capacity (2.0% at 623 K, 2.2% at

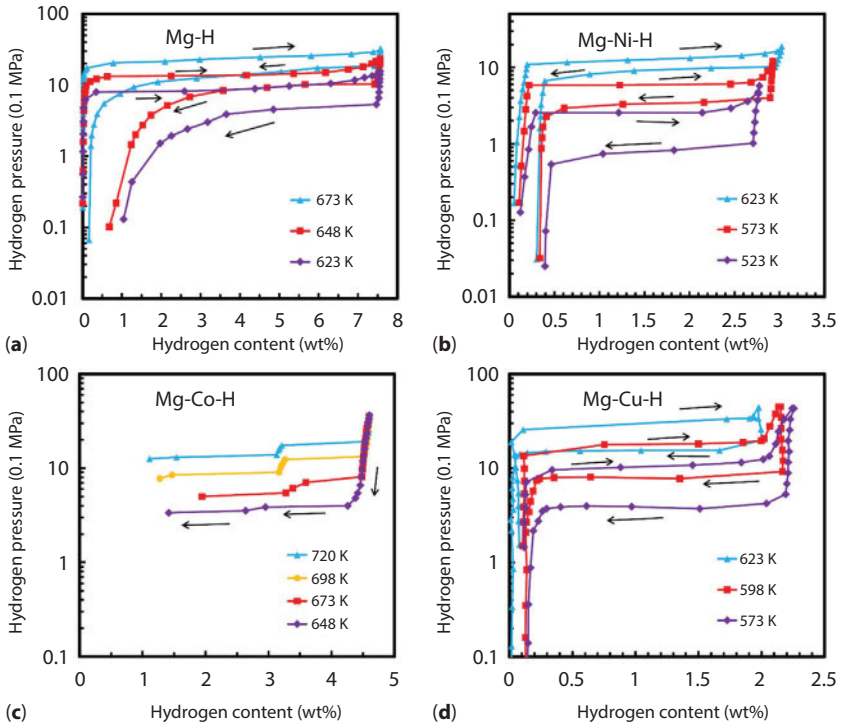

Figure 3.6 Pressure-composition isotherms (PCTs) of hydrogen absorption/desorption steps of different Mg-M-H (M = none, Ni, Co and Cu) systems in nanometer scale.

598 K and 2.3% at 573 K). The difference is thought to be that the hydrogen absorption of the Mg-Ni-H system is more kinetically dominant and the one in the Mg-Cu-H system is more thermodynamically dominant.

For the Mg-H nanoparticle system, the van't Hoff equation indicates an enthalpy change of 79.8 kJ mol^{-1} H_2 and an entropy change of 140.8 J (K mol H_2)$^{-1}$. In Figure 3.7, when we compare these values with our previously reported ones by high-pressure reactive ball milling (enthalpy change of 77.4 kJ mol^{-1} H_2 and entropy change of 137.5 J (K mol H_2)$^{-1}$, average grain size of 5 nm) and by catalyzed chemical solution synthesis method (enthalpy change of 77.7 kJ mol^{-1} H_2 and entropy change of 138.3 J (K mol H_2)$^{-1}$, grain size of 5–100 nm), as well as the ones from commercial micrometer Mg powders (enthalpy change of 78.5 kJ mol^{-1} H_2 and entropy change of 140.0 J (K mol H_2)$^{-1}$, average grain size of 40–50 μm) with some other pioneering groups [21, 50], we can conclude that thermodynamic properties do not change with catalyst and nanosizing in the size range of 5

Table 3.1 The van't Hoff equations, enthalpy and entropy values for desorption reaction of different Mg-based nanostructured systems [47, 48, 50, 53, 54]. (Reproduced with permission from [21]).

System	van't Hoff equation	Enthalpy (ΔH) kJ mol^{-1} H_2	Entropy(ΔS) J (K mol H_2)$^{-1}$
MgH_2	$\ln(p/0.1\ \text{MPa}) = -9604/T + 16.93$	79.8	140.8
Mg_2NiH_4	$\ln(p/0.1\ \text{MPa}) = -7977/T + 15.07$	66.32	125.3
Mg_2CoH_5	$\ln(p/0.1\ \text{MPa}) = -9895/T + 16.70$	82.27	138.8
Mg_3CoH_5	$\ln(p/0.1\ \text{MPa}) = -8800/T + 14.80$	73.16	123.0
MgH_2+$MgCu_2$	$\ln(p/0.1\ \text{MPa}) = -9275/T + 17.61$	77.11	146.4

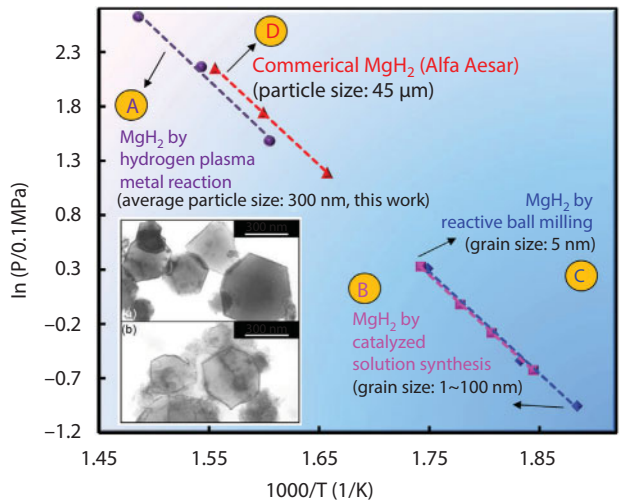

Figure 3.7 The van't Hoff plots of the desorption reactions for four different MgH_2–Mg systems synthesized by different methods (HPMR method, catalyzed chemical solution synthesis, high-pressure reactive ball milling under 30 MPa hydrogen and the commercial one from Alfa Aesar). (Reproduced with permission from [3])

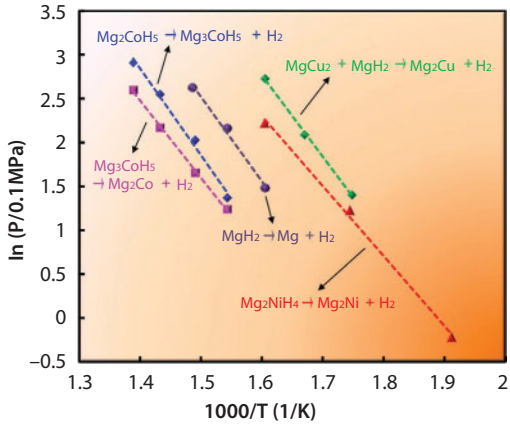

Figure 3.8 The van't Hoff plots for desorption reactions of Mg-H, Mg-Ni-H, Mg-Co-H and Mg-Cu-H nanoparticle samples. (Reproduced with permission from [50])

to 300 nm. It was reported by Wagemans *et al.* in their quantum chemical study that the desorption energy will dramatically decrease only when the crystallite size of the MgH_2 is smaller than 1.3 nm and for MgH_2 nanostructure sample, in order to reduce the desorption temperature from 573 K to 473 K, the nanosize of the MgH_2 sample should be reduced to around 0.9 nm [63], which has not been achieved so far by current nano-processing techniques. Figure 3.8 shows the desorption van't Hoff plot of different Mg-M-H nanoparticle systems. When we compare the enthalpy and entropy changes of our nanostructured Mg-M-H system with the ones of micrometer scale ones, we found that our values agree well with the ones without nanostructure in the literature [64–66]. The enthalpy values indicate stability of the nanostructured hydride systems. From Figure 3.8 and Table 3.1, the following order is suggested:

$$Mg_2CoH_5 > MgH_2 > MgH_2+MgCu_2 > Mg_3CoH_5 > Mg_2NiH_4 \quad (3.7)$$

3.6 Novel Mg-TM (TM=V, Zn, Al) Nanocomposites

3.6.1 Introduction

In-situ formed Mg-based nanocomposites can also be synthesized by HPMR approach. The phase composition of the Mg-based nanocomposites should strongly depend on the interaction of the doped metal, Mg and

H during high cooling processing of HPMR. According to the binary diagrams of the Mg-based systems, some metals can form solid solution or intermetallic compounds with Mg, while others are immiscible with Mg in solid state. Thus, it is interesting to determine the phase compositions of different Mg-based nanocomposites and their hydrogen storage properties. Al is one of the most attractive candidates to decrease the stability of magnesium hydride. There are three Mg-Al intermetallic compounds with wide composition range existing in the Mg-Al binary phase diagram, $Mg_{17}Al_{12}$, $Mg_{42}Al_{58}$ and Mg_2Al_3, and their hydrogen storage capacities are 4.44, 3.17, and 3.02 wt%, respectively [67]. Wang and coworkers [68] reported that the hydrogen uptake capacity of the ball-milled $Mg_{17}Al_{12}$ at 573 K could reach up to 2.19 wt% in 40 min and it can release 2.01 wt% H_2 in 30 min at 613 K. Moreover, besides the enhancement of the hydrogenation/dehydrogenation kinetics of Mg with Al addition, the enthalpy of hydrogenation can be decreased due to the endothermic disproportionate reactions of Mg-Al intermetallic compounds [69–71]. Therefore, it has potential to fabricate Mg-Al intermetallic compounds during the HPMR process. As to the Mg-Zn binary systems, they can form several kinds of intermetallic compounds, such as MgZn, $MgZn_2$, Mg_2Zn_3 and Mg_2Zn_{11}. Deledda and coworkers [71] ball milled the Zn and Mg powders to synthesize Mg-Zn intermetallic compounds. However, the final product was the amorphous Mg-Zn phase with a composition of $Mg_{45}Zn_{55}$. They further studied the Mg-Y-Zn alloys and found that the phase evolutions during hydrogen absorption and desorption cycle were pressure dependent, and Mg_4Zn_7 decomposed into MgH_2 and $MgZn_2$ if the pressures were above 1.0 MPa [72]. These stoichiometric Mg-Zn compounds may barely form at very high cooling rate during the HPMR process because only non-stoichiometric compounds with wide composition range are relatively easy to nucleate and grow into intermetallic compound nanoparticles. Vanadium is a specific metal, which can absorb and release hydrogen under moderate pressure and temperature [73]. Liang *et al.* [74] found that the MgH_2–5 at% V nanocrystalline prepared by ball milling completely released hydrogen within 1000 s at 523 K. Kondo and Sakurai [75] demonstrated that ball-milled Mg_2CaV_3 ternary alloy could uptake 3.3 wt% H_2 even at 298 K. According to the Mg-V binary diagram, the two metals are immiscible in solid state [76], and V hydride produced by HPMR may disperse on the surface of Mg. Thus, we herein will review the phase compositions and morphologies of novel Mg-TM (TM=Al, V, Zn) nanocomposites prepared by HPMR approach, and compare the influences of different metal elements on the hydrogen storage properties of Mg-based materials [77–79].

3.6.2 Structure and Morphology of Mg-TM Nanocomposites

Figure 3.9 shows the XRD pattern of the Mg-7 at% Al nanocomposite, it can be observed that the pattern is composed predominantly of the α-Mg (hcp) structure, and the weak diffraction peak centered at 36° proves the existence of the intermetallic compound $Mg_{17}Al_{12}$ [77]. Generally, that stoichiometric compound particles cannot form at the very high cooling rate of 10^5 K s^{-1} during the HPMR process [80, 81]. Although the stoichiometric compound $Mg_{17}Al_{12}$ contains 58.6 at% Mg, this compound has an extremely broad composition range of approximately 45 to 60.5 at% Mg in the Mg-Al binary system [82], which contributes to the formation of the $Mg_{17}Al_{12}$ compound. The Mg nanoparticles of about 150 nm in Figure 3.9b are polyhedral in shape, and the inset HRTEM image near the edges of the Mg-Al nanoparticles clearly shows a core/shell structure and the shell is composed of $Mg_{17}Al_{12}$ phase. Surprisingly, no Mg oxide phase is detectable on the surface of the Mg-Al nanocomposite particles, which is ascribed to the fact that the $Mg_{17}Al_{12}$ shell provides much higher chemical stability than Mg. It can be seen from Figure 3.9c that the as-prepared Mg-10.2 at% V nanocomposite sample predominantly contains α-Mg (hcp) together with a certain amount of fcc-VH_2 rather than Mg-V intermetallic phase [78]. The three weak diffraction peaks of MgH_2 at 27.95°, 35.74° and 54.62° can also be discernable, suggesting that a small amount of MgH_2 forms in the Mg-V nanocomposite, which is attributed to the catalytic effect of VH_2 nanoparticles dispersed on the surface of the Mg nanoparticles. There are two types of particles in Figure 3.9d, which are different from the Mg-Al nanocomposite of core/shell structure. The big particles vary from 50 to 150 nm with an average of about 100 nm. They are hexagonal in shape, similar to the pure Mg nanoparticles prepared by HPMR [83]. The small particles decorate the surface of the big particles. The inset electron diffraction pattern in Figure 3.9d of one big particle together with several tens of small particles can be indexed by the hexagonal structure of α-Mg (hcp) with the diffraction zone axis of [$3\bar{8}\bar{7}$], indicating that the big particle is a single-crystal Mg. The ring pattern can be indexed to VH_2 with fcc structure, implying that the small particles belong to VH_2. In the Mg-6.9 at% Zn system, no other diffraction peaks can be detected except for the α-Mg (hcp) phase (see Figure 3.9e), proving that Zn partially dissolved in the α-Mg structure [79]. A broad and diffusive peak between 40 and 43° indicates the formation of amorphous Mg-Zn phase during the solidification at very high cooling rate of 10^5

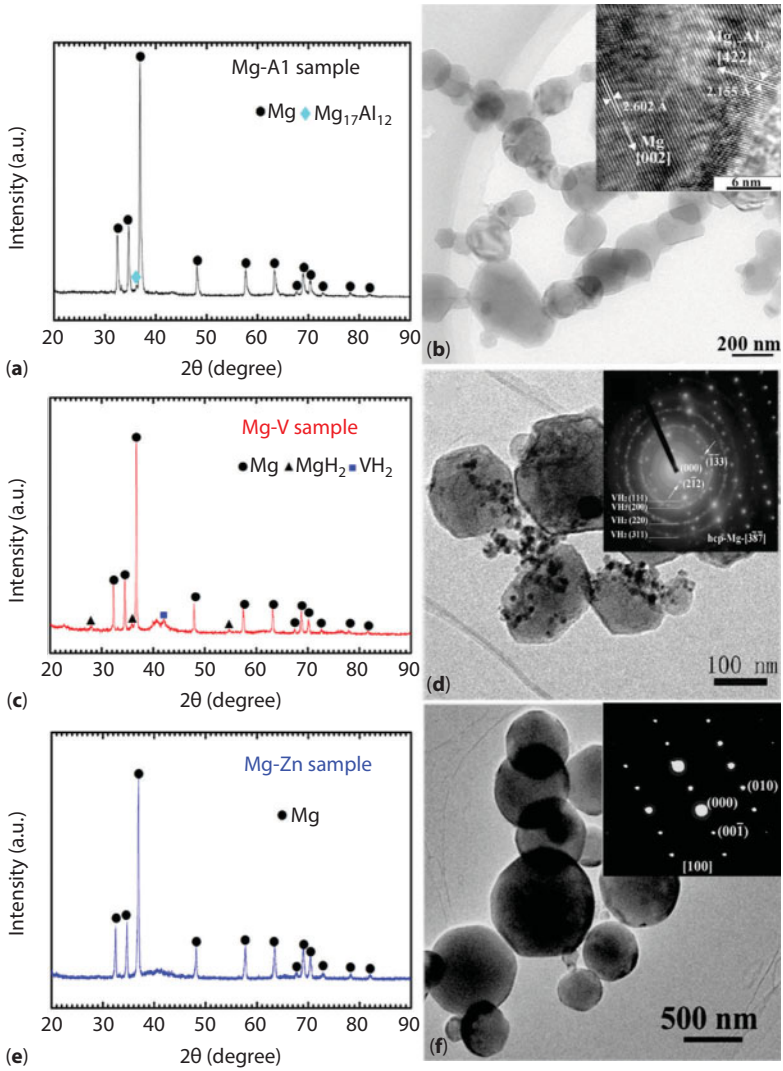

Figure 3.9 XRD pattern (a) and TEM (b) images of Mg-Al nanocomposite, the inset figure is the HRTEM image of the Mg-Al nanocomposite; XRD pattern (c) and TEM (d) images of the Mg-V nanocomposite, the inset figure is the SAED image of the Mg-V nanocomposite; XRD pattern (e) and TEM (d) images of the Mg-Zn nanocomposite, the inset figure is the SAED of the Mg-Zn nanocomposite.

K/s in the HPMR processing. The amorphous Mg-Zn phase promoted the homogeneous growth of the composite particles into the spherical shape rather than the polyhedral or hexagonal shape (see Figure 3.9f). This is different from that of the Mg-Al and Mg-V nanocomposites. Furthermore,

the diffraction peak of MgO around 42.9°, which often appears in the Mg particles prepared by HPMR [83], cannot be detected in Figure 3.9e. This indicates that the addition of Zn effectively suppressed the pyrophoricity of Mg, leading to the decrease of MgO content in the nanoparticles after passivation. In addition, the electron diffraction pattern reveals that each particle belongs to a single crystal structure (see the inset figure in Figure 3.9f). The pattern can be indexed by the hexagonal structure of α-Mg (hcp) with a diffraction zone axis of [100]. The halo ring from amorphous structure could not be detected in the electron diffraction pattern due to the low content of the amorphous phase. This is different from those of the Mg-Al and Mg-V nanocomposites of core/shell or particle decoration structures.

3.6.3 Hydrogen Absorption Kinetics

Absorption kinetics curves at 623, 573, and 523 K of the Mg-TM (TM=Al, V, and Zn) nanocomposites show that the Mg-V nanocomposite displays the best absorption kinetics properties while the Mg-Zn nanocomposite is the worst (see Figure 3.10a–c), and the Mg-Al nanocomposite possesses the highest absorption capacity among the Mg-TM (TM=Al, V, Zn) nanocomposites [77–79] for its low concentration of Al element in the nanocomposite. The Mg-V nanocomposite can uptake 4.6 wt% H_2 within 1 min at 623 K, while the Mg-Al and Mg-Zn can only absorb 4.0 and 3.0 wt% H_2 within 1 min (see Figure 3.10a). When temperature decreases to 573 K, the Mg-V nanocomposite can reach a saturation hydrogen absorption value of 4.2 wt% just within 5 min, the Mg-Al nanocomposite can absorb 90% (5.0 wt%) of the saturation hydrogen absorption content (5.9 wt% at 573 K) within 10 min, and the Mg-Zn nanocomposite can absorb 86% (5.0 wt%) of the saturation hydrogen absorption content (5.8 wt% at 573 K) even in 30 min (see Figure 3.10b). Even at the low absorption temperature of 523 K, the Mg-V nanocomposite can reach its saturation hydrogen absorption value of 3.8 wt% within just 10 min, showing fast kinetics properties. Moreover, the Mg-Al nanocomposite can absorb 4.5 wt% H_2 in 20 min and reache a value of 5.5 wt% in 50 min, showing faster kinetics properties than Mg-Zn nanocomposite (see Figure 3.10c). Generally, transition metals with d-electrons can more effectively improve the hydrogen association/dissociation rates than the light metals [74]. However, the Mg-Al nanocomposite exhibits better kinetics properties, suggesting that the core/shell structure is beneficial to enhance the hydrogen storage properties.

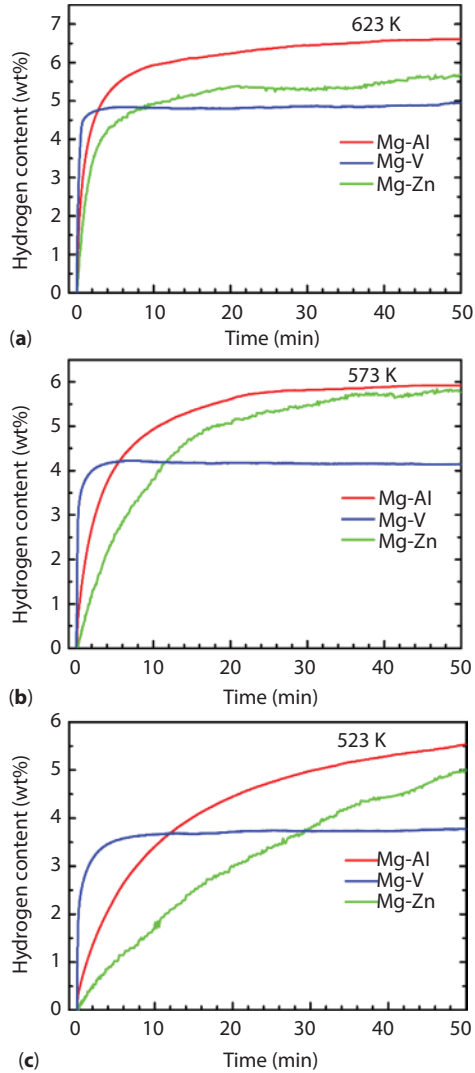

Figure 3.10 Hydrogen absorption curves under 4 MPa hydrogen pressure of the Mg-Al, Mg-V, and Mg-Zn nanocomposites at (a) 623 K, (b) 573 K and (c) 523 K.

3.6.4 Phase Evolution During Hydrogenation/ Dehydrogenation

Figure 3.11a,b shows the phase evolution during the hydrogenation/dehydrogenation process of the Mg-Al, Mg-V, and Mg-Zn nanocomposites [77–79]. After hydrogenation at 673 K, the Mg particle core transforms

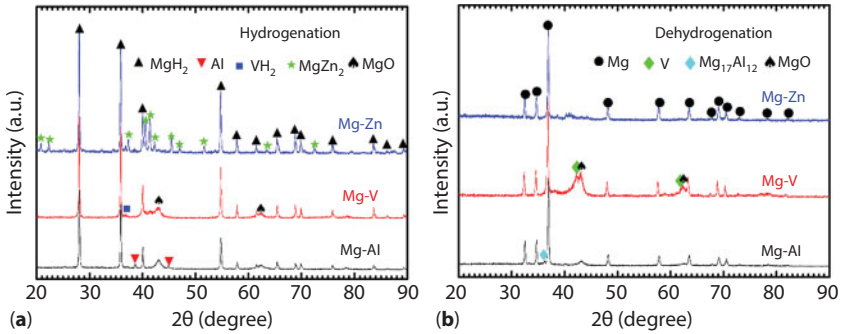

Figure 3.11 XRD patterns of the Mg-Al, Mg-V, and Mg-Zn nanocomposites: (a) after hydrogenation in 4 MPa hydrogen at 673 K, (b) after dehydrogenation under 100 Pa at 673 K.

into MgH_2, whereas the particle shell of $Mg_{17}Al_{12}$ changes into MgH_2 and Al [77]. The V in the Mg-V system transforms to VH_2 after hydrogenation [78]. In the Mg-Zn nanocomposite, most of the Mg in the Mg-Zn nanocomposite transforms into MgH_2, and the rest of the Mg combines with Zn to form intermetallic $MgZn_2$ [79] (see Figure 3.11a). After the dehydrogenation process at 673 K, the $Mg_{17}Al_{12}$ shell recovers, indicating the reaction between Al and Mg. This is of great importance for sustaining excellent hydrogen storage reversibility. For the Mg-V nanocomposite, MgH_2 dehydrogenates and changes completely into α-Mg after the dehydrogenation process, and VH_2 transforms into V, indicating the reversibility of the V/VH_2 catalyst. It is observed from the dehydrogenated XRD pattern of the Mg-Zn nanocomposite at 673 K, MgH_2 decomposes almost completely and transforms into α-Mg. The diffraction peaks of $MgZn_2$ disappear and several unidentified peaks are observed between 40 and 50°. Accordingly, $MgZn_2$ probably transforms into the complex Mg-Zn intermetallic compounds of several phases under the low hydrogen pressure during the desorption process such as MgZn, Mg_2Zn_3 and Mg_2Zn_{11}.

3.6.5 Summary

The Mg-TM (TM=Al, V, Zn) nanocomposites with different structures and morphologies can be successfully prepared by HPMR approach. Al reacts with Mg to form $Mg_{17}Al_{12}$ phase, and the Mg-Al particles display a Mg/$Mg_{17}Al_{12}$ core/shell structure. As to the Mg-V system, V cannot react with Mg, and the VH_2 particles formed during the HPMR process uniformly disperse on the surface of the Mg nanoparticles. For the Mg-Zn system,

Zn partially dissolves in the Mg structure and the rest forms amorphous Mg-Zn phase. The $Mg_{17}Al_{12}$ shell, the decorated VH_2 particles, and the amorphous Mg-Zn phase can suppress the formation of MgO on the Mg nanoparticles. After hydrogenation/dehydrogenation cycle, the $Mg_{17}Al_{12}$ shell recovers and the VH_2 nanoparticles change to V, whereas the complex Mg-Zn intermetallic compound is formed in the Mg-Zn nanocomposite. The Mg-V nanocomposite shows the best hydrogen absorption kinetics properties, and the Mg-Al nanocomposite exhibits better kinetics properties than that of Mg-Zn nanocomposite, suggesting that the core/shell structure is beneficial to the hydrogen absorption rate. Moreover, the $Mg/Mg_{17}Al_{12}$ nanocomposite shows the highest hydrogen storage capacity among these Mg-TM nanocomposites. Thus, the creation of the novel nanoparticle-decorated structure with intermetallic shell by HPMR approach is promising to enhance the hydrogen storage properties of Mg-based materials.

3.7 Summary and Prospects

The HPMR method was used to successfully fabricate Mg and Ni, Co, Cu metal nanoparticles. The mean particle size of Mg is around 300 nm and the average size of Ni, Co and Cu nanoparticles is 30–50 nm. With the HPMR method, the obtained Mg nanoparticles have a much larger particle size than the transition metals because Mg has a much lower melting point and faster evaporation rate during plasma synthesis under the same conditions. The Mg_2Ni, Mg_2Co and Mg_2Cu nano alloys and $Mg_{85}Ni_{15}$ nanocomposite are synthesized from these Mg, Ni, Co and Cu metal nanoparticles under much simpler conditions than those from micrometer-scale metals. And the nanostructured Mg-based materials show much enhanced hydrogen storage kinetics because nanostructured samples show larger surface area and smaller particle and grain size than micrometer ones. This means that the nanometer samples have greater contact area for the solid-solid and solid-hydrogen reaction in the metals and alloys, and much shorter distance for matter transfer and hydrogen diffusion in the nanoparticles during the hydrogen absorption process. However, downsizing does not change the desorption enthalpy and entropy in our size range of 5–300 nm in nanostructured Mg-based hydrogen storage systems. The novel Mg-TM nanocomposites produced by HPMR not only prevent the enlargement of Mg particle during hydrogenation/dehydrogenation but also effectively enhance the sorption kinetics of Mg/MgH_2. Nevertheless, these nanocomposites still fail to absorb/desorb hydrogen below 373 K. To achieve this

goal, it is desirable to confine Mg particle to several nanometers and dope more efficient catalysts on the surface of Mg.

Based on these results, we can say that it is difficult to alter the thermodynamics (desorption enthalpy and entropy) in Mg-based material systems to make these materials capable of desorbing nearly one atmosphere hydrogen below 373 K, and we may even reach the obtainment of nanostructured Mg-based materials with a size of around 5–300 nm. This means it remains challenging to develop Mg-based nanostructured materials for onboard hydrogen storage. However, for large-scale stationary energy storage, especially to combine with solid oxide fuel cell (SOFC) technologies, Mg-based materials are very promising due to the low cost of Mg, great abundance of Mg in the earth's crust, and large energy density of the hydrides [3, 21, 84, 85].

Acknowledgments

H. Shao acknowledges Macau Science and Technology Development Fund (FDCT) for the funding support (Project No.:118/2016/A3), which was also partially supported by Start-up Research Fund from the University of Macau (SRG2016–00088-FST). T. Liu acknowledges the Joint Fund of the National Natural Science Foundation of China and Baosteel Group Corporation (No. U1560106), the Aeronautical Science Foundation of China (No. 2016ZF51050), and the Scientific Research Foundation for the Returned Overseas Chinese Scholars (State Education Ministry).

References

1. Toyota, https://ssl.toyota.com/mirai/fcv.html, accessed on Nov. 14, 2017.
2. Schlapbach, L., Zuttel, A., Hydrogen-storage materials for mobile applications. *Nature* 414(6861), 353, 2001.
3. Shao, H., He, L., Lin, H., Li, H.W., Progress and trends in Magnesium-based Materials for energy-storage research: A review. *Energy Technol.* 6(3), 445, 2018.
4. Power Electronics News, http://www.powerelectronicsnews.com/technology/solar-storage-moves-out-of-the-lab-into-mainstream, accessed Nov., 2017.
5. Crivello, J.C., Dam, B., Denys, R.V., Dornheim, M., Grant, D.M., Huot, J., Jensen, T.R., de Jongh, P., Latroche, M., Milanese, C., Milčius, D., Walker, G.S., Webb, C.J., Zlotea, C., Yartys, V.A., Review of magnesium hydride-based materials: Development and optimisation. *Appl. Phys. A*, 122(2), 97, 2016.
6. Varin, R.A., Zbroniec, L., Polanski, M., Bystrzycki, J., A review of recent advances on the effects of microstructural refinement and nano-catalytic

additives on the hydrogen storage properties of metal and complex hydrides. *Energies* 4(1), 1, 2011.
7. Berube, V., Radtke, G., Dresselhaus, M., Chen, G., Size effects on the hydrogen storage properties of nanostructured metal hydrides: A review. *Int. J. Energ. Res.* 31(6–7), 637, 2007.
8. Khafidz, N.Z.A., Yaakob, Z., Lim, K.L., Timmiati, S.N., The kinetics of light-weight solid-state hydrogen storage materials: A review. *Int. J. Hydrogen Energy*, 41(30), 13131, 2016.
9. Rusman, N.A.A., Dahari, M., A review on the current progress of metal hydrides material for solid-state hydrogen storage applications. *Int. J. Hydrogen Energy* 41(28), 12108, 2016.
10. Sakintuna, B., Lamari-Darkrim, F., Hirscher, M., Metal hydride materials for solid hydrogen storage: A review. *Int. J. Hydrogen Energy*, 32(9), 1121, 2007.
11. Ouyang, L., Cao, Z., Wang, H., Hu, R., Zhu, M., Application of dielectric barrier discharge plasma-assisted milling in energy storage materials–A review. *J. Alloys Compd.* 691, 422, 2017.
12. Wang, H., Lin, H.J., Cai, W.T., Ouyang, L.Z., Zhu, M., Tuning kinetics and thermodynamics of hydrogen storage in light metal element based systems–A review of recent progress. *J. Alloys Compd.* 658, 280, 2016.
13. Webb, C.J., A review of catalyst-enhanced magnesium hydride as a hydrogen storage material. *J. Phys. Chem. Solids* 84, 96, 2015.
14. Zhu, M., Lu, Y.S., Ouyang, L.Z., Wang, H., Thermodynamic tuning of Mg-based hydrogen storage alloys: A review. *Materials* 6(10), 4654, 2013.
15. Sadhasivam, T., Kim, H.T., Jung, S., Roh, S.H., Park, J.H., Jung, H.Y., Dimensional effects of nanostructured Mg/MgH_2 for hydrogen storage applications: A review. *Renew. Sust. Energ. Rev.* 72, 523, 2017.
16. Satyapal, S., Petrovic, J., Read, C., Thomas, G., Ordaz, G., The U.S. Department of Energy's National Hydrogen Storage Project: Progress towards meeting hydrogen-powered vehicle requirements. *Catal. Today* 120(3–4), 246, 2007.
17. Barkhordarian, G., Klassen, T., Bormann, R., Fast hydrogen sorption kinetics of nanocrystalline Mg using Nb_2O_5 as catalyst. *Scripta Mater.* 49(3), 213, 2003.
18. Awad, A.S., El-Asmar, E., Tayeh, T., Mauvy, F., Nakhl, M., Zakhour, M., Bobet, J.L., Effect of carbons (G and CFs), TM (Ni, Fe and Al) and oxides (Nb_2O_5 and V_2O_5) on hydrogen generation from ball milled Mg-based hydrolysis reaction for fuel cell. *Energy* 95, 175, 2016.
19. House, S.D., Vajo, J.J., Ren, C., Rockett, A.A., Robertson, I.M., Effect of ball-milling duration and dehydrogenation on the morphology, microstructure and catalyst dispersion in Ni-catalyzed MgH_2 hydrogen storage materials. *Acta Mater.* 86, 55, 2015.
20. Orimo, S., Fujii, H., Ikeda, K., Notable hydriding properties of a nanostructured composite material of the Mg_2Ni-H system synthesized by reactive mechanical grinding. *Acta Mater.* 45(1), 331, 1997.
21. Shao, H., Xin, G., Zheng, J., Li, X., Akiba, E., Nanotechnology in Mg-based materials for hydrogen storage. *Nano Energy* 1(4), 590, 2012.

22. Matsuda, J., Shao, H., Nakamura, Y., Akiba, E., The nanostructure and hydrogenation reaction of $Mg_{50}Co_{50}$ BCC alloy prepared by ball-milling. *Nanotechnology* 20(20), 204015, 2009.
23. Konarova, M., Tanksale, A., Norberto Beltramini, J., Qing Lu, G., Effects of nano-confinement on the hydrogen desorption properties of MgH_2. *Nano Energy* 2(1), 98, 2013.
24. Zlotea, C., Cuevas, F., Andrieux, J., Matei Ghimbeu, C., Leroy, E., Léonel, E., Sengmany, S., Vix-Guterl, C., Gadiou, R., Martens, T., Latroche, M., Tunable synthesis of (Mg–Ni)-based hydrides nanoconfined in templated carbon studied by *in situ* synchrotron diffraction. *Nano Energy* 2(1), 12, 2013.
25. Jeon, K.J., Moon, H.R., Ruminski, A.M., Jiang, B., Kisielowski, C., Bardhan, R., Urban, J.J., Air-stable magnesium nanocomposites provide rapid and high-capacity hydrogen storage without using heavy-metal catalysts. *Nat. Mater.* 10(4), 286, 2011.
26. Baldi, A., Palmisano, V., Gonzalez-Silveira, M., Pivak, Y., Slaman, M., Schreuders, H., Dam, B., Griessen, R., Quasifree Mg-H thin films. *Appl. Phys. Lett.* 95(7), 071903, 2009.
27. Xin, G., Yang, J., Wang, C., Zheng, J., Li, X., Superior (de)hydrogenation properties of Mg-Ti-Pd trilayer films at room temperature. *Dalton. Trans.* 41(22), 6783, 2012.
28. Bao, S., Yamada, Y., Okada, M., Yoshimura, K., Electrochromic properties of Pd-capped Mg-Ni switchable mirror thin films. *Electrochemistry* 76(4), 282, 2008.
29. Xu, J.L., Li, Y., Wang, F.H., Effect of Al content on the electrochemical properties of $Mg_{2-x}Al_xNi$ thin film hydride electrodes. *Electrochim. Acta* 55(1), 148, 2009.
30. Palmisano, V., Filippi, M., Baldi, A., Slaman, M., Schreuders, H., Dam, B., An optical hydrogen sensor based on a Pd-capped Mg thin film wedge. *Int. J. Hydrogen Energy* 35(22), 12574, 2010.
31. Xu, J., Niu, D., Fan, Y.J., Electrochemical hydrogen storage performance of $Mg_{2-x}Al_xNi$ thin films. *J. Power Sources* 198, 383, 2012.
32. Ouyang, L.Z., Chung, C.Y., Wang, H., Zhu, M., Microstructure of Mg-Ni thin film prepared by direct current magnetron sputtering and its properties as a negative electrode. *J. Vac. Sci. Technol. A* 21(6), 1905, 2003.
33. Zhu, C.Y., Hosokai, S., Akiyama, T., Direct synthesis of MgH_2 nanofibers from waste Mg. *Int. J. Hydrogen Energy* 37(10), 8379, 2012.
34. Zhang, Y.H., Liu, Z.C., Li, B.W., Ma, Z.H., Guo, S.H., Wang, X.L., Structure and electrochemical performances of $Mg_2Ni_{1-x}Mn_x$ (x=0–0.4) electrode alloys prepared by melt spinning. *Electrochim. Acta* 56(1), 427, 2010.
35. Zhang, Y.H., Wang, H.T., Zhai, T.T., Yang, T., Qi, Y., Zhao, D.L., Hydrogen storage characteristics of the nanocrystalline and amorphous Mg-Nd-Ni-Cu-based alloys prepared by melt spinning. *Int. J. Hydrogen Energy* 39(8), 3790, 2014.

36. Zhang, Y.H., Hu, F., Li, Z.G., Lu, K., Guo, S.H., Wang, X.L., Hydrogen storage characteristics of nanocrystalline and amorphous Mg_2Ni-type alloys prepared by melt spinning. *J. Alloys Compd.* 509(2), 294, 2011.
37. Song, W.J., Li, J.S., Zhang, T.B., Hou, X.J., Kou, H.C., Dehydrogenation behavior and microstructure evolution of hydrogenated magnesium-nickel-yttrium melt-spun ribbons. *RSC Adv.* 5(67), 54258, 2015.
38. Edalati, K., Emami, H., Ikeda, Y., Iwaoka, H., Tanaka, I., Akiba, E., Horita, Z., New nanostructured phases with reversible hydrogen storage capability in immiscible magnesium–zirconium system produced by high-pressure torsion. *Acta Mater.* 108, 293, 2016.
39. Edalati, K., Emami, H., Staykov, A., Smith, D.J., Akiba, E., Horita, Z., Formation of metastable phases in magnesium–titanium system by high-pressure torsion and their hydrogen storage performance. *Acta Mater.* 99, 150, 2015.
40. Hongo, T., Edalati, K., Arita, M., Matsuda, J., Akiba, E., Horita, Z., Significance of grain boundaries and stacking faults on hydrogen storage properties of Mg_2Ni intermetallics processed by high-pressure torsion. *Acta Mater.* 92, 46, 2015.
41. Shao, H., Felderhoff, M., Schuth, F., Weidenthaler, C., Nanostructured Ti-catalyzed MgH_2 for hydrogen storage. *Nanotechnology* 22(23), 235401, 2011.
42. Bogdanović, B., Liao, S., Schwickardi, M., Sikorsky, P., Spliethoff, B., Catalytic synthesis of magnesium hydride under mild conditions. *Angew. Chem. Int. Edit.* 19(10), 818, 1980.
43. Bogdanović, B., Ritter, A., Spliethoff, B., Active MgH_2-Mg systems for reversible chemical energy-storage. *Angew. Chem. Int. Edit.* 29(3), 223, 1990.
44. Bogdanović, B., Magnesium hydride: A homogeneous-catalysed synthesis and its use in hydrogen storage. *Int. J. Hydrogen Energy* 9(11), 937, 1984.
45. Vons, V.A., Anastasopol, A., Legerstee, W.J., Mulder, F.M., Eijt, S.W.H., Schmidt-Ott, A., Low-temperature hydrogen desorption and the structural properties of spark discharge generated Mg nanoparticles. *Acta Mater.* 59(8), 3070, 2011.
46. Shao, H.Y., Liu, T., Li, X.X., Preparation of the Mg_2Ni compound from ultrafine particles and its hydrogen storage properties. *Nanotechnology* 14(3), L1, 2003.
47. Shao, H.Y., Liu, T., Li, X.G., Zhang, L.F., Preparation of Mg_2Ni intermetallic compound from nanoparticles. *Scripta Mater.* 49(6), 595, 2003.
48. Shao, H.Y., Xu, H.R., Wang, Y.T., Li, X.G., Synthesis and hydrogen storage behavior of Mg-Co-H system at nanometer scale. *J. Solid State Chem.* 177(10), 3626, 2004.
49. Shao, H.Y., Xu, H.R., Wang, Y.T., Li, X.G., Preparation and hydrogen storage properties of Mg_2Ni intermetallic nanoparticles. *Nanotechnology* 15(3), 269, 2004.
50. Shao, H., Wang, Y., Xu, H., Li, X., Preparation and hydrogen storage properties of nanostructured Mg_2Cu alloy. *J. Solid State Chem.* 178(7), 2211, 2005.
51. Shao, H.Y., Wang, Y.T., Li, X.G., Synthesis and properties of nanostructured Mg_2Ni-based compounds. *Mater. Sci. Forum* 475–479(3), 2445, 2005.

52. Xie, L., Shao, H.Y., Wang, Y.T., Li, Y., Li, X.G., Synthesis and hydrogen storing properties of nanostructured ternary Mg-Ni-Co compounds. *Int. J. Hydrogen Energy* 32(12), 1949, 2007.
53. Shao, H.Y., Liu, T., Wang, Y.T., Xu, H.R., Li, X.G., Preparation of Mg-based hydrogen storage materials from metal nanoparticles. *J. Alloys Compd.* 465(1–2), 527, 2008.
54. Shao, H., Cheng, C., Liu, T., Li, X., Phase, microstructure and hydrogen storage properties of Mg-Ni materials synthesized from metal nanoparticles. *Nanotechnology* 25(13), 135704., 2014.
55. Li, X., Shao, H., Liu, T., Synthesis of nanoparticles and their properties by hydrogen plasma metal reaction, in: *Trends in Nanotechnology Research*, Dirote, E.V. (Ed.), Editor, Nova Scientific Publishers, 2004.
56. Shao H., Li, X., Kinetics and thermodynamics of nanostructured mg-based hydrogen storage materials synthesized from metal nanoparticles. *Adv. Mat. Res.* 924, 189, 2014.
57. Shao, H., Preparation and properties of nanostructured magnesium-based hydrogen storage materials, College of Chemistry and Molecular Engineering, Peking University, Beijing, 2005.
58. Shao, H., Wang, Y., Xu, H., Li, X., Hydrogen storage properties of magnesium ultrafine particles prepared by hydrogen plasma-metal reaction. *Mater. Sci. Eng., B* 110(2), 221, 2004.
59. Ohno, S., Generation rate of ultrafine metal particles in hydrogen plasma-metal reaction. *J. Jpn. Inst. Met.* 48, 640, 1984.
60. Li, L.Q., Saita, I., Akiyama, T., Intermediate products during the hydriding combustion synthesis of Mg_2NiH_4. *J. Alloys Compd.* 384(1–2), 157, 2004.
61. Saita, I., Li, L.Q., Saito, K., Akiyama, T., Hydriding combustion synthesis of Mg_2NiH_4. *J. Alloys Compd.* 356, 490, 2003.
62. Shao, H., Heat modeling and material development of Mg-based nanomaterials combined with solid oxide fuel cell for stationary energy storage. *Energies* 10(11), 1767, 2017.
63. Wagemans, R.W.P., van Lenthe, J.H., de Jongh, P.E., van Dillen, A.J., de Jong, K.P., Hydrogen storage in magnesium clusters: quantum chemical study. *J. Am. Chem. Soc.* 127(47), 16675, 2005.
64. Stampfer, J.F., Holley, C.E., Suttle, J.F., The magnesium hydrogen system. *J. Am. Chem. Soc.* 82(14), 3504, 1960.
65. Reilly, J.J., Wiswall, R.H., Reaction of hydrogen with alloys of magnesium and copper. *Inorg. Chem.* 6(12), 2220, 1967.
66. Reilly, J.J., Wiswall, R.H., Reaction of hydrogen with alloys of magnesium and nickel and the formation of Mg_2NiH_4. *Inorg. Chem.* 7(11), 2254, 1968.
67. Andreasen, A., Hydrogenation properties of Mg–Al alloys. *Int. J. Hydrogen Energy* 33(24), 7489, 2008.
68. Wang, X.L., Tu, J.P., Zhang, P.L., Zhang, X.B., Chen, C.P., Zhao, X.B., Hydrogenation properties of ball-milled MgH_2–10wt%$Mg_{17}Al_{12}$ composite. *Int. J. Hydrogen Energy* 32(15), 3406, 2007.

69. Crivello, J.C., Nobuki, T., Kato, S., Abe, M., Kuji, T., Hydrogen absorption properties of the -$Mg_{17}Al_{12}$ phase and its Al-richer domain. *J. Alloys Compd.* 446–447, 157, 2007.
70. Yabe, H., Kuji, T., Thermal stability and hydrogen absorption/desorption properties of $Mg_{17}Al_{12}$ produced by bulk mechanical alloying. *J. Alloys Compd.* 433(1–2), 241, 2007.
71. Deledda, S., Haubacka, B.C., Fjellvag, H., H-sorption behaviour of mechanically activated Mg–Zn powders. *J. Alloys Compd.* 446–447, 173, 2007.
72. Martin, S., Andersson, Y., Hydrogen absorption in Mg–Y–Zn ternary compounds. *J. Alloys Compd.* 446–447, 134, 2007.
73. Daniel, L.C., Powers, G.J., The storage of hydrogen as metal hydrides. *Ind. Eng. Chem. Process Des. Dev.* 13(2), 182, 1974.
74. Liang, G., Huot, J., Boily, S., Van Neste, A., Schulz, R., Catalytic effect of transition metals on hydrogen sorption in nanocrystalline ball milled MgH_2–Tm (Tm=Ti, V, Mn, Fe and Ni) systems. *J. Alloys Compd.* 292, 247, 1999.
75. Kondo, T., Sakurai, Y., Hydrogen absorption–desorption properties of Mg–Ca–V BCC alloy prepared by mechanical alloying. *J. Alloys Compd.* 417(1–2), 164, 2006.
76. Massalski, T.B, Okamoto, H. (Eds.), *Binary Alloy Phase Diagrams*, ASM International: Materials Park, OH, 1990.
77. Liu, T., Qin, C., Zhang, T., Cao, Y., Zhu, M., Li, X., Synthesis of Mg@$Mg_{17}Al_{12}$ ultrafine particles with superior hydrogen storage properties by hydrogen plasma–metal reaction. *J. Mater. Chem.* 22(37), 2012.
78. Liu, T., Zhang, T., Qin, C., Zhu, M., Li, X., Improved hydrogen storage properties of Mg–V nanoparticles prepared by hydrogen plasma–metal reaction. *J. Power Sources* 196(22), 9599, 2011.
79. Liu, T., Zhang, T., Zhang, X., Li, X., Synthesis and hydrogen storage properties of ultrafine Mg–Zn particles. *Int. J. Hydrogen Energy* 36(5), 3515, 2011.
80. Liu, T., Shao, H., Li, X., Synthesis and characteristics of Ti–Fe nanoparticles by hydrogen plasma–metal reaction. *Intermetallics* 12(1), 97, 2004.
81. Liu, T., Shao, H., Li, X., Synthesis of Fe–Al nanoparticles by hydrogen plasma–metal reaction. *J. Phys. Condens. Matter* 15, 2507, 2003.
82. Massalski T.B., Okamoto, H., Subramanian, P.R., Kacprzak, L., Scott, W.W., *Binary Alloy Phase Diagrams*. vol. 1, American Society for Metals: Metals Park, OH, 1986.
83. Liu, T., Zhang, Y., Li, X., Preparations and characteristics of Ti hydride and Mg ultrafine particles by hydrogen plasma–metal reaction. *Scripta Mater.* 48, 397, 2003.
84. Delhomme, B., Lanzini, A., Ortigoza-Villalba, G.A., Nachev, S., de Rango, P., Santarelli, M., Marty, P., Leone, P., Coupling and thermal integration of a solid oxide fuel cell with a magnesium hydride tank. *Int. J. Hydrogen Energy* 38(11), 4740, 2013.
85. de Rango, P., Marty, P., Fruchart, D., Hydrogen storage systems based on magnesium hydride: From laboratory tests to fuel cell integration. *Appl. Phys. A* 122(2), 126, 2016.

4

Hydrogen Storage in Ti/Zr-Based Amorphous and Quasicrystal Alloys

Akito Takasaki[1,*], Łukasz Gondek[2], Joanna Czub[2], Alicja Klimkowicz[1], Antoni Żywczak[3] and Konrad Świerczek[4]

[1]Shibaura Institute of Technology, College of Engineering, Department of Engineering Science and Mechanics, Tokyo, Japan
[2]AGH University of Science and Technology, Faculty of Physics and Applied Computer Science, Krakow, Poland
[3]AGH University of Science and Technology, Academic Center for Materials and Nanotechnology, Krakow, Poland
[4]AGH University of Science and Technology, Faculty of Energy and Fuels, Krakow, Poland

Abstract

Icosahedral (i) quasicrystals, which have a new type of translational long-range order and display a non-crystallographic rotational symmetry, were first observed in the Al-Mn alloy. Since the discovery of the Ti-Zr-Ni i quasicrystal phases (i-phases), studies on their hydrogen storage properties have been extensively conducted for not only their industrial applications as hydrogen storage media, but also scientific interest in their local structures, using a proton as a probe. The Ti/Zr-based i-phase has been mainly produced either by rapid-quenching or annealing the amorphous phase obtained by mechanical alloying (MA). We have systematically studied hydrogenation of the Ti/Zr-based amorphous and i-phase powders synthesized by MA and subsequent annealing respectively. In this chapter, we have reviewed the recent progress in the studies on hydrogenation of the Ti-Zr-Ni alloys and summarize our recent research results on both gaseous and electrochemical hydrogenation properties of the amorphous and the i-phase powders. The effects of the substitution or addition of some chemical elements on the microstructures and the hydrogenation properties have been investigated. Additionally, a comparison between the amorphous and the i-phases on the hydrogen properties as well as the results reported for the samples prepared by rapid-quenching will be made.

**Corresponding author*: takasaki@shibaura-it.ac.jp

Mehmet Sankir and Nurdan Demirci Sankir (eds.) Hydrogen Storage Technologies, (117–146) © 2018 Scrivener Publishing LLC

Keywords: Icosahedral quasicrystal, amorphous phase, hydrides, mechanical alloying, rapid quenching, gaseous hydrogenation, electrochemical hydrogenation, titanium-zirconium-nickel alloys

4.1 Introduction

For the recently growing hydrogen economy, efficient hydrogen storage is the limiting factor. Among the considered methods, conventional pressurization delivers a volumetric storage capacity up to 40 g L^{-1} (under 70 MPa). The capacity of the liquefied hydrogen is greater, however, still equal to about 72 gH_2 L^{-1}. This system requires expensive cooling and yet a constant heat input from the surroundings leads to inevitable hydrogen evaporation or boil-off [1, 2]. Alternatively, material-based hydrogen storage is proposed and many different materials are suggested. Metal hydrides, such as $LaNi_5$ or MgH_2 and their modifications, are well known in the literatures [3, 4]. The constant search for improvement of the hydrogen storage properties has led to the discovery of many new promising materials with unique properties.

Among them, icosahedral (i) quasicrystals, which have a new type of translational long-range order and a non-crystallographic rotational symmetry, seem to be especially interesting, because the occurrence of the i-quasiperiodic order enforces the formation of a greater number of interstitial sites that may be occupied by hydrogen atoms (protons) [5]. The first i-quasicrystal phase (i-phase) was observed for the Al-Mn alloy in 1984 by Shechtman *et al.* [6]. The i-phase with the $Ti_{80-x}Zr_xNi_{20}$ (x = 20–60) composition was first observed over a wide concentration range in the rapid-quenched alloys of the Ti-Zr-Ni systems [7], and then the presence of the stable Ti-Zr-Ni i-phase that can be formed by annealing as-cast crystalline alloys, whose initial microstructure was mostly the C14 Laves phase, was reported by Kelton *et al.* [8]. Here, Ti and Zr have strong chemical affinities with hydrogen while Ni has less but enhances decomposition of hydrogen molecules into protons as catalysis similar to the one in $LaNi_5$. Since then, the studies on the hydrogen storage properties of the Ti-Zr-Ni i-phase have been extensively conducted not only towards their industrial applications but also scientific interest in their local structures.

In this chapter, we focus on the evaluation of gaseous and electrochemical hydrogen storage in the Ti-Z-Ni related phases, such as the amorphous and the i-phase synthesized by mechanical alloying (MA) and subsequent annealing. The comparison to those of the i-phase produced by rapid-quenching is also partially made. Throughout the chapter, we present our recent results for different Ti-Zr-Ni stoichiometries, mainly focusing

on how several kinds of substitution of chemical elements optimize the Ti-Zr-Ni composition in order to maximize their hydrogen or discharge capacity after gaseous or electrochemical hydrogenation. The effect of substitution of transition metals, such as Co and Fe, for Ni on gaseous hydrogen storage properties, is also being investigated.

4.2 Production of Ti/Zr-Based Amorphous and Quasicrystal Alloys

Rapid-quenching, such as melt spinning, is widely used to produce amorphous alloys in the form of ribbons. Mechanical alloying, which is a physical milling process through a solid-state reaction, can also produce amorphous alloy powders. The first i-phase reported by Shechtman *et al.* [6] for alloys of Al with 10–14 at% Mn, Fe or Cr was metastable. They were produced by rapid-quenching, which is the same method as for the amorphous alloys. After the discovery of stable quasicrystal alloys produced by the conventional casting method (slow cooling from the melt), they have been produced by various processes involving different routes, which are concisely summarized in ref. [9]. The first stable single i-phase reported was the Al_6Li_3Cu alloy produced by slow casting, with a triacontahedral shape. Besides the conventional solidification processes, such as rapid-quenching and slow casting, MA can also produce quasicrystal alloy powders. The first i-phase directly produced (without subsequent annealing) by MA was the Al-Cu-Mn system. The other methods used to produce quasicrystal alloys are the vapor condensation or vapor evaporation technique, such as vapor deposition, laser abrasion, electron beam evaporation or sputtering, multilayer deposition from each element and subsequent annealing, crystallization from an amorphous phase.

The Ti/Zr-based quasicrystals were firstly produced by rapid-quenching, as mentioned in Section 4.1. It was suggested that they were unstable, but some of the Ti-Zr-Ni as-cast alloys initially containing only the C14 hexagonal Laves and α-solid solution (hexagonal) phases transformed into the i-phase during annealing in vacuum [8], which suggests that they were stable. We produced several kinds of the Ti/Zr-based quasicrystals having various chemical compositions by either rapid-quenching or MA. However, for the Ti/Zr-based quasicrystal powders mentioned in this chapter, annealing in vacuum was necessarily needed after the MA process to transform the amorphous phase into the i-phase, although the i-phase ribbons could be directly produced by rapid-quenching. Depending on the initial chemical compositions, the minor phases, such as the solid

solution phase and the Ti_2Ni-type phase, could mostly form after subsequent annealing.

The transmission electron microscopy (TEM) technique is very helpful to identify the presence of the i-phases because they extend special rotational symmetries, such as tenfold or fivefold directions of the icosahedral symmetry, which are not allowed for normal crystals. The TEM study is comparatively easy for the ribbons produced by rapid-quenching (using the ion thinning technique), although it is somewhat difficult for the fine powder samples after MA. Figure 4.1 shows a bright field image

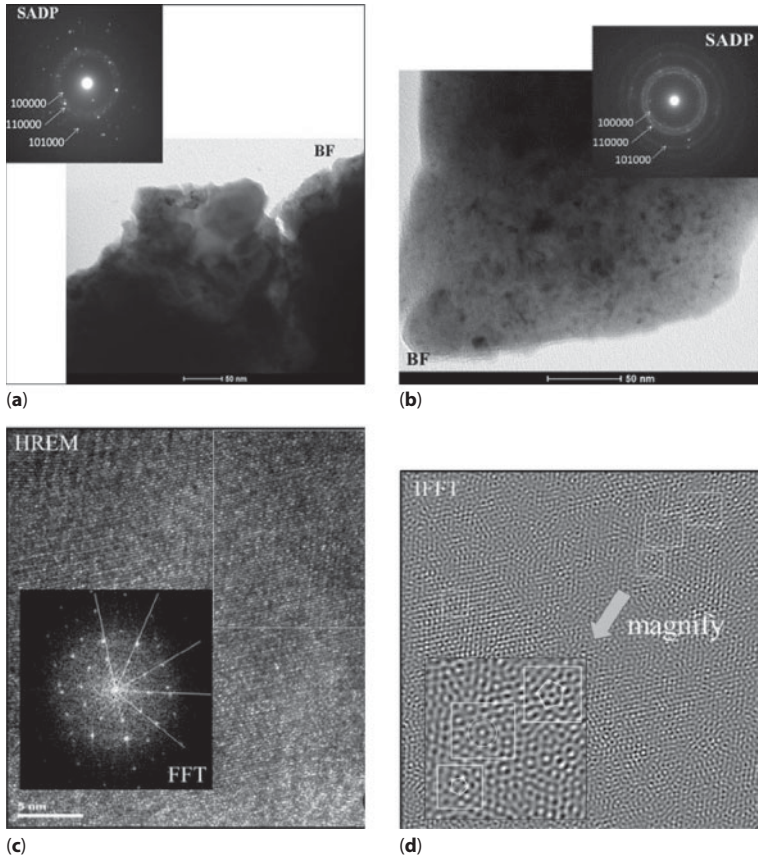

Figure 4.1 The bright field images and the corresponding selected area diffraction patterns for the $Ti_{45}Zr_{38}Ni_{17}$ powders: (a) after MA and subsequent annealing, and (b) after the hydrogen absorption/desorption cycle, and (c) the high- resolution transmission electron microscopic (HREM) image with the corresponding fast Fourier transform (FFT) image; (d) the inverse FFT image derived from the FFT image for the powders after MA and subsequent annealing.

and the corresponding selected area diffraction (SAD) patterns, a high-resolution transmission electron microscopic (HREM) image and the corresponding fast Fourier transform (FFT) image (a digital diffractogram), and an inverse fast Fourier transform (IFFT) image (the simulated atomic arrangement) derived from the FFT image for the $Ti_{45}Zr_{38}Ni_{17}$ i-phase powder synthesized by MA and subsequent annealing. The SAD pattern after dehydrogenation is also included in Figure 4.1. Because the powder on the Cu grid consisted of finer particles, with an average grain size of about 50 nm, the SAD pattern indicates some Debye-Scherrer rings, although three of the rings can be indexed as those for the i-phase. However, it was difficult to obtain direct evidence of the existence of the i-phase. In the HREM image, a relatively disordered region (the upper right-hand region shown in a white square), as well as an ordered one (with a lattice image), can be observed, suggesting the mixtures of phases. The FFT image, derived from the disordered region, indicates a tenfold rotational symmetry. In the IFFT image, some atomic arrangements consist of a five- or tenfold rotational symmetry, which is the evident proof for the existence of the i-phase in the powders after MA and subsequent annealing [10]. After hydrogen desorption, the i-phase still remained stable.

The Ti/Zr-based ribbons were produced by rapid-quenching to investigate the effect of the quenching conditions on the local microstructures. The alloy with a nominal composition of $Ti_{45}Zr_{38}Ni_{17}$ (at%) was firstly prepared by arc melting of a mixture of high purity elements with purities of 99.9% or higher in the Ti-gettered argon atmosphere. To minimize the oxygen contamination, the sample chamber was evacuated to 0.1 Pa and filled with high purity argon gas several times again. To ensure homogeneity, the 30 g ingot was remelted five times. Thin ribbons with 10 mm in width and 30 μm in thickness were prepared by single-roller melt spinning under argon atmosphere at a constant over-pressure of 50 kPa and a linear copper wheel speed of 20–50 m s^{-1}. A cooling rate from 10^5 to 10^6 K s^{-1} can be achieved with this technique, what is fast enough to solidify liquids and to form a non-equilibrium phase.

Figure 4.2 shows the XRD patterns and SEM images of both sides of the ribbon directly obtained from melt spinning. The locations and the heights of the main XRD peaks follow the Bancel scheme for indexing icosahedral peaks [11] and confirm the quasicrystal phase for both sides of the ribbon. The dimensions of the ribbons depend on many parameters, among which the nozzle diameter, ejection gas pressure and the circumferential speed of the copper wheel are the most important. The width and the thickness of the ribbons increase with increasing the ejection gas pressure and nozzle diameter. Increasing the wheel speed results in a decrease of the ribbon

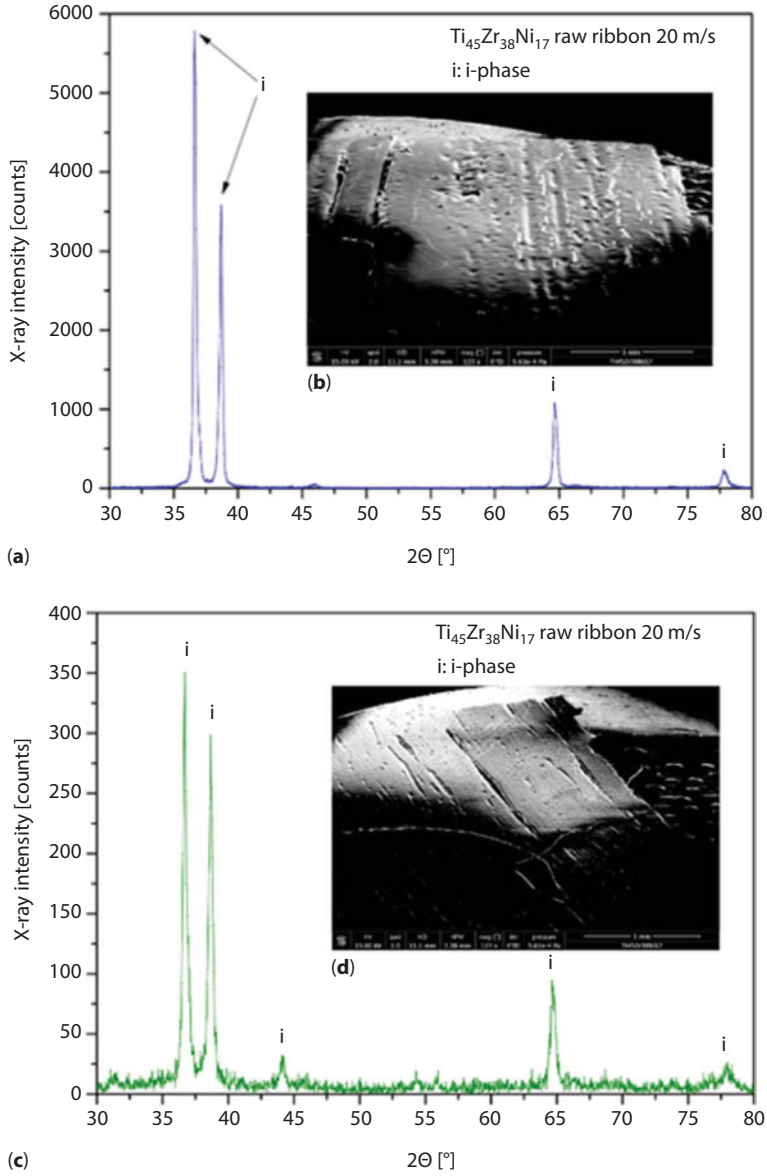

Figure 4.2 Comparison of both sides of the ribbon and the SEM images for the $Ti_{45}Zr_{38}Ni_{17}$ i-phase: (a) X-ray diffraction pattern of the air-side surface; (b) SEM image of the air-side surface; (c) X-ray diffraction pattern of the wheel-side surface; (d) SEM image of the wheel-side surface.

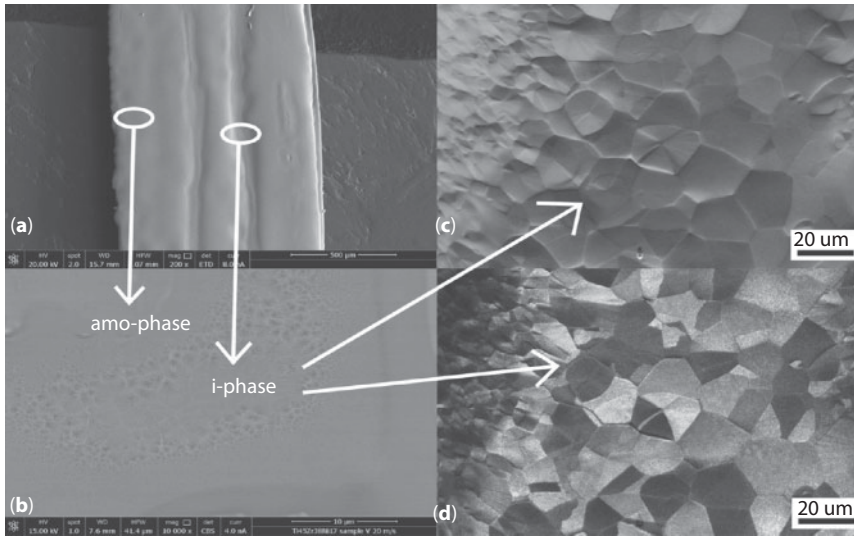

Figure 4.3 The SEM images of (a) the air side of the ribbon (low magnification); (b) the air side of the ribbon (different region of phases: the quasicrystal [the i-phase] and the amorphous [the AMO-phase]); (c) a topography image of the quasicrystalline surface (EBSD – the topography mode); (d) EBSD – the dark field diffraction contrast mode.

width and thickness and in an increase of the cooling rate. The influence on the cooling rate is much more important than the influence on the cross-section dimensions. Namely, the microstructure, the amount of the quasicrystal region and the properties of the ribbons depend on the cooling rate (high speed cooling rate – more amorphous structure). It is the reason why the intensity of the XRD peaks for the quasicrystalline phase of the air-side surface of the ribbon is a few times greater in comparison to the wheel-side surface of the ribbon.

The microstructure of an individual melt-spun ribbon is somewhat variable from the wheel side to the air side. The wheel-side surface of the ribbons is macroscopically smooth, while the air-side surface is rough (Figure 4.3(a)). Even though it is normal that the air-side surface is rougher than the wheel side (solidification ends there because of the slower cooling rate), the roughness of ribbons is more likely connected to the centrifugal force. The ribbon obviously consists of two phases: the quasicrystal grains (the i-phase) in the amorphous (the AMO-phase) matrix (Figure 4.3(b)). The stability of the solid-liquid interface decreases with the reduction of the cooling rate on the air surface, and the structure becomes more quasicrystalline. The grains sizes are large in the central quasicrystal region

and are reduced in the amorphous area direction (Figure 4.3(c) and Figure 4.3(d)).

4.3 Hydrogen Storage in T-Zr-Based Amorphous Alloys

4.3.1 Gaseous Hydrogenation

Although the amorphous alloys of the Ti-Zr-Ni-T (T – transition metal) compositions synthesized by MA are well-established in the literature, the corresponding amorphous hydrides/deuterides have been recently obtained for $Ti_{45}Zr_{38}Ni_{17-x}T_x$, where T = Fe or Co [12, 13]. The main problem with the search for the synthesis route of amorphous hydrides/deuterides is metastability of amorphous alloys. Namely, a number of trials for hydrogenating the amorphous alloys based on the Ti-Zr-Ni-T family can be found in the literature [14–18]. However, in all cases the primary amorphous alloys decomposed when exposed to hydrogen pressure and temperature, forming a number of simple hydrides of different compositions. Particularly, the phases such as TiH_2, ZrH_2 and $(ZrTiT)H_2$ were usually observed [16, 17]. An interesting fact is that the decomposed hydrided amorphous samples exhibited a similar hydrogen capacity to the i-phase hydrides of the corresponding compositions, while reversibility was apparently not possible.

For the above reasons, the search for a procedure that allows maintaining the amorphous nature of the considered alloys is of the utmost importance in the context of materials science and hydrogen storage. Therefore, extensive research has been conducted on the optimization of the hydrogenation/deuterization thermodynamics of the Ti-Zr-Ni-T alloys. As a result, a number of amorphous hydrides of different T substitutions were synthesized [12, 13, 19]. It was established that depending on the composition, the uptake is required of around 0.4–0.5 MPa of H_2 pressure with temperature ranging from 25 °C to 110 °C. Depending on the temperature, the reaction kinetics could be easily tuned from a range of minutes to tenths of hours. This feature is crucial for an investigation of the reaction nature, e.g., by such time-consuming techniques as *in-situ* neutron diffraction. On the other hand, shifting the reaction to a high-kinetic regime has to be performed carefully in order to avoid decomposition of the sample. Table 4.1 presents the achieved hydrogen concentrations for the discussed amorphous alloys. Apparently, the introduction of different substitutions for Ni has led to a decrease in the total hydrogen concentration. The largest

Table 4.1 Comparison of the hydrogen uptakes for the Ti-Zr-Ni-T amorphous alloys.

Alloy	H concentration [wt%]	Uptake kinetics
$Ti_{45}Zr_{38}Ni_{17}$	2.35	normal
$Ti_{45}Zr_{38}Ni_{15}Mn_2$	2.24	fast
$Ti_{45}Zr_{38}Ni_{13}Mn_4$	2.33	fast
$Ti_{45}Zr_{38}Ni_{13}Fe_4$	2.31	slow
$Ti_{45}Zr_{38}Ni_9Fe_8$	2.26	slow
$Ti_{45}Zr_{38}Ni_{13}Co_4$	2.13	normal
$Ti_{45}Zr_{38}Ni_9Co_8$	2.11	normal

decrease was evidenced for the Co substitution, while for the other elements changes were not significant. However, different dopings had a great influence on the reaction kinetics. The kinetics of a typical reaction for 5 g of the $Ti_{45}Zr_{38}Ni_{17}$ powder (referred to as "normal" in Table 4.1) yielded around 120 min when a hydrogen pressure of 0.4 MPa at 50 °C was applied. Introducing Mn speeded up the reaction, while Fe doping slowed it down by a factor of 5.

Reports on amorphous hydrides have rarely been published. Moreover, there is a common belief that as a matter of fact, the amorphous hydrides are just the nanostructural crystalline hydrides. This is related to differences in the affinity for hydrogen exhibited by different elements of the alloy. From this point of view, the introduction of hydrogen into amorphous alloys should lead to the formation of nano-hydrides for some of the elements. Therefore, any claim about obtaining a truly amorphous hydride needs to be supported by a set of complementary data. First of all, a local technique such as TEM must be used to exclude an appearance of nano-hydrides. Secondly, the X-ray diffraction (XRD) technique is not particularly well suited for the investigation of hydrides, as the cross section for X-ray scattering on a hydrogen atom is negligibly small. For this reason, XRD could be considered as an auxiliary method. Indeed, some information can be derived from such experiments but it is related only to the distribution of heavier atoms [12]. Therefore, neutron diffraction is the primary choice for deuterated samples, as deuterium is a good neutron scatterer. Additionally, the *in-situ* experiments under deuterium pressure are relatively easy to conduct.

An example of such complementary research is presented in Figure 4.4. The main diagram presents the formation of the amorphous deuteride ($Ti_{45}Zr_{38}Ni_{13}Fe_4$). As can be seen, the primary broad reflection related to distribution of the Ti-Zr-Ni-Fe distances at around 2.5 Å is visible at the beginning of the deuterization process. However, three subsequent changes in the diffraction patterns can be observed after a deuterium uptake. At first, some additional intensities appear for an interatomic distance of 2–2.7 Å (0–300 min) and much smaller for 1.6 Å. The former intensity is related to the deuterium-deuterium distances of D atoms distributed in the amorphous matrix when the Switendick criterion is obeyed. The latter more focused intensity appears for 1.6 Å due to distribution of the deuterium-metal distances, which can be deduced if the typical radiuses of Ti, Zr, Ni and Fe atoms and the radius of a D atom are taken into account. This feature is very broad and structureless. Therefore, it is a clear sign that nano-hydrides like Ti-H, Zr-H, etc., are not formed. The second step of the reaction occurring between 300 and 600 min is much faster, so the changes in the diffraction patterns are clearly visible. Namely, a significant increase

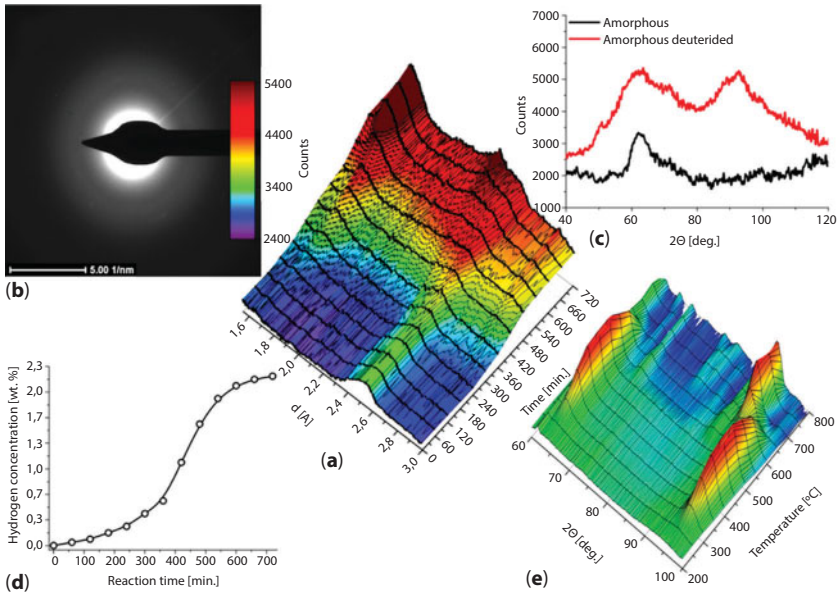

Figure 4.4 (a) *In-situ* synthesis of the amorphous $Ti_{45}Zr_{38}Ni_9Fe_8$ hydrides/deuterides as seen by neutron diffraction performed under 0.4 MPa of D_2 pressure at 20 °C; (b) SAD-TEM image of the synthesized amorphous hydride; (c) neutron diffraction patterns before and after deuteration; (d) hydrogen uptake occurring during collecting of the neutron diffraction patterns; and (e) thermal evolution of the deuterided amorphous alloy.

of the background intensity can be observed (this is related to very strong incoherent scattering on hydrogen, which is the main spurious phase of deuterium with the purity of 99.8%). Apart from that, the further increase of intensities around 1.6 Å and much smaller around 2–2.7 Å is evidenced. This step of the reaction reduces the space available for deuterium atoms, which is tantamount to leaving the solid solution regime. Therefore, deuterium atoms are forced to form short-range clusters with metal atoms. In the last step, there are no significant changes, as the amorphous structure with incorporated deuterium is basically established.

The diffraction patterns for the sample prior to and after deuteration (see Figure 4.4 (c)) are a good indicator of the formation of the fully amorphous deuteride with the broad distribution of the metal-metal, metal-deuterium and deuterium-deuterium distances. The latter shows no features in the diffraction pattern, which can be related to breaking the Switendick rule. The TEM diffraction patterns for the obtained deuteride exhibit no sign of the crystalline phases, confirming the excellent quality of the samples [12].

According to our data presented in refs. [12, 13, 19], the hydrided amorphous alloys showed exceptional properties concerning the structural phase diagram. Particularly, the $Ti_{45}Zr_{38}Ni_{17-x}Mn_xD_{148}$, $Ti_{45}Zr_{38}Ni_{17-x}Fe_xD_{148}$, and $Ti_{45}Zr_{38}Ni_{17-x}Co_xD_{142}$ ($x < 8$) amorphous deuterides underwent structural transition at about 300 °C into the glassy quasicrystalline (partially disordered) phase, as depicted in Figure 4.4. The main characteristic feature of this newly discovered phase is the existence of just two reflections within the entire diffraction pattern, which is quite surprising for such a complex alloy (Figure 4.4 (e)). However, closer inspection of the thermal evolution of the deuterated quasicrystalline phase of $Ti_{45}Zr_{38}Ni_{17}$ led to the conclusion that two reflections are at the same 2Θ angles as the main reflections for the deuterated i-phase. Therefore, the "glassy quasicrystalline state" was suggested.

The uniqueness of the deuterated phases is reflected in the fact that deuterium is fully dispersed and equivalent to the other constituents of the amorphous alloy. During heating, deuterium was not released up to temperature of 500 °C at which the next structural transition occurred. Once again, such behavior was similar to that evidenced for the deuterated i-$Ti_{45}Zr_{38}Ni_{17}$ alloy [12].

The role of deuterium in the thermal evolution of the amorphous Ti-Zr-Ni-T alloys is surprisingly important [12, 13, 19]. Namely, for the raw amorphous alloys the sequence of phase transitions is usually as follows: amorphous (AMO), i-phase (quasicrystalline), w-phase (approximant) and c-phase (cubic) [20]. The Fe-doped alloys were an exception, as they formed the cubic phases directly from the amorphous alloy. On the

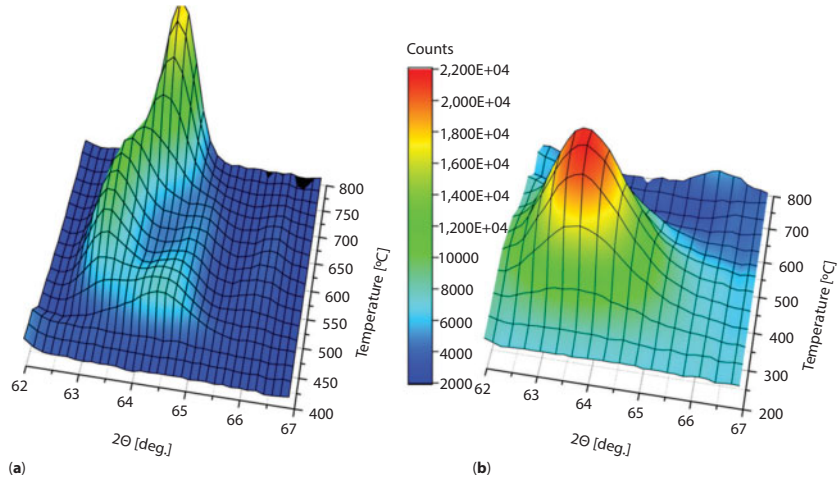

Figure 4.5 Comparison of thermal evolution of the main reflections for the amorphous (a) $Ti_{45}Zr_{38}Ni_{13}Fe_4$ and (b) $Ti_{45}Zr_{38}Ni_{13}Fe_4D_{148}$.

other hand, thermal evolution after deuteration was very similar to that for the other alloys from this family, for which the glassy-quasicrystalline state was formed and then the transformation into the c-phase occurred. An example of such behavior is presented in Figure 4.5. Apparently, the introduction of deuterium promoted an occurrence of the phase transition from the amorphous phase in much lower temperatures than for the raw alloy. The transition for the amorphous $Ti_{45}Zr_{38}Ni_{13}Fe_4$ started at around 450 °C, while for the corresponding deuteride it started at around 225 °C. The latter transformation, which was quasi-continuous, was very similar to the formation of the icosahedral phase for the raw alloys.

It must be emphasized that the release of deuterium from the glassy quasicrystals is associated with the structural phase transition into a mixture of unknown phases, which finally turns into some cubic phase. Therefore, this transition is nonreversible; hence, much attention is paid to establishing the procedure of deuterium/hydrogen desorption without losing the metastable glassy quasicrystalline state.

The behavior of the raw and deuterated/hydrided Ti-Zr-Ni-T alloys discussed above seems to be universal for this family. The phase diagrams summarizing the research on this issue are presented in Figure 4.6. It is evident that the nature of the quasi-continuous transition from the amorphous into the quasicrystalline state for the raw alloys strongly depended on the changes in the stoichiometry [12, 13, 19]. Namely, the partial substitution of Mn or Co for Ni led to a decrease or increase of the threshold temperature for the above-mentioned transition. The Fe doping seemed to be a special case, as it

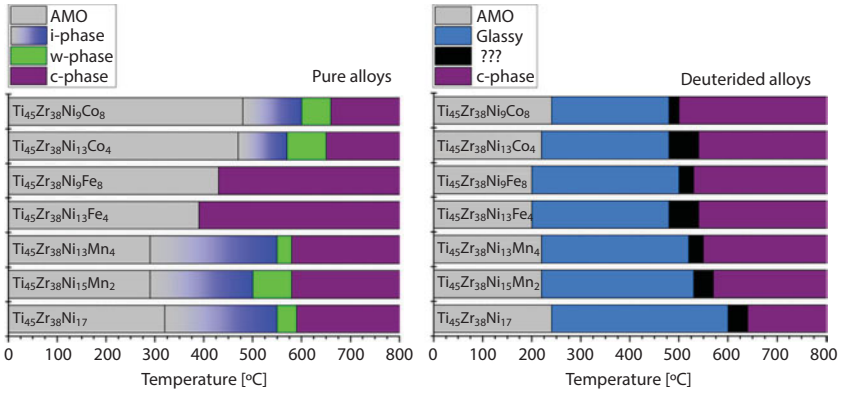

Figure 4.6 The composition-temperature phase diagrams of several $Ti_{45}Zr_{38}Ni_{17-x}T_x$ alloys [19].

prevented from the occurrence of the i-phase. The situation changed drastically when the phase diagram of the corresponding deuterides was analyzed (Figure 4.6). Firstly, the introduction of deuterium lowered the temperature threshold at which the glassy quasicrystalline phase started to form. What is more, the temperature threshold was hardly dependent on the composition; it changed slightly in the temperature range of 225–250 °C. Secondly, the range of stability of the glassy quasicrystalline phase was much broader than for the corresponding i-phase for the raw alloys. Thirdly, the glassy phase was present for all known deuterated amorphous alloys of the Ti-Zr-Ni-T composition, including the Fe doped one. Lastly, the upper limit for an existence of the glassy phase, which is related to the deuterium/hydrogen desorption, seemed to be more even in the case of the corresponding transition for the raw alloys (the i-phase into the w-phase).

4.3.2 Electrochemical Hydrogenation

The electrochemical measurements reported in this chapter were mainly performed in a three-electrode cell, in which the powder mixtures containing 25 wt% active materials (Ti-Zr-Ni) and 75 wt% nickel powder (99.9% pure) were compacted at a pressure of 10 MPa, and used as working electrodes. The counter electrode and reference electrode were $Ni(OH)_2$/NiOOH and Hg/HgO, respectively.

The discharge capacity of the $Ti_{45}Zr_{38}Ni_{17}$ amorphous electrode produced by MA was 5.9 mAh g^{-1} [21]. The discharge capacities increased with the increasing Ni substitution for Zr or Ti, and better discharge performance was obtained for the electrodes by the substitution of Ni for Zr from the

standard composition ($Ti_{45}Zr_{38}Ni_{17}$). The highest discharge capacity recorded was equal to about 60 mAh g^{-1} for the $Ti_{45}Zr_{30}Ni_{25}$ amorphous electrode but the amorphous phase converted to the (Ti, Zr)H_2 fcc hydride after electrochemical hydrogenation [22], indicating no possible reversibility the same as the one after the gaseous hydrogenation mentioned in Section 4.3.1.

The substitution of Ti for Zr while keeping the Ni amount at 25 at% improved the discharge capacity. The discharge capacity achieved for the ($Ti_{49}Zr_{26}Ni_{25}$) electrode was about 130 mAh g^{-1} at the first hydrogen cycle, which decreased gradually to 110 mAh g^{-1} at the 15 charge/discharge cycling, and the amorphous phase partially converted to a (Ti, Zr)H_2 hydride after the cycling [23].

4.4 Hydrogen Storage in the Ti/Zr-Based Quasicrystal Alloys

In this chapter, we focus on the Ti/Zr-based i-phases, while attempts at hydrogenating several other systems by either gaseous or electrochemical hydrogen loading are reported. The system based on Zn-Mg-Y with the nominal composition of $Zn_{60}Mg_{30}Y_{10}$ synthesized by MA was shown to exhibit the i-phase under different preparation conditions. However, the hydrogen capacity registered in the pressure-composition (PC) isotherm test at 300 °C was 0.9 wt% with a plateau at 0.35 MPa. The lower decomposition temperature of 445 °C was recorded for the sample with the occurrence of more hexagonal phase [24, 25]. Another widely studied system was Ti–V–Ni (the i-phase). It was first introduced by Zhang *et al.* in 1985 [26] and further studied in terms of electrochemical hydrogen storage performance. In the case of this system, the occurrence of the i-phase caused an increase of the discharge capacity [27]. Unfortunately, a decrease in the capacity was observed for the Ti- and V-based alloys after a number of cycles, which was explained by a joint effect of pulverization of the particles of the material and the dissolution of Ti and V into the KOH solution [28]. The effective remedy to this problem is the Cu coating proposed by Sun *et al.* [29]. The coating of 10 wt% Cu on the $Ti_{1.4}V_{0.6}Ni$ alloy (the i-phase) improved the capacity retention and the coated sample showed the discharged capacity of 130 mAh g^{-1} even after 100 cycles, exceeding 70 mAh g^{-1} registered for the uncoated one. Alternatively, the composite of Ti-V-Ni with 1 wt% $NaAlH_4$ was shown to deliver the discharged capacity above 220 mAh g^{-1} after 80 cycles [30]. Improvement in the electrochemical capacity of this system was achieved by the addition of ZrH_2. The maximum discharge capacity of 83.2 mAh g^{-1} was recorded for $Ti_{45}Zr_{38}Ni_{17}$

(the i-phase) + 10 wt% ZrH_2 composite material. The ZrH_2 simultaneously enhanced the high-rate dischargeability and the cycling stability. Such improvement can be credited to the relatively weak Zr-H bond strength that causes a fairly easy entry of most of the hydrogen atoms to the i-phase structure during the electrochemical reaction [31].

4.4.1 Gaseous Hydrogenation

The maximum hydrogen capacity measured for the $Ti_{45}Zr_{38}Ni_{17}$ i-phase powders, synthesized by MA and subsequent annealing, reached about 60 at% (2.23 wt%) by gaseous hydrogen loading during high-pressure measurement at 300 °C. Such a level exceeds that for traditional hydrides of $LaNi_5$ and TiFe [32, 33]. The hydrogen absorption and desorption pressure-composition (PC) isotherms measured at temperatures of 250, 300 and 350 °C at hydrogen pressures up to 2 MPa are shown in Figure 4.7. The maximum hydrogen storage capacity (H/M) at 250 °C was about 1.3 and decreased to about 1.05 with increasing hydrogenation temperatures. Hydrogen absorbed during the absorption process still remained in the powders even after the desorption process. All the PC isotherms were steep, and no plateau pressure was observed [10]. Plateaus are not generally observed for the

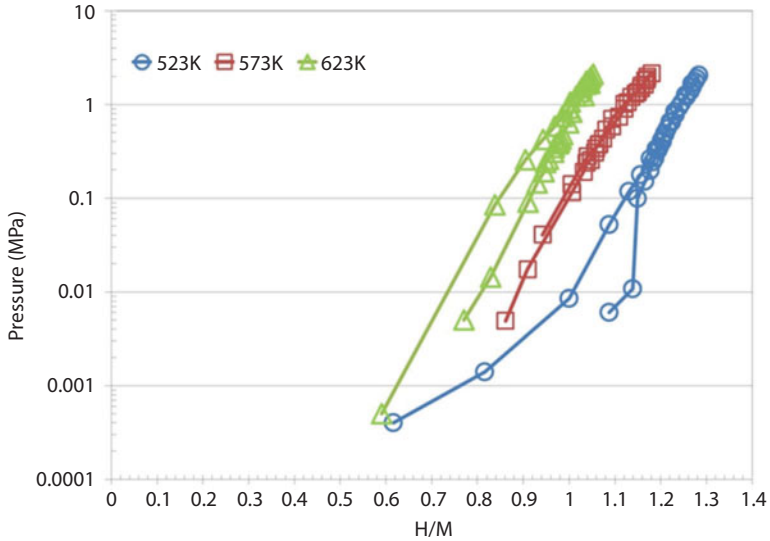

Figure 4.7 The absorption and desorption pressure-composition isotherms for the $Ti_{45}Zr_{38}Ni_{17}$ i-phase powders produced by mechanical alloying and subsequent annealing [10].

amorphous hydrides, while they are clearly present for the corresponding crystalline alloys [34]. Therefore, the hydrogen sorption characteristics of the i-phase are similar to those for the amorphous powder.

The substitution of chemical elements in the Ti/Zr-based i-phase powders may change the hydrogen desorption properties, providing an opportunity to search for an i-phase that has better properties as hydrogen storage materials. An activation energy for hydrogen desorption, which can be estimated from hydrogen desorption spectra measured at several heating rates using the Kissinger equation [35], is one of the important factors for hydrogen storage materials. It has been found that for $Ti_{45+x}Zr_{38-x}Ni_{17}$ the activation energy increased monotonically with increasing Ti concentration in the powders, indicating that the volume of the tetrahedral interstitial sites in the i-phase should decrease with increasing Ti concentration, evidenced by the shrinking quasilattice constant, making it harder to release hydrogen located at the interstitials [36].

The hydrided/deuterated quasicrystals of the $Ti_{45}Zr_{38}Ni_{17-x}Co_x$ (x=0, 4, 8) compositions remain stable under ambient conditions as reported in refs. [13, 37]. Thermal desorption spectroscopy revealed that hydrogen is released mainly above 350 °C [37]. This observation was confirmed by neutron diffraction, which is suitable for tracking deuterium influence on the structure of the material. Namely, the diffraction patterns of the deuterated i-phase of the $Ti_{45}Zr_{38}Ni_{17}$ alloy showed an additional high-intensity reflection when compared to the pure i-phase at around 97 deg. of 2Θ, as depicted in Figure 4.8. Thermal evolution of the diffraction pattern clearly indicated that significant changes started to occur at roughly 400 °C (see the inset in Figure 4.8). However, the final release of deuterium/hydrogen originates from the structural transition from the i-phase into some multiphase alloy with the only recognized Ti_2Ni precipitation [12]. The partial substitution of Co for Ni also produced the Ti_2Ni-type crystal and the C14-like Laves phases after MA and subsequent annealing. The maximum hydrogen storage capacity at 300 °C and at an initial hydrogen pressure of 3.8 MPa was about 59 at% (2.22 wt%) for the $Ti_{45}Zr_{38}Ni_9Co_8$ alloy, but the i-phase transformed into metal hydride(s), which cannot return to the i-phase even after dehydrogenation due to the disproportionation reaction [18].

The surface layer becomes the main barrier for hydrogen absorption in the TiZrNi ribbons. The oxidation layer is observed on the surface of the ribbons. It was suggested to plasma-etch the metallic ribbons for 20 min of 50W at 0.466 Pa Ar before hydrogen absorption to remove the oxygen layer from the surface, which prevents hydrogen diffusion into the sample [38]. After the etching process, a thin layer of Pd was coated for 10 min [39] using an rf-sputtering system to prevent oxidation, enhancing the kinetics

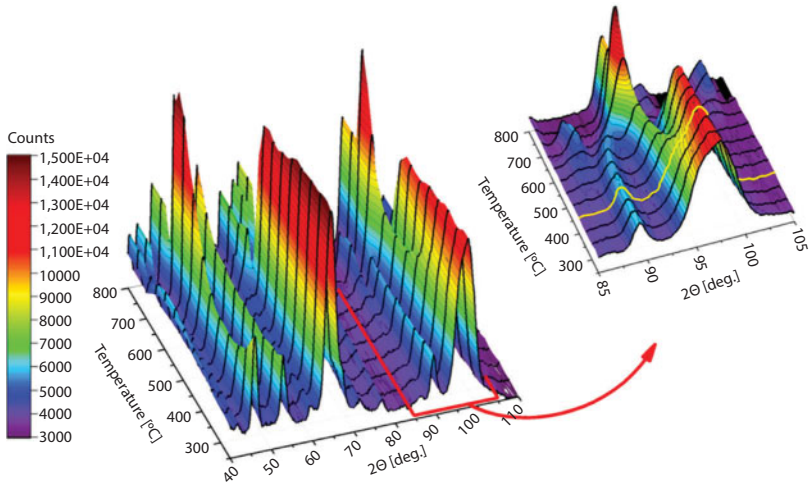

Figure 4.8 Thermal evolution of the deuterated $Ti_{45}Zr_{38}Ni_{17}$ quasicrystal as seen by neutron diffraction.

of hydrogen dissociation when the samples were exposed to air before hydrogen loading [40].

4.4.2 Electrochemical Hydrogenation

The maximum discharge capacity of the $Ti_{45}Zr_{38}Ni_{17}$ i-phase electrode synthesized by MA and subsequent annealing at room temperature (298 K) was 23.9 mAh g^{-1} [21], and about 17 mAh g^{-1} for the one produced directly by rapid-quenching [41] at a current density of 15 mA/g. Both discharge capacities are almost the same and slightly higher than that for the amorphous electrode (5.9 mAh g^{-1}) with the identical chemical compositions mentioned in Section 4.3.2. The theoretical charge capacity of the $Ti_{45}Zr_{38}Ni_{17}$ i-phase electrode estimated from its chemical composition is 795 mAh g^{-1}, if one assumes the maximum H/M of 1.9, indicating that the protons were strongly bound with the neighboring atoms in the quasilattice so that they cannot come out even during the discharge process.

Similar to the amorphous electrodes mentioned in Section 4.3.2, the discharge performance could be improved by the substitution of Ni for Ti or Zr. The maximum discharge capacity achieved was about 100 mAh g^{-1} for the $Ti_{45}Zr_{30}Ni_{25}$ electrode, and the i-phase still remained stable even after several hydrogen cyclings [22].

The discharge performance for the $Ti_{45}Zr_{38-x}Ni_{17+x}$ ($0 \le x \le 8$) ribbons produced by rapid-quenching was also investigated to compare with those

synthesized by MA and subsequent annealing. Although the coherence length of the i-phase depended on the amount of substitution of Ni for Zr, all the ribbons were the i-phase with a negligible amount of the C14 Laves phase (hcp). The i-phase was stable without forming any metal hydride against charging/discharging cycle until the 15th cycle. The maximum discharge capacity achieved was about 90 mAh g^{-1} for the ($Ti_{45}Zr_{30}Ni_{25}$) i-phase electrode [41]. The substitution of Ti for Zr (or Zr for Ti) from the ($Ti_{45}Zr_{30}Ni_{25}$) was also attempted to optimize the chemical composition to obtain the best discharge capacity. The discharge capacity decreased with an increasing amount of Zr substituted for Ti, and the maximum discharge capacity achieved was 130 mAh g^{-1} for the ($Ti_{49}Zr_{26}Ni_{25}$) electrode at the first discharge process [42].

The substitution of Pd for Ni improved the first discharge capacity to about 220 mAh g^{-1} (the $Ti_{49}Zr_{26}Ni_{22}Pd_3$ electrode produced by MA and subsequent annealing) but dropped to about 130 mAh g^{-1} from the second cycle. The main phase was the i-phase with the Ti_2Ni-type fcc crystal, C14 Laves and α-Ti/Zr phases [23]. Table 4.2 summarizes the hydrogen concentrations achieved by both electrochemical and gaseous hydrogen loading for the i-phase powders synthesized by MA and subsequent annealing. Some of the literature data for the i-phases with related compositions are also included in Table 4.2 for comparison.

Electrochemical impedance spectroscopy (EIS) is a commonly used method of characterization for various electrochemical systems. Usually, a relatively small voltage amplitude is applied, and the current response of the system is recorded in a wide range of frequencies (e.g., from mHz to MHz). Typically, Nyquist or Bode plots are used to visualize the recorded data [44, 45]. If an equivalent circuit is properly constructed, refined values

Table 4.2 Hydrogen concentrations achieved for the i-phase.

Alloy	**Hydrogenation method**	**H concentration [wt%]**
$\mathbf{Ti_{41}Zr_{42}Ni_{17}}$*	Electrochemical	2.52
$\mathbf{Ti_{45}Zr_{38}Ni_{17}}$*	Gaseous	2.23
$\mathbf{Ti_{49}Zr_{34}Ni_{17}}$*	Electrochemical	2.63
$\mathbf{Ti_{53}Zr_{30}Ni_{17}}$*	Electrochemical	2.66
$\mathbf{Ti_{61}Zr_{22}Ni_{17}}$*	Electrochemical	2.80
$\mathbf{Ti_{39}Zr_{38}Ni_{17}Pd_6}$**	Gaseous	2.18

*Data from [36]. **Data from [43], for Deuterium.

of resistances, capacitances, inductances, etc., may be interpreted as corresponding to the intrinsic properties of components of the electrochemical system and/or occurring in the system electrochemical processes. Commonly, in the case of an electrochemical cell consisting of two electrodes and an electrolyte, the equivalent circuit consists of ohmic resistance R_O connected in a series with two (or more) parallelly connected resistances *R* and so-called constant phase elements *CPE* [45]. Such connected *R*s and *CPE*s are visible in the form of semicircles in the Nyquist plots, and depending on the frequency range at which they are observed, corresponding high (HF), middle (MF) or low frequency (LF) indexes are used to distinguish the elements. While there is no general method to unambiguously ascribe the nature of each of the refined elements, for the electrochemical cell the ohmic resistance R_O is thought to mainly arise from an ionic resistance of the electrolyte, R_{HF} corresponds to the film resistance of the solid electrolyte interphase (SEI), while resistances visible at lower frequencies stand for the charge transfer and diffusion processes, respectively. It should also be mentioned that both anode and cathode contribute to all the discussed elements. However, it is sometimes possible to establish which electrode has a dominant influence in a particular frequency range.

In the following section, results of the EIS measurements are discussed, which were performed for five kinds of the i-phase electrodes comprised of $Ti_{45}Zr_{38}Ni_{17}$, $Ti_{45}Zr_{30}Ni_{25}$, $Ti_{37}Zr_{38}Ni_{25}$, $Ti_{49}Zr_{26}Ni_{25}$ and $Ti_{49}Zr_{26}Ni_{22}Pd_3$. Since electrochemical hydrogenation involves the introduction of hydrogen into the bulk of the material, the EIS spectra were measured for different values (10, 50 and 100%) of the depth of discharge (DOD) at room temperature in a frequency range of 1 Hz–300 kHz. For the measurements, the respective powder mixtures containing 25 wt% of the active material and 75 wt% of Ni powder (99.9% purity) were mixed and compacted at a pressure of 10 MPa in order to form the working electrodes. The studies were conducted in three-electrode configuration, with the counter and reference electrodes being $Ni(OH)_2$/NiOOH and Hg/HgO, respectively. The cell's electrolyte was a 6 M aqueous solution of KOH. The first charging step (hydrogenation of the i-phase) was carried out for 14 h, while subsequent charging steps lasted for 2 h. The current density was maintained at 70 mA g^{-1} for all hydrogenation steps. For discharging (dehydrogenation) steps, a cutoff potential was set at −0.6 V versus the Hg/HgO reference electrode. During discharge, the current density was set at a 15 mA g^{-1}. After the charge/discharge processes, the electrode was relaxed for 10 min. The details of the electrochemical measurement and the preparation of the powder samples have already been published and can be found elsewhere [21–23].

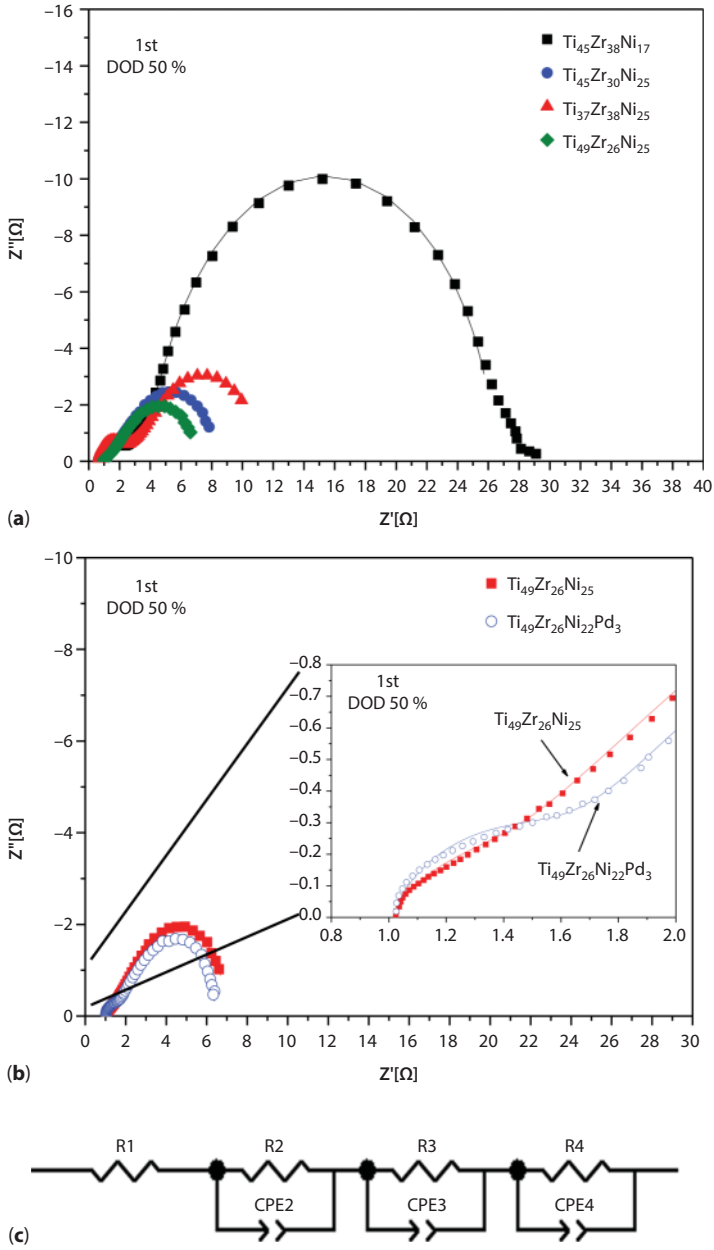

Figure 4.9 The Nyquist plot for the i-phase electrodes at 50% DOD at the 1st discharge cycle: (a) after substitution of Ni for Ti or Ni, (b) after substitution of Pd for Ni, and (c) the equivalent circuit used for fitting of the data.

Figure 4.9 (a) and (b) show the EIS results (the Nyquist plots) for different i-phase electrodes at 50% DOD at the 1st discharge cycle. The impedance spectra can be initially interpreted as consisting of two semicircles, but a closer look and performed refinements indicated the presence of an additional *R-CPE* component. This corresponds to the equivalent circuit as shown in Figure 4.9(c). Such a circuit was also proposed previously by Kuriyama *et al.* [46] for a metal hydride electrode. Since the lowest frequencies were not measured, the Warburg resistance element (related to the diffusion processes) was not included. As described above, R_O can be mainly related to the electrolyte resistance between the working and reference electrodes. For the particular system, R_{HF} and CPE_{HF} mainly consist of the contact resistance and the contact capacitance between the current collector and alloy pellet, while R_{MF} and CPE_{MF} are related to particle-to-particle (grain boundary), respectively. Of most interest to the characterization of the active material in the electrode are R_{LF} and CPE_{LF}, which correspond to the charge transfer resistance for the metal hydride electrode and the double-layer capacitance, respectively. As can be seen, the semicircle at the low frequencies is the largest for the standard i-phase composition $Ti_{45}Zr_{38}Ni_{17}$. For the materials with the higher Ni content ($Ti_{45}Zr_{30}Ni_{25}$, $Ti_{37}Zr_{38}Ni_{25}$, $Ti_{49}Zr_{26}Ni_{25}$) the charge transfer is greatly reduced. Some further reduction is also visible when Ni in $Ti_{49}Zr_{26}Ni_{25}$ is replaced partially by Pd, forming the $Ti_{49}Zr_{26}Ni_{22}Pd_3$ i-phase.

Figure 4.10 (a) and (b) show the refined charge-transfer resistances for the i-phase electrodes as a function of the DOD degree at the 1st and 3rd cycle, respectively. The charge-transfer resistances for the $Ti_{45}Zr_{38}Ni_{17}$ (standard composition) electrode are higher than those for any other electrodes at any DOD, indicating that the discussed substitution indeed reduced the charge-transfer resistance, which also resulted in the increased maximum discharge capacity (Figure 4.11).

The results are in agreement with the literature data in which, for example, Liu *et al.* [47, 48] reported for the i-phase alloys which were produced by either MA or melt-spinning methods that both the substitution of Ni for Ti and Zr in Ti-Zr-Ni-Cu and the partial substitution of Pd for Ni in Ti-Zr-Ni-Pd reduced the charge-transfer resistance and consequently improved the electrochemical activity. Also, Liu *et al.* [49] mentioned that an addition of Ce in the Ti-V-Ni i-phase alloys reduced the charge-transfer resistance and improved the electrochemical reversibility of the electrode. The charge-transfer resistance for $Ti_{45}Zr_{38}Ni_{17}$ decreased with an increasing degree of DOD, probably because of reduction of the oxide layer produced after MA and subsequent annealing during the discharging process.

The grain boundary resistance data as a function of DOD are shown in Figure 4.12. Contrary to the charge-transfer, all values of resistances

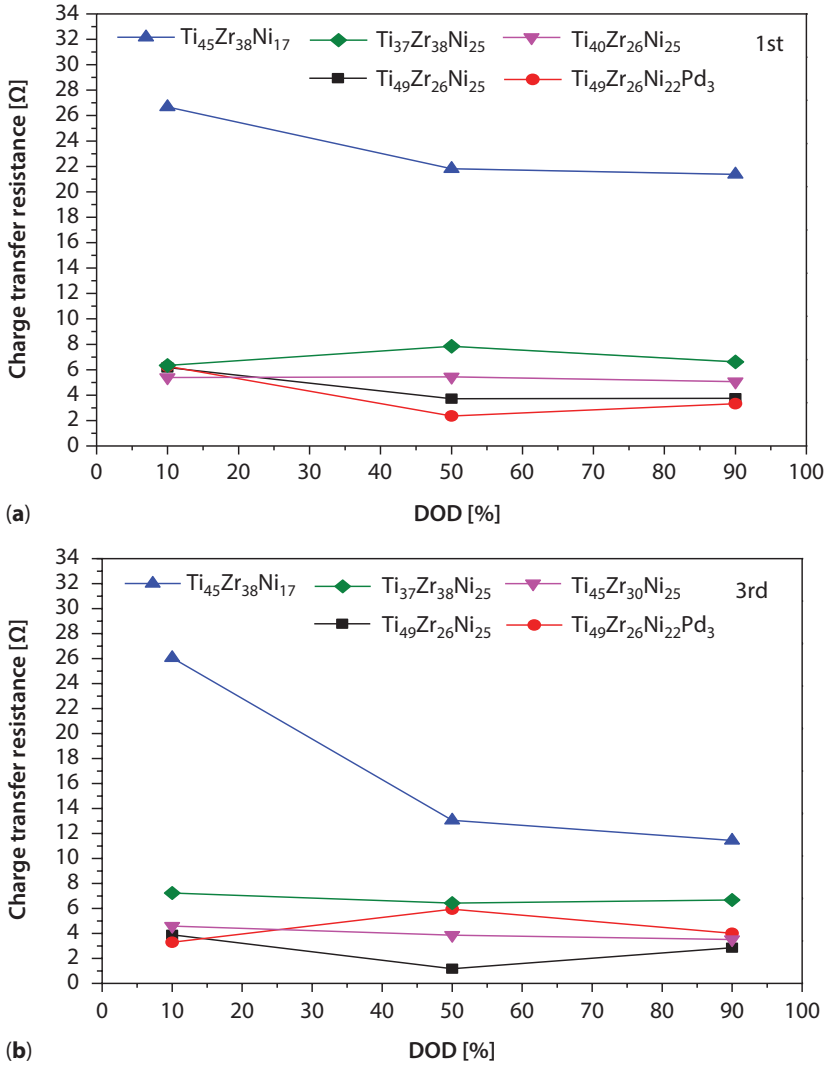

Figure 4.10 The charge transfer resistances for the i-phase electrodes as a function of DOD during the (a) 1st and (b) 3rd cycle.

recorded for the grain boundaries are similar. Nevertheless, the $Ti_{45}Zr_{38}Ni_{17}$ electrode again shows the highest ones at any DOD. Since the grain boundary resistance is influenced mainly by the grain size and the method of preparation of the electrode (in this case pressing of the pellet with Ni),

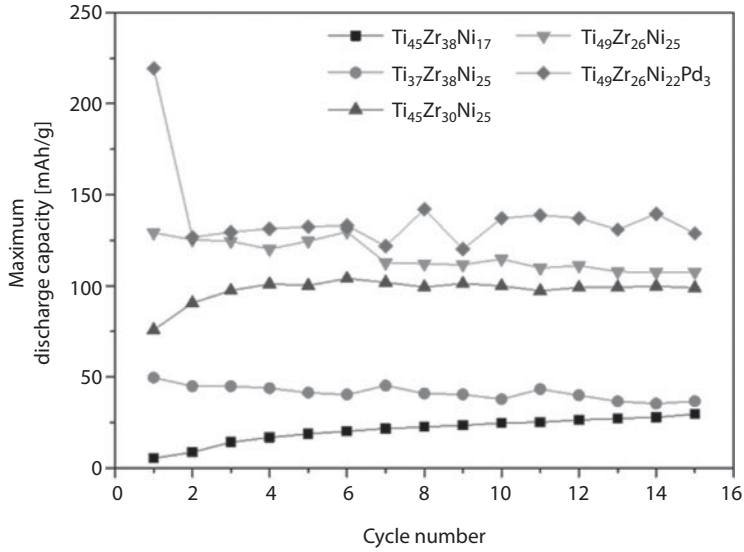

Figure 4.11 The maximum discharge capacity as a function of a cycle number for the i-phase electrodes.

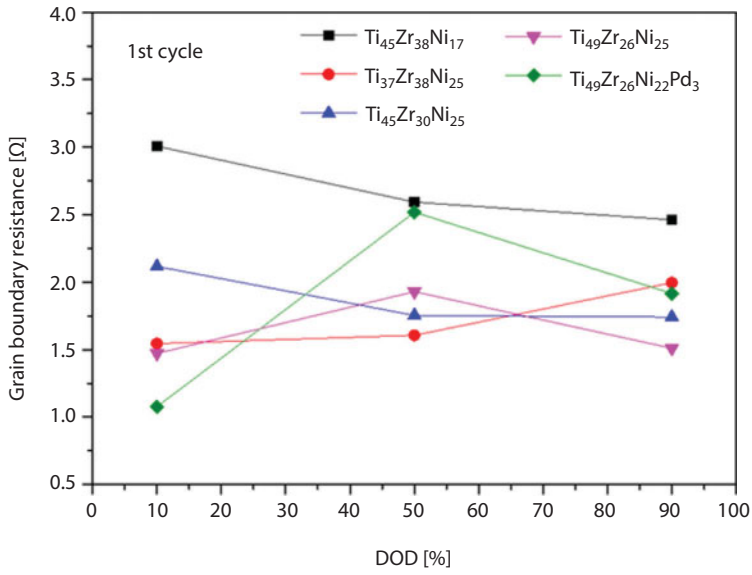

Figure 4.12 The grain boundary resistances for the i-phase electrodes as a function of DOD (1st cycle).

similar low values recorded for all samples indicate comparable microstructural features and a lack of resistive oxide phase at the grain boundaries. This may also be used as an indication of properly conducted MA and heat treatment processes.

4.5 Comparison of Amorphous and Quasicrystal Phases on the Hydrogen Properties

Although the Ti-Zr-Ni i-phases, which contained the Ti_2Ni-type phase as a minor phase, was mostly stable after the first gaseous hydrogenation, the amorphous phase generally converted to metallic (amorphous) hydrides after the high-pressure hydrogenation mentioned in Section 4.3.1. However, hydrogen cycling decreased the coherence length of the i-phase and finally enhanced the formation of the fcc hydride phase ($[Ti, Zr]H_2$), due to either the decreasing order of the i-phase or the decomposition of the Ti_2Ni-type phase [14].

The distributions of the site energies for hydrogen in the i-phase and the amorphous powders were estimated from the fit to the PC isotherms preliminarily measured at 150 °C, as shown in Figure 4.13. Although some hydrogen atoms in the i-phase are more strongly bound (probably by Ti and Zr atoms) than those in the amorphous phase (the site energy of the prominent peak for the i-phase [0.18 eV] is slightly lower than that for the amorphous phase), the distribution of the site energies of hydrogen for the i-phase is wider than that for the amorphous phase, indicating that some other hydrogen atoms in the i-phase are more weakly bound than those in the amorphous phase [50]. However, the distribution seems to be almost similar for the i-phase and the amorphous one, indicating the similarity in their local atomic environments. The building block of the Ti-Zr-Ni i-phase is believed to belong to the Bergman two-shell atomic cluster, which contains 20 tetrahedral interstitials within its inner shell, 120 between its inner shell and outer shells, and no octahedral interstitials [51]. The amorphous phases exhibit no long-range ordering but short-range ordering is present. They are also believed to possess many tetrahedral or octahedral interstitials [52, 53].

As mentioned in Section 4.3.2 and 4.4.2, the maximum discharge capacities of the amorphous electrodes were relatively lower than those of the i-phase ones with identical chemical compositions. Furthermore, the i-phase seemed to be stable even after several charge/discharge cycles, but the amorphous converted to metallic hydrides, suggesting no reversibility.

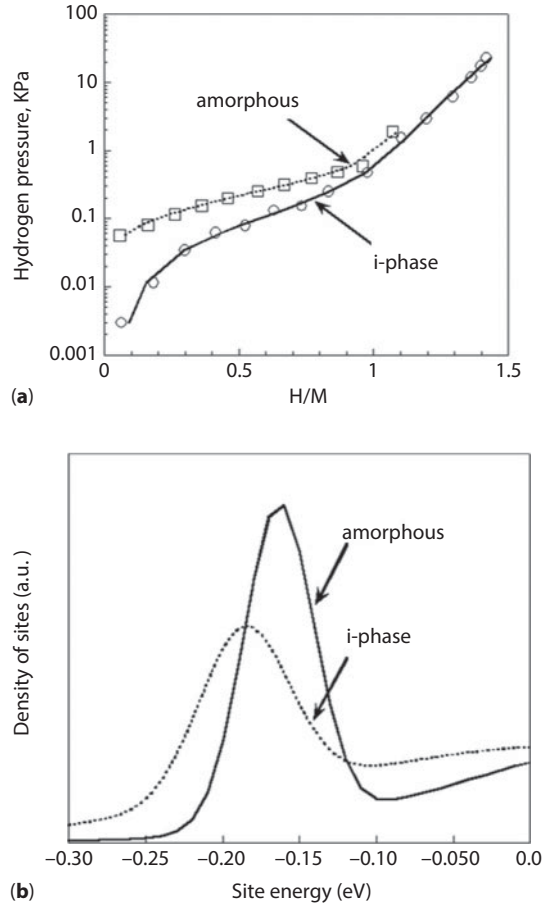

Figure 4.13 (a) The absorption pressure-composition isotherms measured at low hydrogen pressures, and (b) the estimated density of sites for the $Ti_{45}Zr_{38}Ni_{17}$ amorphous and i-phase powers produced by MA and subsequent annealing respectively [50].

4.6 Conclusions

A variety of the Ti-Zr-Ni amorphous phases and the i-phases can be synthesized by MA and subsequent annealing respectively. In this chapter, we first summarized the microstructural evolution of the T-Zr-Ni powders obtained after both MA and subsequent annealing and rapid-quenching, and secondly mainly reviewed our recent research progress on hydrogenation of Ti-Zr-Ni amorphous phases and i-phases by either gaseous or electrochemical hydrogen loading. Although some substitutions of chemical

elements improved both the hydrogen and discharge capacities, the partial substitution of transition metals for Ni decreased these capacities. The hydrogenation of the Ti-Zr-Ni amorphous related phases, in which Ni was partially substituted with transition metals, converted to the fully amorphous hydrides with extraordinary thermal evolution into the glassy (partially disordered) quasicrystalline phases, whose behavior seemed to be universal for the amorphous compositions, allowing formation of the i-phases. For the Fe-doped Ti-Zr-Ni alloys, where no possibility of i-phase forming was evidenced, the introduction of deuterium promoted the formation of the glassy quasicrystals in a similar manner to the other investigated compositions (see Figure 4.6). Moreover, the temperature evolution of the deuterated alloys is very uniform concerning transition temperatures and the sequences of the observed phases. The above findings conclude that the introduction of deuterium/hydrogen into the amorphous alloys has more influence on the structural properties than actual Ni substitution by other 3d metals. On the other hand, the i-phases were comparatively stable even after several hydrogenation cycles. The high-pressure PC isotherms for the $Ti_{45}Zr_{38}Ni_{17}$ i-phase were indicated, and the local atomic environments, such as conditions of interstitials in the structures, simulated from the fits of the low-pressure PC isotherms, were suggested to be similar for the amorphous phase and the i-phase.

References

1. Züttel, A., Materials for hydrogen storage. *Mater. Today* 6(9), 24–33, 2003.
2. Ahluwalia, R.K., Peng, J.K., Dynamics of cryogenic hydrogen storage in insulated pressure vessels for automotive applications. *Int. J. Hydrogen Energy* 33, 4622–4633, 2008.
3. Safizadeh, F., Ghali, E., Houlachi, G., Electrocatalysis developments for hydrogen evolution reaction in alkaline solutions – A review. *Int. J. Hydrogen Energy* 40, 256–274, 2015.
4. Klimkowicz, A., Takasaki, A., Gondek, Ł., Figiel, H., Świerczek, K., Hydrogen desorption properties of magnesium hydride catalyzed multiply with carbon and silicon. *J. Alloys Compd.* 645(1), S80-S83, 2015.
5. Dubois, J.-M., *Useful Quasicrystals*, pp. 424–431, World Scientific, 2005.
6. Shechtman, D., Blech, I., Gratias, D., Cahn, J.W., Metallic phase with long-range orientational order and no translational symmetry. *Phys. Rev. Lett.* 53, 1951–1953, 1984.
7. Sibirtsev, S.A., Chebotnikov, V.N., Molokanov, V.V., Kovneristyl, Yu.K. Quasicrystals in the Ti-Zr-Ni system. *JETP Lett.* 47, 744–755, 1988.
8. Kelton, K.F., Kim, W.J., Stroud, R.M., A stable Ti-based quasicrystal. *Appl. Phys. Lett.* 70, 3230–3232, 1997.

9. Tsai, A.P., Metallurgy of quasicrystals, in: *Physical Properties of Quasicrystals*, Stadnik, Z.M. (Ed.), pp. 5–10, Springer Series in Solid-State Science, vol. 126, Springer: Berlin, Heidelberg, 1999.
10. Tominaga, T., Takasaki, A., Shibato, T., Świerczek, K., HREM observation and high-pressure composition isotherm measurement of $Ti_{45}Zr_{38}Ni_{17}$ quasicrystal powders synthesized by mechanical alloying. *J. Alloys Compd.* 645, S292-S294, 2015.
11. Bancel, P.A., Heiney, P.A., Stephens, P.W., Goldman, A.I., Horn, P.M., Structure of rapidly quenched Al-Mn. *Phys. Rev. Lett.* 54, 2422–2425, 1985.
12. Rusinek, D., Czub, J., Niewolski, J., Gondek, Ł., Gajewska, M., Takasaki, A., Hoser, A., Żywczak, A., Structural phase transitions in the $Ti_{45}Zr_{38}Ni_{17-x}Fex$ nano-alloys and their deuterides. *J. Alloys Compd.* 646, 90–95, 2015.
13. Żywczak, A., Rusinek, D., Czub, J., Sikora, M., Stępień, J., Gondek, Ł., Takasaki, A., Hoser, A., Amorphous hydrides of the $Ti_{45}Zr_{38}Ni_{17-x}Co_x$ nano-powders. *Int. J. Hydrogen Energy* 40, 15534–15539, 2015.
14. Takasaki, A., Kelton, K.F., High-pressure hydrogen loading in $Ti_{45}Zr_{38}Ni_{17}$ amorphous and quasicrystal powders synthesized by mechanical alloying. *J. Alloys Compd.* 347, 295–300, 2002.
15. Zhernovenkova, Yu.V., Andreev, L.A., Kaloshkin, S.D., Sviridova, T.A., Tcherdyntsev, V.V., Tomilin, I.A., Hydrogen absorption in amorphous and quasicrystalline $Ti_{45}Ni_{17}Zr_{38}$ powders synthesized by mechanical alloying. *J. Alloys Compd.* 434–435, 747–750, 2007.
16. Żywczak, A., Shinya, D., Gondek, Ł., Takasaki, A., Figiel, H., Hydriding of $Ti_{45}Zr_{38}Ni_{17-x}Fe_x$ nanocompounds. *Sol. State Commun.* 150, 1–4, 2010.
17. Żywczak, A., Gondek, Ł., Figiel, H., Żukrowski, J., Czub, J., Takasaki, A., Structural and hyperfine properties of $Ti_{48}Zr_7Fe_{18}$ nano-compounds and its hydrides. *J. Alloys Compd.* 509, 3952–3957, 2011.
18. Takasaki, A., Żywczak, A., Gondek, Ł., Figiel, H., Hydrogen storage characteristics of $Ti_{45}Zr_{38}Ni_{17-x}Co_x$ (x = 4, 8) alloy and quasicrystal powders produced by mechanical alloying. *J. Alloys Compd.* 580, S216–S218, 2013.
19. Rusinek, D., Physical properties of Ti-Zr-X (X=Mn, Co, Ni, Cu) alloys, PhD Thesis, AGH Kraków, 2015.
20. Kim, W.J., Gibbons, P.C., Kelton, K.F., A new 1/1 crystal approximant to the stable Ti-Zr-Ni icosahedral quasicrystal. *Phil. Mag. Lett.* 76, 199–206, 1997.
21. Takasaki, A., Zając, W., Okuyama, T., Szmyd, J., Electrochemical Hydrogenation of $Ti_{45}Zr_{38}Ni_{17}$ Quasi Crystal and Amorphous Powders Produced by Mechanical Alloying. *J. Electrochem. Soc.* 156 (2009) A521–A526, 2009.
22. Takasaki, A., Okuyama, T., Szmyd, J., Synthesis of Ti-Zr-Ni amorphous and quasicrystal powders by mechanical alloying, and their electrochemical properties. *J. Mater. Res.* 25, 1575–1582, 2010.
23. Ariga, Y., Takasaki, A., Kimijima, T., Swierczek, K., Electrochemical properties of $Ti_{49}Zr_{26}Ni_{25-x}Pd_x$ (x = 0–6) quasicrystal electrodes produced by mechanical alloying *J. Alloys Compd.* 645, S152–S154, 2015.
24. Tsai, A.P., Murakami, Y., Niikura, A., The Zn-Mg-Y phase diagram involving quasicrystals. *Philos. Mag. A* 80, 1043–1054, 2000.

25. Luo, X., Grant, D.M., Walker, G.S., Hydrogen storage properties for Mg–Zn–Y quasicrystal and ternary alloys. *J. Alloys Compd.* 645, S23–S26, 2015.
26. Zhang, Z., Ye, H.Q., Kuo, K.H., A new icosahedral phase with m35 symmetry. *Philos. Mag. A* 52, L49–L52, 1985.
27. Hu, W., Yi, J.H., Zheng, B.J., Wang, L.M., Icosahedral quasicrystalline $(Ti_{1.6}V_{0.4}Ni)_{100-x}Sc_x$ alloys: Synthesis, structure and their application in Ni-MH batteries. *J. Solid State Chem.* 202, 1–5, 2013.
28. Miao, H., Gao, M., Liu, Y.F., Zhu, D., Pan, H.G., An improvement on cycling stability of Ti–V–Fe-based hydrogen storage alloys with Co substitution for Ni. *J. Power Sources* 184, 627–632, 2008.
29. Sun, L., Lin, J., Cao, Z., Liang, F., Wang, L., Electrochemical hydrogen storage properties of $Ti_{1.4}V_{0.6}Ni$ alloy comprising quasicrystal coating with Cu. *J. Alloys Compd.* 650, 15–21, 2015.
30. Liang, F., Lin, J., Wu, Y., Wang, L., Enhanced electrochemical hydrogen storage performance of TiVNi composite employing $NaAlH_4$. *Int. J. Hydrogen Energy* 42, 14633–14640, 2017.
31. Zhao, J., Zhai, X., Tao, X., Li, Z., Wang, Q., Liu, W., Wang, L., Improved electrochemical hydrogen storage capacity of $Ti_{45}Zr_{38}Ni_{17}$ quasicrystal by addition of ZrH2. *J. Mater. Sci. Technol.* pp. 995–998, 2017.
32. Takasaki, A., Han, C.H., Furuya, Y., Kelton, K.F., Synthesis of amorphous and quasicrystal phases by mechanical alloying of Ti 45 Zr 38 Ni 17 powder mixtures, and their hydrogenation. *Phil. Mag. Lett.* 82, 353–361, 2002.
33. Takasaki, A., Kelton, K.F., Hydrogen storage in Ti-based quasicrystal powders produced by mechanical alloying. *Int. J. Hydrogen Energy* 31, 183–190, 2006.
34. Bowman Jr., R.C., Hydrogen storage materials. *Mater. Sci. Forum* 31, 197–227, 1988.
35. Kissinger, H.E., Reaction kinetics in differential thermal analysis. *Anal. Chem.* 29, 1702–1706, 1957.
36. Takasaki, A., Kelton, K.F., Hydrogen storage in Ti-Zr/Hf-Ni quasicrystal and related crystal powders synthesized by mechanical alloying, in: *Quasicrystal, Type System, and Techniques*, Puckermann, B.E. (Ed.), pp. 127–146, Nova Science, 2011.
37. Żywczak, A., Rusinek, D., Czub, J., Sikora, M., Stępień, J., Gondek, Ł., Gajewska, M., Takasaki, A., Hoser, A., Icosahedral hydrides of the $Ti_{45}Zr_{38}Ni_{17-x}Co_x$ nano-powders. *J. Alloys Compd.* 656, 702–706, 2016.
38. Choi, S., Lee, S., Kim, J., Pressure–composition–temperature curves and structure stability induced by hydrogen in TiZrNi quasicrystals. *Philos. Mag.* 91, 2937–2943, 2011.
39. Kim, J.Y., Gibbons, P.C., Kelton, K.F., Hydrogenation of Pd-coated samples of the Ti–Zr-based icosahedral phase and related crystalline phases. *J. Alloys Compd.* 266, 311–317, 1998.
40. Huang, H.G., Dong, P., Yin, C., Zhang, P.C., Bai, B., Dong, C., Characterization and hydrogen absorption at low temperature of suction-cast $Ti_{45}Zr_{38}Ni_{17}$ quasicrystalline alloy. *Int. J. Hydrogen Energy* 33, 722–727, 2008.

41. Takasaki, A., Kuroda, C., Lee, S.-H., Kim, J.-Y., Electrochemical properties of $Ti_{45}Zr_{38-x}Ni_{17+x}$ ($0 \le x \le 8$) quasicrystals produced by rapid-quenching. *J. Alloys Compd.* 509S, S782–S785, 2011.
42. Ariga, Y., Takasaki, A., Kuroda, C., Kulka, A., Electrochemical properties of $Ti_{45-x}Zr_{30+x}Ni_{25}$ (x = −4, 0, 4) quasicrystal and amorphous electrodes produced by mechanical alloying. *J. Alloys Compd.* 580, S251–254, 2013, 2013.
43. Huogen, H., Liang, C., Xiaoqing, D., Rong, L., Deuterium storage of $Ti_{39}Zr_{38}Ni_{17}Pd_6$ icosahedral quasi-crystal. *Rare Metal Mat. Eng.* 44(7), 1581–1586, 2015.
44. Lvovich, V. *Electrochemical Impedance Spectroscopy - Theory and Applications*, John Wiley & Sons, New York, 2012.
45. Barsoukov, E., Macdonald, J.R. (Eds.), *Impedance Spectroscopy Theory, Experiment, and Applications*, John Wiley & Sons, Inc.: Hoboken, New Jersey, 2005.
46. Kuriyama, N., Sakai, T., Miyamura, H., Uehara, I., Ishikawa, H., Iwasaki, T., Electrochemical impedance and deterioration behavior of metal hydride electrodes. *J. Alloys Compd.* 202, 183–197, 1993.
47. Liu, B., Wu, Y., Wang, L., Crystallographic and electrochemical characteristics of icosahedral quasicrysyalline $Ti_{45-x}Zr_{35-x}Ni_{17+2x}Cu_3$ (x = 0–8) powders. *J. Power Sources* 162, 713–718, 2006.
48. Liu, B., Zhang, Y., Mi, G., Zhang, Z., Wang, L., Crystallographic and electrochemical characteristics of Ti–Zr–Ni–Pd quasicrystalline alloys. *Int. J. Hydrogen Energy* 34, 6925–6929, 2009.
49. Liu, W., Duan, Q., Liang, F., Lin, J., Jiang, D., Effect of Ce on electrochemical properties of the TiVNi quasicrystal material as an anode for Ni/MH batteries. *Int. J. Hydrogen Energy* 38, 14810–14815, 2013.
50. Takasaki, A., Huett, V.T., Kelton, K.F., Hydrogenation of Ti–Zr–Ni quasicrystals synthesized by mechanical alloying. *J. Non Cryst. Solids* 334–335, 457–460, 2004.
51. Gibbons, P.C., Kelton, K.F., Toward industrial applications, in: *Physical Properties of Quasicrystals*, Stadnik, Z.M. (Ed.), pp. 403–431, Solid-State Sciences Series vol. 126, Springer, 1999.
52. Bernal, J., A geometrical approach to the structure of liquids. *Nature* 183, 141–147, 1959.
53. Finney, J.L., Wallance, J., Interstice correlation functions; a new, sensitive characterisation of non-crystalline packed structures. *J. Non Cryst. Solids* 43, 165–187, 1981.

5

Electrochemical Method of Hydrogenation/Dehydrogenation of Metal Hydrides

N.E. Galushkin*, N.N. Yazvinskaya and D.N. Galushkin

Laboratory of electrochemical and hydrogen energy, Don State Technical University, Town of Shakhty, Russia

Abstract

In this chapter, it is experimentally proved that during a Ni-Cd batteries long service life (more than five years), hydrogen accumulation in large quantities takes place in the form of nickel hydrides in a sintered nickel matrix of oxide-nickel electrodes. The capacity of the sintered nickel matrix of the oxide-nickel electrode as a hydrogen absorber was quantified as 20.1 wt% and 400 kg m^{-3}. These values exceed three times all the earlier data obtained by traditional methods for any reversible metal hydride.

It is also proved that the thermal runaway can be used as a new high-performance method of desorption of hydrogen from metal hydrides. On its kinetic and thermodynamic parameters, this method is considerably superior to requirements established by the United States Department of Energy (U.S. DOE) for onboard hydrogen storage systems. For its processing, the thermal runaway does not require any certain temperature or pressure. It can work at any temperature and pressure of ambiance. Hydrogen desorption by the method of thermal runaway runs with the aid of electrochemical reactions. This is why this process is easily controllable by electrotechnical methods and hence it is far less inertial than the thermal processes used in the traditional thermo-chemical method.

Keywords: Hydrogen storage, hydride, hydrogenation, dehydrogenation, thermal runaway, oxide-nickel electrode, gravimetric capacity

**Corresponding author*: galushkinne@mail.ru

Mehmet Sankir and Nurdan Demirci Sankir (eds.) Hydrogen Storage Technologies, (147–176) © 2018 Scrivener Publishing LLC

5.1 Introduction

The power industry is fundamental to the economics of every country in the entire world. Nowadays, the main energy sources are hydrocarbons (gas, crude oil, coal). Nevertheless, their reserves are limited. Moreover, when hydrocarbon raw materials are burnt, billions of tons of toxic substances are discharged into the atmosphere. The adverse impact to the environment is the main reason for the mass proliferation of chronic diseases among the earth's population. That is why in latter years, more and more attention has been paid to environmentally friendly renewable power generation methods. One of the mainstream directions is hydrogen energetics [1–5].

Hydrogen is the ideal energy carrier. It possesses the highest specific heat as compared to all other energy carriers: 120.9 MJ/kg (in comparison, petrol's specific heat is equal to 43 MJ/kg). At hydrogen burning, environmentally friendly water is released as steam.

The main obstacle for the widespread introduction of hydrogen energetics to the world is an absence of hydrogen storage systems featured with both sufficient specific capacity and high reliability. A safe and most effective method of hydrogen storage is its accumulation in solid media, such as sorbent materials and hydrides [6–13]. In a number of countries all around the world, development programs for hydrogen accumulation systems have been approved with specified requirements developed for them.

In the most comprehensive form, the criteria for onboard hydrogen storage systems were defined by the U.S. Department of Energy (DOE) in close collaboration with the automotive industry [14]. The most important of them are criteria for those systems' specific capacity and kinetic and thermodynamic parameters. The goal for the specific capacity by the year 2020 is the achievement of a gravimetric capacity of more than 5.5 wt% and that of a volumetric capacity of more than 40 kg m^{-3}.

Recently, huge efforts have been put into the development of hydrides possessing a gravimetric capacity of not less than 5.5 wt% [6–13]. In this respect, lately the most intensively investigated compounds have been complex hydrides of light elements and hydrides of magnesium [6, 8, 13]. Among all common hydrides, the hydrides of both magnesium and its alloys have the highest volumetric capacity and gravimetric capacity (110 kg m^{-3} and 7.66 wt% respectively for MgH_2). Theoretical gravimetric capacities of some complex hydrides are higher than that of magnesium hydride [13]. However, in practice, as a rule, a reversible capacity of complex hydrides is less than that of MgH_2 [6].

Unfortunately, in spite of all their exertions so far, researchers have failed to develop a hydrogen storage system meeting all U.S. DOE criteria.

Namely, the absence of onboard hydrogen storage systems with the necessary parameters is the main obstacle to a large-scale introduction of hydrogen power generation to the global economy.

At present, there exist three methods or three technologies for obtaining metal hydrides.

Firstly, there is the chemical method of obtaining hydrides. In the framework of this method, metal hydrides are synthesized with the aid of chemical interactions [13]. However, obtaining metal hydrides via chemical interactions is possible only for a limited number of hydrides [15]. Besides, this process is irreversible. In principle, a regeneration of initial hydrides used for chemical reactions is possible but it is inexpedient based on economic considerations. That is why this method is considered to be unacceptable for hydrogen storage systems.

Secondly, there is the thermo-chemical method of hydrogen accumulation in metal hydrides. In the framework of this method, a process of hydrogenation/dehydrogenation is determined by setting certain values of hydrogen pressure and temperature, i.e.:

$$MeH_n \xleftarrow{P_1,T_1} \xrightarrow{P_2,T_2} Me + \frac{n}{2}H_2 \tag{5.1}$$

where Me is a metal or an alloy, while P_1, T_1 and P_2, T_2 are pressure and temperature of a process of hydrogenation or dehydrogenation respectively.

At present, this method is the main one for hydrogen storage systems. However, its features has a number of shortages, too. Firstly, it is inertial. For hydrogen release initiation, metal hydrides must be heated up to a certain temperature, after which, with some retardation (depending on a hydride type), the hydrogen starts releasing. A similar situation is typical for hydrogen release termination, too. But the processes of both heating/cooldown and hydrogen release (from hydrides) initiation/ceasing are quite inertial. Secondly, both launching and ceasing the process of hydrogen release from hydrides require an additional energy supply to the system, which lowers the power-producing effectiveness of hydrogen storage systems. Thirdly, in the framework of the thermo-chemical method, the rate of hydrogen release from metal hydrides is rather small. For increasing it and therefore improving kinetic parameters of the system, increasing temperature is needed, which worsens the system's thermodynamic parameters badly. That is why, until now, no metal hydrides have been found, which—in the framework of the thermo-chemical method—would meet the criteria of the U.S. DOE on both kinetic and thermodynamic parameters.

Thirdly, there exists the electrochemical method of hydrogen accumulation in metal hydrides. In the course of electrolyte decomposition, for example, in alkaline medium or on a cathode, hydrogen is released.

$$2e^- + 2H_2O \rightarrow H_2 + 2OH^- \text{ (cathode)} \quad (5.2)$$

$$2OH^- \rightarrow 1/2O_2 + H_2O + 2e^- \text{ (anode)} \quad (5.3)$$

The released hydrogen is adsorbed on the cathode; then, the bulk of the hydrogen escapes into the ambient atmosphere, while a pittance of hydrogen penetrates the cathode in depth. At first, hydrogen exists inside of the cathode in its non-bound state (α-phase), while in the case of long-lasting electrolysis, hydrogen starts forming bound states with the metal of the cathode (β-phase), i.e., metal hydrides [13, 16]. In the course of common electrolysis during several hours, a hydride is formed in the uppermost thin layer of a cathode [16]. That is why the gravimetric capacity of a cathode as a hydrogen accumulator turns out to be rather small. This method of hydrogen accumulation in a cathode was known long ago [13]. However, the electrochemical method has never been considered to be a method of hydrogen accumulation for hydrogen storage systems. Our opinion about the effectiveness of an electrochemical method of hydrogen accumulation changed drastically, after which we started investigating the thermal runaway phenomenon in alkaline batteries [16–26].

During the charging of some types of nickel-cadmium batteries at constant voltage or during their floating charge, the effect known as thermal runaway may be observed [27]. In the case of thermal runaway in a battery, a charging current grows sharply, an electrolyte is transformed into steam, and an inflammation and explosion are also possible.

The experimental research [25] showed that as a result of the thermal runaway, from a KSX-25 battery (with sintered electrodes with capacity 25 Ah), approximately 486 liters of steam-gas mixture are released. After a mixture cooldown, it turned out that 297 liters of gas and 152 ml of water were obtained in the measuring container, which corresponds to approximately 189 liters of steam. The analysis of the released gas conducted by means of the VOG-2M gas analyzer showed that it consisted of 95.6% hydrogen and 4.4% oxygen. The absolute error in the concentration percentage was 0.3–0.5. Thus, 284 liters of hydrogen and 13 liters of oxygen were released from the batteries. Suppose that the released oxygen is connected with the electrolyte decomposition (judging by electrochemical reactions [HPMS121.2,3]); during the thermal runaway, 20.9 ml of electrolyte must be decomposed. The rest of the electrolyte is released from the battery in the form of steam. On average, the KSX-25 battery

contains about 180 ml of electrolyte. After completion of the thermal runaway, some amount of electrolyte stays in the electrode pores in spite of the very high temperature of battery electrodes (more than 300 °C [17, 25]). Besides which, it is worth saying that the amount of the released hydrogen (284 liters [H_2]) exceeds much of its content in the whole electrolyte if it is to decompose into hydrogen and oxygen (about 224 liters [H_2]). These experimental studies make it quite clear that the hydrogen was inside of the KSX-25 battery even before the thermal runaway.

Theoretically, one may suppose two versions of hydrogen emergence in the nickel-cadmium batteries. Firstly, hydrogen can appear in the battery electrodes because of some technological processes of the electrodes' manufacturing. Then, in new batteries, hydrogen should be present in an amount equal to or exceeding its content in batteries that feature a rather long operating life. Secondly, it is possible that the hydrogen is accumulated in the electrodes of the nickel-cadmium batteries during their operation.

According to the operation manual of the KSX-25 battery, it is charged in two stages: firstly by a current of 10A over a period of 3 h, and secondly by a current of 5A over a period of 2 h. Consequently, these batteries overcharge by a factor of 1.6 as compared to their nominal capacity. Overcharge is required for complete charging of the batteries. Thus, in the course of charging, almost 15 Ah is used for electrolyte decomposition with the evolution of hydrogen and oxygen. Consequently, one charging of a KSX-25 battery produces 6 L of hydrogen and 3 L of oxygen. In the course of a KSX-25 battery's operation, electrolyte is added when required, as this is an ordinary vented battery. That is why, in principle, the amount of hydrogen found can be accumulated by a battery for 284/6 = 48 charge-discharge cycles. By the end of its life span, a KSX-25 battery is likely to have gone through thirty times as many charging-discharging cycles. Therefore, it can, in principle, accumulate the discovered amount of hydrogen.

These experimental results showed that the electrochemical method of hydrogen accumulation in metal hydrides can be of great significance for hydrogen storage systems and yet it has been studied very little.

5.2 Electrochemical Method of Hydrogenation of Metal Hydrides

5.2.1 Hydrogen Accumulation in Electrodes of Cadmium-Nickel Batteries Based on Electrochemical Method

In order to inspect the accumulation of substantial volumes of hydrogen in the electrodes of cadmium-nickel batteries in the framework of the

electro-chemical method (in the course of their charging) the following batteries were used: KSX-25 (with sintered electrodes with capacity 25 Ah). If hydrogen is accumulated in battery electrodes, its amount must be increased in proportion to their operation. That is why for examination of the hydrogen accumulation, batteries were used with various operation life. For evaluation of the amount of hydrogen accumulated in electrodes of KSX-25 batteries, the latter were subjected to thermal decomposition in a thermal chamber.

The experimental installation was represented by a metal thermal chamber in the form of a tube 1.8 m long and 2 cm in diameter (Figure 5.1). The sealed end of the tube was placed into a muffle furnace. Into the other tube end, a rubber plug was inserted with a duct for gas withdrawal. As under the high temperature action, the observed electrode was adhered to the thermal chamber walls, for the convenience of taking it out after conducting the experiment, it was placed into a cartridge. For reducing a heat exchange in the thermal chamber, a round porous ceramic plug 20 cm long was placed above the cartridge.

The intake chamber (2) for gas collecting was a hermetically sealed glass reservoir filled with water. Its capacity was 5 L. At the bottom of this reservoir, a number of tubes were inserted through a rubber plug: a long tube for supplying gas from the thermal chamber to the top of the reservoir, a tube for removing excess water, and a leg of a manometer tube (1) for controlling the pressure of the gas accumulated above the water (Figure 5.1).

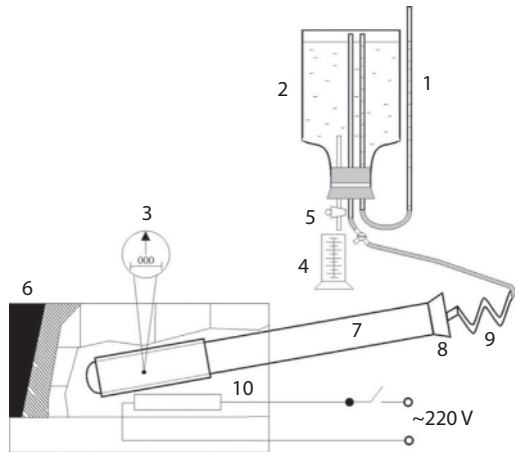

Figure 5.1 The experimental setup to study the process of gas release from the heated electrodes: (1) manometer, (2) intake chamber accumulating gas, (3) thermocouple, (4) retort, (5) tap, (6) muffle furnace, (7) metal thermal chamber, (8) rubber plug with a tube for gas extraction, (9) standard coil and (10) heater.

Heating the electrode in the thermal chamber resulted in a release of gas from it. This gas was partially cooled while passing through the standard coil (9) prior to entry into the gas intake chamber. As the gas entered the chamber, the pressure above the water increased, and this was registered by the manometer. In order to make a balance between the internal pressure in the intake chamber and atmospheric pressure, a part of the water was removed from the intake chamber into the retort (4). The water level in the retort gave an indication of the amount of the gas having entered to the intake chamber during the period studied [28–30].

Each electrode was decomposed at 800 °C. The reasons for choosing this temperature were as follows. In preliminary experiments, it was determined that a visible release of gas started at about 340 °C for the cadmium electrodes and at about 660 °C for the oxide-nickel electrodes. A great release of the gas starts at temperatures over 740 °C for both the oxide-nickel and cadmium electrodes. The rate of gas release grows with temperature increase; however, when the temperature exceeds 800 °C, this increase becomes negligible. Thus, the temperature of 800 °C was chosen as an optimum value for thermal decomposition of both cadmium and oxide-nickel electrodes.

Each cadmium electrode was decomposed in 7 days on average, while each oxide-nickel electrode was decomposed in 13 days on average in the working mode of 11 h per every 24 h. The amount of gas released from each electrode per day decreased from 4 L during the first days to 100–120 ml during the last days for each cadmium electrode, and from 6 L per day to 100–150 ml per day for each oxide-nickel electrode. The thermal decomposition process was stopped when the amount of the gas released in a 24 h period was less than 100 ml.

For conducting the experiment, six KSX-25 batteries were chosen with an operation life from 0 to 7 years. One cadmium and one nickel electrode were taken from each battery. Then the above said electrodes were subjected to thermal decomposition in the described installation. The experiment was repeated three times for each battery. Table 5.1 demonstrates the average values calculated for three experiments for the amount of hydrogen inside an electrode for each type of electrode.

For the gas testing, a VOG-2M volumetric and optical gas analyzer was used. The absolute error in the percentage concentrations was 0.3–0.5. Analysis of the gas released from both electrodes showed that it consisted only of hydrogen.

Table 5.1 (batteries no. 3–6) demonstrates that the electrodes of the KSX-25 batteries with a long service life contain a huge amount of hydrogen.

Table 5.1 Hydrogen content in oxide-nickel and cadmium electrodes of the KSX-25 batteries with different service life.[a]

No. of the battery	**1**		**2**		**3**		**4**		**5**		**6**	
Period of operation (years)	new		1.5		4.0		5.0		7.1		6.4	
Type of electrode	Ni	Cd	Ni	Cd	Ni	Cd	Ni	Cd	Ni	Cd	Ni	Cd
Amount of gas released, liters	0	0	19.6	13.2	30	12	36	19.9	35.8	19.8	36	20

[a]The relative error in the data in Table 5.1 is 5–7%.

Hydrogen is absent in electrodes of new nickel-cadmium batteries, but during its operation, the amount of hydrogen inside of the electrodes increases (Table 5.1, batteries no. 1–3). The amount of hydrogen absorbed by the electrodes stops increasing after five years of service life, i.e., the maximum capacity of the electrodes for hydrogen storage is reached after that time (Table 5.1, batteries no. 4–6).

The data in Table 5.1 relate to one battery electrode. In a KSX-25 battery there are 14 cadmium and 15 nickel electrodes. Therefore, in one KSX-25 battery there are approximately 820 L of hydrogen (Table 5.1, battery no. 6). In the case of operation according to the relevant use and maintenance manual, the KSX-25 batteries are overcharged 1.6 times as compared to their nominal capacity. Overcharge is required for complete charging of the batteries. Consequently, one charging of a KSX-25 battery produces 6 L hydrogen and 3 L oxygen. Thus, the found 820 L hydrogen may have been accumulated during 137 charging-discharging cycles. By the end of its life span, a KSX-25 battery is likely to have gone through a ten times greater charge-discharge number of cycles. Therefore, it can, in principle, accumulate the discovered amount of hydrogen.

Let us assess specific parameters of an oxide-nickel electrode as a hydrogen accumulator. An oxide-nickel electrode accumulates approximately 36 liters of hydrogen during the long service life of a KSX-25 battery (Table 5.1). The weight of the electrode is 24 grams. Hence, the specific mass capacity of an oxide-nickel electrode as a hydrogen absorber is equal to 13.4 wt%. The obtained result exceeds 10 times the earlier obtained

results for nickel hydride (obtained with use of traditional methods) [31]; and for any reversible metal hydrides, including magnesium hydride or complex hydrides, it exceeds 2 times [6, 13]. Considering that the physical sizes of an oxide-nickel electrode of a KSX-25 battery are equal to 7.3 × 13.6 × 0.081 cm, we obtain a specific volume capacity of an oxide-nickel electrode as a hydrogen absorber that is equal to 400 kg · m^{-3}. According to this parameter, the obtained result exceeds more than 3 times the earlier obtained results for any reversible metal hydrides [13].

5.2.2 Hydrogen Accumulation in Sintered Nickel Matrix of Oxide-Nickel Electrode

It is possible to physically divide oxide-nickel electrode into two phases: active substance (nickel hydroxide) and sintered matrix (in the case of sintered electrodes present in KSX-25 batteries).

5.2.2.1 Active Substance of Oxide-Nickel Electrodes

Suppose that hydrogen is accumulated in the active substance of oxide-nickel electrodes (nickel hydroxide). In this case, in the course of a nickel hydroxide and acids interaction running with formation of the soluble salt, the intercalary hydrogen will be released because the nickel hydroxide will disappear and the salt will be dissolved in the electrolyte. Here it is possible to use any acid not interacting or slightly interacting with the nickel matrix of the oxide-nickel electrode and forming the soluble salt with the nickel hydroxide. In our studies, we used sulfuric acid, which—in the reaction with the nickel hydroxide—produces the soluble salt (the nickel sulfate) according to the formula:

$$Ni(OH)_2 + H_2SO_4 \rightarrow NiSO_4 + 2H_2O\,. \tag{5.4}$$

The interaction between the sulfuric acid and the active substance of the oxide-nickel electrode can result in two possible situations.

Firstly, hydrogen can just be intercalary in the active substance without entering into chemical linkage or making such chemical bonds that degrade upon interaction of the active substance with the sulfuric acid. In this case, upon interaction of the active substance with the sulfuric acid, the hydrogen must be released in those amounts found in the experiments (Table 5.1). In this case, this fact would confirm the hypothesis that the hydrogen is accumulated in the active substance of oxide-nickel electrodes

in the course of the battery operation in the form of free or slightly bound state.

Secondly, it is possible to suppose that with the active substance of oxide-nickel electrodes, the hydrogen makes solid chemical bonds nondegradable in an interaction with the sulfuric acid. In this case, the mass of the oxide-nickel electrode (after removing nickel hydroxides from it by sulfuric acid) will exceed the mass of the new sintered nickel matrix. Therefore, this fact would confirm the hypothesis that during battery operation, the hydrogen is accumulated in the oxide-nickel electrode active substance in the form of tight chemically bound state.

For testing these hypotheses, 22.6% solution of sulfuric acid was used. In our preliminary experiments, a rate was found for nickel hydroxide dissolution in the sulfuric acid. For this purpose, the oxide-nickel electrodes were placed into the sulfuric acid for various periods of time at 5-minute intervals during a two-hour period. Afterwards, the electrodes were washed with distilled water, dried and weighed. It was found that after 20 minutes of etching, the oxide-nickel electrode mass did not change. In further experiments, the etching period was chosen to equal 30 minutes, which guaranteed better reliability of nickel hydroxide removal from oxide-nickel electrodes. Also, this experiment showed very slight, if any, interaction of the sintered nickel matrix with the sulfuric acid.

For conducting the experiment, 8 oxide-nickel electrodes were chosen from different KSX-25 batteries with operation life equal to 6 years. After washing them out in the distilled water and subsequent drying, the electrodes were weighed and placed into a retort with the sulfuric acid for 30 minutes. The retort was tightly covered with a rubber plug having a tube for gas withdrawal to a measuring container (2) (Figure 5.1), where the gas was accumulated. Then the electrodes were washed out in the distilled water, dried and weighed again. The experiment results are represented in Table 5.2.

Table 5.2 Oxide-nickel electrodes etching in sulfuric acid.

No. of the electrode	**1**	**2**	**3**	**4**	**5**	**6**	**7**	**8**
Initial weight, g	24.1	23.7	24.0	23.5	23.9	23.7	24.1	24
Final weight, g	15.53	15.9	15.5	15.5	15.4	15.2	15.5	15.7
Weight loss, %	35.5	33.0	35.4	34.0	35.6	35.9	35.7	34.6
Amount of hydrogen, ml	0	0	0	0	0	0	0	0

According to the obtained experimental data (Table 5.2), it is possible to make the following conclusions.

Firstly, as a result of oxide-nickel electrode etching in the sulfuric acid, the hydrogen is not released at all. From this fact, it follows clearly that in the form of free or slightly bound state, the hydrogen is never accumulated.

Secondly, the mass loss of the oxide-nickel electrodes after their etching in the sulfuric acid reached 33–36%. According to the data of the KSX-25 batteries producer, a positive electrode contains 30–34% of nickel hydroxide and 1.5–2% of cobalt hydroxide. The results obtained for the electrodes mass loss get exactly into this range. Hence, during battery operation, the nickel hydroxides are not transformed to other stable chemical compounds capable of accumulating the hydrogen.

Thus, the active substance of oxide-nickel electrodes does not accumulate in the hydrogen. That is why based on the experimental data of the first (Table 5.1) and second (Table 5.2) groups of experiments, it is possible to confidently affirm that the hydrogen is accumulated in the sintered nickel matrix of an oxide-nickel electrode. It should be observed that transition elements, to which nickel belongs, are capable of accumulating hydrogen [13, 15, 32–34].

5.2.2.2 Sintered Nickel Matrices of Oxide-Nickel Electrodes

For possible testing of hydrogen accumulation in a sintered nickel matrix, the installation represented in Figure 5.1 was used. However, the thermal chamber was manufactured in the form of the tube (3.2 m long and 2 cm in diameter) made from a heatproof alloy stable at temperatures up to 1800 °C.

The sintered nickel matrix (in coiled state) was placed into a ceramic crucible. Then the crucible was inserted into the thermal chamber. For heat exchange suppression inside of the thermal chamber above the crucible, two round porous ceramic plugs 20 cm long were inserted. Then the thermal chamber was heated up to 1600 °C so that the nickel sintered matrix inside of the crucible was melted. Hydrogen started being released from the nickel matrix at the temperature 660 °C. This value is close to the temperature values of dissociation of hydrides of other transition metals [13, 15, 32].

For conducting the experiment, four KSX-25 batteries were chosen with an operation life of more than five years. From each battery, three oxide-nickel electrodes were taken. The electrodes were etched in the sulfuric acid during a 30-minute period with the purpose of removing nickel hydroxide. Then the electrodes were washed in distilled water and dried. Then the electrodes were subjected to thermal decomposition in

the above-described installation. In Table 5.3, average amounts are given of hydrogen inside of electrodes calculated for three electrodes from four chosen batteries.

The analysis of the released gas in the experiment conducted with use of the VOG-2M gas-analyzer showed that the gas consisted only of hydrogen. The absolute error in the percentage concentrations was 0.3–0.5.

In the crucible, after its extraction from the thermal chamber, a piece of metallic nickel remained. Hence, the sintered nickel matrix consists of two elements: hydrogen and metallic nickel, i.e., nickel hydride.

Let's evaluate the gravimetric capacity of the sintered nickel matrix of oxide-nickel electrode as a hydrogen absorber. The oxide-nickel electrode accumulates approximately 36 liters of hydrogen during its long service life (more than five years) (Table 5.3). The weight of the oxide-nickel electrode is 24 g, and the weight of the nickel hydroxide is 8 g. Hence, the gravimetric capacity of the oxide-nickel electrode as a hydrogen absorber equals 13.4 wt% [28, 29]. While the gravimetric capacity of the sintered nickel matrix as a hydrogen absorber is equal to 20.1 wt%, this value exceeds three times the earlier data obtained based on the traditional thermo-chemical method for any reversible metal hydrides, including magnesium hydride or complex hydrides [6, 13]. Considering that the physical sizes of the oxide-nickel electrode and sintered nickel matrix of the KSX-25 battery equal 7.3 × 13.6 × 0.081 cm, we obtain a volumetric capacity of the oxide-nickel electrode and that of the sintered nickel matrix as a hydrogen absorber equal to 400 kg m^{-3} [28, 29]. The obtained result exceeds more than 3 times the earlier results obtained for any reversible metal hydrides [13].

The reasons for such high specific parameters of an oxide-nickel electrode are not quite clear yet. Thus, a large amount of experimental and theoretical research is required for revealing the above-mentioned reasons. However, it should be noted that in an oxide-nickel electrode there are a number of factors present which contribute to hydrogen accumulation. At present, these factors are under intensive research [6–13].

Table 5.3 Hydrogen content in metal-ceramic nickel matrixes of oxide-nickel electrodes of the KSX-25 batteries with different service life.[a]

No. of the battery	**1**	**2**	**3**	**4**
Period of operation (years)	6.1	6.5	7.1	6.7
Amount of gas released, liters	36.2	35.8	36.1	36

[a]The relative error in the data in Table 5.3 is 5–7%.

Firstly, the sintered oxide-nickel electrode in a KSX-25 battery is made from finely divided nickel powder with strongly collapsed crystalline structure. Any imperfections of metal crystalline structure (particularly dislocations) are traps for hydrogen, as they decrease the energy of hydrogen atom as compared to their location in normal interstice. Besides which, they are the centers of hydrogen absorption, and also contribute to hydrogen penetration depth into the metal. Hence, imperfections of the metal crystalline structure cause a sharp rise of hydrogen miscibility in it. With the abovementioned purpose, the hydrides used in modern hydrogen storage systems are ground down in ball mills [9, 10].

Secondly, an oxide-nickel electrode contains nickel oxides. It is a well-known fact that the oxides of transition metals act as catalysts of hydrogen accumulation [11, 12].

Thirdly, the electrodes are densely packed. Thus, hydrogen evolved at the cadmium electrode during charging of the battery may penetrate into the pores of both the oxide-nickel, and cadmium electrodes. Hence, in all probability, the oxide-nickel electrode accumulates hydrogen not electrochemically, but due to the high capillary pressure. According to works presented in refs. [35, 36] the amount of hydrogen C accumulated in metal is related to the external pressure of hydrogen P by the formula:

$$C = K\sqrt{P}\ . \tag{5.5}$$

Capillary pressure in the electrode pores is inversely proportional to pore radius R, i.e.:

$$P = A/R \tag{5.6}$$

where A = 0.2 μm MPa – proportionality constant for the given electrolyte.

In porous electrode the main pores have an average radius of the order of several dozens of microns. However, the finely divided powder, used for manufacturing of sintered matrix of the electrodes, has microfissures with dimensions from several hundreds angstrom to the size of crystalline lattice of the metal. Thus, hydrogen accumulating in the microfissures as the result of electrolyte decomposition may have pressure of up to 100 MPa and higher [17].

Lastly, the process of hydrogen accumulation in the batteries' electrodes takes place all through their service life. This is more than five years in the present study. The KSX-25 battery operates in the floating charge mode. So, most of the time, the battery recharges. During this process, its electrolyte decomposes into hydrogen and oxygen. Hydrogen is characterized by a

very high diffusion permeability. For example, at the temperature of 20 °C the diffusivity of hydrogen in nickel is approximately 10^{10} times higher than diffusivity of nitrogen or oxygen [13, 15]. These features explain why upon dissociation of an electrolyte into hydrogen and oxygen in a battery, only hydrogen accumulates in the electrodes, while oxygen escapes into the atmosphere.

With the aid of the thermo-chemical method, the process of hydrides preparation could take from several minutes to several hours. Analysis of research papers on hydrides over the last 20 years has shown that most probably no experiments were conducted for obtaining transition metal hydrides at high external hydrogen pressures lasting for really long time periods. However, exposure to external pressure is a significant factor in any processes of penetration of one substance into another. Especially when the penetration process is extremely slow, as in our case.

It appears that the high capillary pressure of hydrogen acting throughout an exceedingly long time on the strongly destroyed crystalline structure of the electrodes' metal over the catalyst (oxide of transition metal) allowed the accumulation of 20 times more hydrogen as compared to the traditional methods of nickel hydrides preparation. This supposition, of course, requires separate research, both experimental and theoretical.

Thus, based on the conducted experimental studies and also on the experimental studies completed by us within the last decade [17–25, 28, 29], it is possible to assert univocally that in the course of long-term usage of nickel-cadmium batteries it happens that in the sintered nickel matrix of oxide-nickel electrode, large volumes of hydrogen are accumulated in the form of nickel hydrides. It is notable that hydrogen, being a component of the nickel hydrides, is bonded very strongly (β-phase) because the hydrogen starts to be released along with sintered nickel matrix heating only after reaching temperatures of more than 660 °C. Besides which, specific capacity of the obtained nickel hydrides as hydrogen absorbers in the sintered nickel matrix (of oxide-nickel electrode) considerably exceed the specific capacity of all the currently known metal hydrides (both reversible and nonreversible type) obtained with use of traditional methods. We believe that this fact is of great practical importance.

It must be noted that an oxide-nickel electrode by its specific parameters of hydrogen accumulation exceeds the requirements of the U.S. Department of Energy [14]. However, due to the high temperature of hydrogen desorption and low speed of absorption/desorption, the given hydrides cannot be used as hydrogen accumulators for future hydrogen-fueled vehicles if the thermo-chemical method of hydrogen desorption is used. However, in a previous study [37] a conceptually new method was

presented of hydrogen desorption from hydrides, which will be discussed below. In the framework of this method for hydrogen extraction from hydrides, the electrochemical reaction of the thermal runaway is used. By using the electrochemical reaction of the thermal runaway for hydrogen desorption from hydrides, it will probably be possible to use the obtained nickel hydrides (Table 5.3) as hydrogen accumulators for future vehicles fueled by hydrogen.

Similar research was performed by us for a number of other nickel-cadmium batteries with sintered electrodes (KSL-15, KSX-6, KSX-3.5, etc.) [21, 23, 24]. In all cases, after five years of operation, the gravimetric capacity of the oxide-nickel electrodes as hydrogen accumulators coincided with limits of experimental error 5%.

Also, we would like to highlight that the phenomenon of large volumes of hydrogen storage in the electrodes of Ni–Cd batteries in the course of their operation has just recently been found [17]. This phenomenon is quite an unusual one. It allows accumulating hydrogen in metal hydrides in volumes considerably exceeding hydrogen volumes in all known hydrides obtained with the use of the thermo-chemical method. Undoubtedly, an investigation of this complicated and poorly studied phenomenon requires the conduction of further research, both theoretical and experimental.

5.3 Electrochemical Method of Dehydrogenation of Metal Hydrides

5.3.1 Introduction

In the previous section, it was shown that based on the electrochemical method, it is possible to obtain metal hydrides with high gravimetric and volumetric capacities: 20.1 wt% and 400 kg m^{-3} [29]. These values exceed three times the values obtained previously (based on the traditional thermo-chemical method) for any reversible metal hydrides, including magnesium hydrides and complex hydrides [6, 13]. Besides which, the obtained values of the gravimetric capacity exceed almost four times the criteria set by the U.S. DOE for hydrogen storage systems [14]. But for hydrogen desorption from nickel hydrides (with use of the thermo-chemical method), a high temperature is required (800 °C). Besides the hydrogen desorption runs very slowly (it lasts about 140 hours at the temperature of 800 °C) [17, 28, 29]. Thus, the nickel hydrides obtained from the use of the thermo-chemical method for hydrogen desorption do not meet the criteria of the kinetic and thermodynamic parameters of the U.S. DOE. In this section,

we shall consider the thermal runaway as a potential new effective method of hydrogen desorption from hydrides.

With this purpose in mind, let us give more detailed consideration to the criteria for the kinetic and thermodynamic parameters set by the U.S. DOE [14] for onboard hydrogen storage systems. The kinetic and thermodynamic criteria of the U.S. DOE are given in Table 5.4.

In Table 5.4, the parameters 2–4 determine the limits of inertance of hydrogen storage systems, while parameter 1 defines the minimum critical rate of hydrogen release from the system. The first parameter is meant for a car of the middle class 3000 lb in weight with a powerplant of about 150 kW. This parameter is not convenient for kinetics assessment of hydrogen release from a system of its storage as it is standardized on the power level of the powerplant. It is better to standardize this kinetic parameter on the weight or on the volume of a hydrogen storage system.

An average volume of a fuel tank of a car of this class is about 70 liters. Hence, petrol mass in the fuel tank is about 52.5 kg. Using the first parameter from Table 5.4 and the calculated mass, we shall find the hydrogen minimum full flow rate standardized on the system mass:

$$V = 5.714 \cdot 10^{-5}\ \text{wt\%}\ \text{s}^{-1}. \tag{5.7}$$

The peak value for the rate of the hydrogen full flow from the system was found in a previous study [38]. It turned out to be equal to $8.333 \cdot 10^{-4}$ wt% s^{-1}.

Table 5.4 DOE technical targets: onboard hydrogen storage systems.

Discharging rates	**Units**	**Value**
1) Minimum full flow rate	(g s^{-1}) kW^{-1}	0.02
2) Start time to full flow (20 °C)	s	5
3) Start time to full flow (–20 °C)	s	15
4) Transient response at operating temperature 10%–90% and 90%–0%	s	0.75
5) Min/max delivery temperature	°C	–40/85
6) Min delivery pressure from storage system*	bar (abs)	3FC/35ICE
7) Max delivery pressure from storage system*	bar (abs)	100

*FC = fuel cell, ICE = internal combustion engine

It will be observed that some contemporary magnesium-based hydrides [39] and complex hydrides [40] have these kinetic parameters. However, hydrogen desorption from these hydrides runs at high temperatures. That is why on thermodynamic parameters, these hydrides do not meet the criteria set by the U.S. DOE.

Now let us consider the thermodynamic parameters set by the U.S. DOE for onboard hydrogen storage systems (Table 5.4, parameters 5–7). For evaluation of hydrides applicability to hydrogen accumulating units, let us calculate their enthalpy of dehydrogenation. For this, we shall make use of the van't Hoff's equation [13]:

$$\ln(P) = \Delta H/RT - \Delta S/R \tag{5.8}$$

Thereupon for enthalpy minimum and maximum, from permissible ranges of temperature and pressure values (Table 5.4), we obtain the following estimations: $\Delta H = -43.3$ kJ mol^{-1}(H_2) at (T = 85 °C, P = 3 bar) and $\Delta H = -21.3$ kJ mol^{-1}(H_2) at (T = –40 °C, P = 100 bar). In the calculations, it was taken into account that dehydrogenation entropy of different hydrides is approximately equal to –130 J K^{-1} mol^{-1}(H_2) [13]. The hydrides with lower values of the enthalpy require higher energy consumption for their dehydrogenation, while the hydrides with much higher enthalpy values are not stable and hardly suitable as materials for hydrogen storage.

Let us give consideration to methods of hydrogen desorption from hydrides. At the present time, two methods of hydrogen desorption exist.

The first one is the chemical method of hydrogen desorption. In the framework of this method, hydrides interact with water and this reaction runs with hydrogen release:

$$MeH_n + nH_2O \rightarrow Me(OH)_n + nH_2\,. \tag{5.9}$$

According to the reaction (5.9), a hydrogen amount is turned into being twice its content in the initial hydride. The reaction (5.9) is quite irreversible. A regeneration of initial hydrides for the reaction (5.9) is principally possible but inexpedient for economic considerations. The reaction (5.9) is possible only for a limited number of hydrides [15]. At present, this desorption method is considered to be unacceptable for hydrogen storage systems.

The second hydrogen desorption method is the thermo-chemical one discussed in Section 5.1.1. At the present time, this method is the main one for hydrogen storage systems.

5.3.2 Thermal Runaway as the New Method of Hydrogen Desorption from Hydrides

In this section, the possibility of using the thermal runaway process in alkaline batteries as a new method of hydrogen desorption from metal hydrides is inspected. In Section 5.2.2 it was shown that as a result of long operation (more than 5 years) of alkaline batteries a lot of hydrogen is accumulated in their electrodes. Notably, the hydrogen is accumulated in the sintered matrix of the electrodes in the form of metal hydrides [17, 28, 29]. For the experimental studies, we used KSX-25 batteries with sintered electrodes featuring 25 Ah capacity.

Let us study the kinetic and thermodynamic parameters of the thermal runaway process in those batteries as indexes of the new method of hydrogen desorption from metal hydrides. We are going to compare these parameters with similar parameters obtainable based on the traditional thermo-chemical method of hydrogen desorption from metal hydrides. In the experiments, the KSX-25 batteries with an operation life of 7 years were used.

5.3.2.1 Thermo-Chemical Method of Hydrogen Desorption

Let us make use of the installation shown in Figure 5.1 to examine the rate of hydrogen release from the electrodes of the KSX-25 batteries based on the thermo-chemical method of hydrogen desorption. The thermal decomposition of oxide-nickel and cadmium electrodes took place at a temperature of 800 °C. The process of the thermal decomposition of electrodes ceased when a daily hydrogen release became less than 100 ml. The hydrogen release rate was measured every hour: it was determined based on the volume of hydrogen released during five minute intervals. The results of the experimental studies are presented in Figure 5.2.

In the experiments (Figure 5.2), a very high temperature was used for hydrogen desorption from metal hydrides, which considerably exceeded the requirements of the U.S. DOE (Table 5.4) for hydrogen storage systems. However, in spite of such high temperature, the rate of the hydrogen released from electrodes using the thermo-chemical method was quite low.

5.3.2.2 Thermal Runaway: A New Method of Hydrogen Desorption from Metal Hydrides

According to the studies [19], the probability of thermal runaway increases with the growth of battery temperature and voltage of its charge. That is

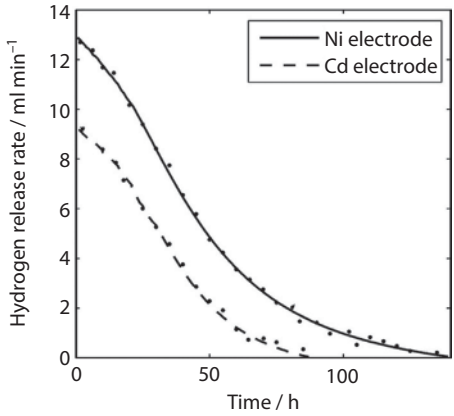

Figure 5.2 Changes of hydrogen evolution rate versus time for oxide-nickel and cadmium electrodes of the KSX-25 battery at 800 °C.

why, for the probability of thermal runaway to increase, battery cycling was conducted in the thermal chamber at a temperature of 45 °C. Charging was conducted at high voltage of 2.2V during a 10-hour period. A discharge was performed according to the operation manual of the KSX-25 battery under a current of 10A to a voltage of 1V. Thermal runaway is a very rare phenomenon [17, 21]. In this experiment, in spite of the severe conditions of cycling, we had to perform 350 cycles of charge-discharge before the thermal runaway was initiated.

In the course of the thermal runaway, the voltage was measured on the terminals of a battery. A charge current was measured with a shunt resistance of 0.001 Ohm and maximum current of 500A.

The steam-gas mixture released from the battery [17, 18] was cooled down while passing through the standard coil cooler. The steam was cooled down and transformed into water, which was collected in a special storage reservoir. The released gas was collected in an elastic container (1070 liters in volume) and measured. A gas composition was found with the aid of the VOG-2M gas analyzer. The absolute error in the concentration percentage was 0.3–0.5.

As a result of the thermal runaway, the battery released 281 liters of hydrogen, 10 liters of oxygen and 151 ml of water collected in a special storage reservoir, which corresponds to approximately 188 liters of steam. As it was shown in Section 5.1.1, a small amount of oxygen released from the battery in the course of the thermal runaway is connected with the additional process of electrolyte decomposition (5.2, 5.3).

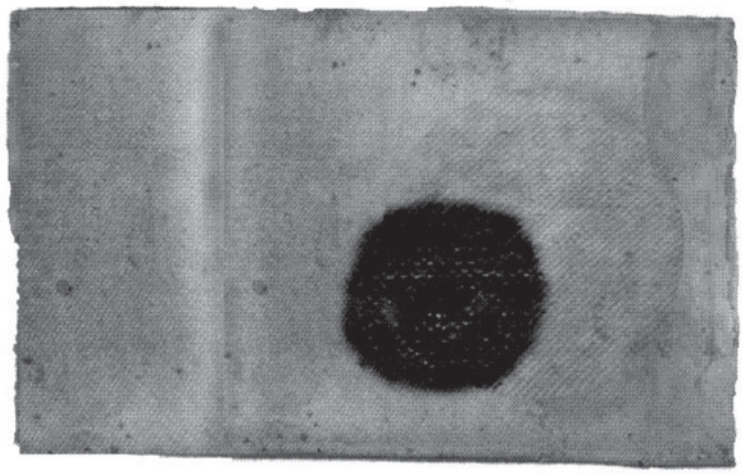

Figure 5.3 Oxide-nickel electrode of KSX-25 battery after thermal runaway.

The volume (in wt%) of the hydrogen desorbed versus the time was determined in two stages. Firstly, the volume of the released hydrogen versus the time in the thermal runaway process was measured. Secondly, the mass of the electrodes participating in the thermal runaway process was evaluated; it was done based on the area of circles of the burned separator on the electrodes in places where the thermal runaway occurred (Figure 5.3).

Based on the obtained data, the volume of desorbed hydrogen in wt% versus the time was calculated. The obtained data are presented in Figure 5.4.

From the Figure 5.4 it is seen that the total volume (in wt%) of the hydrogen desorbed in the process of the thermal runaway is approximately equal to a gravimetric capacity of these electrodes found by the experiments presented in Section 5.2.1.

During the thermal runaway (for approximately 4 minutes [Figure 5.4]), the battery released 281 liters of hydrogen. Thus, the thermal runaway sharply accelerates the hydrogen exit from hydrides as compared to the thermo-chemical method.

5.4 Discussion

Let us evaluate the kinetic and thermodynamic parameters of oxide-nickel and cadmium electrodes as hydrogen storage systems with the use of both the thermal runaway and thermo-chemical method of dehydrogenation.

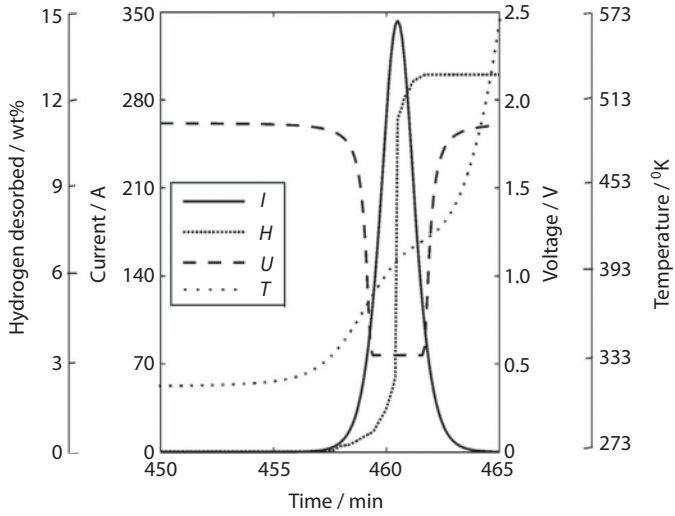

Figure 5.4 Change in parameters of the KSX-25 battery during thermal runaway: *I* is the charging current of the battery, *U* is the voltage of the battery terminals, *H* is the hydrogen desorbed, *T* is the temperature of the battery positive terminal.

In a case using the thermo-chemical method of dehydrogenation, at the initial moment, the rate of hydrogen release from oxide-nickel electrodes was equal to 12.8 ml min^{-1} (Figure 5.2). The average weight of the oxide-nickel electrodes is 24 g. Thus, the rate of the hydrogen full flow from the oxide-nickel electrode is equal to $7.94 \cdot 10^{-7}$ wt% s^{-1}. The similar evaluations for cadmium electrodes gave the value $7.35 \cdot 10^{-7}$ wt% s^{-1}. The obtained values for the rate of hydrogen full flow from the studied electrodes are approximately a hundred times less than minimum allowable full flow rate (criterion 5.7) set by the U.S. DOE for onboard hydrogen storage systems. Besides, the hydrogen desorption took place at the temperature of 800 °C. This value greatly exceeds the thermodynamic parameters set by the U.S. DOE (Table 5.4).

Let us assess the kinetic and thermodynamic parameters of electrodes of KSX-25 batteries in the case where thermal runaway is used as the new method of hydrogen desorption from hydrides. The hydrogen desorption rate was determined using the data (Figure 5.4) within the scale of 20–80% completion of desorption processes [39, 41]. For the rate of hydrogen full flow from oxide-nickel electrodes, we obtained a value of 1.2 wt% s^{-1}. This value exceeds by approximately 20000 times the minimum full flow rate (criterion 5.7) set by the U.S. DOE for onboard hydrogen storage systems.

Let us consider thermodynamic parameters of a thermal runaway. It will be observed that in the case of the thermal runaway, there is no need for additional energy for heating of metal hydrides. On the contrary, during a thermal runaway (Figure 5.4) very high energy is released from a KSX-25 battery (about 5012 kJ [20]), which can also be favorably used. Thus, regarding kinetic and thermodynamic parameters, the thermal runaway considerably exceeds the minimum requirements set by the U.S. DOE [14] (Table 5.4).

However, thermal runaway has a very substantial shortcoming. At common cycling the probability of thermal runaway initiation in alkaline batteries is very low [19]. Besides, the thermal runaway is a stochastic phenomenon and it is hardly repeatable under common conditions [17–21]. Nevertheless, based on the comprehension of the real mechanism of the thermal runaway, this problem can be solved.

According to the standard point of view [27, 42], the scenario for the thermal runaway is as follows. In the case where a battery is recharging for a long time under constant voltage (or at its floating service), heating-up takes place, which results in a decrease of a battery's internal resistance and an increase of recharging current, which in turn magnifies the heating-up, etc. So, the thermal runaway is a result of the positive feedback between the current and the temperature of batteries during their charging under a constant voltage. Besides, as for hermetic batteries, there is a belief that an essential initial contribution to batteries heating-up is made by exothermic reactions of an oxygen cycle.

The KSX-25 batteries investigated by us are not hermetic. They are the typical vented batteries with a densely packed arrangement of electrodes. This is why the oxygen cycle of these batteries is absent.

However, as for the generally accepted mechanism of thermal runaway [27], a lot of experimental facts contradict it (see the analysis refs. [19, 20]).

Firstly, the generally accepted mechanism of thermal runaway supposes that thermal runaway is connected only with intensification (at the expense of lowering of internal resistance) of batteries charging reaction and probably of the reaction of electrolyte decomposition (as the thermal runaway takes place at long-lasting recharging of batteries). In this case, as a result of the thermal runaway from the batteries, a steam-gas mixture must be released consisting of steam (at the expense of electrolyte evaporation because of the high temperature of the thermal runaway) and probably hydrogen and oxygen (at the expense of electrolyte decomposition). Hence, in the released gas, the hydrogen/oxygen ratio must be 2:1. However, the direct experimental studies show (see Section 5.1.1 and refs. [17–20]) that the released gas mixture that resulted from the thermal runaway consists of hydrogen (not

less than 95%). Notably, the electrolyte evaporates in the form of steam and is decomposed to hydrogen and oxygen to a very negligible extent. Besides, in the released gas mixture, the hydrogen amount exceeds its content in the entire electrolyte of the battery in order to be decomposed to hydrogen and oxygen (Section 5.1.1 and [25]). This fact can be explained only based on the assumption that the hydrogen is accumulated inside of the batteries in the course of their operation, which just confirms the experimental studies (Table 5.1 and refs. [28, 29]). It will be observed that in the course of KSX-25 batteries operation, electrolyte is added to them if needed.

Secondly, according to the generally accepted mechanism [27], the thermal runaway runs at the expense of energy, which a battery receives from a recharger. But the direct calorimetric measures showed [20] that as a result of a thermal runaway in a battery, it releases 140 times more energy than the battery receives from the recharger at the same time. This fact can be explained only if it is assumed that the thermal runaway is connected with running of a very powerful exothermic reaction.

There exist a lot of other contradicting experimental data to the generally accepted mechanism of the thermal runaway; those data were analyzed in studies [19, 20].

In the paper [16] there was shown by experiments that an exothermic reaction of the thermal runaway in nickel-cadmium batteries is the reaction of a recombination of accumulated atomic hydrogen:

$$H_{ads\ Cd} + H_{ads\ Ni} \rightarrow H_2 \uparrow, \tag{5.10}$$

which runs in line with the electrochemical mechanism:

$$H_2O + H_{ads} + e^- \rightarrow H_2\uparrow + OH^- \text{ (cathode)} \tag{5.11}$$

$$H_{ads} + OH^- \rightarrow H_2O + e^- \text{ (anode)} \tag{5.12}$$

Hydrogen is present inside of battery electrodes in the form of metal-hydrides, i.e., in atomic form [13]. Reaction 5.10 is a powerful exothermic reaction with heat dissipation in the amount of 436 kJ/mole (hydrogen) [20, 43]. This heat buildup is more intensive than in the case of hydrogen combustion reaction in oxygen, which generates 285.8 kJ/mole (hydrogen) [44, 45].

A rate-limiting step for reaction 5.10 on both a cathode and an anode is found to be a stage of the metal-hydrides disintegration [16].

$$MeH_x \rightarrow Me + H_x. \tag{5.13}$$

Based on all the available experimental data in the papers [16, 18, 19], a new thermal runaway mechanism was proposed. In these papers, it was shown that there are two processes of accumulation that (step-by-step) bring the nickel-cadmium batteries to the thermal runaway. Firstly, there is the process of hydrogen accumulation inside of battery electrodes during their operation. Secondly, there is the process of dendrite accumulation on the cadmium electrodes of the nickel-cadmium batteries. In the papers [28, 29], it was shown that in the course of a long operation of the KSX-25 batteries, in their electrodes, up to 800 liters of hydrogen is accumulated. A thermal runaway initiation is connected with dendrites intergrowth through a separator. In the spot where the dendrite is located, a distance between the electrodes gets cut to a large extent. As a result of this event, in this spot, current density will be much more than in other places on the electrodes. So, this spot will be heated up much more intensively than other parts of electrodes.

As it was shown in the papers [16–20], under electrodes temperature growth, metal hydrides disintegration speeds (reaction 5.13) will rise steeply. For a cadmium electrode at temperatures higher than 340 °C, a rapid disintegration of cadmium hydrides starts, while as for oxide-nickel electrodes, at temperatures higher than 660 °C and even at temperatures half as much, the hydrides disintegration speed is considerably high. According to the studies [16], the hydrides disintegration (eq. 5.13) is a limiting step for electrochemical reactions (eqs. 5.11, 5.12). So, the speeds of the electrochemical reactions (eqs. 5.11, 5.12) can increase a hundred times in proportion to the metal hydrides disintegration growth speed. The above-mentioned temperatures that are high enough are not impossible for the nickel-cadmium batteries. For example, the temperature evaluation in the spots of the thermal runaway as judged by thermal traces on the electrodes (Figure 5.3) showed that during the thermal runaway in these spots, the temperature was much higher than 800 °C. So, the role of the electrochemical reactions (reactions 5.11, 5.12) can become determinative (during batteries charging) at high temperatures that can be created in local spots on electrodes at the expense of dendrites intergrowth.

The electrochemical reactions taking place on metal hydrides (eqs. 5.11, 5.12) are the exothermic reaction proceeding with very high heat production (436 kJ/mole) (hydrogen) [43]. This is why its initiation in a spot of a dendrite intergrowth will lead to even higher electrodes local heating-up in those spots; and in turn, this will lead to even more mass disintegration of hydrides on both electrodes and thus to reaction speeds increasing (eq. 5.11, 5.12). The exothermic reaction (5.10) requires new hydrides for its continuation. In a spot of the reaction initiation (5.10), they will be exhausted; and reaction will shift radially from this point burning

a separator in a form of regular circles, which indeed is observed in the experiments (Figure 5.3 and papers [16, 18, 19]).

Two factors can prevent this exothermic reaction expansion on the entire electrode: Firstly, there is a gas lock, which is formed in a hole of a burned down separator as well as between the electrodes after an evaporation of electrolyte. The second factor is an exhaustion of hydrogen in the electrodes in the thermal runaway location.

This is exactly what the thermal runaway process is. Under regular conditions of alkaline batteries operation, a current generated by electrochemical reactions (5.11, 5.12) is rather small. Even at the charge voltage 1.87V, the current generated by the electrochemical reactions (5.11, 5.12) in a KSX-25 battery is equal to approximately 0.22A [16]. However, in the case of the thermal runaway occurrence, the current generated by the electrochemical reactions (5.11, 5.12) becomes equal to hundreds of amperes; along with it, the voltage on battery terminals falls to values from 0.5 to 0.6V (Figure 5.4) in line with voltage for the reactions (5.11, 5.12) [16].

So, knowing the thermal runaway mechanism, it is possible to induce this phenomenon artificially and reliably. Indeed, for launching of the thermal runaway electrochemical reactions (5.11, 5.12), a great local heating of electrodes is necessary. Under natural conditions of the KSX-25 batteries operation, this is reached at the expense of dendrites sprouting through a separator.

But a powerful local heat-up of electrodes can be caused artificially, too. For this, it is enough to give a voltage to battery terminals sufficient for breakdown through a distance between electrodes in a battery.

In our experiments, the thermal runaway process turned out to be initiated reliably after supplying an impulse of charging voltage to battery terminals more than 100V during 0.5 seconds. Afterwards, for the thermal runaway maintenance, it was sufficient to just keep the charging voltage on the battery terminals more than 1.5V. In our experiments, for the thermal runaway process support, we used the voltage 1.87 V most often.

So, a process of an initiation of the hydrogen desorption with use of the thermal runaway method requires 0.5 seconds. This value exceeds the requirements set by the U.S. DOE for initiation of a hydrogen desorption process ten times (Table 5.4, criterion 2). Besides which, the time of the hydrogen desorption initiation based on the thermal runaway method can even be decreased as a way of increasing the voltage of the breakdown through the distance between electrodes. In order to stop the process of hydrogen desorption, it is enough to stop the electrochemical reactions (5.11, 5.12), i.e., to stop the battery charging process. This can be done virtually instantly. Hence, in the framework of this method, the fourth criterion of the U.S. DOE is satisfied, too (Table 5.4).

It should be noted that in the case of use of the thermal runaway method, the hydrogen desorption process rate can be regulated by electrotechnical methods. With this purpose in mind, let us assess the thermal runaway parameters represented in Figure 5.4. The voltage on the battery terminals in the thermal runaway process is approximately equal to 0.55V, the voltage of the recharger is 1.87V and the maximum current is 342A (Figure 5.4). Therefore, the resistance of the shunt and connecting leads is equal to 0.0039 Ω. Approximately, this resistance value corresponds to direct measures of the shunt and connecting leads resistance. So, the maximum current of the thermal runaway can be decreased by decreasing the voltage of the recharger or increasing the external chain resistance. As a result, the thermal runaway intensity is expected to be decreased proportionally and consequently the hydrogen desorption rate will also be less.

Let us study the battery parameters at the thermal runaway, while using the same recharger voltage (i.e., 1.87V) but increasing by two times the resistance of the shunt and connecting leads. In the experiments, the battery was used with the same operative life as in Figure 5.4. The thermal runaway initiation was conducted according to the method described above.

As a result, the top current of the thermal runaway decreased approximately twice and the full flow rate of hydrogen desorption fell almost nine times down to 0.137 wt% s^{-1} [37].

This way, in the framework of the thermal runaway method used, it is possible to set any required rate of hydrogen desorption. Along with this, in order to perform the hydrogen desorption at small rates in accordance with the requirements of the U.S. DOE (Table 5.4), it is possible to avoid an electrolyte boil-off and a gas block formation between the electrodes, which physically interrupt the reactions (5.11, 5.12) (Figure 5.4). Indeed, according to the equation (5.10), an energy release at the thermal runaway is proportional to the volume of the hydrogen released. This way, by regulating the hydrogen release rate, we shall regulate the energy release too. In this case, a hydrogen storage system (based on the thermal runaway method) will be a system completely controlled by electrotechnical methods. Hence, it will be possible to work in any mode of the hydrogen desorption

5.5 Conclusions

In conclusion, we would like to highlight a number of advantages of the proposed method of hydrogen desorption from metal-hydrides compared to the widely accepted thermo-chemical method.

Firstly, we would like to draw attention to a feature of electrochemical reactions (5.11, 5.12). These electrochemical reactions do not depend on a specific metal. This is why they will proceed on any metals able to form hydrides. Of course, the speed of these reactions on various metals will be different as they depend on the disintegration rate of specific hydrides and on the speed of hydrogen atoms diffusion in these metals [16]. So, the thermal runaway method can be used for hydrogen desorption from any metal-hydrides. For this purpose, in hydrogen storage systems, metal-hydrides should be used not in a form of powders but instead in a form of sintered matrices in an alkaline electrolyte. Besides, as the preliminary experiments showed, sintered matrices can be used as positive and negative electrodes from any metals or alloys able to accumulate hydrogen. Thus, in its scope, this method of hydrogen desorption is identical to the traditional thermo-chemical method.

Secondly, regarding its kinetic and thermodynamic parameters, the thermal runaway method is far superior to the criteria of the U.S. DOE [14] as well as to the best values obtained in the framework of the traditional thermo-chemical method [6–13]. In order to work, it does not require any certain values of temperature or pressure; it can work at any ambient temperature and pressure.

Furthermore, the energy needed for supporting the hydrogen desorption in the case of the thermal runaway method is 140 times less than the energy, which is released by the system of the hydrogen accumulating along with it [20]. Thus, for it to work (unlike the traditional thermo-chemical method), the thermal runaway method does not require any additional energy expenses. On the contrary, when the thermal runaway method is used for hydrogen desorption, a lot of energy is released, which can be used profitably.

Thirdly, the hydrogen desorption in the thermal runaway method runs with the aid of electrochemical reactions (5.11, 5.12). This is why this process is easily controllable by electrotechnical methods, and hence it is much less inertial than the thermal processes used in the traditional method.

Of course, for wide technological introduction of the hydrogen desorption process in the thermal runaway method, further investigations are needed, both theoretical and experimental. Although the experimental investigations which have already been conducted show that this method is very promising. That is why we hope that the studies represented in this chapter will constitute a basis for new hydrogen storage technologies.

References

1. Liu, Z., A preface to the special issue section on "Aspects of hydrogen energy and environmental impact." *Int. J. Hydrogen Energy* 42, 5439, 2017.

2. Scipioni, A., Manzardo, A., Ren, J. (Eds.), *Hydrogen Economy: Supply Chain, Life Cycle Analysis and Energy Transition for Sustainability*, Academic Press: San Diego, 2017.
3. Winter, C.-J., Hydrogen energy—Abundant, efficient, clean: A debate over the energy-system-of-change. *Int. J. Hydrogen Energy* 34, S1, 2009.
4. Chun, D., Woo, C., Seo, H., Chung, Y., Hong, S., Kim, J., The role of hydrogen energy development in the Korean economy: An input–output analysis. *Int. J. Hydrogen Energy* 39, 7627, 2014.
5. Das, L.M., Dutta, V., Hydrogen energy activities in India. *Int. J. Hydrogen Energy* 40, 4280, 2015.
6. Sakintuna, B., Lamari-Darkrim, F., Hirscher, M., Metal hydride materials for solid hydrogen storage: A review. *Int. J. Hydrogen Energy* 32, 1121, 2007.
7. Shahi, R.R., Yadav, T.P., Shaz, M.A., Srivastva, O.N., Studies on dehydrogenation characteristic of $Mg(NH_2)_2$/LiH mixture admixed with vanadium and vanadium based catalysts (V, V_2O_5 and VCl_3). *Int. J. Hydrogen Energy* 35, 238, 2010.
8. Shi, S., Hwang, J.Y., Research frontier on new materials and concepts for hydrogen storage. *Int. J. Hydrogen Energy* 32, 224, 2007.
9. Kojima, Y., Kawai, Y., Haga, T., Magnesium-based nanocomposite materials for hydrogen storage. *J. Alloys Compd.*, 424, 294, 2006.
10. Shang, C.X., Bououdina, M., Song, Y., Guo. Z.X., Mechanical alloying and electronic simulations of (MgH_2 + M) systems (M = Al, Ti, Fe, Ni, Cu and Nb) for hydrogen storage. *Int. J. Hydrogen Energy* 29, 73, 2004.
11. Oelerich, W., Oelerich, B., Klassen, T., Bormann, R., Metal oxides as catalysts for improved hydrogen sorption in nanocrystalline Mg-based materials. *J. Alloys Compd.* 315, 237, 2001.
12. Polanski, M., Bystrzycki, J., Comparative studies of the influence of different nano-sized metal oxides on the hydrogen sorption properties of magnesium hydride. *J. Alloys Compd.* 486, 697, 2009.
13. Broom, D.P., *Hydrogen Storage Materials: The Characterisation of Their Storage Properties*, Springer, 2011.
14. Hydrogen, Fuel Cells & Infrastructure Technologies Program. Multi-year research, development and demonstration plan. Planned program activities for 2005–2015, U.S. Department of Energy, Energy Efficiency and Renewable Energy, 2009.
15. Alefeld, G., Volkl, J. (Eds.), *Hydrogen in Metals: Basic Properties*, vol. 1, Springer-Verlag: Berlin, 1978.
16. Galushkin, N.E., Yazvinskaya, N.N., Galushkin, D.N., study of thermal runaway electrochemical reactions in alkaline batteries. *J. Electrochem. Soc.* 162, A2044, 2015.
17. Galushkin, D.N., Yazvinskaya, N.N., Galushkin, N.E., Investigation of the process of thermal runaway in nickel-cadmium accumulators. *J. Power Sources* 177, 610, 2008.
18. Galushkin, N.E., Yazvinskaya, N.N., Galushkin, D.N., Galushkina, I.A., Thermal runaway in sealed alkaline batteries. *Int. J. Electrochem. Sci.* 9, 3022, 2014.

19. Galushkin, N.E., Yazvinskaya, N.N., Galushkin, D.N., Galushkina I.A., Causes analysis of thermal runaway in nickel-cadmium accumulators. *J. Electrochem. Soc.* 161, A1360, 2014.
20. Galushkin, N.E., Yazvinskaya, N.N., Galushkin, D.N., The mechanism of thermal runaway in alkaline batteries. *J. Electrochem. Soc.*, 162, A749, 2015.
21. Galushkin, N.E., Yazvinskaya, N.N., Galushkin, D.N., Galushkina, I.A., Probability investigation of thermal runaway in nickel-cadmium batteries with sintered, pasted and pressed electrodes. *Int. J. Electrochem. Sci.* 10, 6645, 2015.
22. Yazvinskaya, N.N., Galushkin, N.E., Galushkin, D.N., Galushkina, I.A., Probability investigation of thermal runaway in nickel-cadmium batteries with pocket electrodes. *Int. J. Electrochem. Sci.*, 11, 5850, 2016.
23. Yazvinskaya, N.N., Galushkin, N.E., Galushkin, D.N., Galushkina, I.A., Hydrogen amount estimation in electrodes of nickel-cadmium batteries depending on their operating life. *Int. J. Electrochem. Sci.* 11, 7843, 2016.
24. Yazvinskaya, N.N., Galushkin, N.E., Galushkin, D.N., Galushkina, I.A., Study of effect of batteries capacity on probability of thermal runaway occurrence. *Int. J. Electrochem. Sci.* 11, 8163, 2016.
25. Yazvinskaya, N.N., Galushkin, N.E., Galushkin, D.N., Galushkina, I.A., Analysis of thermal runaway aftereffects in nickel-cadmium batteries. *Int. J. Electrochem. Sci.* 11, 10287, 2016.
26. Yazvinskaya, N.N., Galushkin, N.E., Galushkin, D.N., Galushkina, I.A., Processes of hydrogen release relaxation at thermal decomposition of electrodes of nickel-cadmium batteries. *Int. J. Electrochem. Sci.* 12, 2791, 2017.
27. Guo, Y., Thermal runaway, in: *Encyclopedia of Electrochemical Power Sources*, Garche, J. (Ed.), vol. 4, pp. 241–253, Elsevier: Amsterdam, 2009.
28. Galushkin, N.E., Yazvinskaya, N.N., Galushkin, D.N., Ni-Cd batteries as hydrogen storage units of high-capacity. *ECS Electrochem. Lett.* 2, A1, 2013.
29. Galushkin, N.E., Yazvinskaya, N.N., Galushkin, D.N., Galushkina, I.A., Oxide-nickel electrodes as hydrogen storage units of high-capacity. *Int. J. Hydrogen Energy* 39, 18962, 2014.
30. Galushkin, N.E., Yazvinskaya, N.N., Galushkin, D.N., Pocket electrodes as hydrogen storage units of high-capacity. *J. Electrochem. Soc.* 164, A2555, 2017.
31. Antonov, V.E., Phase transformations, crystal and magnetic structures of high-pressure hydrides of d-metals. *J. Alloys Compd.* 330–332, 110, 2002.
32. Alefeld, G., Völkl, J. (Eds.), *Hydrogen in Metals: Application-Oriented Properties*, vol. 2, Springer-Verlag: Berlin, 1978.
33. Bernardini, M., Comisso, N., Davolio, G., Mengoli, G., Formation of nickel hydrides by hydrogen evolution in alkaline media. *J. Electroanal. Chem.*, 442, 125, 1998.
34. Bernardini, M., Comisso, N., Mengoli, G., Sinico, L., Formation of nickel hydrides by hydrogen evolution in alkaline media: Effect of temperature. *J. Electroanal. Chem.* 457, 205, 1998.
35. Borgschulte, A., Lohstroh, W., Westerwaal, R.J., Schreuders, H., Rector, J.H., Dam, B., Griessen R., Combinatorial method for the development of a catalyst promoting hydrogen uptake. *J. Alloys Compd.* 404–406, 699, 2005.

36. *Hydrogen Systems*, vol. 1, pp. 550–553, Pergamon Press: Oxford, 1986.
37. Galushkin, N.E., Yazvinskaya, N.N., Galushkin, D.N., Thermal runaway as a new high-performance method of desorption of hydrogen from hydrides. *Int. J. Hydrogen Energy* 41, 14813, 2016.
38. Dornheim, M., Barkhordarian, G., Bosenberg, U., Eigen, N., Borgschulte, A., Keller, C., *et al.*, Mg-based reactive hydride composites for hydrogen storage?, in: International Workshop on Functional Materials for Mobile Hydrogen Storage, 20–22 Sept. Geesthacht, Germany, 2006.
39. Dornheim, M., Doppiu, S., Barkhordarian, G., Boesenberg, U., Klassen, T., Gutfleisch, O., *et al.*, Hydrogen storage in magnesium-based hydrides and hydride composites. *Scr. Mater.* 56, 841, 2007.
40. Puszkiel, J., Gennari, F.C., Larochette, P.A., Troiani, H.E., Karimi, F., Pistidda, C., *et al.*, Hydrogen storage in Mg–$LiBH_4$ composites catalyzed by FeF_3. *J. Power Sources*, 267, 799, 2014.
41. Ma, L.P., Wang, P., Cheng, H.M., Hydrogen sorption kinetics of MgH_2 catalyzed with titanium compounds. *Int. J. Hydrogen Energy* 35, 3046, 2010.
42. Vincent, C.A., Scrosati, B., *Modern Batteries*, 2nd ed., pp. 312–315, Butterworth-Heinemann: Oxford, 1997.
43. Blanksby, S.J., Ellison, G.B., Bond dissociation energies of organic molecules. *Acc. Chem. Res.* 36, 255, 2003.
44. National Research Council and National Academy of Engineering, *The Hydrogen Economy: Opportunities, Costs, Barriers, and R&D Needs*, pp. 240–242, National Academies Press, Washington, 2004.
45. Suban, M., Tusek, J., Uran, M., Use of hydrogen in welding engineering in former times and today. *J. Mater. Process. Technol.* 119, 193, 2001.

PART II

CARBON-BASED MATERIALS FOR HYDROGEN STORAGE

Mehmet Sankir and Nurdan Demirci Sankir (eds.) Hydrogen Storage Technologies,
(177–196) © 2018 Scrivener Publishing LLC

6

Activated Carbon for Hydrogen Storage Obtained from Agro-Industrial Waste

Yesid Murillo-Acevedo[1], Paola Rodríguez-Estupiñán[1], Liliana Giraldo Gutiérrez[2] and Juan Carlos Moreno-Piraján[1,*]

[1]Porous Solids and Calorimetry Research Group, Department of Chemistry, University of los Andes, Bogotá, Colombia
[2]Calorimetry Research Group, Department of Chemistry, National University of Colombia, Bogotá, Colombia

Abstract

Hydrogen is not easy to find in nature and can be produced from renewable sources through photoelectrochemical methods, biological processes and eolic energy. Some of the wastes used in activated carbon (AC) preparation are: almond shell, hazelnut shell, olive stone, coffee grounds, coconut shell, rachis of chicken feathers, among others. Chemical or physical activation is used in the preparation of AC to obtain surface areas between 200–1200 m^2/g, but its values depend on the precursor composition and activation method.

Hydrogen storage is related to high surface areas of adsorbents, that is, high microporosity percentage. The AC obtained from agro-industrial wastes show different adsorption capacities by weight. The adsorption is due to van der Waals forces and is important in this type of system.

In this chapter, the aim is to compare different ACs obtained from agro-industrial wastes in hydrogen storage to evaluate its efficiency in relation to the precursors used.

Keywords: Hydrogen storage, activated carbon, agro-industrial waste, adsorption isotherm, isosteric heat adsorption

**Corresponding author*: jumoreno@uniandes.edu.co

Mehmet Sankir and Nurdan Demirci Sankir (eds.) Hydrogen Storage Technologies, (179–196) © 2018 Scrivener Publishing LLC

6.1 Introduction

Hydrogen is important as an energy source, that is, it has a high energy density per unit mass; for example, if you compare its efficiency in the application as a fuel with respect to gasoline [1, 2]. In Table 6.1, an increase of 3.6 times in energy density per liter can be observed for gasoline compared to hydrogen. That is, a gallon of gas generates the same energy density as 3.6 gallons of hydrogen, but if it is compared by its density of mass it is observed that the 3.6 gallons weigh 2.7 times less than the gallon of gasoline [3].

Additionally, hydrogen is considered a green fuel because its combustion does not generate products that affect the environment and human life (reaction 6.1), compared to the combustion of fossil fuels (reaction 6.2) [4].

$$2H_2 + O_2 \rightarrow 2H_2O\Delta H = -482kJ \tag{6.1}$$

$$CH_4 + 2O_2 \rightarrow CO_2 + 2H_2O\Delta H = -810kJ \tag{6.2}$$

Unlike fossil fuels, hydrogen is not easily found in nature and can be produced from renewable resources through photoelectrochemical methods [5], biological processes [6] and wind energy [7].

In its application as fuel, it can be used in internal combustion engines [8] or in fuel cells [9]. However, in its future prospects there is an option for it to be used in home devices, which would require the support of adequate storage technologies that allow safe transport through different conventional methods and the ability to be fed to a fuel cell [10].

The operation of fuel cells requires methods that allow the storage of hydrogen [11], among which are: compressed gases [12], liquefaction [13], metal hydrides [14], among others. Currently, the first two are the most used methods.

Compressed gas is the technology that has been most researched, because hydrogen can be stored at high pressures between 200–700 bar in

Table 6.1 Physical parameters of gasoline and hydrogen fuel.

	Fuel	**Hydrogen**
Energy Density	31 MJ/Liter (44 MJ/kg)	8.5 MJ/Liter (120 MJ/kg)
	117.8 MJ/Gallon	120 MJ/Kg
Mass Density	0.7 kg/Liter	0.071 kg/Liter

special gas containers, which present a high cost and consume energy in large-scale applications [10, 15].

The storage of hydrogen in liquid state reaches a high gravimetric capacity, but the process consumes 30–40% of the stored energy. In the liquefaction process, compressors are used, in which heat exchangers and expansion valves achieve the desired cooling temperature [13].

However, there is the possibility of combining the benefits of gas liquefaction and storage at high pressure. In these processes, high-pressure cryogenic containers are used in which a mass capacity of 7.5 wt% and a volumetric capacity of 40 g/L can be achieved [16].

Now the previously mentioned methods do not meet the criteria for capacity, size, efficiency, cost and safety. For this reason, different investigations have focused on hydrogen adsorption processes in porous materials [17, 18] such as activated carbon (AC) [19] prepared from agro-industrial waste [20–24]. The United States Department of Energy has established different objectives for hydrogen storage systems, where the minimum gravimetric and volumetric capacity are included (Table 6.2).

The objectives that have been set for storage are high and still difficult to achieve, which is why hydrogen adsorption has become a viable and promising storage method. This is because the adsorption/desorption cycle exhibits rapid kinetics and is a completely reversible system. For this purpose, different porous materials have been used such as zeolites [25], metal-organic framework (MOF) [26], nanoporous carbons [27], graphene [28] and activated carbons [17, 19, 21–24, 29].

The oil price crisis has reduced export revenues for countries such as Colombia, this has led to rethinking economic policies. Thus, the agro-industry is presented as an opportunity in a system of global food supply and demand.

Table 6.2 Maximum capacities of storage systems.

Storage	**Units**	**2020**	**2025**
Gravimetric System			
Specific usable energy (net useful energy / maximum system mass)	kWh/kg (kg H_2/kg system)	1.5 (0.045)	1.8 (0.055)
Volumetric System			
Usable Energy Density (net useful energy / maximum system mass)	kWh/L (kg H_2/L system)	1.0 (0.030)	1.3 (0.040)

Activated carbons (ACs) can be obtained from artificial and natural precursors, with high fixed carbon content. Of the natural ones, cellulosic or lignocellulosic precursors are preferred because they have high density and volatile matter content, this allows the obtainment of materials with greater resistance and yield [30]. For example, fruit husks, seeds, and other agro-industrial by-products have been used to obtain granular ACs. Specifically, some waste that has been used in the preparation of AC are: almond shell [31], hazelnut peel [32], olive stones [33], coffee beans [34], African palm kernel [35], coconut shell [35], orange peel [36], tangerine peel, chicken feather rachis, among many others.

In the next four decades, food production will exponentially increase; it should increase between 70–100% by 2050 according to the world population growth (9000 million people). According to the United Nations Food and Agriculture Organization (FAO), Colombia is considered as a nation in the world food pantry, because it has extensions of land to expand the agricultural frontier. Among the growing industries are the coconut industry, African palm industry and poultry industry.

However, industries generate different types of waste that are disposed of and are not exploited, such as: coconut shell (CS), African palm kernel (APK) and rachis of chicken feathers (RCF). This type of waste can be disposed of incorrectly and end up in rivers and sewers, causing environmental problems. These types of wastes are analyzed for the purpose of determining the main selection criteria of precursors in the preparation of AC.

6.2 Experimental

The precursors using CS, APK and RCF were subjected to different activations under the conditions described below:

1. Coconut Shell: CA monoliths from CC are obtained by chemical activation with $ZnCl_2$, the precursor was ground to a particle size <38 μm, and it was added to a $ZnCl_2$ solution of 40 wt% for 7 h at 85 °C; the mixture was heated until all the solution was evaporated. The impregnated particles were compacted at a pressure of 150 MPa in a cylindrical mold 2 cm in diameter at 150 °C. The monoliths were carbonized in a horizontal furnace at a heating rate of 2 °C min^{-1}, nitrogen flow 100 mL min^{-1} to 500 °C with a residence time of 1 h.
2. African Palm Kernel: The African palm kernel was ground to a particle size of 2 mm and subsequently it was impregnated

with a LiOH solution at a 1:2 ratio (LiOH: Palm kernel) at 100 °C. The dry and impregnated sample is subjected to different levels of microwave irradiation and exposure times. The obtained sample must be cooled and washed to match the pH of the distilled water.

3. Rachis of Chicken Feather: The feathers are cleaned manually and separated from the rachis, the latter is the precursor, and this is dried at 50 °C and cut to a length of 2 cm. Subsequently, a thermal treatment is carried out under nitrogen atmosphere for 24 h, and the material obtained is sieved to a particle size between 0.27 to 0.55 mm. Prior to the activation process the sample should be dried at 105 °C for 24 h, which is carbonized under nitrogen atmosphere at a heating rate of 5 °C/min and 3.5 h residence at the desired temperature.

6.3 Results and Discussion

The CS and APK precursors have a high composition percentage of cellulose and lignin (see Table 6.3). However, it is observed that the cellulose percentage is double for the CS. On the other hand, the percentage of lignin for CS and APK corresponds to 46 and 50%, these are close values (see Figure 6.1). The RCF in comparison to the other precursors is composed mainly by proteins, the most abundant is the keratin form of 90% keratin, 8% water and 1% lipids (see Figure 6.2) [37, 38].

Another parameter for selection of the precursors is that they have a low inorganic matter content; as seen in Table 6.4 the percentage of ash is in a

Table 6.3 Composition of agro-industrial and poultry residues.

	Cellulose (%)	**Lignin (%)**	**Hemicellulose (%)**	**Keratine (%)**	**Others (%)**
Coconut Shell	14	46	32	–	8
African Palm Kernel	7	50	26	–	17
Rachis of Chicken Feathers	–	–	–	90	10

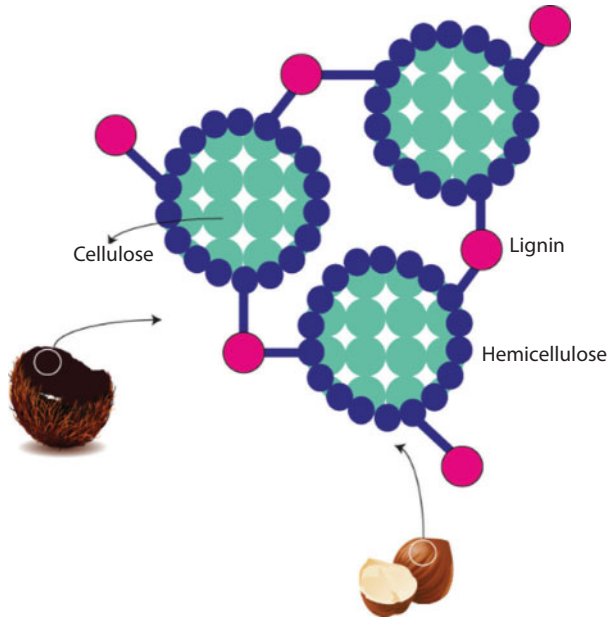

Figure 6.1 Spatial arrangement of cellulose hemicellulose and lignin in the cell walls of lignocellulosic biomass.

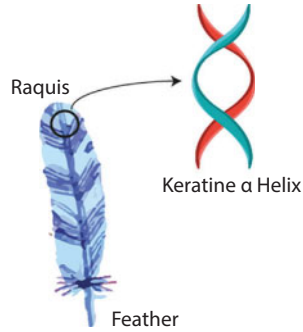

Figure 6.2 A general schematic view of the structural components of the feather rachis.

range between 0.31–1.49%. On the other hand, the percentages of volatile matter are high, between 72–79%, which is important because this parameter allows a greater control of the performance in the preparation of the CA. The proximate analysis of these three materials shows a fixed carbon content suitable for the production of AC [39, 40].

In the production of AC, an activation process must be carried out; in this process, the low porosity precursor is converted to a porous material

Table 6.4 Proximate analysis precursors.

	Moisture (%)	Volatile matter (%)	Ash (%)	Fixed carbon (%)
Coconut Shell	2,06	79,0	0,31	18,7
African Palm Kernel	11,0	72,0	1,00	16,0
Rachis of Chicken Feathers	12,3	78,0	1,49	8,18

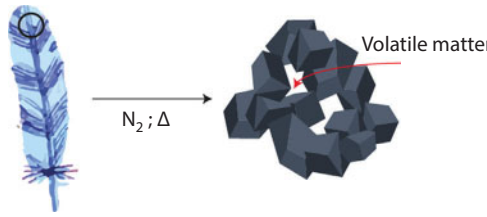

Figure 6.3 Thermal pyrolysis of turkey feathers.

with adsorbent characteristics. The methods used in its preparation are physical and/or chemical activation, where the development of porosity occurs by different mechanisms and depends on the methodology used.

Carbonization is a thermal treatment carried out in the presence of an inert gas, generally nitrogen, whose objective is to eliminate non-carbonaceous species and convert the precursor into a mass of carbon; this structure has a porosity that is blocked by the condensation of volatile matter and tars that are subsequently distilled in pyrolysis (Figure 6.3) [41].

In these processes it is important to consider the variables that affect the process such as heating rate, final carbonization temperature and residence time. These variables influence the char structure obtained.

Figures 6.4 and 6.5 show the thermal stability of the APK and RCF obtained by thermogravimetry.

Figure 6.4 shows the pyrolysis of the APK in which two processes are evident: (I) between 200–320 °C with a maximum speed at 280 °C and (II) 320–380 °C with a maximum speed at 360 °C. In Table 6.3, it is shown that the main components of the precursor are cellulose (7%), lignin (50%) and

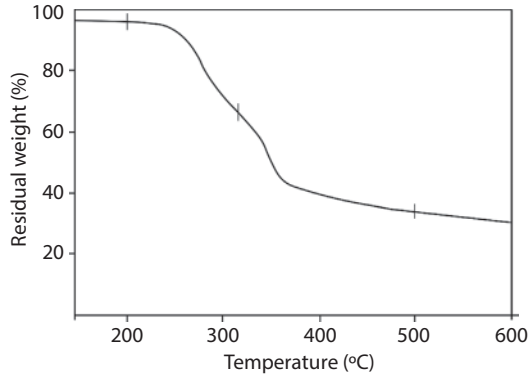

Figure 6.4 Thermogravimetric curve for palm kernal shell.

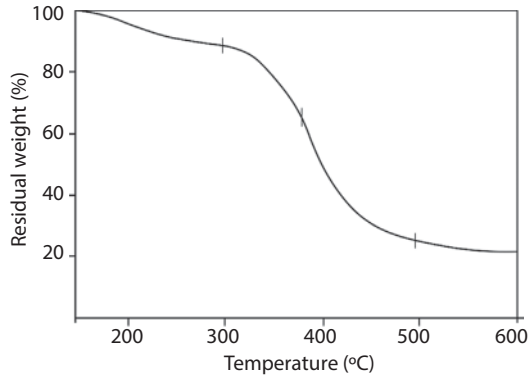

Figure 6.5 Thermogravimetric curve for chicken feathers crude.

hemicellulose (26%). Generally, in lignocellulosic materials it is observed that decomposition processes occur at temperatures between 150–400 °C. Different research has found that lignin decomposes at low temperatures of approximately 170 °C, followed by hemicellulose and cellulose that decompose in a range between 200–400 °C where the highest percentage of mass loss occurs [38].

It is important to clarify that there are differences between the pyrolysis process of APK and RCF due to the differences in composition that exist between lignocellulosic materials. Other variables that have been found in this type of analysis are the way in which each species is cultivated, including the weather and other factors.

In the chicken feather rachis, the main component is keratin in which a loss of 30% at 200 °C is observed in the TGA (Figure 6.5). However, when the temperature increases between 300–450 °C, high mass loss of 72% occurs. In the pyrolysis of this material different compounds containing N and S are produced, which come from the amino acids that make up the protein. Nitrogen is present in aromatic and aliphatic nitriles, pyrroles, pyridines and amides, while S is present as sulfides, thiols, thiazoles and thiophenes [41].

Another methodology for obtaining AC is chemical activation, in which a reaction is carried out between the activating agent and the precursor in inert atmosphere. The porous structure is developed due to the thermal process that is carried out and its textural characteristics depend on the activating agent used in its preparation.

The effect of activating agents on the activation processes are:

- $ZnCl_2$ Activation: Generally, $ZnCl_2$ is used as an activating agent with precursors that have a high content of oxygen PE lignocellulosic materials. There is a high reactivity between the hydroxyl groups of the lignocellulosic material and the activating agent. The acidity of the $ZnCl_2$ solution generates the degradation of lignin and cellulose due to the solvation of Zn ions and proton production that catalyze degradation reaction equation 6.3.

$$Zn[H_2O]_2^{+2} \leftrightarrow ZnOH[H_2O]_5^{+} + H^{+} \tag{6.3}$$

When the impregnated material is added to thermic treatment a high amount of water vapor can be observed due to the dehydration process. For this reason, the activating agent is considered a Lewis acid that produces Zn-O complexes and it can interact with non-bonding electrons of oxygen found in lignocellulosic materials as OH groups and form bonds between monomers (Figure 6.6).

After these reactions, randomly oriented carbonaceous structures are obtained. In these structures can be produced spaces that increase the surface area compared with the biopolymers that composed the lignocellulosic materials. The thermal activation process is related to the melting point of $ZnCl_2$. Generally, the temperature used is between 300–600 °C. The activating agent is volatilized at high temperatures (756 °C), causing a decrease in pore volume and surface area. On the other hand, the concentration variation produces different textural parameters, for example, to lower relation

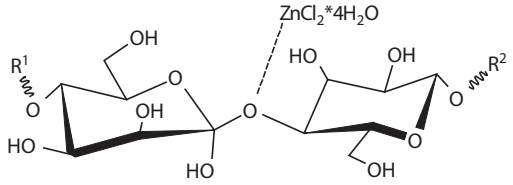

Figure 6.6 $ZnCl_2$ effect in lignocellulosic materials.

Table 6.5 Zn concentration effect on development of microporosity.

Sample	SBET (m^2/g)	Vo (cm^3/g)	Vmeso (cm^3/g)	Vtotal (cm^3/g)	% Microporosity
0,15 g Zn/g AC	660	0,26	0,03	0,29	89,7
0,17 g Zn/g AC	845	0,34	0,02	0,36	94,4
0,19 g Zn/g AC	884	0,35	0,03	0,38	95,1
0,23 g Zn/g AC	924	0,37	0,01	0,38	97,3

(0,71 g Zn/g AC) in obtained microporous materials (Table 6.5). However, the increase in surface area and pore volume is related to heterogeneous microporous materials [42].

Hydroxide/Microwave Activation: The activation with metal hydroxides is different from that carried out with $ZnCl_2$. Generally, this activation is used with high-rank carbons or chars due to the carbonaceous structure reaction with activating agent after the carbonization process. This process is carried out in three steps: (I) Disorganized carbon atoms are removed from carbonaceous matrix, (II) Carbon atoms are converted in carbonate and (III) Metallic atoms are produced due to hydroxide reduction and interlayer between graphenic layers [42]. The general reaction of the process is shown in the following equation 6.4:

$$MOH + C \leftrightarrow M + H_2 + M_2CO_3 \tag{6.4}$$

In the conventional activation processes, the heat source is located in the environment of material. For this reason, the heat is transferred to

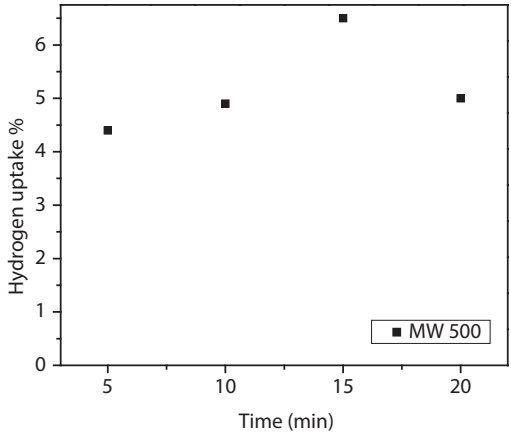

Figure 6.7 Effect in the hydrogen storage: Time of irradiation.

material by convection, conduction and radiation. However, the external surface of the material is mostly exposed compared with the internal part and it which generate temperature gradients.

The difference in conventional and microwave activation processes is related to heating patterns. In other words, the heat is generated by molecules reorientation because of electromagnetic waves at that frequency carried directly over activating agents. Among other benefits are found the elimination of temperature gradients and selective heating for chemical reactions.

The lignocellulosic materials are considered poor radiation absorbers, which is a reason for seeking activating agent be the main absorber. In this way the waves interact directly with the particles within the material, providing a fast volumetric heating. In summary, different research in the area claims that microwave radiation is used to generate high sintering temperatures, short processing times and high energy saving [42].

- High pressure adsorption of hydrogen to –196 °C

Of the precursors used, the AC obtained by Kernel Palm Shell shows high adsorption capacity of hydrogen with a maximum of 6.5%. The adsorption capacity is affected by irradiation time and power. As shown in Figure 6.7, the irradiation time increases to constant power as well as hydrogen adsorbed amount. But when the irradiation time increases up to 15 minutes it shows that the adsorbed amount decreases. That is, the maximum values of adsorption can be obtained at 15 minutes of irradiation [17, 43].

Different research about gas storage has introduced different variables into the preparation of porous materials and it has been found that the textural parameters, such as porosity, surface area and adsorption heat, are important in this application.

The isotherms obtained of these materials are characteristic of micro- and mesoporous materials, which according to IUPAC classification are type 1(a) and 4. The hysteresis presence (H4) is associated with micropores fill. Table 6.6 shows the textural parameters as surface area, micropore volume and total volume. Thus, the power increase produces high surface areas up to maximum 800W, but above this value a decrease in the textural parameters can be observed [44].

The pore size distribution is a parameter that allows describing the relation that exists between hydrogen storage and textural parameters. The adsorption process can be explained like a interaction Lennard-Jones site of a single center [45], which is described in the equation 6.5:

$$U_{gg}(r) = -4\varepsilon_{gg}\left[\left(\frac{\sigma_{gg}}{r}\right)^{6} - \left(\frac{\sigma_{gg}}{r}\right)^{12}\right] \tag{6.5}$$

where ε_{gg} and σ_{gg} represent the geometric and energetic parameters of LJ potential and r represents the intermolecular separation. That is, the relation between theoretical and experimental isotherms can be interpreted in terms of the generalized adsorption isotherm (equation 6.6):

$$N_{exp}(p/p_0) = \int_{H_{min}}^{H_{max}} N(p/p_0, w) f(w) dw \tag{6.6}$$

Table 6.6 Textural parameters of AC from palm kernel shells: Chemical activation (LiOH/microwaves).

Sample	SBET (m^2/g)	V_0 (cm^3/g)	Vmeso (cm^3/g)	Vt (cm^3/g)
CPA W600	750	0,34	0,03	0,37
CPA W700	810	0,37	0,05	0,42
CPA W800	1350	0,48	0,02	0,50
CPA W1000	1100	0,43	0,03	0,46

where $N_{exp}(p/p_0)$ are the experimental data of adsorption isotherm, w is the pore width, $N(p/p_0,w)$ is the simulated isotherm in a single pore width w and $f(w)$ is the distribution function of pore size.

The U.S. Department of Energy has established that the average optimum pore size is in a range between 5–6 angstroms. If different pore sizes are compared based on the molecular size of the hydrogen it is found that for pores larger than 10 Å the isotherms become linear but with a contribution in the amount adsorbed. However, if the pore sizes are less than 10 Å, it is found that there is high hydrogen adsorption due to the potential between the pore walls.

These interaction measures between the different pore sizes with the adsorbed amount can be correlated with the isosteric heat of adsorption and its variation depends on the coverage factor or the filling of pores. The energetic information that can be extracted is related to the energy characteristic of adsorbent-adsorbate, energetic sites distribution and adsorption mechanism. On the other hand, the primary pore size can be estimated with this parameter.

The isosteric heat of adsorption (q_{st}) is defined as the sum of heat due to the fluid-fluid interaction equivalent to heat of condensation (q_{f-f}), non-specific interaction fluid-solid (q_{f-s}) and specific interactions fluid-energetic sites ($q_{f-\mathrm{HES}}$) in the following equation 6.7:

$$q_{st} = q_{f-f} + q_{f-s} + q_{f-HES} \tag{6.7}$$

Figure 6.8 shows the contribution of isosteric heat of hydrogen adsorption in slit pores of different pore sizes. In the first step, the heat observed corresponds to the system where there is a low coverage factor in which it is assumed that molecules within any pore width equivalent to the kinetic diameter are isolated and there is no liquid phase within the pore. The heat of fluid-fluid interactions becomes insignificant [46, 47].

The interaction sites are high at low coverage and decrease with the factor (θ) increase. The high values are obtained due to interaction between solid surface with high concentration of energy sites.

In porous materials, the adsorption energy is increased by the effect of multiple interactions with adjacent walls. If the molecular size was very small compared to the pore size, the adsorption process would be comparable with adsorption on a flat surface.

The isosteric heat increases as the pore size decreases at any pressure. The attractive contribution of gas-gas interactions becomes strong in small pore sizes where the adsorbate structure can be more compact.

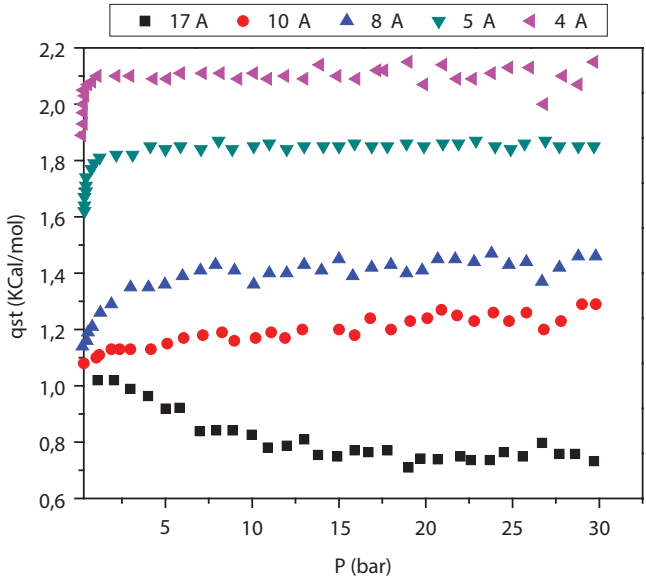

Figure 6.8 Isosteric enthalpy of adsorption of various effective widths for H_2 at 77K.

6.4 Conclusions

Activated carbons have been prepared from waste from different agro-industries in Colombia: poultry industry, African oil palm industry and coconut industry. The wastes used were chicken feather spine, coconut shell and palm kernel shell. The ACs were obtained by chemical activation and thermal treatment with different characteristics.

Different activation methods were used but it is observed that activation with LiOH and the use of different microwave irradiation powers allows increased storage capacity of hydrogen. This capacity is related to the textural characteristics, specifically with the pore size distribution.

The average pore widths desired to obtain greater storage are in a range between 3.6–10 Å. If the average diameter of the pore decreases, the hydrogen adsorption is increased. This is correlated with isosteric heat, which depends on pore geometry. That is, when the the pore size is closer to molecular size the isosteric heat increases due to the interactions existing within the pore walls.

The maximum hydrogen storage capacities proposed by the U.S. Department of Energy remain a challenge. The properly treated agro-industrial wastes allow the obtainment of porous materials that have adequate characteristics for energy storage. Although these did not reach the

objective, they can be considered an economic material and can be used in other applications that require smaller storage capacities.

Acknowledgments

The authors thank the Framework Agreement between the Universidad de los Andes and the Universidad Nacional de Colombia and the act of agreement established between the chemistry departments of the two universities. The authors appreciate the grant for the funding of research programs for Associate Professors, full Professors and Emeritus Professors, announced by the Faculty of Sciences of the Universidad de los Andes (Colombia), 11-28-2017, 2018-2019, according to the project "Thermodynamic Characterization of the Adsorption of Contaminants on Porous Adsorbents."

References

1. Eftekahari, A., Fang, B., Electrochemical hydrogen storage: Opportunities for fuel storage, batteries, fuel cells, and supercapacitors. *Int. J. Hydrogen Energy* 42(40), 25143–25165, 2017.
2. Zhang, F., Zhao, P., Niu, M., Maddy, J., The survey of key technologies in hydrogen energy storage. *Int. J. Hydrogen Energy* 41(33), 14535–14552, 2016.
3. Wilberforce, T., El-Hassan, Z., Khatib, F.N., Al Makky, A., Baroutaji, A., Carton, J.G., Olabi, A.G., Developments of electric cars and fuel cell hydrogen electric cars. *Int. J. Hydrogen Energy* 42(40), 25695–25734, 2017.
4. Konnov, A.A., On the role of excited species in hydrogen combustion. *Combust. Flame* 162(10), 3755–3772, 2015.
5. Li, R., Latest progress in hydrogen production from solar water splitting via photocatalysis, photoelectrochemical, and photovoltaic-photoelectrochemical solutions. *Cuihua Xuebao/Chinese J. Catal.* 38(1), 5–12, 2017.
6. Khetkorn, W., Rastogi, R., Incharoensakdi, A., Lindblad, P., Madamwar, D., Pandey, A., Larroche, C., Microalgal hydrogen production – A review. *Bioresour. Technol.* 243, 1194–1206, 2017.
7. López Ortiz, A., Meléndez Zaragoza, M.J., Collins-Martínez, V., Hydrogen production research in Mexico: A review. *Int. J. Hydrogen Energy* 41(48), 23363–23379, 2016.
8. Karagöz, Y., Güler, I., Sandalci, T., Yüksek, L., Dalkiliç, A.S., Effect of hydrogen enrichment on combustion characteristics, emissions and performance of a diesel engine. *Int. J. Hydrogen Energy* 41(1), 656–665, 2016.
9. Yilmaz, A.E., Ispirli, M.M., An investigation on the parameters that affect the performance of hydrogen fuel cell. *Procedia - Soc. Behav. Sci.* 195, 2363–2369, 2015.

10. Singh, S., Jain, S., Ps, V., Tiwari, A.K., Nouni, M.R., Pandey, J.K., Goel, S., Hydrogen: A sustainable fuel for future of the transport sector. *Renew. Sustain. Energy Rev.* 51, 623–633, 2015.
11. Niaz S, Manzoor, T., Pandith, A.H., Hydrogen storage: Materials, methods and perspectives. *Renew. Sustain. Energy Rev.* **50**, 457–469, 2015.
12. Hwang, H.T., Varma, A., Hydrogen storage for fuel cell vehicles. *Curr. Opin. Chem. Eng.* 5, 42–48, 2014.
13. Valenti, G., Hydrogen liquefaction and liquid hydrogen storage, in: *Compendium of Hydrogen Energy*, Gupta, R.B., Basile, A., Veziroglu, T.N. (Eds.), pp. 27–51, Elsevier, 2016.
14. Mirabile Gattia, D., Montone, A., Di Sarcina, I., Nacucchi, M., De Pascalis, F., Re, M., Pesce, E., Vittori Antisari, M., On the degradation mechanisms of Mg hydride pellets for hydrogen storage in tanks. *Int. J. Hydrogen Energy* 41(23), 9834–9840, 2016.
15. Azuma, M., Oimatsu, K., Oyama, S., Kamiya, S., Igashira, K., Takemura, T., Takai, Y., Safety design of compressed hydrogen trailers with composite cylinders. *Int. J. Hydrogen Energy* 39(35), 20420–20425, 2014.
16. Tan, H., Zhao, Q., Sun, N., Li, Y., Proposal and design of a natural gas liquefaction process recovering the energy obtained from the pressure reducing stations of high-pressure pipelines. *Cryogenics (Guildf).* 80, 82–90, 2016.
17. Thomas, K.M., Hydrogen adsorption and storage on porous materials. *Catal. Today* 120(3–4), 389–398, 2007.
18. Roszak, R., Firlej, L., Roszak, S., Pfeifer, P., Kuchta, B., Hydrogen storage by adsorption in porous materials: Is it possible? *Colloids Surfaces A Physicochem. Eng. Asp.* 496, 69–76, 2016.
19. Tellez-Juárez, M.C., Fierro, V., Zhao, W., Fernández-Huerta, N., Izquierdo, M.T., Reguera, E., Celzard, A., Hydrogen storage in activated carbons produced from coals of different ranks: Effect of oxygen content. *Int. J. Hydrogen Energy* 39(10), 4996–5002, 2014.
20. Sethia, G., Sayari, A., Activated carbon with optimum pore size distribution for hydrogen storage. *Carbon N. Y.* 99, 289–294, 2016.
21. Liu, X., Zhang, C., Geng, Z., Cai, M., High-pressure hydrogen storage and optimizing fabrication of corncob-derived activated carbon. *Microporous Mesoporous Mater.* 194, 60–65, 2014.
22. Heo, Y.-J., Park, S.-J., Synthesis of activated carbon derived from rice husks for improving hydrogen storage capacity. *J. Ind. Eng. Chem.* 31, 330–334, 2015.
23. Li, G., Li, J., Tan, W., Jin, H., Yang, H., Peng, J., Barrow, C.J., Yang, M., Wang, H., Yang, W., Preparation and characterization of the hydrogen storage activated carbon from coffee shell by microwave irradiation and KOH activation. *Int. Biodeterior. Biodegrad.* 113, 386–390, 2016.
24. Md Arshad, S.H., Ngadi, N., Aziz, A.A., Amin, N.S., Jusoh, M., Wong, S., Preparation of activated carbon from empty fruit bunch for hydrogen storage. *J. Energy Storage* 8, 257–261, 2016.

25. Dong, J., Wang, X., Xu, H., Zhao, Q., Li, J., Hydrogen storage in several microporous zeolites. *Int. J. Hydrogen Energy* 32(18), 4998–5004, 2007.
26. Ren, J., Musyoka, N.M., Langmi, H.W., North, B.C., Mathe, M., Kang, X., Liao, S., Hydrogen storage in Zr-fumarate MOF. *Int. J. Hydrogen Energy* 40(33), 10542–10546, 2015.
27. Yang, S.J., Jung, H., Kim, T., Park, C.R., Recent advances in hydrogen storage technologies based on nanoporous carbon materials. *Prog. Nat. Sci. Mater. Int.* 22(6), 631–638, 2012.
28. Shiraz, H.G., Tavakoli, O., Investigation of graphene-based systems for hydrogen storage. *Renew. Sustain. Energy Rev.* 74, 104–109, 2017.
29. Akasaka, H., Takahata, T., Toda, I., Ono, H., Ohshio, S., Himeno, S., Kokubu, T., Saitoh, H., Hydrogen storage ability of porous carbon material fabricated from coffee bean wastes. *Int. J. Hydrogen Energy* 36(1), 580–585, 2011.
30. González-García, P., Activated carbon from lignocellulosics precursors: A review of the synthesis methods, characterization techniques and applications. *Renew. Sustain. Energy Rev.* 82, 1393–1414, 2018.
31. Omri, A., Lambert, S.D., Geens, J., Bennour, F., Benzina, M., Synthesis, Surface characterization and photocatalytic activity of TiO_2 supported on almond shell activated carbon. *J. Mater. Sci. Technol.* 30(9), 894–902, 2014.
32. Kwiatkowski, M., Broniek, E., An analysis of the porous structure of activated carbons obtained from hazelnut shells by various physical and chemical methods of activation. *Colloids Surfaces A Physicochem. Eng. Asp.* 529, 443–453, 2017.
33. Djeridi, W., Ouederni, A., Wiersum, A.D., Llewellyn, P.L., El Mir, L., High pressure methane adsorption on microporous carbon monoliths prepared by olives stones. *Mater. Lett.* 99, 184–187, 2013.
34. Laksaci, H., Khelifi, A., Trari, M., Addoun, A., Synthesis and characterization of microporous activated carbon from coffee grounds using potassium hydroxides. *J. Clean. Prod.* 147, 254–262, 2017.
35. Hidayu, A.R., Muda, N., Preparation and characterization of impregnated activated carbon from palm kernel shell and coconut shell for CO_2 capture. *Procedia Eng.* 148, 106–113, 2016.
36. Fernandez, M.E., Nunell, G.V., Bonelli, P.R., Cukierman, A.L., Activated carbon developed from orange peels: Batch and dynamic competitive adsorption of basic dyes. *Ind. Crops Prod.* 62, 437–445, 2014.
37. Jung, S.-H., Oh, S.-J., Choi, G.-G., Kim, J.-S., Production and characterization of microporous activated carbons and metallurgical bio-coke from waste shell biomass. *J. Anal. Appl. Pyrolysis* 109, 123–131, 2014.
38. Yahya, M.A., Al-Qodah, Z., Zanariah Ngah, C.W., Agricultural bio-waste materials as potential sustainable precursors used for activated carbon production: A review. *Renew. Sustain. Energy Rev.* 46, 218–235, 2015.
39. Ma, Z., Yang, Y., Ma, Q., Zhou, H., Luo, X., Liu, X., Wang, S., Evolution of the chemical composition, functional group, pore structure and crystallographic structure of bio-char from palm kernel shell pyrolysis under different temperatures. *J. Anal. Appl. Pyrolysis* 127, 350–359, 2017.

40. Bhatnagar, A., Vilar, V.J.P., Botelho, C.M.S., Boaventura, R.A.R., Coconut-based biosorbents for water treatment—A review of the recent literature. *Adv. Colloid Interface Sci.* 160 1–2, 1–15, 2010.
41. Kluska, J., Kardaś, D., Heda, Ł., Szumowski, M., Szuszkiewicz, J., Thermal and chemical effects of turkey feathers pyrolysis. *Waste Manag.* 49, 411–419, 2016.
42. Härmas, M., Thomberg, T., Kurig, H., Romann, T., Jänes, A., Lust, E., Microporous–mesoporous carbons for energy storage synthesized by activation of carbonaceous material by zinc chloride, potassium hydroxide or mixture of them. *J. Power Sources* 326, 624–634, 2016.
43. Qajar, A., Peer, M., Rajagopalan, R., Foley, H.C., High pressure hydrogen adsorption apparatus: Design and error analysis. *Int. J. Hydrogen Energy* 37(11), 9123–9136, 2012.
44. Lam, S.S., Liew, R.K., Wong, Y.M., Yek, P.N.Y., Ma, N.L., Lee, C.L., Chase, H.A., Microwave-assisted pyrolysis with chemical activation, an innovative method to convert orange peel into activated carbon with improved properties as dye adsorbent. *J. Clean. Prod.* 162, 1376–1387, 2017.
45. Gallouze, M., Kellou, A., Drir, M., Adsorption isotherms of H2 on defected graphene: DFT and Monte Carlo studies. *Int. J. Hydrogen Energy* 41(12), 5522–5530, 2016.
46. Kumar, K.V., Castro, M.C.C.M. de, Martinez-Escandell, M., Molina-Sabio, M., Rodriguez-Reinoso, F., Heat of adsorption and binding affinity for hydrogen on pitch-based activated carbons. *Chem. Eng. J.* 168(2), 972–978, 2011.
47. Bae, Y.S., Snurr, R.Q., Optimal isosteric heat of adsorption for hydrogen storage and delivery using metal-organic frameworks. *Microporous Mesoporous Mater.* 132(1–2), 300–303, 2010.

7

Carbonaceous Materials in Hydrogen Storage

R. Pedicini[1,2,*], I. Gatto[1], M. F. Gatto[1,3,4] and E. Passalacqua[1]

[1]CNR-ITAE, Institute for Advanced Energy Technologies "Nicola Giordano," Messina, Italy
[2]Department of Physics, University of Calabria, Rende, Italy
[3]Dipartimento di Scienze Chimiche, Biologiche, Farmaceutiche ad Ambientali, and C.I.R.C.M.S.B., University of Messina, V.le F. Stagno D'Alcontres 31, Vill. S. Agata, 98166, Messina, Italy

Abstract

Hydrogen storage is one of the main issues hindering the spread of fuel cell-based applications and, more generally, the advent of the so-called "hydrogen economy." On the one hand, classical gas compression and liquefaction systems provide a relatively efficient and consolidated approach, but involve enormous security problems, and compression and refrigeration costs are high. On the other hand, there are several alternative approaches to hydrogen storage, essentially based on hydrogen chemisorption or physisorption processes on various support materials. In this chapter, an overview is presented of a proposed large and interesting class of materials, the carbonaceous materials, which are attractive candidates for hydrogen storage due to a combination of adsorption ability, high specific surface area, pore microstructure, and low-mass density. In general, it is possible to distinguish: a) materials consisting only of carbon atoms (carbon nanofibers, single- and multi-walled nanotubes, etc.); b) materials containing carbon and other light elements (polyaniline, polypyrrole, etc.); c) composite materials made by polymeric matrix (hyperbranched poly(amide-amine) with vanadium oxide, metal oxide anchored to a polyetheretherketone matrix, etc.); d) waste and natural materials (coconut flesh, coffee bean wastes, etc.).

Keywords: H_2 storage, carbonaceous material properties, physisorption and chemical sorption

**Corresponding author*: rolando.pedicini@itae.cnr.it

Mehmet Sankir and Nurdan Demirci Sankir (eds.) Hydrogen Storage Technologies, (197–228) © 2018 Scrivener Publishing LLC

7.1 Introduction

A sustainable provision of energy is one of the greatest challenges for mankind. Energy generated from sustainable sources has to be transported and stored in an efficient and ecologically friendly way. Hydrogen is an important energy carrier in current sustainable energy scenarios.

The development of hydrogen as an energy vector in the future will strongly depend on the storage performance. Today, several solutions are considered for storing hydrogen. Each solution presents advantages and disadvantages according to economic criteria, energy, mass and density of storage capacity, security and kinetic storage/removal. For embedded systems, a suitable mode of storage is based on the use of solid materials, some of which can absorb hydrogen in a reversible manner under certain conditions of temperature and pressure. This mode is promising because densities of hydrogen stored in this form can reach values higher than that of liquid hydrogen [1].

Since in this field there are several materials studied, it can be useful to divide them into two big classes: Hydrogen Chemisorption, in which the activated sites of the material interact with the atomic hydrogen by chemical bonds and Hydrogen Physisorption. Regarding the chemisorption process, metal hydrides, complex hydrides and chemical hydrides are more studied. Their main characteristic is high hydrogen storage capacity [2, 3], even if it is necessary to activate them using hydrogen adsorption/desorption cycles under different temperature and pressure conditions [4]. Other drawbacks of these metallic materials are: slow thermodynamic and kinetic reactions [5], high costs and sensitivity to air [6].

Regarding the hydrogen physisorption process, the molecular hydrogen interacts with the material, generally on the surface imperfections, through weak bonds (such as van der Waals forces), operating as a sponge. The following materials are part of this class: metal organic frameworks (MOFs) [7], nanoporous carbon [8], carbon nanotube [9, 10], carbon multi-walled, big area of polymeric materials, such as polyaniline (PANI), polypyrrole (PPy), polythiophene (PTh), used as an activation material for porous carbon, hyperbranched polyurea (P-Urea), hyperbranched poly(amide-amine) (PAMAM), polymer-dispersed metal hydrides (PDMH) and microporous polymers. Among these materials are included composite polymers based on metal oxide, such as Mn, anchored onto a functionalized polymeric matrix [11–13]. Innovative materials from natural sources have been of increasing importance in recent years, in particular, some researchers have reported interesting results for coconut flesh, coffee bean wastes and chicken fibers [14].

In this work, an overview will be presented of the interesting class of carbonaceous materials, that will be distinguished by four classes: a) materials consisting only of carbon atoms; b) materials containing carbon and other light elements; c) composite materials made by polymeric matrix; d) waste and natural materials.

7.2 Materials Consisting of Only Carbon Atoms

Life could not exist on Earth without carbon. In fact, this element makes up biological macromolecules (carbohydrates, proteins, nucleic acids and lipids) and many organic compounds. This is a consequence of carbon's ability to bind to itself and to nearly all elements in the Periodic Table [15]. However, in nature, we can find elemental carbon in three allotropic forms: diamond, graphite and amorphous carbon. These three forms have different crystal lattice and carbon hybridization, which has repercussions on the mechanical, thermal, electric and optic properties of these materials. For example, the network of sp3 carbon atoms makes diamond the hardest material in Mohs scale; instead, a sp2 carbon network makes graphite flaky and soft. In the last half century, other carbon allotropic forms have been discovered: fullerenes, nanotubes and graphene. Nowadays, they are applied as new materials, particularly, alloys and plastics of the last generation. They have exceptional properties and are one of the interesting systems for hydrogen storage.

Among all materials studied in hydrogen storage application, in this overview the following materials will be reported: graphite, carbon nanofibers, graphene and carbon nanotubes.

7.2.1 Graphite

The graphite crystal lattice consists of stacks of parallel 2D graphene sheets (honeycomb pattern) composed only by sp2 carbon atoms. The 2pz orbitals of carbon atoms overlap in parallel to form out-of- plane π bonds. Thus, graphite is anisotropic because in-plane bonds are different than out-of-plane ones. Elastic modulus is higher parallel to the plane than it is perpendicular to the plane. A π orbital is delocalized on the whole graphene sheet, making it thermally and electrically conductive in-plane [16].

Adjacent graphene sheets are separated by 0,335 nm of distance and linked by weak interactions of van der Waals of π–π type.

Although graphite has a high polarizability to allow the hydrogen physisorption by London dispersion forces, the storage capability is very low

because its interlayer distance (dynamic diameter of hydrogen is 0,406 nm) and specific superficial area are small [17].

For these reasons, the storage materials research has been focalized on graphite derivatives (graphene and nanofibers) in recent years. Another efficient method to increase specific superficial area of graphite is the intercalation of doping agents (alkaline and earthy alkaline metals and their derivatives) enlarging interlayer distance.

7.2.2 Carbon Nanofibers

Carbon nanofibers are obtained by catalytic growth of gas hydrocarbon (methane, ethane) or CO_2 on metal catalysts (alloys of Fe, Co, Ni, Cr, V o Mo). These catalysts operate in the range of temperature 700–1200 K. Then, carbon nanofiber can be producted with a graphitic structure [18]. Carbon nanofibers have a diameter in the range of 3–100 nm and a length between 0,1 and 1000 μm. Their form depends on catalyst particles morphology: in fact, herringbone, card deck (platelet) or tubular carbon nanofibers can be obtained. Chambers *et al.* measured adsorption/desorption properties of different graphite nanofiber types by a volumetric system. [19].

Many other authors have not been able to repeat the results of Chambers *et al.* (about 70 wt% of hydrogen adsorption) but they are limited to a range of 1–15 wt% [20]. Thus, new carbon nanofibers have been designed in the last 5 years to solve the problem of increasing interlayer distance in graphite, hydrogen storage capabilities and the reproducibility of measurement.

Hung-Chih Wu *et al.* synthesized a new mesoporous carbon nanofiber, called turbostratic carbon nanofibers, with CVD (carbon vapor deposition) technique [21]. The turbostratic CNFs are 90–150 nm in diameter and several μm in length. They have a very rough surface and high porosity caused by stochastic orientation of different graphitic layers (Figure 7.1).

A thermal treatment at 973 K makes turbostratic CNFs rougher and increases interlayer distance, as reported in Figure 7.2.

The hydrogen storage capacity, measured by PCT system, has produced turbostratic CNFs that have a 1,5 wt% hydrogen storage capacity at 1 MPa of pressure and 77 K, instead exfoliated turbostratic CNFs have a 5 wt% one. Hung-Chih Wu *et al.* demonstrated the importance of defect and interlayer distance of graphite crystals.

As an evolution of turbostratic CNFs, Xing *et al.* designed mesoporous carbon nanofibers (MCNF) with hierarchical nanoarchitecture. These nanofibers are printed on a porous aluminum oxide mold charged with colloidal silica as co-template or porogen. A phenolic resin is paid into

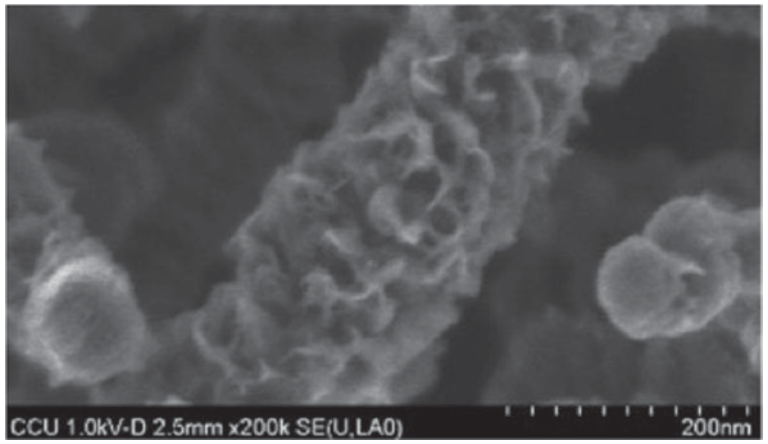

Figure 7.1 SEM image of as-produced turbostratic CNF. (Reproduced with permission of Elsevier)

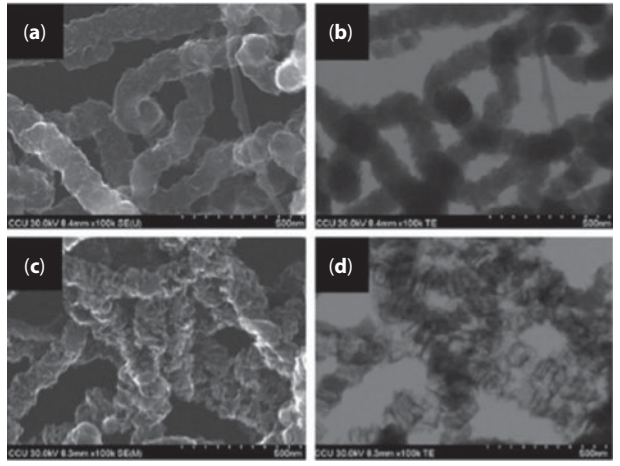

Figure 7.2 CNFs SEM and TEM images before (a,b) and after (c,d) thermal treatment. (Reproduced with permission of Elsevier)

pores of mold and carbonized. These nanofibers have a diameter of 240 nm, 50–60 μm of length and pores in the range 10–25 nm [22].

The as-prepared MCNFs not only have high surface area, but large mesopores too: all that announces excellent hydrogen storage. Xing *et al.* examined the electrochemical hydrogen storage capability of these nanofibers. The galvanostatic discharge measurements result in a hydrogen desorption capacity of 679 mA h g^{-1}, corresponding to 2,51 wt% hydrogen uptake, at a

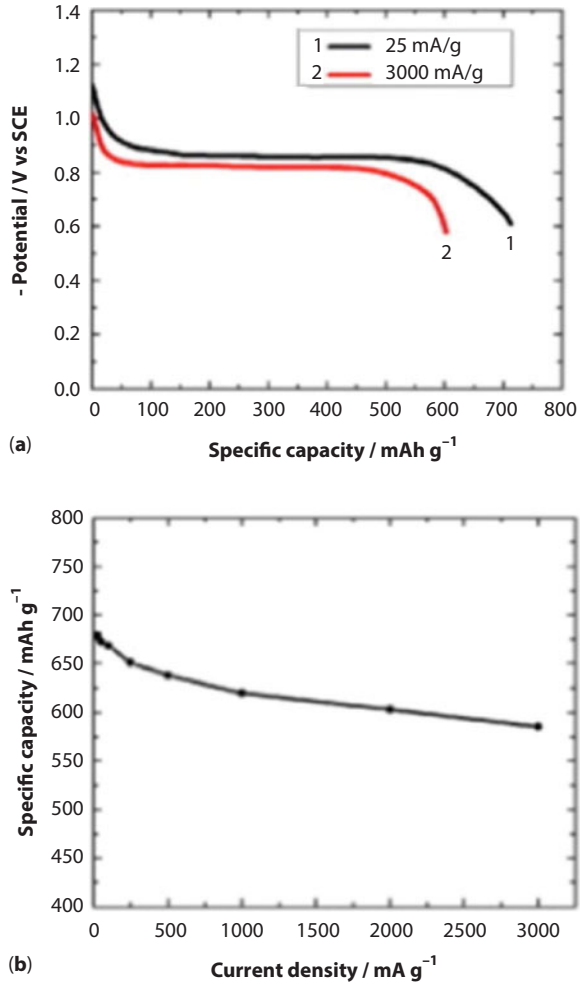

Figure 7.3 H_2 galvanostatic discharge measurements. (Reproduced with permission of Elsevier)

discharge rate of 25 mA g^{-1}. With increasing discharge rate, there is a parabolic decrease of hydrogen uptake (Figure 7.3).

7.2.3 Carbon Nanostructures

Another method to increase specific surface area is using the surface properties of nanostructures: they have a high area/volume ratio. Nowadays, it is possible to obtain carbon nanostructures exfoliating graphite. It is a single layer of graphite, so it has a 2D structure [23]. Graphene can be

rolled to form 1D structure, called carbon nanotube, and wrapped to form a 0D structure, called fullerene [24].

7.2.4 Graphene

In the last years, graphene has received more attention in the research of new hydrogen storage materials. Sarkar *et al.* studied a new method to store hydrogen on graphene by chemisorption [25]. They used the Benkeser reaction to hydrogenate graphene: it consists of a catalytic reduction (hydrogenation) of PAH (Poly Aromatic Hydrocarbon) by alkyl primary amines as reductant and lithium or calcium metal as catalyst. Hydrogen capability of graphene is estimated by TGA under N_2 atmosphere to be in the range of 273–1273 K. Between 673–873 K, hydrogen decomposition takes place.

Thus, the H_2 storage obtained by TGA is 14,67 wt% versus the previous maximum storage value of 4 wt% reported in the literature. As mentioned above, the defects on a surface increase adsorption capability of a material. Thus, another example of graphene system for hydrogen storage is hierarchical graphene. Guo *et al.* [26] synthesized this new graphene-based material. It is developed from graphite oxide by a first thermal at 423 K under vacuum pretreatment and then a thermal treatment at 873 K under Ar flux. The SEM characterization shows wavelike sheets connected with each other to form pores with diameters between 50 and 200 nm.

Hydrogen adsorption and desorption isotherms of both carbonaceous materials, conducted at 77 K from a pressure of 0,1 MPa, describe a reversible hydrogen physisorption. The hierarchical carbon had an H_2 sorption capability of about 4 wt%, three times higher than that of the prehierarchical carbon (1,40 wt%).

7.2.5 Carbon Nanotubes (CNTs) and Carbon Multi-Walled Nanotubes (MWCNTs)

Two types of carbon nanotubes exist: single-walled carbon nanotubes (SWCNTs) and multi-walled ones (MWCNTs). The first type is constituted by one rolled graphene layer, instead MWCNTs are constituted by many concentric SWCNTs.

Recently, Zhao *et al.* [27] studied SWCNTs storage properties having dimensions of about 1,3 nm in diameter.

The experiments of hydrogen uptake and release were carried out by a PCT volumetric gas system. SWCNTs were tested at different temperatures (303 K, 203 K and 77 K) and at 10 MPa of pressure for 2 h. They obtained the best result at 77 K of 1,73 wt% of hydrogen adsorbed and 1,23 wt% released.

Barghi *et al.* characterized hydrogen storage capacity of commercial MWCNTs with average diameter of 7,4 nm and specific surface area of 441,3 $m^2 g^{-1}$ and average pore volume of 0,82 $cm^2 g^{-1}$ [28]. They demonstrated that hydrogen uptake on MWCNTs is a combination of reversible physisorption and irreversible chemisorption. The measurements at 0,5 MPa of pressure and 298 K for 5 h demonstrate that MWCNTs reach equilibrium of hydrogen adsorption in 4 h. They adsorb 90% of hydrogen in the first hour of the experiment (Figure 7.4); this fast charging time is

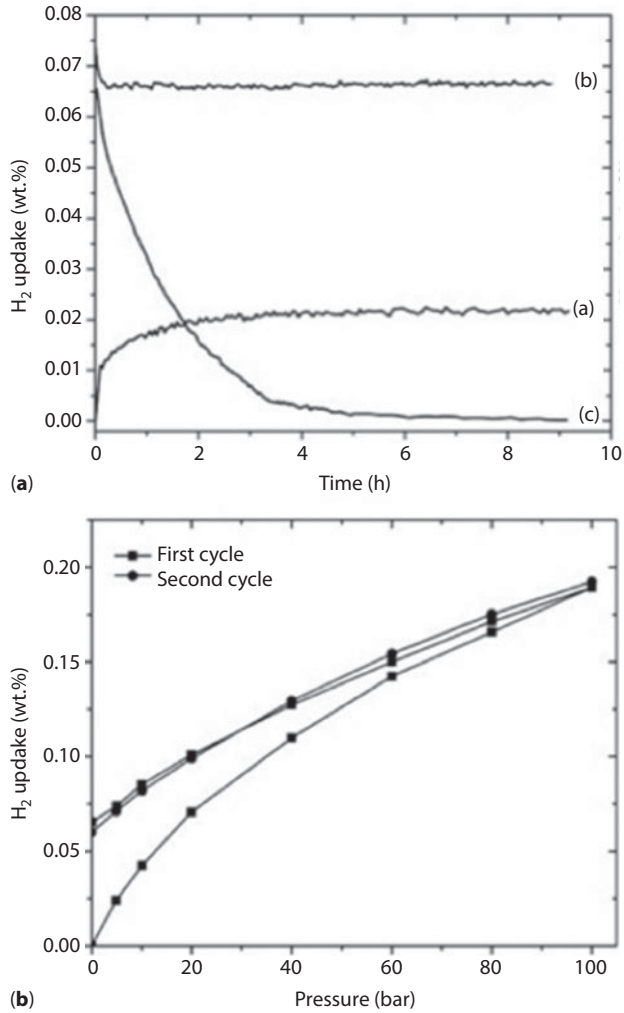

Figure 7.4 (a) Hydrogen adsorption/desorption cycles, (b) H_2 physisorption and chemisorption after cycles. (Reproduced with permission of Elsevier)

an important consideration in terms of the eventual practical application. After the first adsorption/desorption cycle, 35% of adsorbed hydrogen remains in MWCNTs: in fact, a second adsorption/desorption cycle does not highlight any desorbed hydrogen quantity. A treatment in vacuum at 393 K shows a loss of hydrogenated MWCNTs weight corresponding to chemisorbed hydrogen. However, the maximum quantities of physisorbed and chemisorbed hydrogen are 0,13 and 0,058 wt%, respectively: values which are very low.

Defects in structure are important in hydrogen storage capability of carbon nanotubes, too. There are several methods to introduce defects into CNTs; for example, by ball milling, acid washing, irradiation and doping with metals. Lee *et al.* used microwave irradiation on commercial MWCNTs [29]. They analyzed hydrogen uptake of four samples corresponding to 0, 5, 10 and 14 minutes of microwave exposition. MWCNTs were thermal pretreated and, subsequently, submitted at a pressure variation to a maximum of 3 MPa at 298 K. The MWCNTs submitted at microwave exposition for 10 min result in the highest hydrogen adsorption value (0,83 wt%), demonstrating that the hydrogen storage properties of MWCNTs depend on the damage entity.

7.3 Materials Containing Carbon and Other Light Elements

Microporous materials have good potential in hydrogen storage since they have unique features such as adsorption on the surface, inter- and intragrain boundaries and bulk absorption [30].

Hydrogen storage in microporous material is a physical storage approach, which includes compressed or liquefied molecular hydrogen and hydrogen adsorbed in the pores of the polymeric materials [31].

The major advantages of this class of materials are light weight, complete adsorption and desorption with no appreciable hysteresis, ease of manufacturing and cheapness. Many polymers are studied, some of which are unmodified and others synthetic, and they can be modified to improve their hydrogen storage capability.

In this context, attention will be focused on polyaniline (PANI), polypyrrole (PPy), polythiophene (PTh), hyperbranched polyurea (P-Urea), hyperbranched poly(amide-amine) (PAMAM), microporous polymers, conjugated microporous polymers (CMPs), hyper-cross-linked polymers (HCPs) and porous aromatic frameworks (PAFs).

7.3.1 Polyaniline (PANI), Polypyrrole (PPy) and Polythiophene (PTh)

All these polymers had conflicting results; Cho *et al.* [32] reported that PANI and PPy treated with HCl solution reach a very high hydrogen sorption of 6 and 8 wt% respectively, at room temperature and under 9,3 MPa. Unfortunately, these promising results were not reproduced by other researchers utilizing the same procedure and reagents [33]. In another work, PANI composites were synthetized using SnO_2, multiwalled carbon nanotubes and aluminum powder as filler. It has been shown that a PANI nanocomposite material can store just under 0,35 wt% hydrogen at 398 K and 6 MPa. The inclusion of multiwalled carbon nanotubes has little effect on the hydrogen sorption capabilities, reaching only 0,4 wt% of H_2 sorption at 398 K and 7 MPa. The insertion of tin oxide does not produce a significant difference in terms of H_2 storage. The main H_2 capture gain is revealed utilizing aluminum powder reaching 5 wt% at 383 K and 7 MPa [34]. An interesting approach is that of modified PANI utilizing different cross-linking agents; these kinds of materials showed a high surface area reaching a value up to 632 $m^2\ g^{-1}$. The hydrogen storage values, operating at 77 K and 60 MPa, were about 2,5 wt% [35, 36].

Interesting research on nanoporous polypyrrole having permanent mesopores on the surface, internal pores, and pockets with sponge-like structures was carried out. The prepared nanoporous polypyrrole materials, using a simple solid-state vapor-phase polymerization method, have been observed to reach a maximum reversible hydrogen adsorption capacity of 2,2 wt% at 77 K.

A method for the preparation of a new type of nanoporous material, hyper-cross-linked PANI, with permanent porous structure and specific surface areas over 630 $m^2\ g^{-1}$ has been developed. This reaction is carried out with commercial PANI and diiodoalkanes or paraformaldehyde using both conventional and microwave-assisted processes. The hydrogen storage capacities of these materials were also tested and a capacity of 2,2 wt% at 77 K and 3 MPa was found for the best adsorbent [35].

Another kind of polymer, polythiophene, was studied for H_2 storage application. This kind of untreated polymer does not show any ability to capture H_2, so, an activation process utilizing KOH solution, produces porous carbons with a surface area up to 3000 $m^2\ g^{-1}$. A very high hydrogen storage value, 5,71 wt%, was found at 77 K and 2 MPa, while at 0,1 MPa hydrogen uptake decreases at 2,33 wt% [37, 38].

7.3.2 Hyperbranched Polyurea (P-Urea) and Poly(Amide-Amine) (PAMAM)

An interesting polymeric area is related to hyperbranched polymers. These materials are characterized by three-dimensional nanoparticles; they are formed by a central part, with polydisperse polymers, including linear polymer segments, with multiple functional end groups in the periphery. They are characterized by their large surface area, globular structure and good solubility. Moreover, they also show a broad polydispersity and their structure is not perfectly branched. Since a consistent percentage of H_2 sorption occurs on the materials surface, some researchers have utilized urea groups to modify the surface structure [39]. In this contest, hyperbranched polyurea (P-Urea) was characterized under cryogenic conditions up to 2 MPa. These isotherm tests reveal a linear correlation between the hydrogen storage percentage and the pressure. The trend shows that at 0,5 MPa, 0,3 wt% of H_2 sorption, increasing the pressure until 1,5 MPa increases its H_2 storage capability up to 1 wt%. At the end of the test, at over 2 MPa, it stores about 1,4 wt% [40].

Another interesting class is hyperbranched poly(amide-amine) (PAMAM). This nitrogenated polymer shows, under cryogenic conditions, an adsorption of 0,9 wt% of H_2 operating at 2,5 MPa.

7.3.3 Microporous Polymers (PIMs)

Polymers of intrinsic microporosity (PIMs) are currently very attractive materials for hydrogen storage due to their high surface area and the opportunity to cast into films. The microporosity derives from their "rigid and contorted macromolecular chains that do not pack efficiently in the solid state" [41]. In the PIMs structure, polymer chains are normally aromatic heterocyclic ladder-type structures and must be quite rigid and contorted to avoid rotational freedom around the backbone [42]. PIMs with fused cyclic structure form solids with a large number of interconnected free volumes; they have advantages such as lightweight constituent elements (e.g., C, H, N, and O), high chemical stability and medium-to-high thermal stability. Different synthesis routes permit yielding of intrinsic microporosity, in particular dibenzodioxane reaction, imidization and amidization. The dibenzodioxane reaction is the most common route to form covalent bonds and produce ladder polymers with high average molecular weights [43, 44]. In this reaction, the polymer is obtained by mixing equal quantities of two monomers (a catechol and an aryl halide). In the imidization method, the reaction occurs between two monomers containing an

anhydride and a diamine group. The amidization method consists of a condensation reaction between two aromatic monomers containing diamine and carboxyl functional groups. The three methods produce polymers with different characteristics related to the molecular weight, the polymer morphology, the polymer composition and porosity.

The PIMs are potentially viable for hydrogen storage and among the PIMs studied for this application the highest H_2 capacity was measured with the star triptycene-based microporous polymer (STP) synthesized from trihalotriptycenes by nickel(0)-catalyzed Ullmann cross-coupling. The synthesized polymer (STP-II) with higher surface area (1990 $m^2 g^{-1}$) has shown a H_2 uptake of 1,92 wt% at 77 K and 0,1 MPa [45]. Other triptycene-based polymers, Trip(Me)-PIM and Trip(i-Pr)-PIM, with a surface of 1760 and 1601 $m^2 g^{-1}$, have produced a H_2 uptake of 1,80 wt% and 1,83 wt% at 77 K and 1 bar respectively, and around 3 wt% for both at 1 MPa under the same temperature conditions [46].

Greater uptake at higher pressure ranges has been reported for OFP-3, a polyimide network-based polymer, for which a hydrogen uptake of 3,94 wt% at 1 MPa and 77 K was measured [47], which is the highest H_2 capacity among polymers with intrinsic microporosity. Therefore, PIMs have shown hydrogen uptake results comparable to those of inorganic and organic porous materials such as zeolites and MOFs and even carbon materials with similar surface areas. However, these surface areas are still lower than other materials and improvements in the hydrogen capacity of PIMs are necessary. Novel and more efficient PIMs could be obtained by employing either modified monomers or particular moieties/subunits for synthesis or post-processing treatments of pre-synthesized PIMs.

7.3.4 Conjugated Microporous Polymers (CMPs)

Conjugated microporous polymers (CMPs) have recently received considerable research interest for hydrogen storage because of their finely tunable microporosity, large surface areas, and high stability. CMPs are typically prepared by metal-catalyzed cross-coupling (or homocoupling) chemistry such as Pd-catalyzed Suzuki and Sonogashira cross-coupling polycondensation [48], Ni-catalyzed Yamamoto reaction [49], oxidative polymerization [50] and Schiff-base reaction [51]. The unmatched feature of CMPs is that they combine π-conjugation and permanent porous structure in a bulk material. Liao *et al.* report a conjugated microporous polycarbazole network and its pyridine-, bipyridine-, and cyano-functionalized networks that exhibit large surface area (1126 $m^2 g^{-1}$). They proposed a new synthesis route to microporous polycarbazole networks via the Yamamoto reaction. The high

physicochemical stabilities, surface areas, and tunable functionalities make them attractive for selective gas uptake. These porous networks possess moderate H_2 storage capacity (1,35 wt% at 0,1 MPa and 77 K) and high isosteric heat of H_2 adsorption (10,3 kJ mol^{-1}) [52]. Moreover, a series of novel thiophene-based conjugated microporous polymers with high content of sulfur have been synthesized on the basis of ferric chloride-catalyzed oxidative coupling polymerization. All the CMPs possess micropores and the BET specific surface areas vary between 350 and 1320 $m^2 g^{-1}$. H_2 storage capacity ranging between 1,28 wt% and 2,17 wt% at 0,1 MPa and 77 K, was obtained with these thiophene-based conjugated microporous polymers [53].

7.3.5 Hyper-Cross-Linked Polymers (HCPs)

Hyper-cross-linked polymers represent another class of predominantly microporous organic materials that can exhibit high surface areas [54–57]. The permanent porosity in hyper-cross-linked materials is a result of extensive chemical cross-links that prevent the polymer chains from collapsing into a dense, nonporous state [58, 59]. The most well-studied hyper-crosslinked materials are "Davankov-type" [60] resins, which are prepared by post-cross-linking of polystyrenic networks and can exhibit apparent BET surface areas as high as 2090 $m^2 g^{-1}$ [61]. A hyper-cross-linked polystyrene (BET surface area 1466 $m^2 g^{-1}$) can reversibly adsorb up to 3,04 wt% H_2 at 77 K and 1,5 MPa [62]. Similar low-pressure sorption properties for a hyper-cross-linked polystyrene material and much lower H_2 storage capacities for a range of commercially available macroporous polymer sorbents were described by Germain *et al.* [63]. Wood *et al.* [64] have synthesized hyper-cross-linked polymer networks through the Friedel-Crafts-catalyzed self-condensation of bischloromethyl monomers such as dichloroxylene (DCX), 4,4'-bis(chloromethyl)-1,1'-biphenyl (BCMBP), and 9,10-bis(chloromethyl)anthracene (BCMA).

These materials are predominantly microporous and exhibit BET surface areas up to 1904 $m^2 g^{-1}$ and a Langmuir surface area of 2992 $m^2 g^{-1}$ by varying the structure of monomer. Moreover, the resulting materials are able to adsorb up to 3,7 wt% H_2 at 77 K and 1,5 MPa. It was demonstrated that it is possible to control the porosity in the polymers by the level of cross-linking and by changes in the rigid monomeric unit.

7.3.6 Porous Aromatic Frameworks (PAFs)

A new class of materials based on porous aromatic frameworks (PAFs) was recently synthesized [65] through Yamamoto-type Ullmann cross-coupling

reaction to obtain a diamond-like structure. The obtained PAFs-type solids are stable and robust materials, although with higher irregular internal structure that reduces their porosity and associated crystallinity. The hydrogen uptake reaches 5,9 wt% at 10 MPa and 298 K. Recently, Rochat *et al.* [66] prepared composite materials consisting of PIMs and PAFs with large accessible surface areas and maintained microporosity by varying the PAFs content from 0,5 to 37,5 wt%. At low pressure (0,1 MPa) and 77,4 K, the hydrogen uptake was found to increase with the amount of PAF in the membranes. The film made of PIM alone was found to take up 0,78 wt% H_2, while for composite materials it varies from 0,8 to 1,15 wt%. High-pressure hydrogen uptake measurements were performed at 10 MPa and the same temperature; in this case the H_2 uptake increased from 2,60 wt% for PIMs alone to 4,79 for the composite material containing 37,5 wt% PAF, even though with a PAF content > 20 wt% it is difficult to obtain the films due to the increased brittleness of the composite. The PIM/PAF combination could represent a good opportunity for the development of materials with light weight and good thermal and mechanical stability able to store significant amounts of hydrogen.

7.4 Composite Materials Made by Polymeric Matrix

The main purpose of composite polymers is to obtain the synergic effect of the polymer and inorganic compound. Composites materials have a peculiar structure, i.e., a phase-separated structure, with a nanoscale interface between the polymer matrix and the inorganic compound (nanophase-separated structure). Nevertheless, only a few studies have been published up to now on the promising chemical-physical characteristics of composite polymer for hydrogen storage application.

Moreover, the mechanical properties of the polymers damp down the mechanical stress that the embedded hydrogen storage material (e.g., a metal hydride) can undergo during sorption cycles, though there is still the open question of whether the hosting polymer plays a role in modifying the hydrogen storage capacity of compounds like metal hydride. A possible explanation could be the interactions between hydrogen and the polymer chains and/or metal hydrides supported on these polymers. These interactions are generally a combination of covalent, ionic, metallic, H-bonds and van der Waals interaction [67]. Some transition metal oxides, such as TiO_2 and MnO_2, have been tested as dopants to improve the hydrogen sorption properties of light metals [68] and complex [69] hydrides, and could possibly also play a positive role in the interaction of the hydrogen with the polymer matrix.

Among all these materials, particular attention will be given to composite poly(amide-amine) (PAMAM), polymer dispersed metal hydrides (PDMHs) and metal oxide anchored to a polymeric matrix.

7.4.1 Composite Poly(Amide-Amine) (PAMAM)

As previously seen, untreated PAMAM has very little capacity to store hydrogen; on the contrary, PAMAM composite with vanadium oxide (VOx), has shown promising results. The adsorption measurements were carried out under the same conditions of temperature and pressure. To verify the real gain in terms of H_2 sorbed, VOx was characterized alone, showing a 0,6 wt% at 2 MPa of adsorption. The H_2 adsorption trend of both PAMAM, previously reported, and VOx are linear; thus, their H_2 storage capacity has a direct proportionality. On the contrary, composite PAMAM reveals an increase of H_2 sorption reaching 2 wt% under the same measuring conditions (2,5 MPa) [70]. It is thought that the amide and amine groups of PAMAM could penetrate into the layers of the VOx and form exfoliated structure.

7.4.2 Polymer-Dispersed Metal Hydrides (PDMHs)

Another interesting class of materials are polymer-dispersed metal hydrides (PDMHs). The aim is to disperse metal hydrides in a particular polymeric matrix with a final product having a high H_2 storage capacity due to the presence of metal alloy and low density, since polymeric matrix gives these properties to the hybrid material. The dispersion of the metal hydride in a polymeric matrix increases the metal alloy stability, particularly during H_2 charge/discharge cycles; in addition, a possible small quantity of hydrogen could be stored in the polymeric layers. The volumetric tests carried out by Sievert apparatus at 673 K and at about 7 MPa have revealed a reversible H_2 sorption of about 0,4 wt% [71].

Other interesting studies have been performed on $LaNi_5$ particles dispersed into polyethylene (PE-$LaNi_5$) and polysiloxane (PS-$LaNi_5$) polymers [72, 73]. Both these polymers act mainly as a cover for the metal alloy with the aim of avoiding the occurrence of surface passivation. Another important feature is their ability to disperse better metal particles. PS-$LaNi_5$ composites have been obtained by adding metallic powder to the liquid monomer. Two important results have been obtained: PS-$LaNi_5$ containing a high percentage of metal alloy showed a better H_2 storage capacity as compared to the PS-$LaNi_5$ with low presence of metal alloy; moreover, the high percentage of metals gives both longer desorption times and lower

H_2 storage capacity compared to $LaNi_5$ powders. The maximum hydrogen storage obtained by PS-$LaNi_5$ at 295 K and 1 MPa is about 0,2 wt%, which is not comparable to PS-$LaNi_5$ and $LaNi_5$ alone; in fact they reach about 1 wt% under the same experimental conditions.

Pentimalli *et al.* have conducted an interesting study based on coverage of metal alloy utilizing a polymeric matrix. The acrylonitrile-butadiene-styrene (ABS) copolymer was obtained from bulk polymerization, while they used $LaNi_5$ powder as a metal alloy [74, 75]. After different experimental steps, the obtained ABS powder had a low specific area of 0,35 $m^2 g^{-1}$. The powder metal–polymer composite was obtained by mixing the starting metal and polymeric powders. At the end of this process, the obtained powder was consolidated into cylindrical pellets by hot pressing. In order to verify the matrix inertness under H_2 cycling, the stability of the polymer was investigated by IR, NMR and SEM characterizations before and after 25 hydriding-dehydriding cycles. No modifications were detected in the spectra after hydrogenation with respect to those obtained for the starting materials.

7.4.3 Mn Oxide Anchored to a Polymeric Matrix

An innovative way to obtain a hybrid material based on a functionalized polymer containing a nanometric metal oxide was followed by Pedicini *et al.* [11].

A commercial poly-ether-ether-ketone (PEEK) was selected as a polymeric matrix for its known chemical-physical characteristics. The commercial PEEK does not have any hydrogen storage capability since it is not possible to anchor any metal oxides in the monomeric units. A standardized functionalization procedure was followed [11], obtaining a highly chlorosulfonated (100%) PEEK (SPEEKCl). This amorphous material shows a low surface area (19,16 $m^2 g^{-1}$) slightly higher than commercial PEEK (9,72 $m^2 g^{-1}$). This could be attributable to the introduction of chlorosulfonic groups. The manganese oxide was chosen for both its crystalline structure and easy production method based on an *in-situ* reaction. As a precursor was chosen $KMnO_4$, which in acid environment oxidizes chloride ion in chlorine gas by reducing it at Mn^{+4}. By changing the reaction time and temperature, several powders with different amounts of Mn oxide (ranging from 7 to 78 wt%) were obtained. All these materials show a low surface area slightly higher than SPEEKCl polymer. The variation of Mn oxide content is evidenced by the change in color and appearance of the powders, as evident in Figure 7.5.

Sample containing the lowest percentage of manganese oxide (Figure 7.5a) shows a spongy appearance and dirty white color very similar

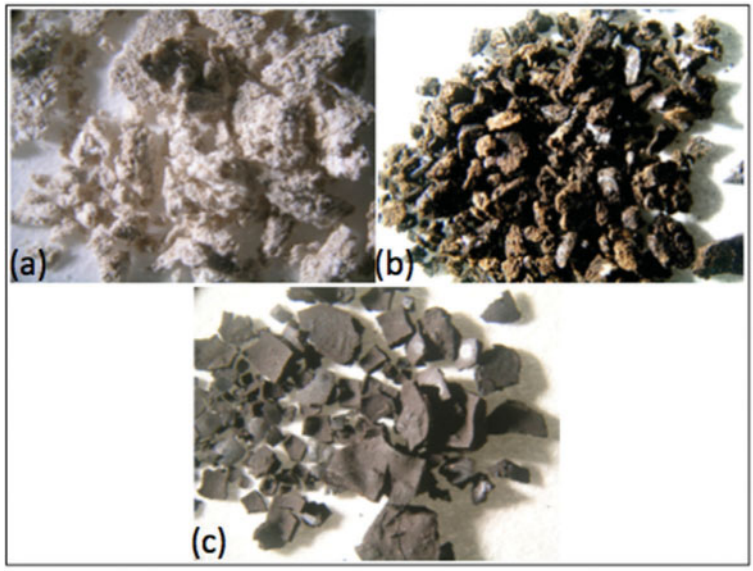

Figure 7.5 Sample with 7, 20 and 80 wt% Mn oxide. (Reproduced with permission of Elsevier)

to the polymeric precursor, as reported in ref. [11]. When the metal oxide content is increased the material tends to become darker and less spongy (Figure 7.5b,c). The influence of the oxide amount on the structural properties of the prepared samples is evidenced by XRD profiles of all samples, as shown in Figure 7.6.

The amorphous zone at about 20° 2θ, is due to the structure of the chlorosulfonated PEEK; this profile is maintained in all the developed samples and decreases by increasing the manganese oxide content and almost disappears in the sample with the highest oxide percentage. All the samples present three characteristic peaks (12°, 37° and 66° 2θ) of the layered Birnessite-type manganese oxide [76]. The crystal planes related to the Birnessite structure, by following JCPDS data n° 05–673, are: angle 12° 2θ (100), 37° 2θ (003) and 66° 2θ (005).

To verify the possible H_2 sorption capability three synthesized powders with 15, 20 and 78 wt% Mn oxide have been characterized by using a Sievert-type gas sorption analyzer.

The tests have been performed at 323 K and 383 K. For each test a sequence of different steps of hydrogen pressure was used to charge the samples (1, 2, 4, 6 MPa). Figures 7.7–7.9 show the hydrogenation curves obtained for the three samples at 383 K.

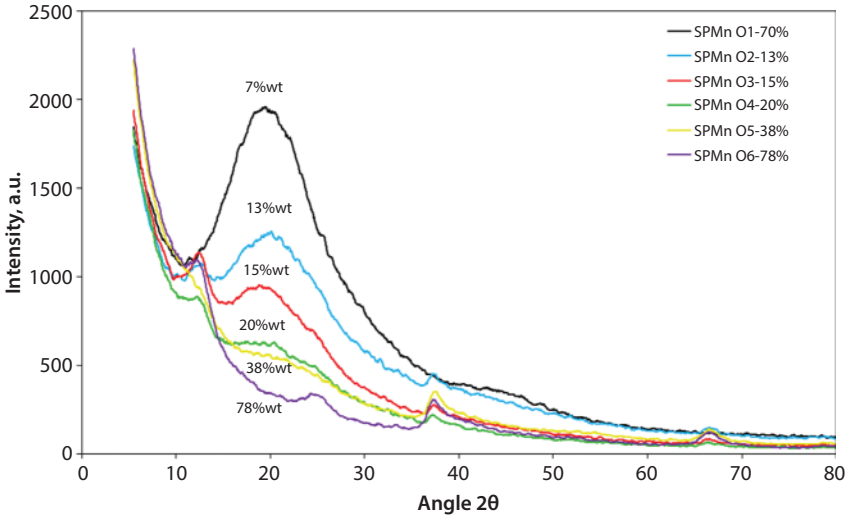

Figure 7.6 SPMnO XRD comparison. (Reproduced with permission of Elsevier)

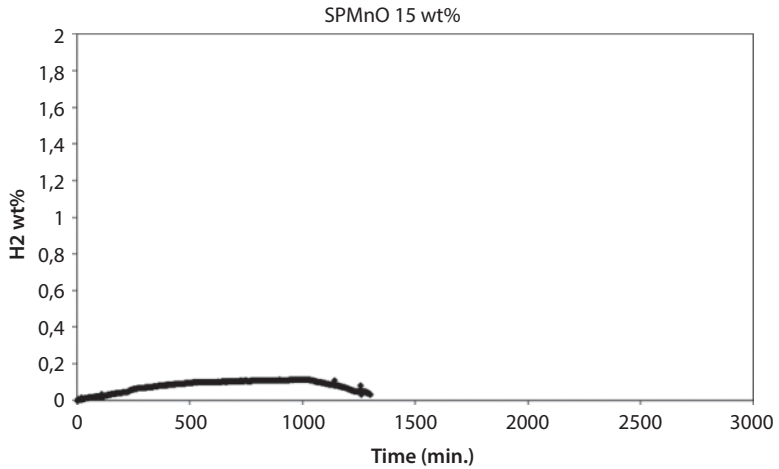

Figure 7.7 SPMnO15 wt% H_2 sorption. (Reproduced with permission of Elsevier)

Interestingly, for 15 wt% sample (Figure 7.7) the hydrogen saturation (0,10 wt%) is reached with a hydrogen pressure (i.e., 4 MPa) lower than that required for sample with 20 wt%, for which H_2 sorption does not start before 6 MPa with a higher value of around 0,18 wt% (Figure 7.8).

A remarkable result was obtained for the sample with a much higher percentage of metal oxide; in fact, hydrogen capacity at 1 MPa is already

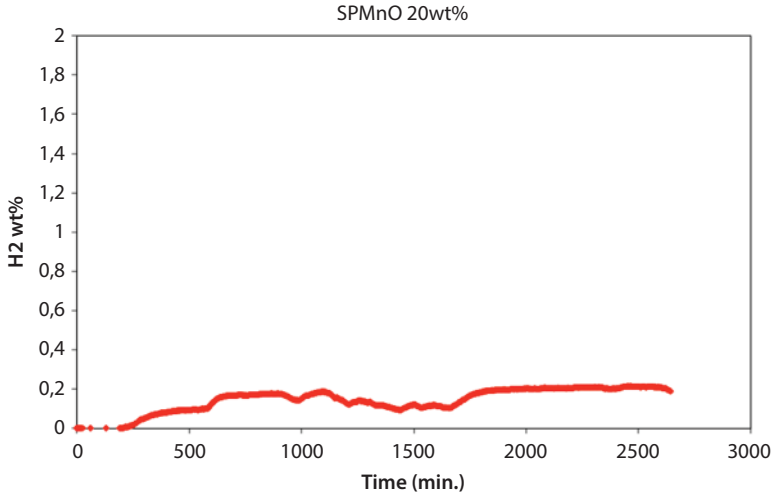

Figure 7.8 SPMnO20 wt% H_2 sorption. (Reproduced with permission of Elsevier)

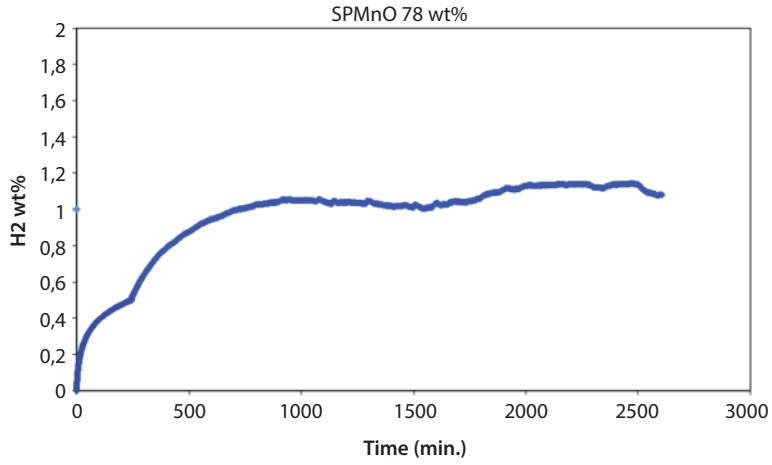

Figure 7.9 SPMnO78 wt% H_2 sorption. (Reproduced with permission of Elsevier)

0,5 wt% (Figure 7.9). When the saturation at this pressure occurs, a successive step was directly performed at 6 MPa. Under this condition the H_2 sorption is slightly more than 1 wt% even after 1000 min, which has been, up to now, a value never reached for polymer-based systems not under cryogenic conditions. To verify the H_2 sorption kinetics at lower temperature (323 K) sample was chosen with 78 wt% oxide [13]. The kinetics are shown in Figure 7.10a. The H_2 sorption does not reach saturation in any

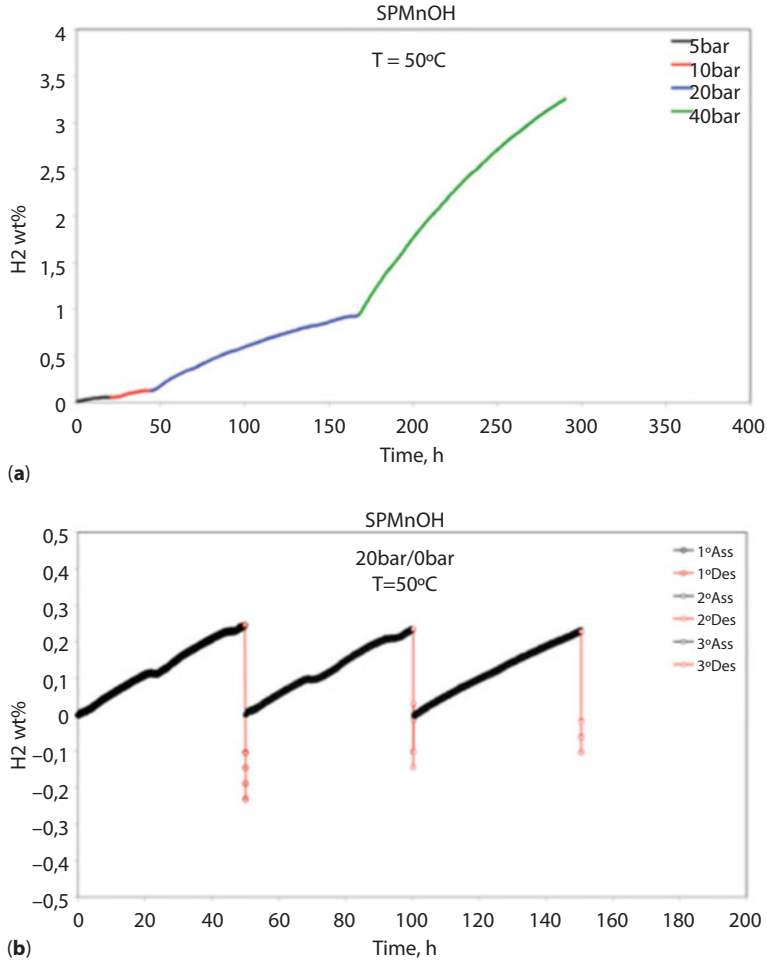

Figure 7.10 (a) H_2 sorption test and (b) H_2 ads/des cycles. (Reproduced with permission of Elsevier)

P steps and the kinetics reaction is very slow. In any case, at 2 MPa the H_2 sorption is more than 1 wt% while at 4 MPa the maximum H_2 sorption value was more than 3 wt%. The reversibility of the H_2 sorption/desorption cycles was performed at 323 K, with the aim of evaluating the stability of the material after sorption tests. As shown in Figure 7.10b, reversible cycles were reached and the previous H_2 sorption value at 2 MPa was confirmed (in the same time). Another important fact is that the short time of the desorption process (5 min) was sufficient to evacuate H_2 completely.

A further confirmation of the stability of the developed material after volumetric testing was obtained by XRD analysis, in which the profiles

before and after testing didn't show substantial differences, maintaining unaltered the crystallographic structure.

To evaluate how much energy is necessary to give desorb H_2 from the material, a modeling study by *ab-initio* density functional theory (DFT) was carried out. A supercell, containing 2 × 2 × 3 unit cells of MnO_2 and having 24 Mn and 48 O, was used. Hydrogen atoms are gradually placed in different locations inside the voids. For each number of H atoms several configurations were calculated (with H atoms in different locations) in order to find the one with the lowest energy.

Desorption energy (ΔE) starts from the high value of about 365 kJ mol^{-1} when the H number is 2 and decreases drastically at about 150 kJ mol^{-1} for n = 36. This starting value is higher than some metal hydrides; for instance, MgH of about 100 kJ mol^{-1} or BeH of about 240 kJ mol^{-1} [77].

Starting from the experimental H_2 sorption value (it was considered to be 1,7 wt% instead of the 3 wt% really obtained), the number of the respective H atoms calculated corresponds to 36, with desorption energy value of 150 kJ mol^{-1}. To verify the influence of Mn oxide percentage in H_2 storage capacity a further study was followed, obtaining samples with MnO_2 content over 78 wt%. The maximum reachable value was 85 wt% but the corresponding H_2 sorption value was about 1 wt% almost constantly for any loading.

Moreover, after the first H_2 sorption test, the performances were not reproduced. This phenomenon was clear after XRD postmortem analyses, where a crystalline structure was revealed corresponding to $Mn_2O_{3;}$ this means that the H_2 reacted with the oxide, reducing Mn^{+4} to Mn^{+3}.

7.5 Waste and Natural Materials

Nowadays, the research on materials finalized to reach hydrogen storage targets is addressed not only towards materials with new or improved properties but also towards new precursors that are easier or cheaper to prepare, and are sustainable. These materials can be transformed into porous activated carbons by carbonization followed by KOH activation. Several authors have studied the possibility of using waste from natural biomaterials for this purpose, and in this section some of the most recent results in this field are reported.

Hydrothermally carbonized organic materials, such as furfural, glucose, starch, cellulose and eucalyptus sawdust [78], have been used as precursors to produce high-surface area (up to 2700 $m^2 g^{-1}$) and narrow micropore size distribution in carbons of supermicropore range (0,7–2 nm). In particular,

high hydrogen uptakes of 5,6 and 6,4 wt% have been measured at 77 K and 2 MPa for cellulose and eucalyptus sawdust-based hydrochar respectively.

One of the most curious materials studied for hydrogen storage was derived from chicken feather fibers (CFFs) pyrolyzed by a two-step process [79]. A wide range of microporosities were obtained maintaining the second-step pyrolysis temperature between 673 K and 723 K for 0,5–2 h. The maximum excess H_2 storage capacity of 1,5 wt% was obtained at 77 K and pressures below 2 MPa, using 1 h pyrolysis in the optimal temperature range. The estimated adsorption energy for PCFFs was in the range of 5–6 kJ mol^{-1}, typical for physisorption on materials. The notable H_2 adsorption of PCFFs was justified by the abundance of microporosity and the nanopores available for H_2 penetration. PCFFs are an interesting future option because they are a waste material and require only relatively low temperature heat treatments.

Akasaka *et al.* [80] have investigated the hydrogen storage ability at 298 and 77 K of porous carbon materials with microporous structures fabricated from coffee bean wastes. Carbon materials were prepared from waste coffee beans by steam activation with weight ratios of KOH to carbon materials to obtain porous carbon material with specific surface area varying from 780 to 2070 $m^2 g^{-1}$. The hydrogen storage ability showed a linear relationship with specific surface area increasing and the micropore volume size. The maximum amount of stored hydrogen was 0,6 wt% at 298 K and 4 wt% at 77 K in the sample with a specific surface area of 2070 $m^2 g^{-1}$.

A series of activated carbons have been derived from hemp (*Cannabis sativa* L.) stem [81]. Samples with BET surface area of 3241 $m^2 g^{-1}$ and total pore volume of 1,98 $cm^3 g^{-1}$ have been obtained. A linear function of specific surface area, total pore volume, and micropore volume with hydrogen uptakes was found and the maximum hydrogen uptakes are 3,28 wt% at 77 K, 0,1 MPa. From the obtained results, the AA deduced that the gas adsorption amount is dominated by ultramicropores at lower pressure, and by larger micropores and mesopores at higher pressure.

Studies on corncob-derived activated carbons indicated that these materials are promising for hydrogen storage [82]. The corncob-derived activated carbons were prepared by varying preparation parameters to regulate the surface area and pore volume. In this way a maximum BET surface area of 3530 $m^2 g^{-1}$ and total pore volume of 1,94 $cm^3 g^{-1}$ were obtained. The results showed the highest hydrogen uptake capacities exceeding 2,85 wt% at 77 K and 0,1 MPa for the sample with surface area of 2988 $m^2 g^{-1}$ and smaller pore size.

Samples were prepared by carbonization of the dry solid endosperm part of coconut [83]. The carbonization was done by heating the solid endosperm coconut at temperature 623 K for 4 h under nitrogen (N2)

atmosphere. Some samples have also been carbonized by heating at 873 K. Since the carbonized dry endosperm already contains pores, no special treatment was done to create pores. The hydrogen storage measurement reveals that the as-synthesized materials have good hydrogen adsorption and desorption capacity with fast kinetics. The material absorbs 8 wt% of hydrogen at liquid nitrogen temperature and 2,3 wt% at room temperature and 7 MPa pressure. It was suggested that this high storage capacity was due to the presence of certain elements such as KCl embodied in carbon matrix or Mg responsible for the spillover effect.

Chitosan, a low-cost and abundant biopolysaccharide, was used as a carbon precursor to prepare highly microporous activated carbons (ACs) [84]. Chitosan-based ACs with high surface areas (922–3066 $m^2 g^{-1}$) and pore volumes (0,40–1,38 $cm^3 g^{-1}$) were tested as hydrogen storage systems; the optimized ACs exhibited excellent hydrogen adsorption capacities at 77 K (2,95 wt% at 0,1 MPa, 5,61 wt% at 4 MPa). The hydrogen adsorption capacity was related to micropores with a width of 0,7–1 nm, while larger pores did not exert any noticeable influence.

Several activated carbons (ACs) have been obtained by hydrothermal carbonization (HTC) of sucrose solutions at different concentrations and successive KOH activation [85]. ACs with surface areas ranging between 790 and 2703 $m^2 g^{-1}$ were prepared. A maximum hydrogen excess adsorption of 0,59 wt% was obtained at 298 K and 10 MPa on the AC with apparent surface area of 2703 $m^2 g^{-1}$. Excess hydrogen uptake depends linearly on the micropore volume; the AA proved that pores having widths ranging from 0,5 to 0,7 nm are the most relevant to store hydrogen at 298 K independently from the pressure.

Hwang *et al.* [86] prepared highly porous carbon fibers based on rice straw and paper mulberry via wet spinning and carbonization process. The porous carbon fibers derived from rice straw showed a high specific surface area of 2260 $m^2 g^{-1}$ and excellent hydrogen storage properties with a gravimetric hydrogen uptake of 4,35 wt% at 77 K and 1 MPa. They found that hydrogen storage capacity of porous carbon fibers depends on the type of source materials.

A porous carbon was derived from the paste of newly growing Indian banyan tree (*Ficus benghalensis*) which was phosphorus-doped [87]. The obtained phosphorous-doped porous carbon material showed a wafer-like morphology with specific surface area of 1406 $m^2 g^{-1}$. This material exhibited hydrogen storage capacity of 1,2 wt% at 298 K and 10 MPa.

Recently, AC produced from empty fruit bunch (EFB) was investigated as possible material for H_2 storage [88]. The total surface areas (BET) of the ACs produced were in the range of 305–687 $m^2 g^{-1}$ and highly microporous

structures, up to 94%, were obtained. A maximum H_2 uptake of 2,14 wt% was observed at 1,9 MPa and 77 K.

Activated carbon materials were also synthesized from jute fibers [89] activated using KOH and heat treated at 973 K to increase the porosity of samples. The surface area of these samples varied from 380 to 1220 $m^2 g^{-1}$ due to carbonization and activation treatment. The sample with a carbon to KOH weight ratio 1:3 showed high surface area of 1224 $m^2 g^{-1}$ and a high hydrogen uptake capacity of 1,2 wt% at 303 K and 4 MPa of H_2 gas pressure. The obtained channel-like structure helps to increase the hydrogen storage capacity.

Starting with olive stones to prepare microporous activated carbons (ACs), Bader *et al.* [90] observed how the activation processes modify the microstructure of ACs and how they affect the ACs hydrogen storage behavior. The KOH activation resulted in the formation of exfoliated graphene sheets and supermicropores (1–2 nm). The absolute hydrogen adsorption of KOH-activated sample at 20 MPa and 77 K is 6,11 wt%, which is among the highest reported for activated carbon samples.

Cigarette butts treated via sequential hydrothermal carbonization and activation have proven to be superporous carbons with ultra-high surface area (4300 $m^2 g^{-1}$) and pore volume (2,09 $cm^3 g^{-1}$), and are almost entirely composed of micropores (> 90%) [91]. Due to the combined effects of high surface area, high microporosity and an oxygen-rich content associated with O-containing functional groups, the carbons exhibit a high hydrogen storage capacity of 8,1 wt% excess uptake, and 9,4 wt% total uptake at 77 K and 2 MPa, and total uptake of 10,4 wt% and 11,2 wt% at 3 and 4 MPa, respectively. Our findings offer new insights into the valorization of a major waste disposal and environmental pollution hazard (discarded cigarette butts) to attractive energy materials with, in the present case, the highest hydrogen uptake capacity reported to date for any carbon or porous material in general. The results of these studies have direct relevance not only for carbon-based sustainable energy storage materials but can also help with the problem of environmental pollution by turning dangerous waste into high-value products.

In Table 7.1, the main results for hydrogen uptake using waste and natural materials are reported.

7.6 Conclusions

Many efforts have been made to develop hydrogen driven solutions; however, hydrogen itself is not a source of energy but an energy carrier to feed

Table 7.1 Main results on H_2 uptake using waste and natural materials under different conditions.

Material	Temperature K	Pressure MPa	H_2 uptake wt%	Ref.
Cellulose	77	2	6,4	[78]
Eucalyptus sawdust	77	2	5,6	[78]
Chicken feather	77	2	1,5	[79]
Coffee beans	298	12	0,6	[80]
Coffee beans	77	4	4,0	[80]
Hemp stem	77	0,1	3,28	[81]
Corncob	77	0,1	2,85	[82]
Coconut	77	7	8	[83]
Coconut	298	7	2	[83]
Chitosan	77	0,1	2,95	[84]
Chitosan	77	4	5,61	[84]
Sucrose	298	10	0,59	[85]
Rice straw	77	1	4,35	[86]
Ficus benghalensis	298	10	1,2	[87]
Empty fruit bunch	77	1,9	2,14	[88]
Jute fibers	303	4	1,2	[89]
Olive stones	77	20	6,11	[90]
Cigarette butt	77	2	9,4	[91]
Cigarette butt	77	3	10,4	[91]
Cigarette butt	77	4	11,2	[91]

fuel cell-based electric systems. To promote the "Green Economy" one of the problems to be solved is hydrogen storage. Many studies on hydrogen storage have been carried out. Among the considered methodologies of the last years, H_2 storage on solid material is increasing in importance due to a lot of research studies in this field. Several classes of materials

have been investigated based on H_2 physisorption (carbonaceous materials, HSA materials, etc.) and chemisorption (complex metal hydride, metal hydrides, etc.). This overview hopes to describe a carbonaceous materials class. In the majority of these materials, the physisorption mechanism occurs during the H_2 sorption. The main characteristic of the carbonaceous materials is their high surface area (starting from 300 $m^2 g^{-1}$ up to around 3000 $m^2 g^{-1}$). Four classes of materials have been taken into consideration: a) materials consisting only of carbon atoms; b) materials containing carbon and other light elements; c) composite materials made by polymeric matrix; d) waste and natural materials. In the first class are involved, in particular, carbon nanofibers (1–15 wt%; 77 K), graphene (14,67 wt%; range of T between 273 K–1273 K), carbon nanotube (1,7 wt%; 77 K) and multiwalled carbon nanotube (about 1 wt%; 298 K). Among the materials belonging to the second class, the most important results were obtained by: composite PANI containing Al powder (5 wt%; 383 K; 7 MPa), P-Urea (1,4 wt%; 77 K; 2 MPa) and PAMAM (0,9 wt%; 77 K; 2,5 MPa), PIMs (3,9 wt%; 77 K; 1 MPa), CMPs (2,17 wt%; 77 K; 0,1 MPa), HCPs (3,7 wt%; 77 K; 1,5 MPa) and PAFs (5,9 wt%; 298 K; 10 MPa). Among the composite materials reported are: composite PAMAM with VOx powder (2 wt%; 77 K; 2,5 MPa), and PDMH (0,4 wt%; 673 K; 7 MPa).

Recently, Pedicini *et al.* have developed a hybrid material based on a functionalized polymer (PEEK) containing different percentages of Mn oxides. The XRD patterns revealed the fundamental peaks of MnO_2 corresponding to lamellar Birnessite structure. The material containing a low Mn oxide amount (15 wt%) showed a H_2 sorption of 1,2 wt% (77 K; 0,1 MPa). Very promising results were reached under mild conditions when a load of 80 wt% Mn oxides was used. From Sievert apparatus, H_2 sorption values of 3 wt% at 323 K and 4 MPa, and 1,1 wt% at 383 K and 6 MPa were obtained.

Furthermore, by using short H_2 sorption/desorption cycles a total reversibility was demonstrated. A Modeling Study, *ab initio* density functional theory, has shown a desorption energy value comparable to metal hydrides, supporting the results obtained in this study.

In the last class, waste and natural materials, several materials are involved (as reported in Table 7.1). Among these, cigarette butts obtained a very high value of hydrogen storage (11,2 wt%; 77K; 4 MPa). In this field, other wastes or natural fibers were tested, showing very high H_2 storage properties under cryogenic conditions. These encouraging results bode well for an increasingly hydrogen-dependent future and, consequently, a more focused approach to eco-sustainability.

References

1. Züttel, A., Materials for hydrogen storage. *Mater. Today* 6, 24, 2003.
2. Orimo, S., Nakamori, Y., Eliseo, J.R., Züttel, A., Jensen, C.M., Complex hydrides for hydrogen storage. *Chem. Rev.* 107, 4111, 2007.
3. Sakintunaa, B., Lamari-Darkrim, F., Hirscher, M., Metal hydride materials for solid hydrogen storage: A review. *Int. J. Hydrogen Energy* 32, 1121, 2007.
4. Yang, J., Sudik, A., Wolverton, C., Activation of hydrogen storage materials in the Li–Mg–N–H system: Effect on storage properties, *J. Alloys Compd.* 430, 334, 2007.
5. Schüth, F., Bogdanović, B., Felderhoff, M., Light metal hydrides and complex hydrides for hydrogen storage. *Chem. Commun.* 20, 2249, 2004.
6. Niaz, S., Manzoor, T., Pandith, A.H., Hydrogen storage: Materials, methods and perspectives. *Renew. Sust. Energ. Rev.* 50, 457, 2015.
7. Rowsell, J.L.C., Millward, A.R., Park, K.S., Yaghi, O.M., Hydrogen sorption in functionalized metal-organic frameworks. *J. Am. Chem. Soc.* 126, 5666, 2004.
8. Ting, V.P., Ramirez-Cuesta, A.J., Bimbo, N., Sharpe, J.E., Noguera-Diaz A., *et al.*, Direct evidence for solid-like hydrogen in a nanoporous carbon hydrogen storage material at supercritical temperatures. *Am. Chem. Soc. Nano.* 9, 8249, 2015.
9. Barghi, S.H., Tsotsis, T.T., Sahimi, M., Chemisorption, physisorption and hysteresis during hydrogen storage in carbon nanotubes. *Int. J. Hydrogen Energy* 39, 1390, 2014.
10. Lamari Darkrim, F., Malbrunot, P., Tartaglia, G.P., Review of hydrogen storage by adsorption in carbon nanotubes. *Int. J. Hydrogen Energy* 27, 193, 2002.
11. Pedicini, R., Saccà, A., Carbone, A., Passalacqua, E., Hydrogen storage based on polymeric material. *Int. J. Hydrogen Energy* 36, 9062, 2011.
12. Pedicini, R., Schiavo, B., Rispoli, P., Saccà, A., Carbone, A., Gatto, I., Passalacqua, E., Progress in polymeric material for hydrogen storage application in middle conditions. *Energy* 64, 607, 2014.
13. Pedicini, R., Sigalas, M., Carbone, A., Gatto, I., Functionalised hybrid Poly(ether ether ketone) containing MnO2: Investigation of operative conditions for hydrogen sorption. *Int. J. Hydrogen Energy* 42, 10089, 2017.
14. Akasaka, H., Takahata, T., Toda, I., Ono, H., Ohshio, S., Himeno, S., Kokubu, T., Saitoh, H., Hydrogen storage ability of porous carbon material fabricated from coffee bean wastes. *Int. J. Hydrogen Energy* 36, 580, 2011.
15. Andreas H., The era of carbon allotropes. *Nat. Mater.* 9, 868, 2010.
16. Rajatendu, S., *et al.*, A review on the mechanical and electrical properties of graphite and modified graphite reinforced polymer composites. *Prog. Polym. Sci.* 36, 5, 638, 2011.
17. Ströbel, R., *et al.*, Hydrogen storage by carbon materials. *J. Power Sources* 159(2), 781, 2006.
18. De Jong, K.P, Geus, J.W, Carbon nanofibers: Catalytic synthesis and applications. *Cat. Rev. Sci. Eng.* 42(4), 481, 2000.

19. Chambers, A., *et al.*, Hydrogen storage in graphite nanofibers. *J. Phys. Chem. B*, 102(22), 4253, 1998.
20. Yueruem, Y., Taralp, A., Veziroglu, T.N., Storage of hydrogen in nanostructured carbon materials. *Int. J. Hydrogen Energy* 34(9), 3784, 2009.
21. Wu, H.-C., Li, Y.-Y., Sakoda, A., Synthesis and hydrogen storage capacity of exfoliated turbostratic carbon nanofibers. *Int. J. Hydrogen Energy* 35(9), 4123, 2010.
22. Xing, Y., *et al.*, Facile fabrication of mesoporous carbon nanofibers with unique hierarchical nanoarchitecture for electrochemical hydrogen storage. *Int. J. Hydrogen Energy* 39(15), 7859, 2014.
23. Virendra, S., *et al.*, Graphene based materials: Past, present and future. *Prog. Mater Sci.* 56(8), 1178, 2011.
24. Allen, M.J., Tung, V.C., Kaner, R.B., Honeycomb carbon: A review of graphene, *Chem. Rev.* 110(1), 132, 2009.
25. Sarkar, A.K., Saha, S., Ganguly, S., Banerjee, D., Kargupta, K., Hydrogen storage on graphene using Benkeser reaction. *Int. J. Energy Res.* 38(14), 1889, 2014.
26. Guo, C.X., Wang, Y., Hierarchical graphene-based material for over 4 wt% physisorption hydrogen storage capacity. *ACS Sustain. Chem. Eng.* 1, 14, 2013.
27. Zhao, T., Ji, X., Jin, W., Yang, W., Li, T., Hydrogen storage capacity of single-walled carbon nanotube prepared by a modified arc discharge. *Fuller. Nanotub. Car. N.* 25(6), 355, 2017.
28. Barghi, S.H., Tsotsis, T.T., Sahimi, M., Chemisorption, physisorption and hysteresis during hydrogen storage in carbon nanotubes. *Int. J. Hydrogen Energy* 39(3), 1390, 2014.
29. Lee, Y.T., *et al.*, A microstructural and neutron-diffraction study on the interactions between microwave-irradiated multiwalled carbon nanotubes and hydrogen, *J. Mater. Sci.* 51(3), 1308, 2016.
30. Baburaj, E.G., Froes, F.H., Shutthanandan, V., Thevuthasan, S., Low cost synthesis of Nano crystalline titanium aluminides, *Interfacial Chemistry and Engineering Annual Report*, Pacific Northwest National Laboratory, Oak Ridge, TENN, USA, 2000.
31. Jurczyk, M.U., Kumara, A., Srinivasan, S., Stefanakos, E., *Int. J. Hydrogen Energy* 32, 1010, 2007.
32. Cho, S.J., Choo, K., Kim, D.P., Kim, J.W., H2 sorption in HCl-treated polyaniline and polypyrrole. *Catal. Today*, 120, 336, 2007.
33. Panella, B., Kossykh, L., Dettlaff-Weglikowska, U., Hirscher, M., Zerbi, G., Roth, S., Volumetric measurement of hydrogen storage in HCl-treated polyaniline and polypyrrole, *Synth. Met.* 151, 208, 2005.
34. Jurczyk, M.U., Kumar, A., Srinivasan, S., Stefanakos, E., Polyaniline-based nanocomposite materials for hydrogen storage. *Int. J. Hydrogen Energy* 32, 1010, 2007.
35. Germain, J., Frèchet, J.M.J., Svec, F., Hyper-cross-linked polyanilines with nanoporous structure and high surface area: potential adsorbents for hydrogen storage. *J. Mater. Chem.* 17, 4989, 2007.
36. Nour, F.A., Lee, S.M., Kim H.J., Geckele, K.E., Nanoporous polypyrrole: Preparation and hydrogen storage properties. *Int. J. Energy Res.* 38, 466, 2014.

37. Sevilla, M., Fuertes, A.B., Mokaya, R., Preparation and hydrogen storage capacity of highly porous activated carbon materials derived from polythiophene. *Int. J. Hydrogen Energy* 36, 15658, 2011.
38. Kaloni, T.P., Giesbrecht, P.K., Schreckenbach, G., Freund, M.S., Polythiophene: From fundamental perspectives to applications. *Chem. Mater.* 29(24), pp. 10248–10283, 2017.
39. Bruchmann, B., Meffert, H., Use of hyperbranched polymers comprising urethane and or urea groups for modifying surfaces, US Patent 20060035091, assigned to BASF Aktiengesellschaft, LudWigshafen (DE), 2006.
40. Rehim, M.H.A., Ismail, N., Abd El-Rahman, A.A., Badawyb, G.T., Hydrogen storing and electrical properties of hyperbranched polymers-based nanoporous materials. *Mater. Sci. Eng. B* 176, 1184, 2011.
41. McKeown, N.B., Polymers of intrinsic microporosity. *ISRN Mater. Sci.* 2012, 1, 2012.
42. Wu, D., Xu, F., Sun, B., Fu, R., He, H., Matyjaszewski, K., Design and preparation of porous polymers. *Chem. Rev.* 112(7), 3959, 2012.
43. Scherf, U., Ladder-type materials. *J. Mater. Chem.* 9(9), 1853,1999.
44. Bailey, W.F., Ladder polymers, in: *The Encyclopaedia of Polymer Science and Engineering*, Mark, H.F. (Ed.), p. 158, John Wiley & Sons: New York, NY, USA, 1993.
45. Zhu X.Z., Chen, C.F., A highly efficient approach to [4]pseudocatenanes by threefold metathesis reactions of a triptycene-based tris[2]pseudorotaxane. *J. Am. Chem. Soc.* 127(38), 13158, 2005.
46. Ghanem, B.S., Hashem, M., Harris, K.D.M., Msayib, K.J, Xu, M., Budd, P.M., *et al.*, Triptycene-based polymers of intrinsic microporosity: organic materials that can be tailored for gas adsorption. *Macromolecules*, 243(12), 5287, 2010.
47. Makhseed, S., Samuel, J., Hydrogen adsorption in microporous organic framework polymer. *Chem. Commun.* 36, 4342, 2008.
48. Jiang, J.X., Trewin, A., Adams, D.J., Cooper, A.I., Band gap engineering in fluorescent conjugated microporous polymers. *Chem. Sci.* 2, 1777, 2011.
49. Schmidt, J., Werner, M., Thomas, A., Conjugated microporous polymer networks via Yamamoto polymerization. *Macromolecules* 42, 4426, 2009.
50. Schmidt, J., Weber, J., Epping, J.D., Antonietti, M., Thomas, A., Microporous conjugated poly(thienylene arylene) networks. *Adv. Mater.* 21, 702, 2009.
51. Gomes, R., Bhanja, P., Bhaumik, A., A triazine-based covalent organic polymer for efficient CO_2 adsorption. *Chem. Commun.* 51, 10050, 2015.
52. Liao, Y., Cheng, Z., Trunk, M., Thomas, A., Targeted control over the porosities and functionalities of conjugated microporous polycarbazole networks for CO_2-selective capture and H_2 storage. *Polym. Chem.* 8, 7240, 2017.
53. Sun, C.J., Zhao, X.Q., Wang, P.F., Wang, H., Han, B.H., Thiophene-based conjugated microporous polymers: Synthesis, characterization and efficient gas storage. *Sci. China Chem.* 60, 1067, 2017.
54. Davankov, V.A., Tsyurupa, M.P., Structure and properties of hyper-crosslinked polystyrene—The 1st representative of a new class of polymer networks. *React. Polym.* 13, 27, 1990.

55. Sidorov, S.N., Bronstein, L.M., Davankov, V.A., Tsyurupa, M.P., Solodovnikov, S.P., Valetsky, P.M., Wilder, E.A., Spontak, R.J., Cobalt nanoparticle formation in the pores of hyper-cross-linked polystyrene: Control of nanoparticle growth and morphology. *Chem. Mater.*11, 3210, 1999.
56. Tsyurupa, M.P., Davankov, V.A., Hyper-cross-linked polymers: Basic principle of preparing the new class of polymeric materials. *React. Funct. Polym.* 53, 193, 2002.
57. Tsyurupa, M.P., Davankov, V.A., Porous structure of hyper-cross-linked polystyrene: State-of-the-art mini-review. *React. Funct. Polym.* 66, 768, 2006.
58. Davankov, V.A., Pastukhov, A.V., Tsyurupa, M.P., Unusual mobility of hyper-cross-linked polystyrene networks: Swelling and dilatometric studies. *J. Polym. Sci., Part B: Polym. Phys.* 38, 1553, 2000.
59. Pastukhov, A.V., Tsyurupa, M.P., Davankov, V.A., Hyper-cross-linked polystyrene: A polymer in a non-classical physical state. *J. Polym. Sci., Part B: Polym. Phys.* 37, 2324, 1999.
60. Davankov, V.A., Rogozhin, S.V., Tsyurupa, M.P., Macronet polystyrene structures for ionites and method of producing same, US Patent 3729457, assigned to Davankov, V.A., Rogozhin, S.V., Tsyurupa, M.P., 1971.
61. Ahn, J.H., Jang, J.E., Oh, C.G., Ihm, S.K., Cortez, J., Sherrington, D.C., Rapid generation and control of microporosity, bimodal pore size distribution, and surface area in Davankov-type hyper-cross-linked resins. *Macromolecules* 39(2), 627, 2006.
62. Lee, J.Y., Wood, C.D., Bradshaw, D., Rosseinsky, M.J., Cooper, A.I., Hydrogen adsorption in microporous hyper-cross-linked polymers. *Chem. Commun.* 25, 2670, 2006.
63. Germain, J., Hradil, J., Fréchet, J.M.J., Svec, F., High surface area nanoporous polymers for reversible hydrogen storage. *Chem. Mater.* 18, 4430, 2006.
64. Wood, C.D., Tan, B., Trewin, A., Niu, H., Bradshaw, D., *et al.*, Hydrogen storage in microporous hyper-cross-linked organic polymer network. *Chem. Mater.* 19, 2034, 2007.
65. Ben, T., Pei, C., Zhang, D., Xu, J., Deng, F., Jing, X., Qiu, S., Gas storage in porous aromatic frameworks (PAFs). *Energy Environ. Sci.* 4, 3991, 2011.
66. Rochat, S., Polak-Krasna, K., Tian, M., Holyfield, L.T., Mays, T.J., Bowen, C.R., Burrows, A.D., Hydrogen storage in polymer-based processable microporous composites. *J. Mater. Chem. A* 5, 18752, 2017.
67. Schmidt, W.R., Activity report of the Unites Technologies Research Center for the Polymer Dispersed Metal Hydride program, DOE contract DEFC36–00G010535.
68. Liu, Z., Lei, Z., Cyclic hydrogen storage properties of Mg milled with nickel nano-powders and MnO_2. *J. Alloys Compd.* 443, 121, 2007.
69. Suttisawat, Y., Rangsunvigit, P., Kitiyanan, B., Kulprathipanja, S., Effect of co-dopants on hydrogen desorption/absorption of $HfCl_4$- and TiO_2-doped NaAlH4, *Int. J. Hydrogen Energy* 33, 6195, 2008.

70. Abdel Rehim, M.H., Ismail, N., Badawy, Abd El-Rahman, A.A., Turky, G., Hydrogen storing and electrical properties of hyperbranched polymers-based nanoporous materials. *Mater. Sci. Eng. B* 176, 1184, 2011.
71. Schmidt, W.R., Hydrogen storage in polymer-dispersed metal hydrides (PDMH), in: *Proceedings of the 2001 U.S. DOE Hydrogen Program Review*, 2001.
72. Checchetto, R., Bazzanella, N., Miotello, A., Carotenuto, G., Nicolais, L., Hydrogen sorption in metal-polymer composites: The role of interfaces. *J. Appl. Phys.* 105, 8, 2009.
73. Checchetto, R., Carotenuto, G., Bazzanella, N., Miotello, A., Synthesis and characterization of polymer embedded LaNi5 composite material for hydrogen storage. *J. Phys. D: Appl. Phys.* 40, 4043, 2007.
74. Pentimalli, M., Padella, F., La Barbera, A., Pilloni, L., Imperi, E., A metal hydride–polymer composite for hydrogen storage applications. *Energ. Convers. Manage.* 50, 3140, 2009.
75. Pentimalli, M., Imperi, E., Zaccagnini, A., Padella, F., Nanostructured metal hydride – Polymer composite as fixed bed for sorption technologies. Advantages of an innovative combined approach by high-energy ball milling and extrusion techniques. *Renew. Energ.* 110, 69, 2017.
76. Zhu. G., Li, H., Deng, L., Liu, Z.H., Low-temperature synthesis of δ-MnO_2 with large surface area and its capacitance. *Mater. Lett.* 64, 1763, 2010.
77. Zdetsis, A.D., Sigalas, M.M., Koukarasad, E.N., Ab initio theoretical investigation of beryllium and beryllium hydride nanoparticles and nanocrystals with implications for the corresponding infinite systems. *Phys. Chem. Chem. Phys.* 16, 14172, 2014.
78. Sevilla, M., Fuertes, A.B., Mokaya, R., High density hydrogen storage in superactivated carbons from hydrothermally carbonized renewable organic materials. *Energy Environ. Sci.* 4, 1400, 2011.
79. Senoz, E., Wool, R.P., Hydrogen storage on pyrolyzed chicken feather fiber. *Int. J. Hydrogen Energy* 36, 7122, 2011.
80. Akasaka, H., Takahata, T., Toda, I., Ono, H., Ohshio, S., Himeno, S., Kokubu, T., Saitoh, H., Hydrogen storage ability of porous carbon material fabricated from coffee bean wastes. *Int. J. Hydrogen Energy* 36, 580, 2011.
81. Yang, R., Liu, G., Li, M., Zhang, J., Hao, X., Preparation and N2, CO2 and H2 adsorption of super activated carbon derived from biomass source hemp (*Cannabis sativa* L.) stem. *Microporous Mesoporous Mater.* 158, 108, 2012.
82. Zhang, C., Geng, Z., Cai, M., Zhang, J., Liu, X., Xin, H., Ma, J., Microstructure regulation of super activated carbon from biomass source corncob with enhanced hydrogen uptake. *Int. J. Hydrogen Energy* 38, 9243, 2013.
83. Dixit, V., Shahi, R.R., Bhatnagar, A., Jain, P., Yadav, T.P., Srivastava, O.N., Hydrogen storage in carbonized coconut meat (kernel). *IJMME* 8, 9, 2014. dai.waset.org/1307–6892/12194.

84. Wróbel-Iwaniec, I., Díez, N., Gryglewicz, G., Chitosan-based highly activated carbons for hydrogen storage. *Int. J. Hydrogen Energy* 40, 5788, 2015.
85. Schaefer, S., Fierro, V., Izquierdo, M.T., Celzard, A., Assessment of hydrogen storage in activated carbons produced from hydrothermally treated organic materials. *Int. J. Hydrogen Energy* 41, 12146, 2016.
86. Hwang, S., Choi, W.M., Lim, S.K., Hydrogen storage characteristics of carbon fibers derived from rice straw and paper mulberry. *Mater. Lett.* 167, 18, 2016.
87. Ariharan, A., Viswanathan, B., Nandhakumar, V., Phosphorous-doped porous carbon derived from paste of newly growing "*Ficus benghalensis*" as hydrogen storage material. *IJC-A* 55A, 06, 2016.
88. Arshad, S.H.M., Ngadi, N., Aziz, A.A., Amin, N.S., Jusoh, M., Wong, S., Preparation of activated carbon from empty fruit bunch for hydrogen storage. *J. Energy Storage* 8, 257, 2016.
89. Ramesh, T., Rajalakshmi, N., Dhathathreyan, K.S., Synthesis and characterization of activated carbon from jute fibers for hydrogen storage. *Renew. Energy Environ. Sustain.* 2, 4, 2017.
90. Bader, N., Zacharia, R., Abdelmottaleb, O., Cossement, D., How the activation process modifies the hydrogen storage behavior of biomass-derived activated carbons. *J. Porous Mater.* 25, 221, 2018.
91. Blankenship, T.S., Mokaya, R., Cigarette butt-derived carbons have ultra-high surface area and unprecedented hydrogen storage capacity. *Energy Environ. Sci.* 10, 2552, 2017.

8

Beneficial Effects of Graphene on Hydrogen Uptake and Release from Light Hydrogen Storage Materials

Rohit R Shahi

Department of Physics, Motilal Nehru National Institute of Technology Allahabad, Allahabad, Uttar Pradesh, India

Abstract

In recent years, the development of hydrogen storage (HS) materials with favorable kinetics and desorption/absorption temperature has attracted considerable attention. The scope of HS materials has been transformed from tradition metal hydrides to lightweight hydrogen storage materials such as alanates, amide-hydride mixtures and magnesium hydride. However, each has its own limitations which is related to their high desorption temperature and slow kinetics. Thus, these materials cannot be used as onboard material for practical application in hydrogen-fueled devices or vehicles. Carbon has many allotropes with novel properties which are useful in many new innovative applications. Different well-known allotropes of carbon are graphite, activated carbon, fullerenes, carbon nanotubes, and the most recent, graphene. Recent studies have demonstrated the beneficial effect of carbon nanomaterial materials (CNFs and CNTs) as catalyst for enhancing hydrogenation/dehydrogenation behavior of different light HS materials. Among different carbon nanomaterials, graphene can also be used as a beneficial additive for different HS materials because it has light weight and high surface area. This is the main reason why it has especially attracted the attention of the hydrogen storage community. Moreover, graphene in its SP^2 hybridized stage is a semimetal with a small number of metallic electrons that can be available at the surface in delocalized or localized forms. There is a need for foreign atoms to saturate dangling bonds during termination of graphene sheet in carbon. Thus, the structure and reactivity can be fine-tuned by intercalation of some inorganic compound and element. The defect in graphene sheet is also beneficial for enhancement of

Corresponding author: rohitrshahi@gmail.com, rohitrshahi@mnnit.ac.in

Mehmet Sankir and Nurdan Demirci Sankir (eds.) Hydrogen Storage Technologies, (229–262) © 2018 Scrivener Publishing LLC

hydrogenation characteristics of HS materials. This chapter discusses general aspects of graphene and describes the characteristics responsible for its beneficial effect in the hydrogenation characteristics of HS materials. Also, it summarizes the current advancement in hydrogenation characteristics of metal and complex hydrides by incorporating graphene as an additive.

Keywords: Hydrogen storage, MgH_2, Li-Mg-N-H, CNTs, CNFs, graphene, catalyst

8.1 Introduction

Growing energy demands, consumption of fossil fuels and global warming are reasons for requiring alternative fuels which emit zero pollution and are recyclable. Hydrogen (H_2) is seen as an ideal clean alternative fuel because it is pollution free and recyclable [1–5]. It is produced from water and burns back to water under cold and hot combustion. Thus, its burning product is water, while the combustion of fossil fuels generates CO_2 and a variety of pollutants. Moreover, hydrogen is highly abundant in the universe, which provides rich sources for generation of hydrogen. Hydrogen possesses higher energy content per mass unit, which is 33% more efficient as compared to the widely used gasoline and coal [6]. This is the reason behind the increasing efforts from research communities and governments all over the world to endorse the forthcoming hydrogen economy. However, there are a few technical barriers to a hydrogen economy becoming reality. These are hydrogen generation, H_2 storage and applications in fuel-cell and IC engine, among which efficient, economical and safe onboard storage of hydrogen presents a huge challenge. It is now well known that storage of hydrogen is a crucial issue of the hydrogen economy, cutting across boundaries of production, distribution and applications [7]. Hydrogen can be stored either as liquid H_2, in compressed gas cylinders, in solid state as metal/chemical hydrides or adsorbed in porous materials. However, each H_2 storage mode has its own disadvantages. For example, (a) high energy cost for liquefaction and to maintain low temperature, (b) safety issues for compressed gas which needs to be operated at high pressures, (c) the chemisorptions of metal hydrides and chemical hydrides are usually hindered by their high thermodynamics, slow kinetics and poor reversibility and (d) the physisorption of H_2 by porous materials exhibits reasonable H_2 uptake at cryogenic temperature. Thus, efficient absorption with reasonable uptake capacities still remains a technological barrier for practical applications [8].

Among various approaches to hydrogen storage, it is generally now believed that storage in the form of hydrides is an efficient and safe storage

mode with high hydrogen density [9]. In order to guide the R&D activities, demonstrate the viability of hydrogen storage technologies and realize the potential hydrogen economy in the future, the United States Department of Energy (U.S. DOE) has proposed a set of technical targets for onboard hydrogen storage system and revised these target time to time. These targets are based on achieving a driving range of 500 km for H_2-powered vehicle. Table 8.1 describes the target set by the U.S. DOE [10].

Based on these target values several light metal hydrides can be considered as promising onboard storage materials. These include $LiBH_4$, MgH_2 $NaAlH_4$ and amide-hydride mixture having theoretical hydrogen storage capacity of ~18.6, 7.6, 5.6 and 11.4 wt% respectively [11]. The major limitation of these materials are high desorption temperature and poor sorption kinetics. However, recent research attempts in this field, such as using catalyst or alloy additives to catalyze or destabilize the hydride system, and decreasing the particle size down to nano-meter order, can remarkably decrease the hydrogen release temperature, increase kinetics and improve the cyclabilities of these hydrides, which make the light metal hydrides one of the promising hydrogen storage candidates. Thus, these materials may become viable with the deployment of suitable catalyst [11].

Recent studies, confirm the importance of nanomaterials in hydrogen storage. Nanomaterials, possessing unusual chemical and physical properties [12, 13], have become the center of interest for environmental remediation and energy-related applications [14, 15]. Among the nanomaterials, carbon nanostructures (CNS), such as carbon nanotube [16, 17], carbon nanofibers [18], carbon nanospheres [19, 20], nanodiamond and fullerene [21], have attracted considerable attention due to their excellent physical, chemical and electronic properties. The remarkable characteristics of carbon nanomaterials result in a wide range of applications in many technically important fields such as adsorption, separation and electrodes, and are widely used in air and water purification, as gas absorbent, catalyst,

Table 8.1 DOE target value for HS materials.

Parameter	Unit	Targets for 2020	Ultimate value
System gravimetric capacity	kW h/kg	18	2.5
	Kg H_2 per Kg system	0.055	0.075
System volumetric capacity	$kWhL^{-1}$	1.3	2.3
	Kg H_2 per L system	0.040	0.070

catalyst supports and scaffolds. Among carbon nanostructures, graphene shows enormous potential for research in various fields [22–25]. Graphene is a wonder material having large surface area, porous geometry and can act as catalyst. These properties of graphene enable its use for environmental pollution control and energy-related systems, especially in hydrogen storage applications. The breakthrough in hydrogen storage techniques strongly depend on the advancement of materials science [26]. Recent studies indicated that graphene can be considered as a promising material for hydrogen storage and related applications [27].

Metal or metal oxide catalysts are the most commonly used traditional catalysts. Metal oxides are widely used as a catalyst in many hydrogenation and dehydrogenation reactions. However, systematic optimization of metal or metal oxide catalyst is difficult because of the substantial chemical complexity of empirically optimized heterogeneous catalysts. Nowadays, for hydrogen storage materials, apart from the traditional catalyst (having high density, due to which dead weight is created for storage application), the focus has been shifted towards the lightweight, high surface area and extremely high active site carbon materials (such as graphite, activated carbon, fullerenes, carbon nanotube, carbon nanofiber and, recently, graphene) [28, 29]. Additionally, due to the light weight and variable hybridization states (sp, sp^2 and sp^3) of carbon-based nanostructured materials (CNS), these materials serve as an effective catalyst to destabilize the bonds in the hydrogen storage materials.

Several reviews already exist in the literature which summarize the hydrogen storage in graphene, but almost none of them focus on the beneficial/catalytic effects of graphene on different light metal hydrides [30]. In this chapter, the effect of doping/addition of graphene is discussed and described. Moreover, particular emphasis on graphene as a template for nanoparticles for enhancing the hydrogen sorption performance of most promising HS materials is analyzed and summarized. We especially emphasize the beneficial effect of graphene on MgH_2, $NaAlH_4$ and $LiBH_4$. The chapter is divided into four sections: we first describe some general aspects of graphene, and then summarize the main characteristics of graphene responsible for its beneficial effects on hydrogen materials, followed by a brief presentation of the beneficial effect of graphene on different hydrogen storage materials.

8.2 General Aspects of Graphene

Carbon atom can bond in a chain, ring and branch network and produce a variety of structures. Nowadays, carbon nanomaterial is being extensively

treated as a technologically important material because of its unique physical and chemical properties. Discovery of carbon-based nanostructures (CNSs) have attracted great interest in the area of materials science and engineering. The unique properties of nanotubes and nanofibers make these materials a technologically important material. The most recent addition in the series of CNSs is graphene. Graphene is a monolayer (or few-layer; <10) of sp2-hybridized carbon atoms that are hexagonally attached, and received great attention due to its notable physical and chemical properties [31, 32]. Graphene has unique properties, e.g., great intrinsic carrying ability, well-developed porosity, active surface area, outstanding electronic properties and promising mechanical and thermal stability, make it a promising material for different applications.

8.2.1 Synthesis of Graphene

Graphite is a well-known material composed of stacked multi-layered graphene sheets. These sheets are bonded together with week van der Waals bonds. Graphene can be synthesized from highly pure graphite sheet by breaking the weak van der Waals bonds. Graphene can be synthesized by different methods, such as exfoliation, mechanical and chemical cleavage. Among the known methods, those presented below are used by the most researchers.

8.2.1.1 Mechanical Cleavage of Highly Oriented Pyrolytic Graphite

Graphene was firstly synthesized by mechanical cleavage of graphite with scotch tape. This remarkably simple method was developed by Novoselov *et al.* by using a common adhesive tape [33]. They repeated the peel-and-stick process a dozen times and produced 1-mm-thick flack graphite. Although the yield of the graphene produced by this method is not good enough, it has unique structural and superior properties. After this pioneering work, several alternative techniques have now been developed for the fabrication of graphene.

8.2.1.2 Chemical Vapor Deposition

This method is another commonly used feasible method of synthesis of graphese by decomposition of ethylene on nickel surface [34]. Single-layer graphene was synthesized from decomposition of ethanol on Ni foil in Ar-atm by flash cooling after CVD. However, a wide variation in synthesis

of layer on the metal surfaces has been reported for the synthesis of graphene by this method.

8.2.1.3 Chemical and Thermal Exfoliation of Graphite Oxide

Graphene can be synthesized through the Chemical exfoliation of GO and r-GO [35–37]. The oxidation method of graphene was discovered by Brodie, Staudenmaier and Hummers [38, 39]. All these methods involve oxidation of graphite in the presence of strong acid and oxidants. The oxidation level depends on the reaction conditions and graphite precursor used. Reducing graphene oxide can partly restore graphite structure, as well as conductivity [40]. The reduced graphene oxide has defects and is widely used as renewable energy materials due to low cost, large productivity and potential for functionalization.

8.2.1.4 Arc Discharge Method

Rao *et al.* first reported the synthesis of graphene sheets by arc discharge method [41]. They used graphite rod as electrode and synthesized pure 2–4-layer graphene sheet; the material was deposited in the inner wall of the arching chamber. Through this method, nitrogen and boron-doped graphene can also be synthesized.

8.2.2 Graphene as a Beneficial Additive for HS Materials

The quest for effective catalyst led to the discovery of graphene as an effective catalyst for the area of HS. Graphene has certain properties that makes it a suitable additive for enhancing sorption behavior of different hydrogen storage materials. Graphene is comparatively cheaper than metal or metal oxide catalysts and is lightweight (due to which it has especially attracted the attention of the hydrogen storage community). Recently, graphene has been explored as catalyst for improving the de/rehydrogenation of different hydrogen storage materials due to the presence of delocalized π bond and the possible interaction with hydrogen atoms [42, 43]. Since light metal hydrides are chemically reactive, the specific chemical inertness is a most important property which makes them an effective catalyst. Some important reactions with carbon matrix exist, due to which the enhancement in sorption behavior has been observed. These are: (a) intercalation, (b) carbide formation and (c) interaction with terminating group, defects and contaminations; and also some important physical properties, such as (d) H_2 diffusion promoter (e) thermal conductivity and (f) dispersion of

catalysts, are responsible for the beneficial effect of carbon materials [30]. These properties are responsible for the beneficial effect of graphene on the sorption behavior of different storage materials.

In comparison to other carbon allotropes, graphene offers the highest carrier mobility, excellent mechanical strength, and thermal and chemical stability [44–46]. In comparison to carbon fibers it has three-dimensional interconnected porous structures [47]. These properties of graphene have encouraged many researchers to use it as a raw material in the area of batteries sensors, solar cell and many others [48]. Moreover, high surface area graphene (approx. 2600 m^2/g) makes it a promising material for two-dimensional supports for metallic and bimettalic nanoparticles [49]. For catalytic application, available defects in graphene can be utilized to form new surface functionalities which further enhanced the interaction with template metal nanoparticles [50, 51]. The requisite for a potential support of metal nanoparticle catalyst is that it must have high surface area and porosity. It has already been reported that porous structure provides a favorable path for the penetration and transportation of the molecules [52]. Figure 8.1 is a schematic representation of the penetration mechanism for nanocatalysts towards graphene sheets [53]. The surface area of the graphene can be increased by several novel methods, e.g., erosion [54], self-assembly [55], thermodynamical cracking [56] and KOH activation. Graphene and metal nanoparticle support graphene can be synthesized with suitable surface area and porosity through chemical reduction [57], chemical vapor deposition growth [58], and exfoliation [59]. The general properties of graphene are summarized in Table 8.2.

Graphene plays a pivotal role as a new catalyst support. Additionally, these catalysts are used for the enhanced hydrogen storage properties of

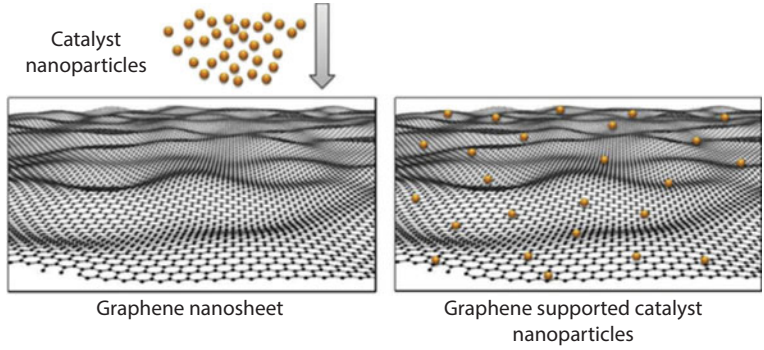

Figure 8.1 Penetration mechanism for nanocatalysts towards graphene sheets. (Reproduced with permission from [53]).

Table 8.2 General properties of graphene.

Properties	Values	Ref.
Tensile strength	130 GPa	[60, 61]
Electron mobility	15×10^3 cm^2/V	[62]
Thermal conductivity	$4.84–5.3 \times 10^3$ W m/K	[63]
Surface area to mass ratio	2600 m^2/g^2	[64]
Charge carrier mobility	2×10^5 cm^2/Vs	[63]

storage materials**.** Recently, graphene decorated with metal nanoparticles and oxides has offered many beneficial effects in the area of energy storage [65–68] and electronics [69, 70] owing to its excellent mechanical, electronic, chemical and structural properties, such as surface area pore geometry and active edge sites, which makes it a processing material towards application of energy conversion/storage, catalysts and nanoelectronics.

The reversibility of most promising hydrogen storage materials is degraded due to the agglomeration of HS materials during cycling. The agglomeration of catalysts/additives can be avoided by templating these catalysts with suitable template. The template must be light (because it creates negative weight for hydrogen storage), stable (so that it will not deform during cycling) and also should be strong enough (so that it will be stable during processing for the material preparation) [71]. In the next section, the beneficial effects of graphene on borohydride, magnesium hydride and alanate HS systems are described.

8.3 Beneficial Effect of Graphene: Key Results with Light Metal Hydrides (e.g., $LiBH_4$, $NaAlH_4$, MgH_2)

8.3.1 Borohydrides (Tetrahydroborate) as HS Material

Alkaline earth borohydrides dehydrogenate according to the following reactions:

$$M(BH_4)_2 \longrightarrow MH_2 + 2B + 3H_2 \quad \text{or} \tag{8.1}$$

$$M(BH_4)_2 \longrightarrow MB_2 + 4H_2 \quad \text{or} \tag{8.2}$$

$$M(BH_4)_2 \longrightarrow 2/3MH_2 + 1/3MB_6 + 10/3H_2 \tag{8.3}$$

On the basis of a large theoretical storage capacity of 18.5 wt% H_2, lithium borohydride ($LiBH_4$) can be widely considered as a leading hydrogen storage candidate for onboard applications [72]. However, due to its strong covalent and ionic bonds, desorption of hydrogen from $LiBH_4$ is not possible at mild temperature [73, 74]. Thus, $LiBH_4$ starts to decompose and release hydrogen at 410 °C and only half of the hydrogen is released below 600 °C [75]. Also, the rehydrogenation reaction has remained an enormous challenge due to extremely rigorous reaction conditions (requiring high pressure and temperature ~35 MPa and 600 °C) [73]. The thermal desorption spectrum exhibits four endothermic peaks. The peaks are attributed to a polymorphic transformation around 110 °C, melting at 280 °C, hydrogen desorption (50% of the hydrogen was desorbed [$LiBH_2$] around 490 °C), and desorption of three of the four hydrogen atoms at 680 °C. Only the third peak (hydrogen desorption) is pressure dependent. The calculated enthalpy (ΔH = 40 kJ/mol of H_2), is far less than that of pure $LiBH_4$ (ca. 74 kJ/mol H_2) [76]. Additives to the borohydride (such as SiO_2) lower the hydrogen desorption temperature for $LiBH_4$ by approximately 100 K. Several studies have revealed that the catalysts show some promising effect on decomposition of $LiBH_4$ [77–79].

8.3.1.1 Effect of Graphene on Desorption Properties of $LiBH_4$

Recently, Xu *et al.* investigated the positive effect of graphene on hydrogen uptake and release from $LiBH_4$ [80]. They reported a doping strategy to improve the dehydrogenation properties of $LiBH_4$ which involves the addition of various quantities of graphene as a host for $LiBH_4$. They found that the graphene-doped $LiBH_4$ revealed superior dehydrogenation and rehydrogenation performance as compared to other carbon nanostructures doped $LiBH_4$. They synthesized graphene by complete oxidation followed by microwave and thermal reduction method. Briefly, 1 g graphite powders and 1 g $NaNO_3$ were placed in a reaction vessel (immersed in an ice bath), followed by slow addition of 35 ml H_2SO_4 and 5 g $KMnO_4$ under violent stirring. To fully oxidize graphite powder to graphite oxide (GO), the mixture was stirred at room temperature for 120 h, followed by the addition of 100 ml of 5 wt% H_2SO_4 aqueous solution and stirred for 2 h, after which 100 ml of 30 wt% H_2O_2 was added. After the centrifugation and washing procedure, GO powders obtained were irradiated in a domestic microwave oven (1100 W for 1 min) and then filtrated, washed and dried at 65 °C for 24 h. These chemically activated GO powders were put in a tube furnace under flowing argon and heated at 800 °C for 1 h. Finally, the products were then centrifuged, washed, and vacuum-dried. The synthesized graphene

has been characterized by TEM analysis (as shown in Figure 8.2). The synthesized graphene sheets have area of a few hundred square nanometers and thickness of approximately 1.9 nm. They also measured the specific surface area of synthesized graphene sheets using the Brunauer–Emmett–Teller (BET) theory; and the specific surface area of graphene sheets was found to be 2340 $m^2 g^{-1}$. Furthermore, they pointed out a hysteresis loop in the nitrogen desorption branch, proving that the prepared graphene sheets were porous with micro-mesopore size distribution centered at 3.6 nm along with a pore volume of 1.9 $cm^3 g^{-1}$. The dehydrogenation temperature of $LiBH_4$ was effectively reduced by the addition of 20 wt% of graphene. The onset desorption temperature of graphene-doped $LiBH_4$ sample was found to be 230 °C and 5.9 wt% of desorbed hydrogen. However, for the case of undoped $LiBH_4$ only 0.6 wt% of hydrogen was released before 360 °C. They also found that in comparison to pure $LiBH_4$, the dehydrogenation peaks of 20 wt% $LiBH_4$-doped samples shift to lower temperatures with an increase of total desorption wt% of 11.6 wt% below 700 °C. With an increase in graphene content, the onset desorption temperature and two maximum desorption peaks from $LiBH_4$ are found to gradually decrease and total desorption of released hydrogen is increased. With the addition of 85 wt% of graphene, the onset desorption and peak desorption temperature is reduced to 195 °C and 310 °C respectively. The dehydrogenation of 85 wt% graphene-doped sample was also found to be 17.9 wt%, which was close to the theoretical storage capacity of $LiBH_4$ (18.5 wt%). This significant improvement may arise due to the synergistic effect of the remarkable increase in the contact area between graphene and $LiBH_4$. Moreover, the confinement of $LiBH_4$ effectively avoided its agglomerations. Thus, according to Xu *et al.* graphene prepared by microwave and thermal reduction technique exhibited significant improvement in the reversible dehydrogenation properties of $LiBH_4$. The onset desorption temperature was reduced

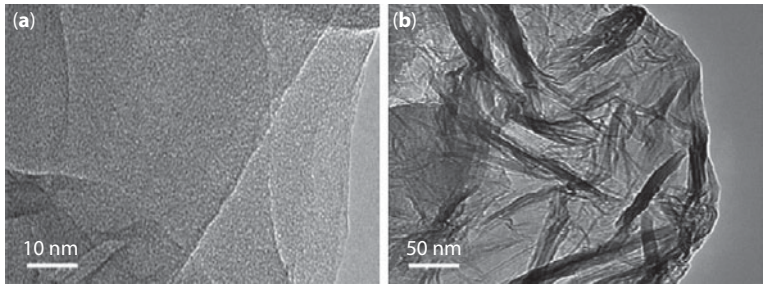

Figure 8.2 TEM micrographs of graphene prepared by microwave and thermal reduction method. (Reproduced with permission from [80])

from 420 to 199 °C and two peaks of maximum desorption temperature decreased from 485 and 610 to 300 °C, and the dehydrogenation enthalpy was also reduced to 34 kJ/mol. Thus, destabilization of $LiBH_4$ using graphene is a new promising method for the catalytic dehydrogenation and rehydrogenation of $LiBH_4$.

Wang *et al.* also investigated the catalytic effect of the graphene-supported Pd (Pd-G) for hydrogen release from $LiBH_4$ [81]. They reported that the 5 wt% Pd-G-60 (with 60 wt% Pd loading) catalyzed $LiBH_4$ has an onset desorption temperature that is 105 °C lower than the pure LiBH4 milled under identical conditions. Also, the dehydrogenation enthalpy was reduced to 43 kJ/mol H_2, which is 31 kJ/mol lower than the pristine $LiBH_4$. More beneficially, when reversible rehydrogenation was achieved, catalyzed $LiBH_4$ can absorb 6.6 wt% at 3 atm H_2 pressure, and at temperature 400 °C for 10 h even at the 30th cycle. The catalytic effect of Pd-G on $LiBH_4$ was more significant as compared to pure graphene or Pd nanoparticles. These beneficial effects are attributed to the homogeneous dispersion of Pd nanoparticles in graphene.

8.4 Alanates as HS Materials

Sodium aluminum hydride ($NaAlH_4$) is considered as a potential candidate for onboard hydrogen storage material due to its high reversible HS capacity (5.6 wt%), low cost and its availability in bulk. This complex hydride has received great attention over the past decade [82]. Alanates are remarkable due to their high storage capacities. However, they decompose in three steps upon dehydrogenation.

$$3NaAlH_4 \rightarrow Na_3AlH_6 + 2Al + 3H_2 \ \ (3.75\ wt\%,\ b/w\ 170–230\ °C) \quad (8.4)$$

$$Na_3AlH_6 \rightarrow 3NaH + Al + 1.5H_2 \ \ (1.85\ wt\%,\ b/w\ 230–260\ °C) \quad (8.5)$$

$$3NaH \rightarrow 3Na + 3/2H_2 \ \ (1.80\ wt\%,\ >400\ °C) \quad (8.6)$$

Due to the thermal stability of NaH, only steps 1 and 2 are focused on hydrogen storage application. Theoretically, $NaAlH_4$ and Na_3AlH_6 contain large amounts of hydrogen, 7.4 and 5.9 wt%, respectively. The reversibility of the above two reactions is a critical factor for practical applications. Although it has good hydrogen-storage capacity, $NaAlH_4$ has not been considered as rechargeable hydrogen carrier due to its irreversibility and poor kinetics, until Bogdanović *et al.* showed that titanium-doped $NaAlH_4$ can

be reversibly dehydrogenated and rehydrogenated [83]. The addition of Ti-based compounds (such as $TiCl_3$ or $Ti[OBu]_4$ to $NaAlH_4$) was found to lower the first decomposition temperature of the hydride, so that 3.7 wt% is released at 353 K, but at the expense of lowering the hydrogen content from 5.5 wt% in the hydride without a catalyst [83, 84]. Furthermore, the reaction is reversible and a complete conversion to product was achieved at 270 °C under 175 bar hydrogen pressure in 2–3 hours [84].

8.4.1 Effect of Graphene on Sorption Behavior of $NaAlH_4$

Xu and Ge theoretically investigated the beneficial effects of graphene with defects and various dopants [85]. The effect of pristine graphene with pentagon-heptagon (5–7) defects and the effect of carbon vacancies, as well as B-, Cl-, N-, S-, O-, P-, F- and OH-doped graphene, has been discussed and described for the highly dispersed sodium alanate through periodic density functional theory (DFT) analysis using the Vienna ab initio simulation package (VASP) [86–88] with projector augmented-wave (PAW) [89] potentials and plane-wave basis sets. Density functional theory (DFT) study shows that pristine graphene, 5–7 pair defects as well as N- and S-doped graphene substrates do not show considerable effect on hydrogen interaction in supported $(NaAlH_4)_4$. In the case of the P-, O-, F- or OH-doped graphene substrates, a metastable dihydrogen with a H-H distance of ~0.96 Å forms upon relaxing supported $(NaAlH_4)_4$. According to Xi and Ge, there is an activation barrier from the metastable dihydrogen state to the molecular H_2 state. The formation of metastable dihydrogen occurs because of less effective charge transfer on these substrates from the supported cluster to graphene with C vacancies and with B and Cl as dopants. On graphene substrates with carbon vacancies as well as B and Cl dopants, H_2 forms instantaneously upon relaxation. These substrates appear to be the ideal substrates for hydrogen release from the highly dispersed $NaAlH_4$. According to structural and charge analysis, C vacancies act as electron-scarce sites, due to which electrons are withdrawn from the supported $NaAlH_4$, which leads to electron localization near the defective sites. The transfer of electronic charge from the negatively charged AlH_4^- units to the vacancy defects destabilizes the complex ion and results in the H_2 formation on the vacancy graphene-supported $NaAlH_4$. On the other hand, B-doped graphene acts as electron acceptor and the distance between Na^+ and substrate is greatly reduced, which can be attributed to the localized electronic charge on the C atoms around B. The negative charge on the C atoms pulls the positively charged Na^+ ions closer, which, in turn, pulls the remaining moiety closer. In the Cl-doped graphene, the out-of-plane

Cl is attracted to the Na atoms of the supported $(NaAlH_4)_4$. Due to this, the entire cluster gets closer to the substrates. The strong Na–Cl interaction mediates a charge transfer from the AlH_4 and reduces the electronic charge on the complex ions, which destabilizes the complex ions, consequently making hydrogen desorption thermodynamically favorable.

The catalytic effect of nitrogen-doped graphene and CNTs as a catalyst for sorption behavior of $NaAlH_4$ was investigated by Kumar *et al.* [90]. Graphene was synthesized from graphite powder (Aldrich) by a two-step process, consisting of oxidation and/or exfoliation of graphite to graphite oxide (GOx) by Hummers' method, followed by chemical reduction of GO_x to graphene. Nitrogen-doped graphene was prepared by annealing GOx in NH_3/Ar (10% NH_3) at 600 °C for 20 min. Synthesized graphene and nitrogen-doped graphene randomly oriented transparent sheets several microns in size were confirmed through SEM micrographs (as shown in Figure 8.3). It was found that N-doped graphene has a superior catalytic effect as compared to pure graphene for enhancing the dehydrogenation kinetics of $NaAlH_4$. The $NaAlH_4$ catalyzed with N-doped graphene desorbed 5.2 wt% of hydrogen within 150 min at 220 °C. The decomposition temperature also decreased for $NaAlH_4$ catalyzed with nitrogen-doped graphene. The activation energy of sodium $NaAlH_4$ is calculated using Kissinger analysis. The total reduction in activation energy for the first and second steps was found to be ~33.9 and ~77 kJ/mol, respectively, for $NaAlH_4$ catalyzed with nitrogen-doped graphene. The rehydrogenation reaction is also facilitated in the presence of N-doped graphene in $NaAlH_4$. This may occur because nitrogen sites in nitrogen-substituted graphene can act as active centers where the activation and dissociation of hydrogen molecules can take place, as in the case of metal nanoparticles. Hydrogen

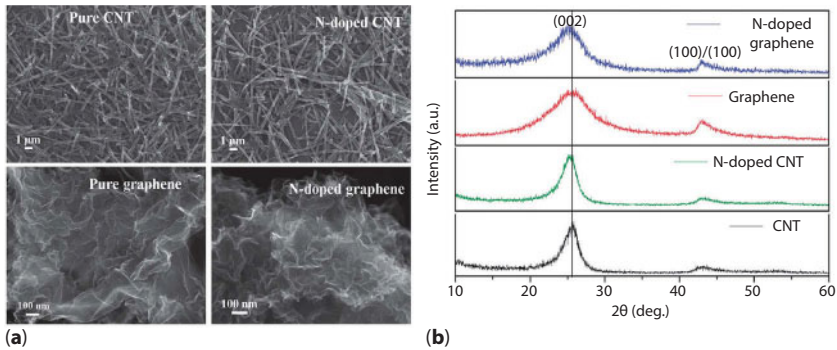

Figure 8.3 (a) SEM and (b) XRD patterns of synthesized carbon nanomaterials. (Reproduced with permission from [90]).

molecules get activated on the nitrogen site and then are dissociated into hydrogen atoms. The layer morphology of carbon graphene favors transport and diffusion of the hydrogen and thus facilitates dehydrogenation. Doping amount of nitrogen in the graphene also affects the performance and structure of these materials. Doping of nitrogen in graphene can be done either during synthesis or by introducing nitrogen after synthesis of graphene. However, the post treatment doesn't change the bulk properties of graphene.

8.4.2 Carbon Nanomaterial-Assisted Morphological Tuning of $NaAlH_4$ to Improve Thermodynamics and Kinetics

An effective way to destabilize $NaAlH_4$ by tuning its morphology through CNSs was developed by Li *et al.* [91]. This phenomenon, known as dissolution-recrystallization, alters the morphology of $NaAlH_4$. In this phenomenon the complex anion reacts with carbon matrix. $NaAlH_4$/carbon nanomaterials of graphene (GN), fullerene and mesoporous carbon (MC) were used to study the effect of morphological tuning of $NaAlH_4$ and destabilized it. The mixture of $NaAlH_4$ and selected carbon nanomaterials was added to dried tetrahydrofuran (THF) solution with vigorous stirring. After the evaporation of THF, $NaAlH_4$ recrystallized and homogeneously dispersed on the surfaces of selected CNSs. Scale-like structure, flower-like structure (with diameter ranging from 5 to 10 μm) and uniform particle (with an average diameter of 2 μm) are found with GNS-, C_{60}- and MC-assisted $NaAlH_4$ sample respectively. The onset desorption temperature decreased to 188, 185 and 160 °C for the samples assisted with GNS, C_{60}, and MC respectively. However, the same for the pristine $NaAlH_4$ is found to be 210 °C. Also, the improvement in kinetics is found to be in the order of MC, C_{60}, and GNS. The enhanced desorption kinetics occur due to both particle refinement and interaction of $[AlH_4]^{-1}$ complex with the carbon matrix. This graphene-assisted morphological tuning improves both the thermodynamics and kinetics destabilization of $NaAlH_4$. Thus, the activation energy for the first, second and third steps is reduced from 128 kJ/mol, 247 kJ/mol and 267 kJ/mol to 115 kJ/mol, 170 kJ/mol and 208 kJ/mol respectively for GNS-assisted $NaAlH_4$. It is believed that the presence of graphene influenced the recrystallization of $NaAlH_4$, which can be attributed to two facts: (a) GNS have a larger surface area due to which there will be a higher number of nucleation sites which may further result in lower energy barriers for nucleation. Since GN has sheet-like structure it can provide a broad and flat field for the nucleation of $NaAlH_4$ and favors the preferential growth along its surfaces that merge to form a continuous

structure. (b) "Pinning effect" between $NaAlH_4$ and GNS would further modify the subsequent growth of $NaAlH_4$; the stronger the pinning effect, the smaller the matrix grains. Both of the factors discussed above are the fundamental reason for the particle refinement of $NaAlH_4$

Further improved hydrogen desorption of $NaAlH_4$ can also be explained on the basis of graphene inducing the particle refinement of $NaAlH_4$. Moreover, graphene possesses an electronegative nature and favors the interaction with $[AlH_4]$ complex when they are in close contact with each other. This would lead to disruption of the charge transfer from Na to AlH_4 complex and weakening of the Al–H bonds, consequently facilitating the hydrogen desorption.

8.5 Magnesium Hydride as HS Material

Magnesium hydride (MgH_2) is a most promising HS material. Hydrogenation of hexagonal close-packed magnesium metal lattice produced magnesium hydride. Initially the formation of α-phase (a solid solution of H in Mg) takes place up to the maximum hydrogen concentrations of 9 at% at 650 °C, due to the tetrahedral occupancy of H-atom. Upon further addition of hydrogen, the β-MgH_2 phase is formed. Noritake *et al.* reported that β-MgH_2 has a body center tetragonal lattice of rutile type with lattice parameters $a = 0.452$ nm and $c = 0.302$ nm, space group $P42/mnm$ and a density 1.42×10^3 kgm^{-3} [92]. The Mg atoms are octahedral coordinated to six H atoms, while the H atoms are coordinated with three Mg atoms in a planar coordination. The slow hydrogenation and dehydrogenation are the major drawbacks of magnesium hydride as hydrogen storage material. However, magnesium hydride still holds interest for many researchers due to its low atomic weight, high hydrogen storage capacity (7.2 wt%), low cost and simplicity of structure, despite its slow kinetics and high operating temperature of 600 K [93–96]. Sakintuna *et al.* have tabulated a list of modified magnesium-based systems, most of which involved ball-milling for material preparation [97]. This leads to increase of surface area, creation of defects and nucleation sites, and also reduces the hydrogen diffusion path. In order to further improve the sorption behavior of MgH_2, several studies have also been reported that the combination of ball-milling with a catalyst provides significant improvement in hydrogenation characteristics. Different metals and intermetallic alloys have been used as catalysts for lowering of decomposition temperature and enhancement in kinetics of MgH_2 [98–104]. The main drawback of these additives is the density of the metal and alloys, which create a negative weight for storage applications. In

recent years, carbon nanostructures have been extensively used as catalyst for improvement of the sorption behavior of hydrogen storage materials [105].

Recently, some reports have appeared to describe MgH_2 admixed (catalyzed) with various carbon nanostructures [105–111]. These studies have the beneficial effect of carbon materials on both the hydriding and dehydriding behaviors. Among these results, Wu *et al.* reported that 5 wt% SWCNTs catalyzed MgH_2 absorbs 6 wt% and 4.2 wt% of hydrogen at 423 K and 373 K respectively [109]. Lillo-Ródenas *et al.* investigated the effect of different carbon materials on decomposition of MgH_2 [106, 107]. The best results were achieved in the mixtures involving CNFs with metallic impurities (Ni and Fe). Wu *et al.* also reported that as-prepared nickel-coated carbon nanofibers (NiCNFs) exhibit a superior catalytic effect on the hydrogenation behavior of magnesium [109]. The result demonstrated that nanocomposite with 5 wt% of NiCNFs absorbs 6 wt% of hydrogen in 5 min at 423 K and absorbs 5.5 wt% of hydrogen within 20 min at 573K. We have also investigated the catalytic effect of SWCNTs, MWCNT, PCNF and HCNF on de/rehydrogenation characteristics of MgH_2 and found that among these catalysts HCNF has the most effect compared to other variants of carbon nanostructures [112, 113]. Furthermore, the catalytic effect of CNFs can be modified by the presence of synthesis acquired metal nanoparticles and the diameter of the synthesized CNFs [114].

8.5.1 Catalytic Effect of Graphene on Sorption Behavior of Mg/MgH_2

Liu *et al.* investigated the catalytic effect of graphene nanosheets (GNS) on de/rehydrogenation characteristics of MgH_2 [115]. High surface area GNS were synthesized through the thermal exploitation technique and used as an additive for MgH_2. The study was focused on the effect of milling duration on hydrogenation behavior of GNS-catalyzed MgH_2. The hydrogenation kinetics and decomposition behavior improved significantly with prolonged milling. They found that absorption of ~6.6 wt% of hydrogen occurred within one min at 300 °C for 20 h mechanically milled sample. However, the uncatalyzed material can absorb 6.3 wt% of hydrogen within 180 min even at 150 °C. Detailed TEM analysis revealed that GN exists at the edge of the sample, which indicates that it had been dispersed in a disorderly and irregular manner in the sample. It is now well known that the dissociation of H_2 molecule to H atom required 4.5 eV. This indicated that the activation barrier for the rehydrogenation of Mg is quite high [116]. Recent studies have already proven that the presence of carbon on the Mg

surface reduced the dissociation barrier of hydrogen molecule to atom, with the barrier being lowered to 1.05 eV; and the atomic hydrogen is also easily diffused into the sublayer through the channels in the presence of GNS [116]. Thus, the presence of GNS facilitates the hydrogenation/dehydrogenation of MgH_2. Moreover, the presence of GNS reduces the possibility of agglomeration of the Mg grains.

Liu *et al.* also reported the effect of few-layer graphene nanosheets for enhancing the hydrogenation characteristics of MgH_2 [117]. They have synthesized GNS by thermal exfoliation of graphene oxide (GO) at 900 °C under a mixture of Ar-H_2 gas for 30 min in a quartz tube. Samples for hydrogenation studies were prepared by ball-milling of 5 wt% GNS with MgH_2 (denoted as MgH_2–5GNS) with powder to ball ratio 1:40 and 0.5 MPa of hydrogen pressure at 450 rpm for 20 h. Figure 8.4(i) presents the different characterizations of synthesized GNS. As clear from the TEM micrograph, most of the sheets agglomerated into thicker sheets with distinct structure. The six-fold symmetrical spot is from graphite nanosheets, which further confirms the disorderly nature of GNS. They found that desorption starts at temperature 267 °C for MgH_2-GNS, which is 35 °C lower than the pure MgH_2. The dehydrogenation peak temperature of MgH_2–5GNS is about 329.5 °C, which is 28 °C lower as compared to the pure MgH_2. They also reported that sample released 6.7 wt% of H_2 during temperature-programmed desorption (TPD) and absorbed 6.6 wt% at 300 °C within 1 min. It can absorb 6.38 wt% within 20 min and 5.91 wt% within 30 min at temperature 250 °C and 200 °C respectively. However, pure milled MgH_2 absorbed only 4.995 wt% within 1 min, 2.65 wt% within 30 min at 300 °C and 200 °C respectively. Moreover, they found that there is no change in hydrogen storage capacity, only a little lower absorption

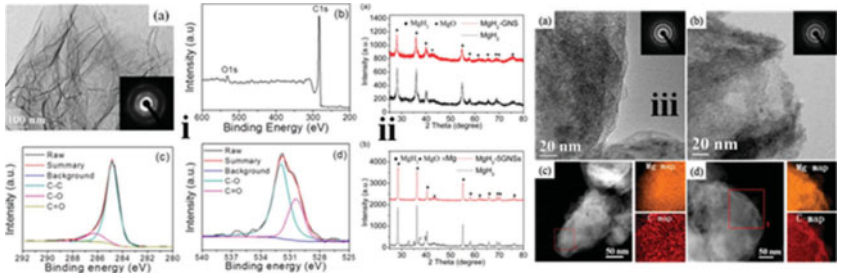

Figure 8.4 **(i)** (a) TEM micrographs of GNS, inset is the SAED of GNS; (b) XPS Spectra; (c) C1s and O1s XPS spectra of GNS. **(ii)** XRD patterns of MGH_2+5GNS (a) before and (b) after cycling. **(iii)** TEM micrograph of MgH2+5GNs (a) before and (b) after cycling; HAADF STEM micrograph and elemental mapping (c) before and (d) after cycling. (Reproduced with permission from [117])

kinetics has been recorded after six cycles. However, for pure milled MgH_2 there is a large decrease in absorption kinetics after six cycles.

They reported that the presence of GNS act as a grain growth inhibitor to prevent the agglomeration of Mg/MgH_2 particles, which is confirmed through XRD and TEM of sample after six cycles, as shown in Figure 8.4(ii-iii). Moreover, GNS act as a catalyst by providing more active edge sites due to the structure of GNS. Finally, they summarized that the de/rehydrogenation characteristics of MgH_2 is influenced by the deployment of highly crumpled, oxygen-containing GNS as the catalyst. They also suggested that suitable GNS with special architecture may become more suitable catalyst as compared to metal-based catalyst, because metal-based catalysts are often high cost, have a noxious effect on the environment and often form by-product during cycling.

8.5.2 Nanoparticles Templated Graphene as an Additive for MgH_2

Liu *et al.* studied the effect of TiB_2 nanoparticles on graphene nanosheets on dehydrogenation of MgH_2 [118]. They synthesized graphene by thermal exfoliation of graphene oxide at 900 °C in a quartz tube under Ar-H_2 mixture for 30 min. TiB_2@GNS was synthesized by solid-state reaction of $Ti(OH)_4$ and KBH_4 [119]. Sample for hydrogenation measurement was prepared by the ball-milling of MgH_2 with the catalyst with 40:1 ball-to-powder ratio for 5 h at 450 rpm under 0.5 MPa of H_2 pressure. They reported that enhancement in hydrogenation characteristics of MgH_2 were observed due to the presence of TiB_2@GNSs. The peak desorption temperatures of 354 °C, 330 °C and 319 °C were found for MgH_2+GNS, MgH_2+TiB_2 and MgH_2+TiB_2@GNS, while desorption temperature for pristine MgH_2 was found at 363 °C. Also, they reported that MgH_2+50%TiB_2@GNSs desorbed 6.5 wt% of H_2 within 10 min, 6.3 wt% within 40 min and 6.0 wt% within 2.5 h at 300, 270 and 240 °C. They reported that GNSs may be functionalized with B atom of TiB_2 in B-doped GNS, and B-doped GNS ribbon edges stimulated H_2 dissociation. Thus, this novel microstructure has excellent characteristics due to both GNSs and TiB_2.

A recent study of Soni *et al.* described the beneficial effect of graphene templated rare earth metal fluorides (La and Ce) for hydrogenation characteristics of MgH_2 [120]. They synthesized CeF_4@Gr by ultrasonication of 0.14 g CeF_4 nanoparticles, produced by the ball milling of commercial CeF_4 particles at 300 rpm for 25 h with 0.004 g of graphene in DMFC (dimethylformamide solvent). Ultrasonication was performed for 10 h at 40 KHz frequency. The resulting sample was dried at 80 °C and produced CeF_4@

Gr. Similarly, they produced the LaF_3@Gr sample. Figure 8.5(i) shows the TEM micrograph of obtained CeF_4@Gr (marked by red arrow), which represents the uniform distribution of CeF_4 NPs over graphene. Also, structural analysis has been performed through XRD, as shown in Figure 8.5(iii). The onset desorption temperature for ball-milled MgH_2 and templated graphene CeF_4 was found to be 245 °C, which was 50, 52 and 75 °C lower than templated graphene MgH_2+LaF_3, MgH_2+CeF_4 and MgH_2+LaF_3 respectively. Moreover, the MgH_2+GrCeF_4 absorbed 5.5 wt% within 2.5 min at 300 °C and 15 atm H_2 pressure. They also evaluated the activation energy for dehydrogenation of different samples and found that 102.34, 93.01 for

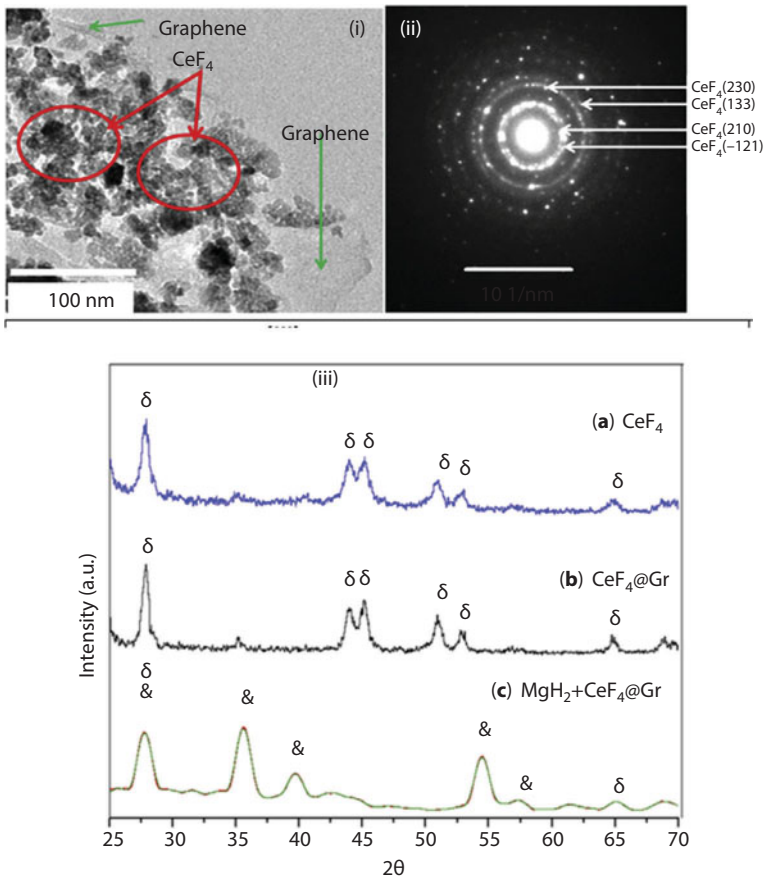

Figure 8.5 **(i)** TEM micrograph of CeF4@Gr; **(ii)** corresponding SAED pattern and **(iii)** XRD patterns of CeF4, CeF4@Gr, MgH2;CeF4@Gr, where δ represents peak of CeF4, & represents the peak of MgH2. (Reproduced with permission from [120])

MgH_2:CeF_4 and MgH_2:CeF_4@Gr. Moreover, they reported a reduction in thermodynamical barrier by 11.28 kJ/mol H_2 from 74.06 kJ/mol H_2 for pristine MgH_2 to 62.78 kj/mol H_2 for MgH_2:CeF_4@Gr. They concluded that the enhanced hydrogenation characteristics of MgH_2:CeF_4@Gr can be attributed to the formation of MgF_2 and CeH_2. MgF_2 weakens the Mg-H bond and CeH_2@Gr may work as grain inhibitor and provides diffusion pathways for Mg/MgH_2. Moreover, the presence of graphene prevents the agglomeration of formed CeF_2 MgF_2, which remains attached to Gr and does not agglomerate, maintaining hydrogenation/dehydrogenation after 24 cycle.

In 2012, Liu *et al.* described the synthesis of a porous Ni nanoparticle anchored on reduced graphene oxide sheets (Ni@rGO) and used this material as a catalyst for de/rehydrogenation of MgH_2 [121]. They synthesized graphene oxide through modified Hummers' method followed by adding some ethylene glycol solution of 0.15 g $NiCl_2.6H_2O$. The mixture was ultrasonicated for 5 h then 3 ml hydrazine hydrate and 0.1 g NaOH were added at 160 °C and refluxed for 3 h. The obtained black solid was centrifuged and washed with distilled water and dried in a vacuum oven at 600 °C for 5 h. The prepared nanocomposite was heat treated at 400 °C under Ar-H_2 mixture. The admixed mixture was prepared through the ball-milling of pre-milled MgH_2 with 5 wt% of Ni@rGO for 2 h. The ball-milling was performed at 5 atm hydrogen pressure at 450 rpm with ball-to-powder ratio of 40:1. Figure 8.6(i-a) shows the XRD patterns of GO; the peaks at 10.3 imply that Go is present and the disappearance of this peak further confirms that the formation of rGO has taken place. Furthermore, the peaks at $2\theta = 44.5$, 51.7 and 76.40 along with the broad peak at $2\theta = 25°$ confirmed the presence of Ni with rGO. The shape and structure of Ni@rGO were revealed by SEM and TEM (Figure 8.6(i-b,c)). The presence of Ni nanoparticles with diameter 50 nm has been reported by the Guang *et al.* Moreover, they further confirmed that Ni nanoparticles are enclosed on the rGO nanosheets. The BET analysis confirmed that Ni@rGO has a surface area of 80 m^2/g.

The MgH_2 with Ni@rGO has lowest onset (160 °C) and peak desorption temperature (247 °C) and desorbed 6.6 wt% of hydrogen while with Ni onset temperature is 190 °C and the peak desorption temperature is 282 °C. It was found that as compared to pristine MgH_2, MgH_2 with Ni@rGo has 110 °C less peak desorption temperature and this is 35 °C lower than MgH_2 with Ni. This suggested that the desorption kinetics of MgH_2 with Ni@rGO was also improved. Also, the study of Guang *et al.* confirmed that kinetics of MgH_2Ni@rGO sample do not degrade after prolonged cycling (9 cycles). The sample can still absorb/desorb 6 wt% within 10 min. Even at lower temperature (at 150 °C), MgH_2 with Ni@rGO can absorb 4.52 wt% of hydrogen within 10 min and achieve maximum capacity at 5.3 wt% in 25 min. They

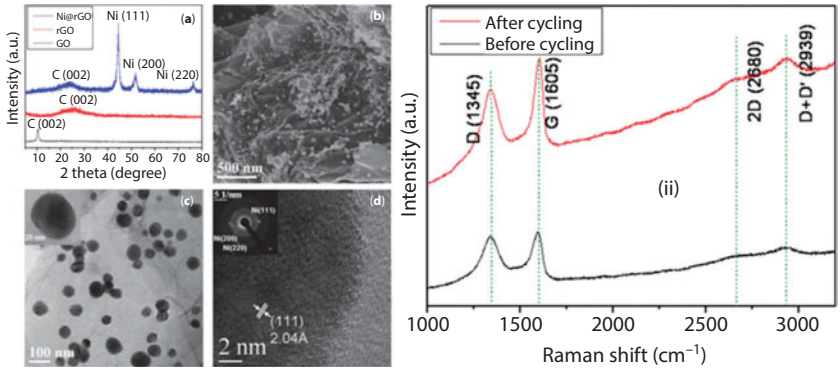

Figure 8.6 **(i)** (a) XRD Patterns of Go, rGO, and Ni@rGO, (b) SEM image of Ni@rGO, (c) TEM image of Ni@rGO, (d) HRTEM image of Ni@rGO, inset in (c) magnified image of individual Ni nanoparticles and inset in (d) the SAED pattern of Ni@rGO nanocomposite. **(ii)** Raman spectra of Ni@rGO composite before and after cycling. (Reproduced with permission from [121])

suggested that the effect of rGO nanosheet behaves as grain growth inhibitor that prevents the agglomeration of MgH_2/Mg during cycling, as well as works to stabilize the Ni nanoparticles. In order to further identify the existence of rGo after prolonged cycle, they performed Raman spectroscopy of as-milled MgH_2Ni@rGO and after 9 cycles, as clear from Figure 8.6(ii), the characteristic graphene peaks around 1345 (D-band), 1605 (G-band), 2680 (D) and 2939 cm^{-1} ($D+D^1$) respectively are presented for both the samples. As it is well known that both the D and G peaks correspond to the vibration of sp^2-hybridized carbon atoms, 2D is the characteristic graphene peak and can be used to determine the number of layers in graphene sample, and $D+D^1$ peaks determine the defects in graphene. The Raman spectra confirmed that the defective rGO sheets are still present after prolonged re/dehydrogenation cycling and still cover the composite surface, thus prevent the agglomeration and improve the cycling stability. Thus, the co-catalyst of graphene nanosheets and Ni-nanoparticles has a synergetic effect on MgH_2 sorption characteristics.

Zhang *et al.* also investigated the effect of another nanohybrid (Ni_2P@GNSs) material on hydrogenation characteristics of MgH_2 [122]. They synthesized graphene through modified Hummers' method; also, Ni_2P/GNS nanohybrid was synthesized through hydrothermal technique. First, 0.95 g $NiCl_6.6H_2O$ and 8.40 mg GO were dispersed in 40 ml of deionized water under ultrasonication and then 1.25 g $CH_3COONa.3H_2O$, 0.20 g CTAB and 0.64 g red phosphorous were respectively added into the solution. The resultant mixture was poured into a Teflon-lined autoclave. The autoclave

was kept at 160 °C for 10 h and cooled to room temperature. The resultant black solid was washed with water and ethanol several times to remove the residual reactants. Finally, the sample was dried at 80 °C for 10 h and Ni_2P@GNS was obtained. Figure 8.7(i) shows the schematic diagram of the

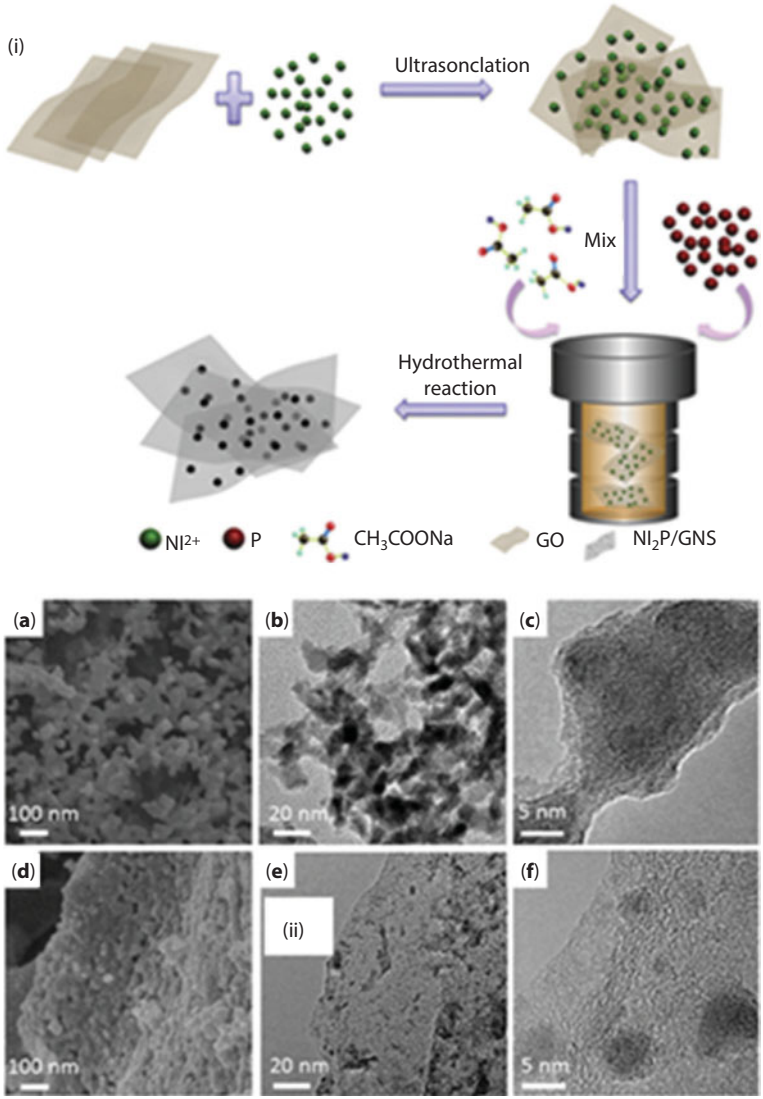

Figure 8.7 **(i)** Illustration of the steps involved in the synthesis of Ni_2P@GNS. **(ii)** SEM, TEM and RTEM images of Ni_2P sample (a–c) and Ni2P@GNSs sample (d–f) respectively. (Reproduced with permission from [122])

synthesis of Ni2P@GNS. The sample for hydrogenation studies was prepared by the ball-milling of MgH_2+catalyst for 5 h at 450 rpm with 40:1 ball-to-powder ratio under 5 bar H_2 pressure. Figure 8.7(ii) shows the SEM and TEM micrograph of Ni_2P/GNS. The Ni_2P has a plate-like morphology with aggregation of numerous nanoparticles. The Ni_2P particles are homogeneously distributed over GNS. The average grain size of Ni_2P was found to be 5 nm. They reported that the onset and peak desorption temperature was reduced appreciably by the deployment of Ni_2P/GNS. The onset desorption temperature was reduced to 237 °C and peak desorption temperature reduced to 302 °C with the addition of Ni_2P/GNS from 335 °C and 380 °C, respectively, as compared to pristine MgH_2. Moreover, Ni_2P/GNS catalyzed MgH_2 desorbed 6.1 wt% H_2 within 20 min at 325 °C, while only 0.2 wt% of H_2 was desorbed by pristine MgH_2 under identical conditions. They reported the beneficial effect was found due to the synergistic effect of Ni_2P and GNS for dehydrogenation of MgH_2. Also, the formation of a small quantity of Mg_2Ni and Mg_3P_2 were observed in dehydrogenated state, which prevents the pulverulent nanoparticles from growing and aggregating, which leads to beneficial effects on the dehydrogenation kinetics. Moreover, GNS provided beneficial effects on hydrogen desorption and provided diffusion channels for the H atom due to its high surface area and defects site. Hence, the catalytic role of Ni_2P/GNS generated a favorable synergetic effect on dehydrogenation of MgH_2.

Liu *et al.* further studied the effect of graphene-supported $NiCeO_x$ hybrid nanocatalyst on the dehydrogenation characteristics of MgH_2 [123]. Graphene-supported hydride nanocatalyst Ni-CeO_x was synthesized by using as-obtained 0.66 g GNS in 100 ml aqueous solution of 1.45 g $Ni(NO_3)_2.6H_2O$ and 0.155 g $Ce(NO_3)_2.6H_2O$, followed by ultrasonication for 2 h. The mixture was cryogenically treated and frozen for 48 h. The frozen dried mixture calcified in 10 V% H_2/Ar flow at 550 °C for 2 h to obtain Ni-CeOx @GNSs. The samples for hydrogenation measurements were synthesized through ball-milling of pre-milled (for 5 h) MgH_2 and synthesized catalyst for 2 h under 0.5 MPa hydrogen pressure. The morphology of synthesized hybrid catalyst was analyzed through SEM and TEM, as shown in Figure 8.8(i). The figure reveals that Ni-CeO_x/GNSs nanocatalysts are very crumpled and have 2D sheet-like structure of GNS. Also, TEM showed Ni-CeO_x having nanoparticles of diameter 20–30 nm which were uniformly distributed on crumpled GNSs. Figure 8.8(ii) shows the DSC profile of the different samples used in the study [123]. The onset desorption temperature was found to be at 205, 234, 245 and 277 °C for $NiCeO_x$@GNSs, Ni@GNSs, CeO@GNS and GNS catalyzed MgH_2, while the same for pristine MgH_2 has been found at 296 °C. The peak desorption

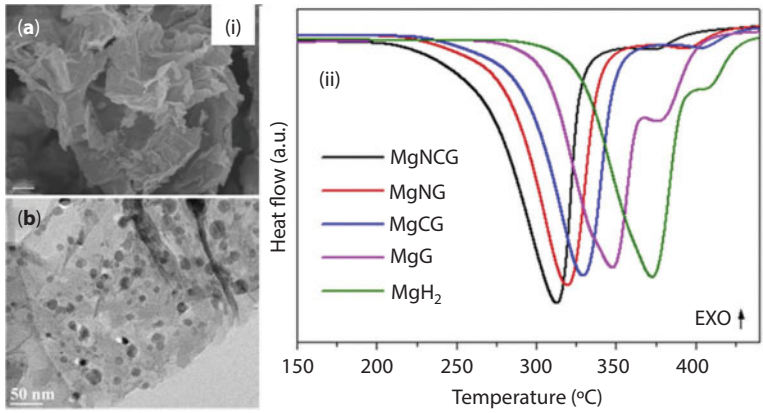

Figure 8.8 **(i)** SEM image (a) and TEM image (b) of Ni-CeOx@GNSs. **(ii)** DSC profile of different samples used in the study. (Reproduced with permission from [123])

temperature has also been reduced by the deployment of Ni-CeO_x@GNSs. The peak desorption temperature was reduced to 60° as compared to pristine MgH_2. At 5 KPa and 300 °C, pristine MgH_2 absorbed only 0.97 wt% within 1 h. However, the MgH_2 catalyzed with GNS, CeO_x@GNS, Ni@GNS and Ni-CeO_x@GNS absorbed 2.24, 5.13, 6.56 and 6.84 wt% under identical conditions of pressure temperature and time. They reported that the synergistic effect of tri-component of the catalyst was highly efficient for the dehydrogenation of MgH_2. The nanocatalyst was distributed homogeneously and served as nucleation sites for the new Mg phase during dehydrogenation reaction process. Moreover, the nanocatalyst having high surface area, porosity and O-defects can provide more diffused channels for H, and hence prevent particles from agglomeration.

Bhatnagar *et al.* investigated the effect of graphene templated Fe_3O_4 nanoparticles (F_3O_4@GNS) on de/rehydrogenation of MgH_2 [71]. They found significant improvement in sorption behavior for F_3O_4@GNS catalyzed MgH_2 as compared to nanocatalyzed MgH_2, GNS catalyzed and Fe_3O_4 catalyzed MgH_2. The MgH_2:F_3O_4@GNS has an onset desorption 142 °C lower than pristine MgH_2 (262 °C) while the same for MgH_2+GNS and MgH_2+Fe_3O_4 was found to be 215 and 298 °C respectively. Also, F_3O_4@GNS catalyzed MgH_2 has good absorption kinetics as compared to the other samples used in the study of Bhatnagar *et al.* MgH_2:F_3O_4@GNS absorbed 6.2 wt% H_2 at 290 °C at 15 atm hydrogen (H) pressure within 2.5 min [71]. While the same for GNS and Fe_3O_4 catalyzed MgH_2 was found to be 4.4 and 5.5 wt% under identical conditions of pressure temperature and within the same time duration. The F_3O_4@GNS also has a

good cyclability, with negligible change in hydrogen storage capacity after 25 hydrogenation/dehydrogenation cycles. Moreover, activation energy and enthalpy of formation was found to be 90.5 kJ/mol and 60.62 KJ/mol respectively (13.44 KJ/mol lower than bulk MgH_2). They reported that formation of MgO, $Mg_{1-x}Fe_xO$ and Fe occurred after first dehydrogenation and remain unaltered after 25 de/rehydrogenation cycles. Moreover, it was found that the particle size of formed MgO, $Mg_{1-x}Fe_xO$ and Fe particles are unaltered after 25 de/rehydrogenation cycles. This happened because the formed phases are attached with GNS. Thus, GNS acted as a grain inhibitor for Mg/MgH_2 and also formed compound during de/rehydrogenation reaction. Hence, the enhancement in catalytic activity is related to the synergistic effect of Fe NPs and GNSs.

8.6 Summary and Future Prospects

Efforts are currently going on to replace fossil fuels with renewable green economic fuels (like hydrogen) but plenty of shortcomings still exist. Towards this direction, storage of hydrogen is a crucial issue for the successful realization of a hydrogen-fueled economy. The challenge is related to the search for a material with the reasonably good storage capacity of hydrogen with excellent cyclability and faster absorption desorption kinetics. There are several materials with good storage capacity (e.g., MgH_2, AlH_3, $LiAlH_4$, $NaAlH_4$, $LiBH_4$, etc.), along with the shortcomings related to kinetics and poor cyclability at required temperature. Efforts are going on to remove these shortcomings by deployment of catalyst and/or material tailoring. The effect of the catalyst can be further enhanced by the nanosize effect and it has been found that this effect is reduced after a few hydrogenation dehydrogenation cycles. Thus, support materials or grain inhibitors are required to overcome this phenomenon. Nowadays, due to its light weight, high surface area, edge defects and curvature effect, graphene is considered as a potential support material for the catalysts. More importantly, the light weight of graphene has attracted researchers working in the area of hydrogen storage to use it as a support material for nanocatalysts. Several reports have appeared in the last five years in which graphene is used as support material for catalyst as well as for nanoparticles of hydrogen storage materials (e.g., Mg). Some interesting and important results were discussed in the present chapter. Also, this chapter described the characteristics of graphene, which are responsible for the beneficial effect of this technologically important material in the area of hydrogen storage. Research into combining light metal hydrides, e.g., MgH_2, $NaAlH_4$, $LiBH_4$,

Li-Mg-N-H HS, system with graphene may lead to improvement in the hydrogen storage performance of abovesaid HS materials. Furthermore, graphene can be used as wrapping material for HS through which the air stability of different HS materials can be modified. Thus, it can be said that graphene is a unique material with several beneficial characteristics which are helpful for hydrogen storage technology.

Acknowledgment

The author would like to acknowledge Prof. O.N. Srivastava (BHU) for the scientific discussions and encouragement. The author also would like to acknowledge Mr. Rajesh K Mishra (MNNIT), Mr. Asish Bhatanagar (BHU) and Mr. Vivek Shukla (BHU) for their help in the preparation of this chapter. Financial assistance received from DST INSPIRE Faculty Research Grant (IFA-12-PH43), New Delhi (India) is gratefully acknowledged.

References

1. Winter, C.-J., Hydrogen energy—Abundant, efficient, clean: A debate over the energy-system-of-change. *Int. J. Hydrogen Energy* 34, S51–S52, 2009.
2. Wang, J., Barriers of scaling-up fuel cells: Cost, durability and reliability. *Energy* 80, 509–521 2015.
3. Schlapbach, L., Züttel, A., Hydrogen-storage materials for mobile applications. *Nature* 414, 353, 2001.
4. Edwards, P.P., Kuznetsov, V.L., David, W.I., Hydrogen energy. *Philos. Trans. A Math. Phys. Eng. Sci.* 365, 1043, 2007.
5. Van den Berg, A.W.C., Areán, C.O., Materials for hydrogen storage: Current research trends and perspectives. *Chem. Commun.* 2008, 668–681, 2008.
6. Hudson, M.S.L., Dubey, P.K., Pukazhselvan, D., Pandey, S.K., Singh, R.K., Raghubanshi, H., Shahi, R.R., Srivastava, O.N., Hydrogen energy in changing environmental scenario: Indian context. *Int. J. Hydrogen Energy* 34, 7358–7367, 2009.
7. Momirlan, M., Veziroglu, T.N., The properties of hydrogen as fuel tomorrow in sustainable energy system for a cleaner planet. *Int. J. Hydrogen Energy* 30, 795–802, 2005.
8. Melaina, M., Eichman, J., Hydrogen Energy Storage: Grid and Transportation Services, National Renewable Energy Laboratory, 2015.
9. Jain, I.P., Hydrogen the fuel for 21st century. *Int. J. Hydrogen Energy* 34, 7368–78, 2009.
10. Supplement 1 to *Original Target Explanation Document*: Onboard Hydrogen Storage Systems for Light-Duty Fuel Cell Vehicles, U.S. Department of

Energy, Office of Energy Efficiency and Renewable Energy and the Freedom CAR and Fuel Partnership, 2015.
11. Schüth, F., Bogdanović, B. Felderhoff, M., Light metal hydrides and complex hydrides for hydrogen storage. *Chem. Commun.* 40, 2249–2258, 2004
12. Thomas, K.M., Adsorption and desorption of hydrogen on metal–organic framework materials for storage applications: Comparison with other nanoporous materials. *Dalton Trans.* 2009, 1487–1505, 2009.
13. Hu, Y.H., Zhang, L., Hydrogen storage in metal–organic frameworks. *Adv. Mater.* 22, E117, 2010.
14. Sculley, J., Yuan D.Q., Zhou, H.C., The current status of hydrogen storage in metal–organic frameworks—updated. *Energy Environ. Sci.* 4, 2721, 2011.
15. U.S. DOE, Targets for onboard hydrogen storage systems for light-duty vehicles. http://www1.eere.energy.gov/hydrogenandfuelcells/storage/pdfs/targets_onboard_hydro_storage_explanation.pdf, 2009.
16. Walker, G.S., Abbas, M., Grant, D.M., Udeh, C., Destabilisation of magnesium hydride by germanium as a new potential multicomponent hydrogen storage system. *Chem. Commun.* 47, 8001, 2011.
17. Peng, B., Liang, J., Tao, Z.L., Chen, J., Magnesium nanostructures for energy storage and conversion. *J. Mater. Chem.* 19, 2877, 2009.
18. Aguey-Zinsou, K.F., Ares-Fernández, J.R., Hydrogen in magnesium: New perspectives toward functional stores. *Energy Environ. Sci.* 3, 526, 2010.
19. Bardhan, R., Ruminski, A.M., Brand, A. Urban, J.J., Magnesium nanocrystal-polymer composites: A new platform for designer hydrogen storage materials. *Energy Environ. Sci.* 4, 4882, 2011.
20. Li, W.Y., Li, C.S., Zhou, C.Y., Ma, H., Chen, J., Metallic magnesium nano/mesoscale structures: Their shape-controlled preparation and mg/air battery applications. *Angew. Chem. Int. Ed.* 45, 6009, 2006.
21. Cheng, F., Tao, Z., Liang, J., Chen, J, Efficient hydrogen storage with the combination of lightweight Mg/MgH_2 and nanostructures. *Chem. Commun.* 48, 7334, 2012.
22. Grochala, W., Edwards, P.P., Thermal decomposition of the non-interstitial hydrides for the storage and production of hydrogen. *Chem. Rev.* 104, 1283, 2004.
23. Orimo, S., Nakamori, Y., Eliseo, J.R., Züttel, A., Jensen, C.M., Complex hydrides for hydrogen storage. *Chem. Rev.* 107, 4111, 2007.
24. Bérubé, V., Radtke, G., Dresselhaus, M., Chen, G., Size effects on the hydrogen storage properties of nanostructured metal hydrides: A review. *Int. J. Energy Res.* 31, 637, 2007.
25. Reardon, H., Hanlon, J.M., Hughes, R.W., Godula-Jopek, A., Mandal, T.K., Gregory, D.H., Emerging concepts in solid-state hydrogen storage: the role of nanomaterials design. *Energy Environ. Sci.* 5, 5951, 2012.
26. Bérubé, B., Radtke, G., Dresselhaus, M., Chen, G., Size effects on the hydrogen storage properties of nanostructured metal hydrides: A review. *Int. J. Energy Res.* 31, 637, 2007.

27. Shao, H., Felderhoff, M., Schuth, F., Weidenthaler, C., Nanostructured Ti-catalyzed MgH2 for hydrogen storage. *Nanotechnology* 22, 235401, 2011.
28. Adelhelm, P., de Jongh P.E., The impact of carbon materials on the hydrogen storage properties of light metal hydrides. *J. Mater. Chem.* 21, 2417, 2011.
29. Wu, C., Cheng, H.-M., Effects of carbon on hydrogen storage performances of hydrides. *J. Mater. Chem.* 20, 5390, 2010.
30. Nagar, R., Vinayan, B.P., Samantaray, S.S., Ramaprabhu, S., Recent advances in hydrogen storage using catalytically and chemically modified graphene nanocomposites. *J. Mater. Chem. A* 5, 22897–22912, 2017.
31. Gao, W., Alemany, L.B., Ci, L., Ajayan, P.M., New insights into the structure and reduction of graphite oxide. *Nat. Chem.* 1, 403–408, 2009.
32. Geim, A.K., Novoselov, K.S., The rise of graphene. *Nat. Mater.* 6, 183–191, 2007.
33. Novoselov, K.S., Geim, A.K., Zhang, Y., Morozov, S.V., Jiang, D., *et al.*, Electric field effect in atomically thin carbon film. *Science* 306, 666–669, 2004.
34. Eizenberg, M., Blakely, J.M., Carbon monolayer phase condensation on Ni(111). *Surf. Sci.* 82, 228–236,1970
35. Hirata, M., Gotou, T., Horiuchi, S., Fujiwara, M., Ohba, M., Thin-film particles of graphite oxide 1: High-yield synthesis and flexibility of the particles. *Carbon* 42, 2929–2937, 2004.
36. Dikin, D.A., Stankovich, S., Zimney, E.J., Piner, R.D., Dommett, G.H.B., *et al.*, Preparation and characterization of graphene oxide paper. *Nature* 448, 457–460, 2007.
37. Tung, V.C., Allen, M.J., Yang, Y., Kaner, R.B., High-throughput solution processing of large-scale graphene. *Nat. Nanotechnol.* 4, 25–29, 2009.
38. Hummers Jr., W.S., Offeman, R.E., Preparation of graphitic oxide. *J. Am Chem. Soc.* 80, 1339–1339, 1958
39. Staudenmaier, L., Verfahren zur darstellung der graphitsaure. *Ber. Deut. Chem. Ges.* 31, 1481, 1898.
40. Zhu, C., Guo, S., Fang, Y., Dong, S., Reducing sugar: New functional molecules for the green synthesis of graphene nanosheets. *ACS Nano* 4, 2429–2437, 2010.
41. Rao, C.N., Sood, A.K., Subrahmanyam, K.S., Govindaraj, A., Graphene: The new two-dimensional nanomaterial. *Angew. Chem. Int. Ed.* 48, 7752–7777, 2009.
42. Wu, Z.-S, Ren, W., Wen, L., Gao, L., Zhao, J., Chen, Z., Zhou, G., Li, F., Cheng, H.-M., Graphene anchored with Co_3O_4 nanoparticles as anode of lithium ion batteries with enhanced reversible capacity and cyclic performance. *ACS Nano* 4, 3187–3194, 2010.
43. Pasricha, R., Gupta, S., Srivastava, A.K., A facile and novel synthesis of Ag–graphene-based nanocomposites. *Small* 5, 2253–2259, 2009.
44. Kou, R., Shao, Y., Wang, D., Engelhard, M.H., Kwak, J.H., Wang, J., *et al.*, Enhanced activity and stability of Pt catalysts on functionalized graphene sheets for electrocatalytic oxygen reduction. *Electrochem. Commun.* 11(5), 954–957, 2009.

45. Dong, L., Gari, R.R.S., Li, Z., Craig, M.M., Hou, S., Graphene-supported platinum and platinum-ruthenium nanoparticles with high electrocatalytic activity for methanol and ethanol oxidation. *Carbon* 48(3), 781–787, 2010.
46. Tavakoli, F., Salavati-Niasari, M., A facile synthesis of CuI-graphene nanocomposite by glucose as a green capping agent and reductant. *J. Ind. Eng. Chem.* 20(5), 3170–3174, 2014.
47. Bong, S., Kim, Y.-R., Kim, I., Woo, S., Uhm, S., Lee, J., *et al.*, Graphene supported electrocatalysts for methanol oxidation. *Electrochem. Commun.* 12(1), 129–131, 2010.
48. Nethravathi, C., Rajamathi, M., Chemically modified graphene sheets produced by the solvothermal reduction of colloidal dispersions of graphite oxide. *Carbon* 46(14), 1994–1998, 2008.
49. Nam, J.-K., Choi, M.-J., Cho, D.-H., Suh, J.-K., Kim, S.-B., The influence of support in the synthesis of dimethyl carbonate by Cu-based catalysts. *J. Mol. Catal. A Chem.* 370, 7–13, 2013.
50. Singh, S.K., Singh, M.K., Kulkarni, P.P., Sonkar, V.K., Grácio, J.J.A., Dash, D., Amine-modified graphene: Thrombo-protective safer alternative to graphene oxide for biomedical applications. *ACS Nano* 6(3), 2731–2740, 2012.
51. Yang, H., Shan, C., Li, F., Han, D., Zhang, O., Niu, L., Covalent functionalization of polydisperse chemicallyconverted graphene sheets with amine-terminated ionic liquid. *Chem. Commun.* 38, 80–82, 2009.
52. Bell, A.T., The impact of nanoscience on heterogeneous catalysis. *Science* 299(5613), 1688–1691, 2003.
53. Julkapli, N.M., Bagheri, S., Graphene supported heterogeneous catalysts: An overview. *Int. J. Hydrogen Energy* 40, 948–979, 2015.
54. Yoo, E.J., Okata, T., Akita T., Kohyama, M., Nakamura, J., Honma, I., Enhanced electrocatalytic activity of Pt subnanoclusters on graphene nanosheet surface. *Nano Lett.* 9(6), 2255–2259, 2009.
55. N'Diaye, A.T., van Gastel, R., Martínez-Galera, A.J., Coraux, J., Hattab, H., Wall, D., *et al. In situ* observation of stress relaxation in epitaxial graphene. *New J. Phys.* 11, 113056, 2009.
56. Wang, D., Kou, R., Choi, D., Yang, Z., Nie, Z., Li, J., *et al.*, Ternary self-assembly of ordered metal oxide-graphene nanocomposites for electrochemical energy storage. *ACS Nano* 4(3), 1587–1595, 2010.
57. Kim, H., Abdala, A.A., Macosko, C.W., Graphene/polymer nanocomposites. *Macromolecules* 43(16), 6515–6530, 2010.
58. Parambhath, V.B., Nagar, R., Sethupathi, K., Ramaprabhu, S., Investigation of spillover mechanism in palladium decorated hydrogen exfoliated functionalized graphene. *J. Phys. Chem. C* 115(31), 15679–15685, 2011.
59. Pumera, M., Ambrosi, A., Bonanni, A., Chng, E.L.K., Poh, H.L., Graphene for electrochemical sensing and biosensing. *TrAC Trends Anal. Chem.* 29(9), 954–965, 2010.
60. Ni, Z.H., Ponomarenko, L.A., Nair, R.R., Yang, R., Anissimova, S., Grigorieva, I.V., *et al.*, On resonant scatterers as a factor limiting carrier mobility in graphene. *Nano Lett.* 10(10), 3868–3872, 2010.

61. Lee, C., Wei, X., Kysar, J.W., Hone, J., Measurement of the elastic properties and intrinsic strength of monolayer graphene. *Science* 321(5887), 385–388, 2008.
62. Balandin, A.A., Ghosh, S., Bao, W., Calizo, I., Teweldebrhan, D., Miao, F., *et al.*, Superior thermal conductivity of single-layer graphene. *Nano Lett.* 8(3), 902–907, 2008.
63. Lee, D.H., Kim, J.E., Han, T.H., Hwang, J.W., Jeon, S., Choi, S.-Y., Versatile carbon hybrid films composed of vertical carbon nanotubes grown on mechanically compliant graphene films. *Adv. Mater.* 22(11), 1247–1252, 2010.
64. Bett, J.A.S., Kinoshita, K., Stonehart, P., Crystallite growth of platinum dispersed on graphitized carbon black: II. Effect of liquid environment. *J. Catal.* 41(1), 124–133, 1976.
65. Cao, H., Li, B., Zhang, J., Lian, F., Kong, X., Qu, M., Synthesis and superior anode performance of TiO_2@reduced graphene oxide nanocomposites for lithium ion batteries. *J. Mater. Chem.* 22, 9759–9766, 2012.
66. Sun, Y., Wu, Q., Shi, G., Graphene based new energy materials. *Energy Environ. Sci.* 4, 1113–1132, 2011.
67. Zhu, Y., Murali, S., Stoller, M.D., Velamakanni, A., Piner, R.D., Ruoff, R.S., Microwave assisted exfoliation and reduction of graphite oxide for ultracapacitors. *Carbon* 48, 2118–2122, 2010.
68. Lv, W., Li, Z., Deng, Y., Yang, Q.-H., Kang, F., Graphene-based materials for electrochemical energy storage devices: Opportunities and challenges. *Energy Storage Materials* 2, 107–138, 2016,
69. Liang, Y., Li, Y., Wang, H., Zhou, J., Wang, J., Regier, T., Dai, H., Co_3O_4 nanocrystals on graphene as a synergistic catalyst for oxygen reduction reaction. *Nat. Mater.* 10, 780–786, 2011.
70. Yan, J.-M., Wang, Z.-L, Wang, H.-L, Jiang, Q., Rapid and energy-efficient synthesis of a graphene–CuCo hybrid as a high performance catalyst. *J. Mater. Chem.* 22, 10990–10993, 2012.
71. Bhatnagar, A., Pandey, S.K., Vishwakarma, A.K., Singh, S., Shukla, V., Soni, P.K., *et al.*, Fe_3O_4@graphene as a superior catalyst for hydrogen de/absorption from/in MgH2/Mg. *J. Mater. Chem. A* 4, 14761, 2016.
72. Orimo, S., Nakamori, Y., Eliseo, J.R., Züttel, A., Jensen, C.M., Complex hydrides for hydrogen storage. *Chem. Rev.* 107, 4111–4112, 2007.
73. Orimo, S., Nakamori, Y., Kitahara, G., Miwa, K., Ohba, N., Towata, S., *et al.*, Dehydriding and rehydriding reactions of $LiBH_4$. *J. Alloys Compd.* 404–406, 427–430, 2005.
74. Wang, P.J., Fang, Z.Z., Ma, L.P., Kang, X.D., Wang, P., Effect of SWNTs on the reversible hydrogen storage properties of $LiBH_4$–MgH_2 composite. *Int. J. Hydrogen Energy* 33, 5611–5616, 2008.
75. Züttel, A., Wenger, P., Rentsch, S., Sudan, P., Mauron, P., Emmenegger, C., $LiBH_4$ a new hydrogen storage material. *J Power Sources* 118, 1–7, 2003.
76. Gennari, F.C., Destabilization of $LiBH_4$ by MH_2 (M = Ce, La) for hydrogen storage: Nanostructural effects on the hydrogen sorption kinetics. *Int. J. Hydrogen Energy* 36, 15231–15238, 2011.

77. Xia, G.L., Leng, H.Y., Xu, N.X., Li, Z.L., Wu, Z., Du, J.L., Yu, X.B., Enhanced hydrogen storage properties of $LiBH_4$ MgH_2 composite by the catalytic effect of $MoCl_3$. *Int. J. Hydrogen Energy* 36, 7128–7135, 2011.
78. Liu, B.H., Zhang, B.J., Jiang, Y., Hydrogen storage performance of $LiBH_4$+1/2MgH_2 composites improved by Ce-based additives. *Int. J. Hydrogen Energy* 36, 5418–5424, 2011.
79. Sridechprasat, P., Suttisawat, Y., Rangsunvigit, P., Kitiyanan, B., Kulprathipanja, S., Catalyzed $LiBH_4$ and MgH_2 mixture for hydrogen storage. *Int. J. Hydrogen Energy* 36, 1200–1205, 2011.
80. Xu, J., Meng, R., Cao, J., Gu, X., Qi, Z., Wang, W., Chen, Z., Enhanced dehydrogenation and rehydrogenation properties of $LiBH_4$ catalyzed by graphene. *Int. J. Hydrogen Energy* 38, 2796–2803, 2013.
81. Xu, J., Meng, R., Cao, J., Gu, X., Song, W.-L., Qi, Z., Wang, W., Chen, Z., Graphene-supported Pd catalysts for reversible hydrogen storage in $LiBH_4$. *J. Alloys Compd.* 564, 84–90, 2013.
82. Van Hassel, B.A., Mosher, D., Pasini, J.M., Gorbounov, M., Holowczak, J., Tang, X., Brown, R., Laube, B., Pryor, L., Engineering improvement of $NaAlH_4$ system. *Int. J. Hydrogen Energy* 37, 2756–2766, 2012.
83. Bogdanović, B., Felderhoff, M., Kaskel, S., Pommerin, A., Sclichte, K., Schüth, F., Improved hydrogen storage properties of Ti-doped sodium alanate using titanium nanoparticles as doping agents. *Adv. Mater.* 15, 1012–1015, 2003.
84. Bogdanović, B., Sandrock, G., Catalyzed complex metal hydrides. *MRS Bull.* 27, 712–716, 2002
85. Xu, L., Ge, Q., Effect of defects and dopants in graphene on hydrogen interaction in graphene-supported $NaAlH_4$. *Int. J. Hydrogen Energy* 38, 3670–3680, 2013.
86. Kresse, G., Furthmuller, J., Efficient iterative schemes for ab initio total-energy calculations using a plane-wave basis set. *Phys. Rev. B* 54, 11169–11186, 1996.
87. Kresse, G., Hafner, J., Ab initio molecular-dynamics for liquid metals. *Phys. Rev. B* 47, 558–561, 1993
88. Blöchl, P.E., Projector augmented-wave method. *Phys. Rev. B* 50, 17953–17979, 1994.
89. Kresse, G., Joubert, D., From ultrasoft pseudopotentials to the projector augmented-wave method. *Phys Rev B* 59, 1758–1775, 1999.
90. Kumar, L.H., Rao, C.V., Viswanathan, B., Catalytic effects of nitrogen-doped graphene and carbon nanotube additives on hydrogen storage properties of sodium alanate. *J. Mater. Chem. A* 1, 3355, 2013.
91. Li, Y., Fang, F., Fu, H., Qiu, J., Song, Y., Li, Y., Sun, D., Zhang, Q., Ouyang, L., Zhu, M., Carbon nanomaterial-assisted morphological tuning for thermodynamic and kinetic destabilization in sodium alanates. *J. Mater. Chem. A* 1, 5238, 2013.
92. Noritake, T., Aoki, M., Towata, S., Seno, Y., Hirose, Y., Nishibori, E., Takata, M., Sakata, M., Chemical bonding of hydrogen in MgH_2. *Appl. Phys. Lett.* 81, 2008–2010, 2002.

93. Bérubé, B., Radtke, G., Dresselhaus, M., Chen, G., Size effects on the hydrogen storage properties of nanostructured metal hydrides: A review. *Int. J. Energy Res.* 31, 637, 2007.
94. Jain, I.P., Lal, C., Jain, A., Hydrogen storage in Mg: A most promising material. *Int. J. Hydrogen Energy* 35, 5133, 2010.
95. Güvendiren, M., Bayboru, E., Ozturk, T., Effects of additives on mechanical milling and hydrogenation of magnesium powders. *Int. J. Hydrogen Energy* 29, 491, 2004.
96. Wu, C., Wang, P., Yao, X., Liu, C., Chen, D., Lu, G.Q., Cheng, H., Effect of carbon/noncarbon addition on hydrogen storage behaviors of magnesium hydride. *J. Alloys Compd.* 414, 259, 2006.
97. Sakintuna, B., Lamari-Darkrim, F., Hirscher, M., Metal hydride materials for solid hydrogen storage: A review. *Int. J. Hydrogen Energy* 32, 1121, 2007.
98. Imamura, H., Sakasai, N., Fujinaga, T., Characterization and hydriding properties of Mg-graphite composites prepared by mechanical grinding as new hydrogen storage materials. *J. Alloys Compd.* 253, 34 1997.
99. Imamura, H., Takesue, Y., Akimoto, T., Tabata, S., Hydrogen-absorbing magnesium composites prepared by mechanical grinding with graphite: Effects of additives on composite structures and hydriding properties. *J. Alloys Compd.* 293, 564, 1999.
100. Imamura, H., Tabata, S., Shigetomi, N., Takesue, Y., Sakata, Y., Composites for hydrogen storage by mechanical grinding of graphite carbon and magnesium. *J. Alloys Compd.* 330, 579, 2002.
101. Imamura, H., Tabatta, S., Takesue, Y., Sakata, Y., Kamazaki, S., Hydriding–dehydriding behavior of magnesium composites obtained by mechanical grinding with graphite carbon. *Int. J. Hydrogen Energy* 25, 837, 2000.
102. Shang, C.X., Guo, Z.X., Effect of carbon on hydrogen desorption and absorption of mechanically milled MgH_2. *J. Power Sources* 129, 73, 2004.
103. Chen, D., Chen, L., Liu, S., Ma, C.X., Chen, D.M., Wang, L.B., Microstructure and hydrogen storage property of Mg/MWNTs composites. *J. Alloys Compd.* 372, 231–237, 2004.
104. Shahi, R.R., Bhatnagar, A., Pandey, S.K., Dixit, V., Srivastava, O.N., Effects of Ti-based catalysts and synergistic effect of SWCNTs-TiF_3 on hydrogen uptake and release from MgH_2. *Int. J. Hydrogen Energy* 39, 14255–14261, 2014.
105. Wu, C., Wang, P., Yao, X., Liu, C., Chen, D., Lu, G.Q., Cheng, H., Effects of SWNT and metallic catalyst on hydrogen absorption/desorption performance of MgH_2. *J. Phys. Chem. B* 109, 22217, 2005.
106. Lillo-Ródenas, M.A., Aguey-Zinsou, K.F., Cazorla-Amorós, D., Linares-Solano, A., Guo, Z.X., Effects of carbon-supported nickel catalysts on MgH_2 decomposition. *J. Phys. Chem. C* 112, 5984, 2008.
107. Lillo-Ródenas, M.A., Guo, Z.X., Aguey-Zinsou, K.F., Cazorla-Amorós, D., Linares-Solano, A., Effects of different carbon materials on MgH_2 decomposition. *Carbon* 46, 126, 2008.

108. Wu, C.Z., Yao, X.D., Zhang, H., Hydriding/dehydriding properties of MgH_2/5 wt.% Ni coated CNFs composite. *Int. J. Hydrogen Energy* 35, 247, 2010.
109. Fuster, V., Castro, F.J., Troiani, H., Urretavizcaya, G., Characterization of graphite catalytic effect in reactively ball-milled MgH_2–C and Mg–C composites. *Int. J. Hydrogen Energy* 36, 9051, 2011.
110. Reyhani, A., Mortazavi, S.Z., Mirershadi, S., Golikand, A.N., Moshfegh, A.Z., H_2 adsorption mechanism in Mg modified multi-walled carbon nanotubes for hydrogen storage. *Int. J. Hydrogen Energy* 37, 1919, 2012.
111. Imamura, H., Kusuhara, M., Minami, S., Matsumoto, M., Masanari, K., Sakata, Y., Itoh, K., Fukunaga, T., Carbon nanocomposites synthesized by high-energy mechanical milling of graphite and magnesium for hydrogen storage. *Acta Mater.* 51, 6407, 2003.
112. Shahi, R.R., Raghubanshi, H., Shaz, M.A, Srivastava, O.N., Studies on the de/re-hydrogenation characteristics of nanocrystalline MgH_2 admixed with carbon nanofibers. *Appl. Nanosci.* 2, 195, 2012.
113. Shahi, R.R., Srivastava. O.N., Catalytic application of carbon-based nanostructured materials on hydrogen sorption behavior of light metal hydrides, in: *Advanced Carbon Materials and Technology*, Tiwari, A., Shukla, S.K. (Eds.), chap. 4, pp. 129–171, Wiley-Scrivener, 2013.
114. Singh, R.K., Raghubanshi, H., Pandey, S.K., Srivastava, O.N., Effect of admixing different carbon structural variants on the decomposition and hydrogen sorption kinetics of magnesium hydride. *Int. J. Hydrogen Energy* 35, 4131, 2010.
115. Liu, G., Wang, Y., Xu, C., Qiu, F., An, C., Li, L., Jiao, L., Yuan, H., Excellent catalytic effects of highly crumpled graphene nanosheets on hydrogenation/dehydrogenation of magnesium hydride. *Nanoscale* 5, 1074, 2013.
116. Du, A.J., Smith, S.C., Yao, X.D., Lu, G.Q., Catalytic effects of subsurface carbon in the chemisorption of hydrogen on a Mg(0001) surface: An ab-initio study. *J. Phys. Chem. B* 110, 1814, 2006.
117. Liu, G., Wang, Y., Jiao, L., Yuan, H., Understanding the role of few-layer graphene nanosheets in enhancing the hydrogen sorption kinetics of magnesium hydride. *ACS Appl. Mater. Interfaces* 6, 11038–11046, 2014.
118. Liu, G., Wang, Y.J., Jiao, L.F., Yuan, H.T., Solid-state synthesis of amorphous TiB_2 nanoparticles on graphene nanosheets with enhanced catalytic dehydrogenation of MgH_2. *Int. J. Hydrogen Energy* 39, 3822–3829, 2014
119. Mondal, T., Bhowmick, A.K., Krishnamoorti, R., Stress generation and tailoring of electronic properties of expanded graphite by click chemistry. *ACS Appl. Mater. Interfaces* 6, 7244–7253, 2014.
120. Soni, P.K., Bhatnagar, A., Shaz, M.A., Srivastava, O.N., Effect of graphene templated fluorides of Ce and La on the de/rehydrogenation behavior of MgH_2. *Int. J. Hydrogen Energy* 42, 20026–20035, 2017.
121. Liu, G., Wang, Y., Qiu, F., Li, Li, Jiao, L., Yuan, H., Synthesis of porous Ni@rGO nanocomposite and its synergetic effect on hydrogen sorption properties of MgH_2. *J. Mater. Chem.* 22, 22542, 2012.

122. Zhang, Q., Xu, Y., Wang, Y., Zhang, H., Wang, Y., Jiao, L., Yuan, H., Enhanced hydrogen storage performance of MgH_2–Ni_2P/graphene nanosheets. *Int. J. Hydrogen Energy* 41, 17000–17007, 2016.
123. Liu, G., Wang, K., Li, J., Wang, Y., Yuan, H., Enhancement of hydrogen desorption in magnesium hydride catalyzed by graphene nanosheets supported Ni-CeO_x hybrid nanocatalyst. *Int. J. Hydrogen Energy* 41, 10786–10794, 2016.

9

Hydrogen Adsorption on Nanotextured Carbon Materials

G. Sdanghi[1,2], G. Maranzana[2], A. Celzard[1] and V. Fierro[1,*]

[1]Jean Lamour Institute, UMR 7198 CNRS – University of Lorraine, Epinal, France
[2]Laboratory of Energetics, Theoretical and Applied Mechanics, UMR 7563 CNRS – University of Lorraine, Vandoeure-Lès-Nancy, France

Abstract

Porous carbons have received noteworthy attention as gas storage materials due to their highly developed textural properties, ensuring a completely reversible hydrogen uptake and release at the same time. Very high surface areas are especially exhibited by nanotextured carbons. Activated carbons, carbon nanotubes, carbon nanofibers, MOF-derived carbons and graphene, among others, have thus been tested as hydrogen adsorbents. However, the different ways of expressing hydrogen storage capacities, and also the different conditions used to measure them, make it difficult to have a clear idea of the real potential for hydrogen storage of a given material. In the first part of this chapter we will present: (i) the essential features of hydrogen adsorption on porous materials; (ii) the determination methods; and (iii) the ways of expressing hydrogen storage capacity: total (or stored), adsorbed, or excess hydrogen. In the second part, we will review the most relevant studies related to hydrogen storage in carbon materials published in the open literature to date. In view of the textural properties of the adsorbents and the storage conditions, a critical analysis of the reported results on hydrogen storage will also be carried out.

Keywords: Hydrogen storage, carbon materials, activated carbons, carbon nanotubes, carbon nanofibers, templated carbons, MOF-derived carbons, exotic carbon materials

**Corresponding author*: Vanessa.Fierro@univ-lorraine.fr

Mehmet Sankir and Nurdan Demirci Sankir (eds.) Hydrogen Storage Technologies, (263–320) © 2018 Scrivener Publishing LLC

9.1 Introduction

9.1.1 Essential Features of Hydrogen Adsorption on Porous Carbon Materials

Hydrogen adsorption onto carbon material surfaces is an alternative to other well-known hydrogen storage methods, i.e., compression, liquefaction, storage in metal hydride alloys and chemical storage in covalent and ionic compounds, due to carbon-enhanced adsorption [1], which ensures high hydrogen storage capacities [2]. Several studies have shown that hydrogen storage in porous carbons is more advantageous than pure compression, especially in applications requiring pressure levels within the range of 5–20 MPa [3, 4]. As a matter of proof, hydrogen vehicles able to achieve an autonomy of 500 km require 5 kg of hydrogen, which can be stored by pure compression at 20 MPa and room temperature in a compressed tank of volume 340 L [5]. On the other hand, if an adsorption system based on carbons had to be used for the same purpose, a volume of only 263 L would be required under the same conditions. Therefore, using adsorption onto carbons instead of pure compression would give a volume gain of around 22% to the hydrogen storage system [3].

Carbon-based materials exhibit several advantages as, most of the time, they present: (i) moderate cost [6]; (ii) high surface areas; (iii) high chemical stability; (iv) possibility of being produced from cheap renewable sources [7]; and (v) low weight with respect to metal hydrides, thus offering a valid solution as hydrogen storage system for fuel cell-powered vehicles [8]. Hydrogen adsorption on carbon materials is a physical phenomenon since no chemical bonds between hydrogen molecules and the carbon surface are involved. Hydrogen interacts with the carbon surface through weak van der Waals forces [9], forming an incomplete monolayer on the adsorbent's surface. Thus, hydrogen adsorption on carbon materials is generally a completely reversible process, with rapid uptake and release kinetics [10] and adsorption energies of around 4–8 kJ/mol [11, 12]. At room temperature, van der Waals interactions are indeed of the same order of magnitude as the thermal motion energy of hydrogen molecules on the carbon surface, so that cooling the system allows strengthening the adsorption forces [13]. Hence, hydrogen physisorption is significantly enhanced at temperatures close to the boiling point of nitrogen, i.e., 77 K. Chemisorption might also take place when transition metals [14] [15] or alkali metals are present on the carbon surface [16], leading to bonding energies of the order of several hundred kJ/mol [17] and to a significant change of the surface charge distribution.

The amount of adsorbed hydrogen on a carbon material is roughly proportional to its specific surface area, i.e., to its micropore volume

[12, 18], but it also depends on the corresponding micropore size distribution and on the average micropore width [19]. A classification proposed by the IUPAC [20] and adopted worldwide separates, based on their width d, the different kinds of pores of a carbon material: (i) *macropores*, $d > 50$ nm; (ii) *mesopores*, $d \sim 2$–50 nm, and (iii) *micropores*, with $d < 2$ nm. Furthermore, micropores can be further subdivided into *supermicropores*, with a width in the range of 0.7–2 nm, and *ultramicropores*, with a width lower than 0.7 nm. Theoretical calculations, assuming that microporous carbons exhibit slit-shaped pores formed by two parallel rigid walls [21], showed that the hydrogen storage capacity is particularly enhanced in carbons having both high microporosity and narrow pores [22]. Figure 9.1 shows the profile of hydrogen density inside a pore, depending on its width. The diameter of the hydrogen molecule is 0.289 nm [23].

Therefore, in broader pores (i.e., $d > 0.7$ nm), hydrogen adsorbs on each of the two facing carbon walls, whereas in narrower pores (i.e., $d < 0.7$ nm), only one single layer can be formed. In this latter case, as hydrogen molecules are in contact with both walls, the van der Waals forces overlap, leading

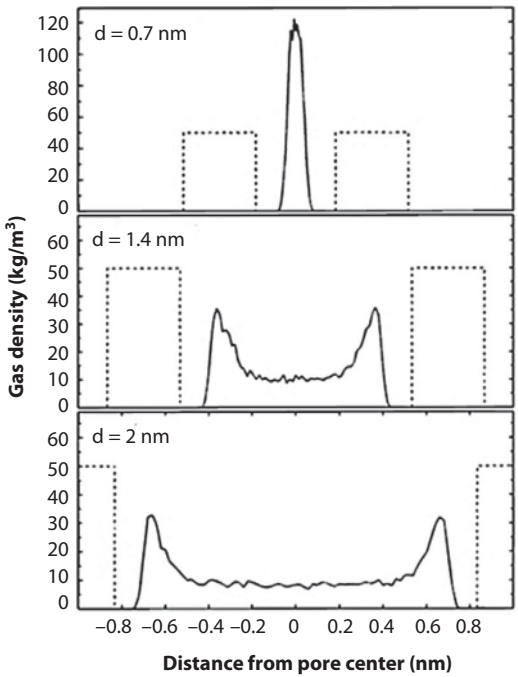

Figure 9.1 Hydrogen density profile inside a slit-shaped pore at T = 300 K and P = 10 MPa, as a function of pore width. (Adapted with permission from [24]. Copyright © 2018 American Chemical Society)

to an increased adsorption potential [24]. Thus, hydrogen density increases asymptotically from the bulk gas density value to a much higher one near the pore walls because of the strength of the adsorption forces. The density of the adsorbed phase is often assumed to be that of liquefied hydrogen, i.e., 0.071 g/cm^3 at 20 K and 0.1 MPa, but several works suggested even higher densities, up to 0.1 g/cm^3 [25]. As a rule of thumb, it is assumed for carbon adsorbents that the hydrogen uptake increases progressively by 1 wt% per 500 m^2/g of specific surface area at 77 K, a behavior known as "Chahine's rule" [26]. In the latter, the BET equation (from Brunauer, Emmett and Teller) is used to calculate the surface area from N_2 adsorption data at 77 K [27], considered as a standard tool for that purpose and allowing an easy comparison of porous materials reported in the literature [28]. The BET method provides the specific surface of an adsorbent from the monolayer capacity of the adsorbent itself, by assuming that: (i) the surface is homogeneous and adsorption occurs equally all over the surface with no preferential sorption sites; (ii) there are no lateral interactions between adsorbed molecules and a molecule can act as a single sorption site for another molecule; (iii) adsorption takes place by multilayer formation, the uppermost layer being in equilibrium with the gas/vapor phase; (iv) once the saturation pressure is reached, the number of adsorbed layers is large enough to assume that the material is surrounded by a condensed liquid phase; (v) the energy of the first adsorbed layer is equal to the heat of adsorption, whereas the energy of each following layer is assumed to be the heat of liquefaction [29].

Particular attention should be paid to the *C* parameter in the BET equation, as it provides information about the interaction of the adsorbent surface with the adsorbate and has to be positive. The BET area (A_{BET}) strongly depends on the range of relative pressures (p/p_0) chosen for fitting the BET equation to the nitrogen isotherm, and therefore it cannot be automatically applied between $p/p_0 = 0.05$ and $p/p_0 = 0.25$. For carbon materials with highly developed porous textures, a good strategy to choose the relative pressures range is to plot the product $V_{ads} \times (1 - p/p_0)$ as a function of p/p_0, starting at $p/p_0 = 0.01$. The maximum value of p/p_0 to be used for fitting the BET equation is the one at which the function $V_{ads} \times (1 - p/p_0)$ reaches its maximum. Nevertheless, the assumptions involved in the BET equation are that: (i) A_{BET} underestimates the surface area when very narrow pores exist, as only one monolayer of nitrogen is adsorbed between two pore walls; (ii) A_{BET} overestimates the surface area when micropores wider than 1 nm exist due to the occurrence of pore filling, which cannot be distinguished from monolayer adsorption by the BET method. For these two reasons, discrepancies exist between values of surface area determined by application of BET and other methods such as density functional theory (DFT).

The DFT is indeed also well-known for obtaining information about specific surface area and pore size distribution of carbon-based materials by modeling physisorption in slit-shaped pores [30]. The nonlocal version of this method (NLDFT) calculates the pore size distribution from the experimental nitrogen adsorption isotherms at 77 K by introducing the non-uniform fluid behavior of the adsorbate confined in the pores [31]. Adsorption of N_2 at 77 K is the routine method to characterize porous solids, but because of diffusional problems in narrow pores, using CO_2 as probe molecule at 273 K was shown to be the most appropriate way to determine the volume as well as the distribution of sizes of the narrowest pores [32]. Furthermore, it has been proved that adsorption isotherms calculated by the NLDFT, which assumes graphite-like, energetically uniform, pore walls do not accurately fit the experimental nitrogen adsorption data. Thus, with the 2D-NLDFT, the surface of the pore walls is treated in two dimensions, introducing in this way the spatial non-uniformity of the surface, giving in turn much better fits [33].

9.1.2 Measurement of the Hydrogen Storage Capacity

The hydrogen storage capacity of a carbon material can be measured by three different techniques: (i) volumetric, (ii) gravimetric and (iii) temperature-programmed desorption (TPD). The *volumetric* method, or *manometric*, consists in introducing a fixed amount of hydrogen into a well-known volume containing the adsorbent to be tested, previously degassed for removing any adsorbed impurity. The amount of hydrogen adsorbed is indirectly measured by pressure variations. Such systems are usually based on Sievert-type devices [34], which are very sensitive to temperature instability and leaks, especially at high pressure. The volumetric differential pressure method solves these disadvantages [35]. In such configuration, a hydrogen reservoir at a fixed pressure is connected with two well-known volumes: the sample-holder cell containing the adsorbent, and a reference volume. Once hydrogen has expanded in both of them, the adsorption phenomenon produces a differential pressure between the sample-holder and the reference, measured by a transducer. The amount of adsorbed hydrogen is then calculated from an equation of state. Despite the evident simplicity in terms of operating principles, the indirect calculation of the amount of hydrogen adsorbed, as well as the high sensitivity to temperature variations, can easily lead to errors.

On the other hand, with the *gravimetric method*, the mass of adsorbed hydrogen is directly measured. The experimental device used for gravimetric measurements of hydrogen adsorption relies on very sensitive

microbalances. After perfect degassing of the adsorbent, increments of pressure up to the set maximal pressure are produced thanks to variable leak valves. For each single increment, the weight change is measured once the equilibrium between hydrogen and carbon is reached [36]. Sophisticated magnetic suspension balances are able to perform more accurate gravimetric measurements [37]. Nevertheless, one of the main issues related to the gravimetric method is the buoyancy effect exerted on the carbon to be tested. As the carbon sorbent is surrounded by hydrogen, it is indeed subjected to an upward force whose value is equal to the weight of hydrogen displaced by the carbon itself, according to the Archimedes' law. Thus, buoyancy can alter the perception of weight, affecting the measurement process and leading to experimental errors [38]. Despite this, gravimetric methods seem to be convenient for measurements close to room temperature [39].

Temperature-programmed desorption (TPD) is another commonly used technique to evaluate the amount of hydrogen adsorbed on porous materials. After thorough outgassing of the carbon material, hydrogen adsorption is performed at a fixed temperature [40]. Desorption is then carried out by increasing the system temperature (even up to 900 K) for a fixed time under inert gas [41]. Both hydrogen and inert gas are then detected by a mass spectrometer, allowing calculation of the amount of hydrogen desorbed. Just like for the gravimetric method, a small amount of carbon is used in TPD experiments, making the accurate evaluation of adsorbed hydrogen amounts difficult [35].

9.1.3 Excess, Absolute and Total Hydrogen Adsorption

Depending on the equipment used to determine the hydrogen storage capacities, different values of what is usually referred to as "hydrogen uptake" can be obtained. Therefore, special care must be taken into account when comparing data from different studies because such uptake may refer to excess, absolute or total hydrogen adsorption, the latter including hydrogen compression in the gas phase. Thus, experimental storage data from the volumetric methods provide values of *excess hydrogen adsorption*, defined as the difference between the hydrogen uptake on the surface of the carbon adsorbent at a specific temperature and pressure, and the amount that would be present in the same volume and at the same temperature and pressure in the absence of adsorption forces [42]. As shown in Figure 9.2, hydrogen isotherms corresponding to excess data exhibit a maximum, in contrast with type I isotherms describing physisorption phenomena in microporous materials, and representing the *absolute hydrogen adsorption*. The latter quantity, derived from gravimetric measurements, is defined as the hydrogen amount contained in a volume, close to the carbon surfaces,

wherein the density of the adsorbate is much higher than the density of the bulk gas phase because of the potential field exerted by the adsorbent. Such volume, sometimes reported as adsorbed volume, cannot be measured experimentally. The adsorbed phase density is often assumed to be similar to the density of liquid hydrogen, even if other approaches consider a pressure-dependent adsorbed phase density [43]. The direct consequence of the latter strategy is that the adsorbed volume, i.e., the volume of the adsorbed phase as explained above, depends both on the amount of hydrogen already adsorbed and on the temperature. On the other hand, by defining a constant adsorbed volume, it is assumed that the adsorbed gas occupies the whole space available for adsorbing a complete monolayer, and hence that the density gradually increases up to an asymptotic value during adsorption [44]. This assumption makes the evaluation of the absolute adsorbed amount easier by using the excess quantity through the following approximation:

$$n_{abs} = n_{exc} + \rho_g V_a \tag{9.1}$$

where ρ_g (mol/m^3) is the density of the bulk gas phase, and V_a (m^3/kg) is the volume of the adsorbed layer of adsorbate. By taking into account all the volumes of the sample-holder not occupied by carbon, i.e., intergranular voids as well as internal porosity, the volume of the adsorbed layer can also be defined as the difference between the total void volume, V_V, and the volume of the bulk gas phase having no interaction with the adsorbent surface, V_g [45]. The value of V_V can be easily determined from helium pycnometry carried out on a representative packing of adsorbent grains, whereas that of V_g only depends on temperature and pressure [46]. Using this definition, the *total hydrogen capacity* is introduced (see Figure 9.2), being the sum of the absolute adsorbed hydrogen amount and the amount of free molecules present in the empty spaces not submitted to the adsorption field, i.e., it is the total amount of gas present in the system [47]:

$$n_{tot} = n_{abs} + \rho_g \left(V_v - V_a \right) = n_{exc} + \rho_g V_v \tag{9.2}$$

The different ways to express hydrogen capacities on carbon materials make it difficult to have a clear idea about their real potential for hydrogen storage. In general, excess and total amounts are identical up to 0.1 MPa, see again Figure 9.2. On the other hand, for high-pressure applications, the corresponding high values of hydrogen density produce clear differences between excess hydrogen adsorption and the total uptake. In fact, the excess hydrogen adsorption increases at low pressure and decreases at high pressure; a maximum is thus obtained, whereas the total uptake monotonically increases with pressure.

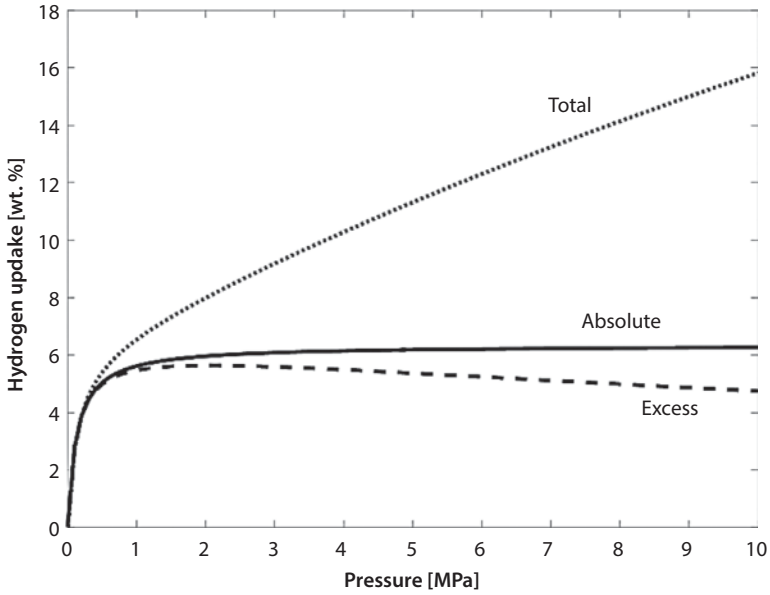

Figure 9.2 Excess, absolute and total hydrogen uptake for the commercial carbon AX-21 at 77 K and in the pressure range 0–10 MPa.

9.2 Hydrogen Storage in Carbon Materials

9.2.1 Activated Carbons

Out of all carbon materials, activated carbons (ACs) are among those providing the highest hydrogen uptakes. ACs are produced from a large variety of low-cost and renewable raw materials through carbonization and simultaneous, or subsequent, activation process, which allows opening and developing the porosity, and hence the surface area. Two activation techniques are used: (i) physical activation, or (ii) chemical activation. Physical activation is generally carried out in two steps. A preliminary thermal pretreatment of the raw material, consisting in a pyrolysis at temperatures typically ranging from 673 to 1023 K [48], increases the carbon content because of the evolution of volatile matter. Next, activation is carried out by controlled gasification of the carbonized materials at high temperature, generally around 1000–1200 K, in a stream of oxidizing gas, mainly CO_2 or H_2O [49]. Several parameters influence the final pore texture such as carbonization temperature, activation temperature, activation time, gas flow rate, and heating rate [50].

In contrast, chemical activation is realized by physically mixing or impregnating the raw material with a chemical acting both as desiccant

and oxidizer at high temperature (KOH, NaOH, H_2SO_4, H_3PO_4, $ZnCl_2$), followed by a heat treatment either in air or under inert gas, depending on the activating agent and on the temperature, within the typical range of 700–1000 K [4]. Chemical activation also requires extensive washing for removing unreacted activating agents and/or activation by-products possibly blocking the pores [51]. Chemical activation is used more than physical activation for preparing activated carbons designed for hydrogen adsorption, since: (i) it ensures a more uniform and narrow microporosity than physical activation; (ii) higher surface areas are usually obtained by chemical activation; (iii) chemical activation is a one-step process [52, 53]. Hydrothermal carbonization is sometimes applied before chemical activation, but the effect on hydrogen storage is still debated [54, 55].

An upper limit of excess hydrogen adsorption equal to 6.4 wt% at 77 K and 4 MPa has been reported for ACs with A_{BET} of 2630 m^2/g [56], in full agreement with Chahine's rule. However, a hydrogen excess of only 1 wt% was observed for the same AC [56] at room temperature and 20 MPa, clearly demonstrating that hydrogen adsorption is particularly favorable at low temperature. One of the highest values of absolute hydrogen adsorption ever reported for ACs was 7.08 wt% at 77 K and 2 MPa, achieved with a KOH-activated carbon exhibiting an A_{BET} as high as 3190 m^2/g and a micropore volume (V_μ) of 1.09 cm^3/g [57]. The same precursor physically activated with CO_2 resulted in an AC with an A_{BET} of 1308 m^2/g and V_μ of 0.47 cm^3/g, and achieved a hydrogen uptake of 4 wt% under the same conditions [57], emphasizing the benefit of adopting chemical activation instead of physical activation.

Agricultural wastes or lignocellulosic materials have been extensively used as AC precursors due to their intrinsic cheapness and renewable nature [49]. ACs produced from olive stones and chemically activated with $ZnCl_2$ and H_3PO_4 presented hydrogen uptakes[1] up to 5 wt% at 1.2 MPa and 77 K for both activating agents [58], although $ZnCl_2$ led to a higher A_{BET} and

[1] Despite being a misleading term, as emphasized in Section 9.1, the words "uptake" or "storage capacity" will be used in some places of this chapter without specifying whether we deal with excess, absolute or total hydrogen amount. This lack of information is due to the fact that the corresponding details were not given in the associated references (see the Chapter Appendix). In most cases, we could deduce from the measurement methods and from the shape of the isotherms which kind of uptake was reported. In other cases, neither such details were given nor did the isotherms allow us to conclude about excess, absolute or total hydrogen amount that was measured or calculated. This is especially true at low pressure, for which all these quantities are rather similar, as shown in Figure 9.2. Therefore, even if the information is missing, talking about "uptake" or "storage capacity" without additional details is still meaningful. In other rare cases, a few results were

V_μ (1533 m^2/g and 0.70 cm^3/g) when compared to H_3PO_4 (1170 m^2/g and 0.52 cm^3/g). The different pore size distributions (PSDs) together with the underestimation of A_{BET} for sorbents with very narrow pores might explain such differences. KOH activation of olive stones produced ACs with good hydrogen storage capacities, thus an excess hydrogen adsorption of 3.6 wt% was achieved at 77 K and 10 MPa [59]. Nevertheless, an excess of 1.22 wt% was measured at room temperature and 20 MPa [59]. A hydrogen absolute adsorption of 6.6 wt% at 77 K and 4 MPa has been achieved through KOH activation of bamboo-derived carbons [60] with an A_{BET} as high as 3208 m^2/g and V_μ up to 1.01 cm^3/g, being one of the best results of hydrogen adsorption on ACs available in the open literature. A maximum hydrogen excess of 4.73 wt% at room temperature and 4 MPa was reported for ACs produced from tamarind seeds, exhibiting an A_{BET} of 1785 m^2/g and a V_μ of 0.94 cm^3/g [61].

In order to enhance the interaction between hydrogen molecules and AC surface, heteroatoms or metal nanoparticles can be introduced into the carbon matrix. Significant effects were obtained at room temperature, as shown by studies on ACs doped with Pd [62]. However, increasing the Pd content produced a decrease of A_{BET} and, furthermore, the amount of adsorbed hydrogen at room temperature was higher for Pd-doped ACs than for non-doped ACs only in the pressure range 0.1–1 MPa. Indeed, at higher pressure, higher Pd contents led to lower hydrogen uptakes. On the other hand, a significant reduction of the hydrogen uptake was obtained by progressively increasing the Pd content at 77 K, due to the fact that physical adsorption increases with surface area at low temperature. The introduction of nitrogen instead of palladium also produced a reduction of A_{BET} and therefore a decrease of the hydrogen storage capacities at 77 K [63]. Studies on boron-modified ACs showed that an increase of A_{BET} can be obtained after modification of the ACs by means of borax decahydrate (BDH) [64]. Thus, whereas non-doped ACs had an A_{BET} of 2228 m^2/g, the boron-modified counterpart exhibited higher values, up to 2704 m^2/g. However, the authors reported lower hydrogen uptakes, 3.74 wt% compared to 4.11 wt% for the non-modified ACs, both at 77 K and 0.1 MPa, likely due to an accumulation of BDH in the pores.

The addition of metal nanoparticles to the AC structure can also be beneficial in terms of hydrogen storage due to the spillover phenomenon, i.e., to the dissociative chemisorption of molecular hydrogen on metal nanoparticles, followed by the migration of atomic hydrogen to the carbon surface and its consequent diffusion along the latter [65]. Hydrogen spillover is enhanced at room temperature, and depends on the type of metal nanoparticles

discarded because they were found not to be trustworthy, with regards to the quite uncommon and unrealistic shape of some published isotherms.

dispersed onto the carbon surface, on their size, on the anchoring strength to the carbon surface, and on the ability of dissociating molecular hydrogen into an atomic one [66]. Moreover, the metal nanoparticles must be well-dispersed to avoid the blocking of the AC porosity. Ruthenium, platinum and nickel nanoparticles on AC surface produced a significant increase of hydrogen uptake at room temperature and 10 MPa [67]. Hydrogen excesses of 1.30, 1.22 and 1.02 wt% were indeed achieved with Ru/AC, Pt/AC and Ni/AC, respectively, compared to 0.6 wt% for the non-doped counterpart under the same conditions, in spite of a decrease of A_{BET} of around 300 m^2/g after doping. Increasing hydrogen uptakes by means of spillover appears to be a promising strategy considering that, on average, a gravimetric capacity lower than 1 wt% is generally achieved at room temperature and moderate pressures for a broad range of non-doped ACs [68].

Figure 9.3 gathers values of hydrogen excess on ACs. Hydrogen excess followed a linear trend with A_{BET} at 77 K and 0.1 MPa. At pressures up to 4 MPa, the data are in good agreement with Chahine's rule. Nevertheless, the most surprising result was the 5 wt% hydrogen uptake obtained at only 1 MPa, a value which is higher if compared with the average values obtained with ACs at this pressure [55]. The AC used in that study was prepared through H_3PO_4 and $ZnCl_2$ chemical activation. The authors pointed out that such a value of hydrogen uptake is related to both the preparation conditions as well as to the post-treatments that enhanced the development of slit-shaped pores, well-suited for hydrogen adsorption.

Figure 9.3b shows hydrogen excess at 298 K. The corresponding values are below 1.5 wt%, even at pressures up to 20 MPa. It also shows that doping is a beneficial strategy at this temperature in order to increase hydrogen adsorption [67]. The hydrogen excess recorded from [61], 4.73 wt%, was much higher than the average values commonly obtained for carbon materials at room temperature. The adsorbent in [61] was an AC prepared through microwave carbonization of tamarind seeds and subsequent KOH activation, and nothing but experimental errors can explain such very high uptake (not shown in Figure 9.3b).

9.2.2 Carbon Nanomaterials

Figure 9.4 shows various carbon nanomaterials commonly investigated for hydrogen adsorption, which revealed very contradictory results.

9.2.2.1 Graphene

Many studies focused on graphene with regards to hydrogen adsorption [69–79]. Graphene is a single basal plane of aromatic (purely sp2) carbon

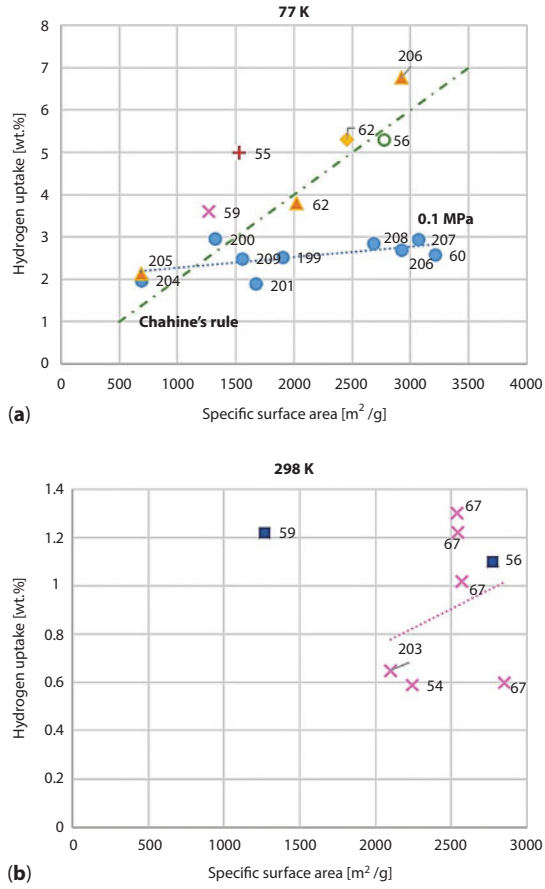

Figure 9.3 Excess hydrogen adsorption on ACs reported by recent works at: (a) 77 K, and (b) 298 K. The labels indicate the corresponding references. (• 0.1 MPa, + 1.2 MPa, ▲ 2 MPa, ♦ 3 MPa, ○ 4 MPa, ×10 MPa, ▪ 20 MPa).

having a trigonal stereochemistry arranged in hexagonal rings [80]. Thus, many sheets of graphene bounded to each other by weak van der Waals interaction form the graphite structure. The study of graphene and its derivatives as a potential system for hydrogen storage kept researchers' attention during the last years. In fact, even if the surface areas are generally lower than those of ACs [18, 77, 79, 81], amazing hydrogen storage capacities were reported [75]. Numerical simulations suggested that the excess hydrogen physisorption in a graphene structure might reach 7 wt% at 77 K and 1 MPa, whereas it would be 1.5 wt% at 293 K and 30 MPa [77]. These values were very close to the maximum excess hydrogen adsorption

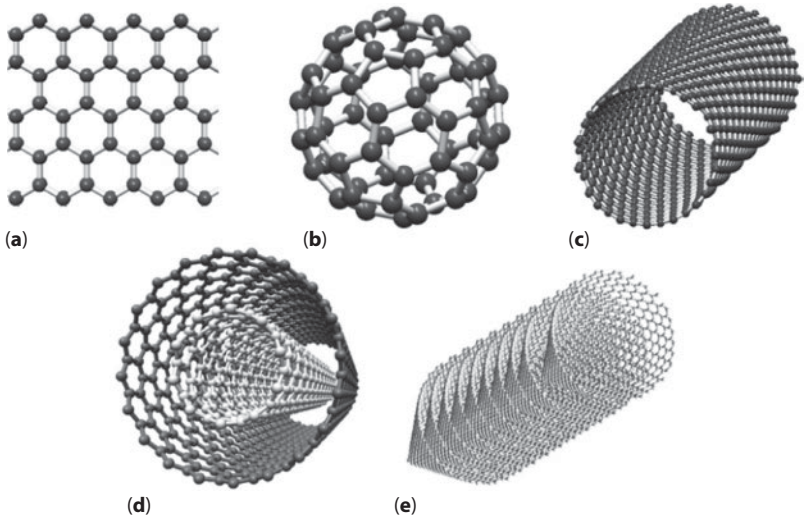

Figure 9.4 Different typologies of carbon nanomaterials investigated for hydrogen adsorption ((a) graphene; (b) fullerene; (c) single-walled carbon nanotube; (d) multi-walled carbon nanotube; (e) carbon nanofiber [platelet-type]).

calculated for a set of loosely packed graphene layers, which is around 8 wt% at 77 K and 4 MPa [82, 83].

Further theoretical studies suggested to incorporate hydrogen in the interlayer spacing between graphene sheets, found that an interlayer distance of 0.6 nm would be ideal to enhance hydrogen adsorption [78]. In order to increase the adsorption capacity of graphene-based structures, several techniques have been applied, such as: (i) doping the nanostructure with heteroatoms like nitrogen [84]; (ii) decorating it with alkali or transition metals [85, 86], and (iii) producing graphene nanostructures by reduction of graphite/graphene oxides [71, 76, 78, 81, 87]. As for the latter method, a maximum excess hydrogen uptake of 7.04 wt% was indeed obtained at 77 K and 6 MPa with a reduced graphene oxide chemically activated with KOH, showing an A_{BET} as high as 3230 m^2/g and a total pore volume (V_T) of 2.2 cm^3/g [87], whose values are comparable to those reported for many ACs. Furthermore, graphene obtained by reducing exfoliated graphite oxides with glucose presented a hydrogen uptake of 2.7 wt% at 2.5 MPa and room temperature, measured with a magnetic suspension balance gravimetric analyser. The A_{BET} of the as-produced carbonaceous sorbent was 1206 m^2/g [88]. Decoration of graphene with transition metals also provided high values of hydrogen capacities at room temperature and 4 MPa: a hydrogen storage capacity of 4.83 wt% was indeed reached by a

Pd-decorated graphene material [89]. Nevertheless, the decoration technique is very challenging, as metal nanoparticles lead to issues related to structural stability [73] and tend to aggregate easily due to strong metal cohesion forces. Moreover, another disadvantage is related to the high cost of noble metal nanoparticles [75].

9.2.2.2 Fullerenes

Fullerenes have also been considered as hydrogen adsorbents. A fullerene can be visualized as a graphene sheet rolled up on itself to form a sphere-shaped or ellipsoid structure. They are also known as "buckyballs," in reference to their resemblance to the worldwide-famous geodesic domes of the architect R. Buckminster Fuller [90]. In fullerenes, carbon atoms form hexagonal and pentagonal rings. The most stable form of fullerenes, C_{60}, consists in a polyhedron with twenty hexagonal rings and twelve pentagonal rings [72]. Several fullerene structures were investigated for hydrogen storage by application of the density functional theory [70, 91–96], suggesting that Li- and Na-doped C_{60} fullerenes are good candidates for storing hydrogen [70]. The same conclusion was derived from the theoretical investigation of B_{38} fullerenes decorated with transition metal atoms such as Ti, Fe, Co and Ni: the evaluation of the average hydrogen adsorption energy revealed that such structures might ensure a hydrogen uptake as high as 7 wt% [93, 95]. All those data still need to be confirmed experimentally.

9.2.2.3 Carbon Nanotubes

Carbon nanotubes (CNTs) are other carbon structures commonly investigated for hydrogen storage. The simplest form, the single-walled carbon nanotube (SWCNT), consists in a graphene sheet rolled up to form a cylinder, whose diameter is of the order of a few nanometers. An arrangement of coaxial graphene sheets, generally between two and fifty coaxial units, leads to multi-walled carbon nanotubes (MWCNTs). SWCNTs generally have a diameter of 1 nm, whereas MWCNTs have an inner diameter ranging from 1.5 to 15 nm and outer diameters from 2.5 to 30 nm. The interlayer distance between two consecutive units in MWCNTs is around 0.35 nm. Generally, the length of both SWCNTs and MWCNTs is of several microns [90, 97]. A worldwide interest in using CNTs for storing hydrogen started in 1997, when outstanding hydrogen uptakes were reported for SWCNTs. A gravimetric storage uptake in the range of 5–10 wt% at room temperature was indeed measured by TPD experiments with SWCNTs synthesized by co-evaporation of cobalt and graphite in an electric arc [98]. Even higher

hydrogen uptakes were reported in 1999 by using alkali-doped MWCNTs. Specifically, it was assumed that Li- or K-doped MWCNTs were able to adsorb a hydrogen amount of 14–20 wt% at moderate temperature conditions, in the range of 473–673 K [99]. However, these values were denied by further experiments, which attributed the unusual values to moisture reacting with the alkali species on the carbon surface [100].

In spite of the controversial reported values [101], CNTs (both in the forms SWCNT and MWCNT) are still considered as promising materials for hydrogen storage. In fact, CNTs are produced from very mature technologies, based on now well-mastered synthesis methods. Chemical vapor deposition (CVD) of a carbon precursor, generally acetylene [102], as well as controlled arc discharge, allow producing CNTs bundles [103] and organized CNTs with hierarchical pore size distribution [104]. Experimental studies showed that CNT bundles, produced through arc discharge at 873 K using Ni-Co alloy powders as catalyst, reached a hydrogen storage capacity of 1.73 wt% at 77 K or 0.67 wt% at room temperature; both measurements were done at 10 MPa [104]. Higher values were achieved by changing the catalyst used for the synthesis. The hydrogen uptake achieved by CNTs without further treatments is, on average, below 1.7 wt% [105] at 298 K and 12 MPa, a value not too far from the hydrogen storage capacities of ACs. This conclusion suggests that is not worth storing hydrogen at room temperature by using pure CNTs.

Controlling the diameters of single tubes, as well as length and interspace layer distance of CNTs, is a strategy to improve the hydrogen adsorption capacity even at moderate temperature [97]. The adsorption potential was proved to be higher in SWCNT bundles than in an isolated SWCNT, since hydrogen molecules are subjected to higher adsorption potentials in the interstitial space between different single tubes [18]. The introduction of defects on SWCNTs in order to increase the interstitial volume within the single structures improved the gravimetric storage capacity of the bundle [106]. Experimental studies showed that the ideal interlayer spacing in a CNT rope, as well as the space among concentric tubes in a MWCNT, is 0.34 nm [107], larger than the kinetic diameter of molecular hydrogen (0.289 nm) [23]. Intercalation using potassium has also been shown to be a good solution for increasing the spacing between single nanotubes in a bundle [106].

An additional way to enhance hydrogen adsorption on CNTs at room temperature consists in functionalizing them with nitrogen or boron, or decorating them with metal nanoparticles. On the one hand, the functionalization can be carried out after the synthesis process, with the possibility of damaging the stability of the carbon structure [108]. On the other hand,

the CVD process allows directly introducing the doping metal or heteroatom into the CNT matrix during the synthesis process, by using precursors containing both carbon and the desired doping metal/heteroatom. Thus, N-doped CNTs were synthesized by using imidazole as a source of carbon and nitrogen [109], leading to an increase of hydrogen storage especially at low temperature, up to 65% higher than that of the non-doped materials at 163 K. However, the achieved value, 0.8 wt% at 163K and 5 MPa, is still low when compared to other carbon adsorbents, suggesting that further improvements are required [109].

In this sense, decorating a functionalized MWCNT (f-MWCNT) with metal nanoparticles produced a significant enhancement of the hydrogen uptake due to the spillover phenomenon. Carboxylate-functionalized MWCNTs were decorated with Fe and Cu nanoparticles in dimethyl formamide, and hydrogen storage capacities up to 0.39 wt% and 0.5 wt% were obtained, respectively, at room temperature and 7 MPa. In contrast, only 0.06 wt% was found for the non-decorated f-MWCNT under the same conditions [110]. Obviously, an essential requirement during CNT functionalization is preventing the obstruction of the available pores, which would decrease A_{BET}. Some studies [111] indeed showed that MWCNTs functionalization with H_2SO_4 and HNO_3 produced a drastic reduction of A_{BET}, from 481 to 23 m^2/g, due to pore blocking, with a consequent reduction of V_μ, from 0.26 to 0.01 cm^3/g. This reduction of porosity decreased the hydrogen adsorption capacity from 0.67 to 0.4 wt% at room temperature and 3.4 MPa. On the contrary, an evident increase of hydrogen adsorption capacity was reported when the same MWCNTs were submitted to KOH activation. Indeed, KOH activation increased A_{BET} up to 995 m^2/g and V_μ up to 0.53 cm^3/g. This development of the pore texture resulted in higher hydrogen adsorption capacity, up to 1.24 wt% under the same experimental conditions. Significant improvements of hydrogen storage capacity, from 0.43 wt% to 2 wt% at room temperature and 1.6 MPa, were also obtained by decorating MWCNTs with Ti nanoparticles through ball-milling and sputtering methods, respectively [112], whereas the hydrogen storage capacity of the pristine MWCNTs was 0.075 wt% under the same conditions. The relatively high value obtained by sputtering is due to the fact that Ti nanoparticles were deposited onto the outer surface of the walls, enhancing in turn the hydrogen storage capacity due to the spillover effect.

Nickel, a more abundant and moderately expensive metal, was also investigated for decorating CNTs for hydrogen storage [113]. After nickel decoration, both A_{BET} and V_μ decreased, but the hydrogen storage capacity increased from 0.40 to 0.87 wt% at 298 K and 10 MPa, again because of the spillover effect. Impregnation of MWCNTs with metal oxides has also been

investigated as a strategy for increasing hydrogen storage. TiO_2/MWCNTs stored up to 0.40 wt% of hydrogen at 298 K and 1.8 MPa, an amount almost five times higher than that of the pure counterpart [114]. Similarly, 0.8 wt% and 0.9 wt% were measured in Co-oxide/MWCNT and Cu-oxide/MWCNT at 298 K and 2.3 MPa respectively, with a nearly tenfold increase compared to the untreated counterpart [115]. Such materials were synthesized by *in-situ* reduction method, using cobalt nitrate hexahydrate and copper nitrate trihydrate respectively.

9.2.2.4 Carbon Nanofibers

Having similar properties to CNTs, carbon nanofibers (CNFs) or graphitic nanofibers (GNFs) have received great attention in view of their hydrogen adsorption capacities. CNFs are fibrous structures whose diameters vary from ten to a few hundred nanometers, consisting of thin filaments of partially or entirely graphitized carbon with graphitic layers that can be arranged in various ways [116]. Depending on the angle that the graphitic sheets form with the fiber's axis, different CNF structures are described: (i) "platelet," if the graphitic layers are perpendicular to the fiber's axis; (ii) "herringbone," for angles of 45°, and (iii) "tubular," if the graphitic layers are concentrically arranged around the fiber's axis. The highest hydrogen uptake ever reported in the literature for a carbon material was obtained in 1998 with GNFs: an astounding 67 wt% of hydrogen stored at room temperature and 12 MPa was reported [117]. Several experimental studies tried to retrieve such a value, but without success: a maximum hydrogen storage of only 0.4 wt% was indeed achieved using a volumetric adsorption apparatus at room temperature and 14 MPa with a GNF thoroughly re-prepared according to the original description [118]. The same sample was also tested through gravimetric measurements, reaching the value of 0.36 wt%.

Generally GNFs are synthesized by thermal decomposition of a carbon precursor in the presence of a catalyst [119], or through the CVD method [120]. A hydrogen storage capacity of 1.1 wt% at room temperature and 12 MPa was measured with a CNF produced by thermal decomposition of methane [119]. It has also been seen that if a further thermal treatment follows, e.g., by heating up to 1500 K, the resultant removal of impurities blocking the surface cavities allows reaching a higher A_{BET}, from 140 to 170 m^2/g, leading in turn to an increase of hydrogen storage capacity from 1.1 to 1.4 wt%. The CVD method was also very effective for synthesizing CNFs for hydrogen storage. Hydrogen adsorption capacities of 0.51 wt%, 0.42 wt% and 0.65 wt% have been achieved at 298 K and 1 MPa by using

pyrolyzed acetylene, ethanol and cotton fiber as precursors for the CVD, respectively, followed by activation with KOH [120].

An enhancement of the hydrogen adsorption capacity of CNFs can be reached by decorating the carbon support with metal nanoparticles [121, 122]. CNFs submitted to thermal treatment at 1300 K and decorated with Ni nanoparticles, loaded by an electroless metal-plating method, exhibited a hydrogen storage capacity as high as 2.2 wt% at room temperature and 10 MPa, owing to both spillover and enhanced A_{BET}, equal to 1310 m^2/g [121]. Such value of hydrogen storage capacity was reached with a nickel content of 5.1 wt% and a metal dispersion rate of 6.6%, partly preventing the pore blocking and thus increasing the storage capacity. CNFs developed from AC microfibers by the CVD method, decorated *in situ* with Ni particles, also showed good improvements of the hydrogen adsorption capacity [122]. The first effect of the Ni decoration was the decrease of the A_{BET}, from 522 to 483m^2/g, due to pore blocking. Whereas hydrogen uptake strictly depended on the specific surface area at 77K, the positive effect of Ni nanoparticles was particularly evident at room temperature. In fact, a decrease of hydrogen storage capacity from 2.1 to 1.6 wt% was obtained at 77 K and 2 MPa, whereas an increase from 0.28 to 0.37 wt% was observed at 298 K and 5 MPa.

Another compelling method for enhancing the hydrogen storage capacity of CNFs consists in performing graphite exfoliation after CVD. It was seen that a hydrogen storage capacity up to 5 wt% can be reached at 77 K and 1 MPa by graphite exfoliation carried out by intercalation with concentrated acid mixture (50/50 sulphuric/nitric acid) followed by a thermal shock [123]. In fact, exfoliation allows the partial separation of graphene layers from the rough CNF surface, providing efficient pathways for hydrogen atoms intercalation between graphene layers, thus increasing the hydrogen uptake. Finally, CNFs produced by renewable sources have also been investigated in terms of economic and environmental issues. CNFs based on rice straw prepared by wet spinning and carbonization process presented a substantial absolute hydrogen adsorption equal to 4.35 wt% at 77 K and 2 MPa [124].

Figure 9.5 shows hydrogen storage capacities reported so far for graphene, CNFs and GNFs. It is not possible to define a clear trend for such materials, confirming that hydrogen physisorption onto these materials is still an unclear topic, as several controversial values were reported. A first rough analysis suggests that graphene seems to be superior to CNTs and GNFs. Data at 77 K (Figure 9.5a) are in good agreement with Chahine's rule; the highest hydrogen uptake of 7.04 wt% was obtained for a carbon material produced from graphene oxide which was next chemically activated

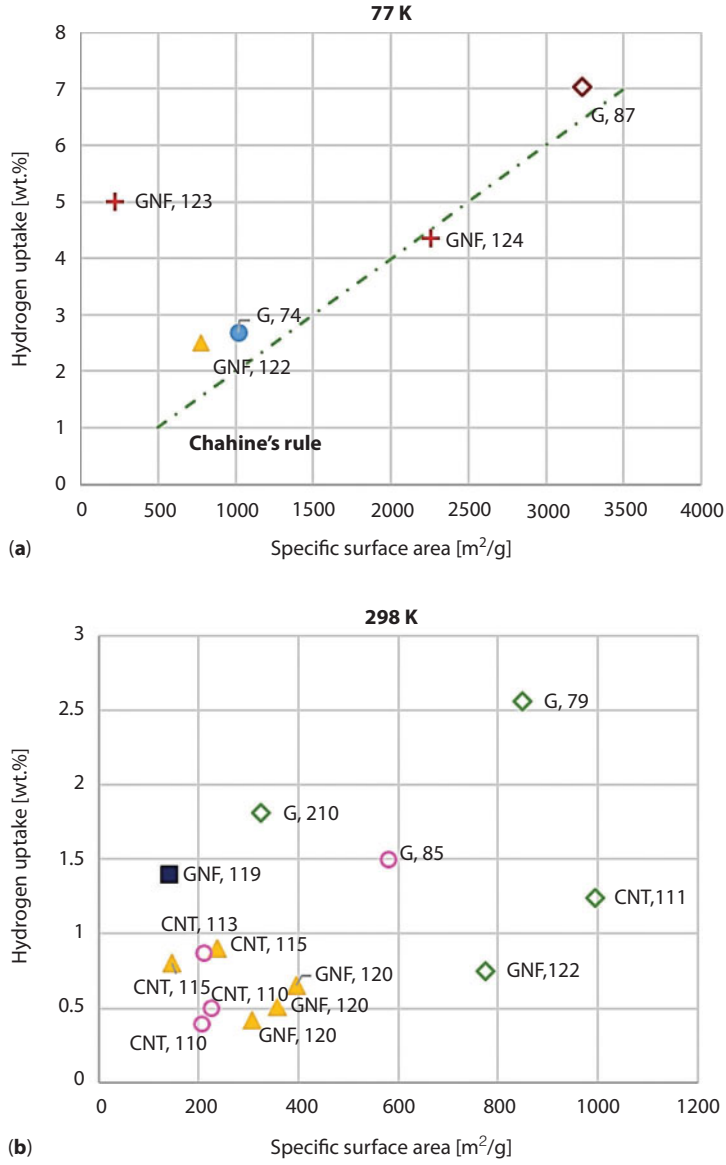

Figure 9.5 Hydrogen storage capacities on graphene, CNTs and GNFs reported by recent works at: (a) 77 K, and (b) 298 K. The labels indicate both the typology of carbon (G=graphene, CNT=carbon nanotube, GNF=graphite nanofiber) and the corresponding references. For clarity, the data are grouped by ranges of pressures (• 0.1 MPa, ▲1-2 MPa, ◊ 3-5 MPa, + 6 MPa, ○ 7-10 MPa, ▪ 12 MPa).

by KOH [87], thereby significantly increasing both A_{BET} and V_{μ}. Data from [123] are even more noteworthy, as a hydrogen uptake as high as 5 wt% was obtained with a GNF of only 226 m^2/g. This material was obtained by exfoliation of a turbostratic GNF. On the other hand, data at 298 K (Figure 9.5b) show that the amount of hydrogen adsorbed on graphene, CNTs and GNFs is lower than 1.5 wt% on materials having values of A_{BET} up to 600 m^2/g. Nevertheless, only a few works obtained hydrogen storage capacities above 2.5 wt% by using graphene. The very high pore volume up to 2.11 cm^3/g, the correspondingly large A_{BET} and the low pore size explain the uptake of 2.56 wt% obtained by a nanoporous graphene [79].

9.2.3 Templated Carbons

9.2.3.1 Zeolite- and Silica-Derived Carbons

Carbon structures with a controlled hierarchical pore texture for hydrogen storage can be produced through the template carbonization method, which is an effective approach to synthesize materials with very ordered pore structures and relatively narrow pore size distribution compared to most other carbons [125]. The hard-templating method consists in preparing microporous and mesoporous carbons by introducing an organic precursor into the pores of an inorganic template, followed by carbonization and removal of the template by leaching with strong acids [126]. The as-produced micro/mesoporous carbon has a pore size comparable to the wall thickness of the template framework, even if shrinkage is unavoidable because of the carbonization process [127]. The inorganic templates commonly chosen for such purpose are porous silica [128–130] and zeolites [127, 131–138]. Silica-based templates especially promote the synthesis of mesoporous carbons, whereas zeolites seem to be appropriate for producing carbons with an enhanced microporosity, well-suited for hydrogen adsorption [139]. Experimental studies showed that the amount of hydrogen potentially stored in a templated carbon depends not only on the typology of the adopted inorganic templates, but also on the nature of the precursors, as well as on the synthesis methods and on the carbonization parameters [127].

In order to achieve high microporosity in templated carbons, a two-step synthesis process was developed: (i) first a liquid impregnation of an organic precursor, followed by polymerization and a preliminary partial carbonization, and (ii) chemical vapor deposition (CVD) of another, different, organic precursor at high temperature, sometimes followed by a further heat treatment at temperatures higher than those used for the

CVD step [132, 133, 138]. The necessity of a two-step process is explained by the imperfect filling of the template by simple impregnation methods, negatively affecting the microporosity of the templated carbon [134]. As a result, a noteworthy absolute hydrogen adsorption of 7.3 wt% at 77 K and 2 MPa was reached by using the zeolite 13X as template, furfuryl alcohol as impregnation agent, and ethylene in the CVD step [138]. The aforementioned templated carbon had an A_{BET} of 3332 m^2/g and a V_T of 1.66 cm^3/g. The excess hydrogen adsorption for this sample was 6.2 wt%, and the total adsorption was 9.22 wt%; such values are among the highest ever reached by a carbon material [138, 140]. Using zeolite 10X as carbon template, furfuryl alcohol for impregnation and acetylene as precursor for CVD, an absolute hydrogen adsorption of 6.09 wt% was reached at 77 K and 2 MPa [137], even if the values of A_{BET} and V_T (3331 m^2/g and 1.94 cm^3/g, respectively), were close to those of the previous case.

A further carbonization step after CVD, consisting in a heat treatment at temperatures up to 1173 K, was fundamental in order to enhance the microporosity of the templated carbon. As a matter of fact, studies carried out on the synthetic zeolite EMC-2, impregnated with furfuryl alcohol and submitted to CVD with ethylene, reported an increase of A_{BET} from 1322 to 1984 m^2/g, and of V_T from 0.78 to 1.06 cm^3/g, leading to an overall increase of the hydrogen uptake capacities from 2.95 to 4.76 wt% [132]. On average, the best results were obtained by using ethylene for the CVD step instead of other carbon precursors like acetonitrile or acetylene [133]. The synthesis parameters strictly influence the resultant values of A_{BET} and V_T: it has been seen that a 3-h-long heat treatment at 1023 K leads to the highest possible hydrogen storage capacities [127]. In fact, short heat treatments at low temperatures lead to lower A_{BET} and V_T, whereas too long treatments at high temperatures can cause the collapse of the zeolite structure, hence a decreased microporosity and a more disordered porous structure, unfavorably affecting the achievable hydrogen uptake [135].

Efforts have been focused on producing cheaper and more competitive templated carbon adsorbents [131, 136]. The possibility of replacing commercial zeolites by cheap unconventional materials as templates was explored, and zeolites from fly ash were investigated [131]. The performances and properties of the fly-ash-derived templated carbon were lower than those obtained from a zeolite X: a hydrogen uptake of 1.2 wt% at 77 K and 0.1 MPa was achieved, compared to the 2.4 wt% obtained under the same conditions by using zeolite X as template [131]. This result can be explained by the lower A_{BET} and V_T of the fly-ash-derived templated carbon (1112 compared to 2577 m^2/g, and 0.48 compared to 1.44 cm^3/g, respectively). A single-step process, consisting in a modified liquid impregnation

by an organic precursor, was also investigated for the synthesis of templated carbons [136]. By using zeolite USY and sucrose as carbon precursor, a derived templated carbon having an A_{BET} of 1127 m^2/g and V_T of 0.817 cm^3/g was produced, achieving a hydrogen storage capacity of 3.52 wt% at 77 K and 2 MPa. These results were undoubtedly lower than those achieved by using the two-step synthesis method.

Inexpensive silica templates were also investigated for the synthesis of templated carbons. Rice husks were used as feedstock for the synthesis of silica-based materials and, for that purpose, were carbonized after impregnation with glycerol [128]. The reported excess hydrogen uptake was equal to 2.41 wt% at 77 K and 7.3 MPa, and increased up to 5.7 wt% when the contribution of hydrogen molecules compressed in the pores was taken into account (total hydrogen storage capacity). Several experiments showed that silica templates are not very relevant for the synthesis of carbon materials designed for hydrogen storage applications [129, 130]. Hydrogen uptakes at room temperature were very low, e.g., a hydrogen storage capacity of 0.67 wt% was obtained at room temperature and 8 MPa [141] with a silica-base-derived template carbon. Theoretical studies suggested that the decoration of the carbon surface with metal nanoparticles might enhance hydrogen adsorption through the spillover phenomenon, but the data reported so far still lack consistency among different research groups, and the mechanism has not been fully revealed yet [142].

9.2.3.2 MOFs-Derived Carbons

Carbon materials with very high surface areas for hydrogen storage were produced from metal-organic frameworks (MOFs) [143]. MOFs are well-known in the context of hydrogen storage: the considerable excess hydrogen adsorption of 9.9 wt% at 77 K and 5.6 MPa that was measured for a MOF called NU-100 (A_{BET} = 6143 m^2/g and V_T = 2.82 cm^3/g) is nowadays among the highest value ever achieved in the framework of hydrogen adsorption [144]. Basically, MOFs consist of inorganic nodes, usually metal or metal oxide clusters, connected by organic linkers, which are generally ditopic or polytopic organic carboxylates or other negatively charged molecules. The connection between inorganic and organic units leads to robust crystalline structures, with A_{BET} ranging from 1000 to almost 10 000 m^2/g [145]. The large variety of possible nodes, linkers, functional groups and crystallographic arrangements may produce a countless number of possible structures [146, 147]. MOFs were also investigated as templates for the synthesis of carbonaceous materials because of their tuneable high porosity, high stability, and low framework density [148, 149], see Figure 9.6. Actually,

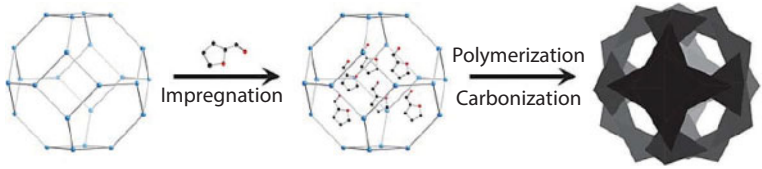

Figure 9.6 Schematic view of carbon materials preparation from MOFs. (Adapted from [153] with permission of Royal Society of Chemistry).

MOFs exhibit very attractive properties: the organic linkers commonly consist of rigid aromatic rings, ensuring a high carbon yield after pyrolysis. This feature allows synthesizing MOF-templated carbons through a single carbonization step so that the infiltration of a second organic precursor, as in the case of zeolite-templating, is not always necessary [132, 133, 150]. Furthermore, some MOFs intrinsically have a high nitrogen content, ensuring in turn the possibility of synthesizing N-doped carbon structures simply by pyrolysis [151, 152]. However, during the carbonization process, carbon-nitrogen bonds can be broken, resulting in a decrease of the nitrogen content in the final carbon structure; even so, nitrogen doping can be ensured by using a second nitrogen precursor, like ethylenediamine or acetonitrile [153].

MOFs based on organic bridges having a high carbon content lead to carbons with a low specific surface area, whereas high surface areas are produced from MOFs whose organic linkers present a low carbon content [154]. Zn-MOFs seem to be a well-suited choice for the production of templated carbons. The higher the Zn/C ratio, the higher the achievable surface area of the MOF-derived carbon; moreover, the Zn metallic node can be easily removed during the carbonization process itself, without affecting the microporosity [155]. The first Zn-MOF investigated for the synthesis of nanoporous carbon was the well-known MOF-5, sometimes referred to as IRMOF-1 (isoreticular metal organic framework) [156]. Results obtained by this pioneering work were very encouraging, since a carbon structure exhibiting an A_{BET} of 2872 m^2/g and a V_T of 2.06 cm^3/g was synthesized by using both the MOF template and furfuryl alcohol as carbon precursors. As a result, a hydrogen uptake of 2.6 wt% was measured at 77 K and 0.1 MPa, a value twice as much as that obtained by using the pristine MOF-5. On the contrary, templated carbons produced from Cr-MOFs showed an A_{BET} significantly lower than the one exhibited by the pristine MOF. This reduction could be explained by the blocking of pores by chromium carbide and oxides produced during the carbonization. As a consequence, both A_{BET} and V_T, as well as the related hydrogen uptake, significantly decreased [155].

The ability of IRMOF-1 to produce suitable carbons for hydrogen storage was investigated in-depth, and a comparison was made with other MOF templates such as IRMOF-3 and IRMOF-8 [157, 158]. In one study, the aforementioned carbonized MOFs were synthesized by direct pyrolysis at 1173 K, without using any additional carbon precursor [157]. The resultant carbons showed a very high A_{BET}, hence a noticeable ultra-micropore volumes: the IRMOF-1-derived carbon exhibited an A_{BET} equal to 3174 m^2/g, higher than that obtained from IRMOF-3 and IRMOF-8 (1678 and 1978 m^2/g, respectively). Furthermore, a V_T of 4.06 cm^3/g was achieved with the IRMOF-1-derived carbon, being one of the highest values ever reported for a carbon material. Almost 16% of V_T involved pores narrower than 0.8 nm, meaning that the carbon exhibited a high ultra-microporosity, being beneficial in terms of hydrogen storage: in fact, a hydrogen uptake of 3.25 wt% was reached at 77 K and 0.1 MPa, surpassing the average values obtained with other benchmark materials. However, a hydrogen storage capacity of only 0.97 wt% was achieved by the IRMOF-1-derived carbon at room temperature and 10 MPa, which is lower than the capacities exhibited by several ACs, CNTs or CNFs. IRMOF-3 was used as template for the synthesis of nanoporous carbon using sucrose as a second precursor [158], with a resulting A_{BET} of 3120 m^2/g and a V_T of 1.93 cm^3/g, of which 98% comprised micropores. The measured hydrogen uptake was 2.45 wt% at 77 K and 0.1 MPa, and 5.1 wt% at 4 MPa and the same temperature. Moreover, it was shown that it is possible to control the porosity of the resultant carbon by varying the amount of additional carbon precursor, sucrose in that case.

Other MOFs structures such as zeolitic imidazolate frameworks (ZIFs) were used for the synthesis of nanoporous carbons. ZIFs have a zeolitic architecture with large pores but a very narrow pore aperture. Furthermore, several ZIFs comprise N-containing methylimidazole ligands which can ensure the doping of the carbon structure by nitrogen. Carbon structures with very attractive features were produced by impregnating ZIF-8 templates with furfuryl alcohol, followed by polymerization of the latter and carbonization [159]. A ZIF-derived carbon with an A_{BET} of 2169 m^2/g and a V_T of 1.50 cm^3/g was synthesized through a 1073 K carbonization process; the pore textures were further developed up to 3405 m^2/g and 2.58 cm^3/g, respectively, by performing carbonization at 1273 K. These enhanced textural features made the hydrogen storage capacity increase from 2.23 wt% to 2.77 wt% at 77 K and 0.1 MPa. A further KOH activation of the as-produced ZIF-8-derived carbon, synthesized at 1173K, led to even better performances. An outstanding hydrogen storage capacity of 6.2 wt% at 77 K and 2 MPa was achieved through gravimetric measurements, with a templated carbon exhibiting an A_{BET} equal to 3188 m^2/g and a pore volume

of 1.94 cm^3/g [160]. This hydrogen storage capacity is one of the highest reported so far for carbon materials. KOH activation was shown to be essential in order to increase the A_{BET} and especially the microporosity of the resultant carbon, giving in turn higher amounts of adsorbed hydrogen.

Further studies examined the possibility of carrying out a direct carbonization of ZIFs without using a second carbon precursor. Thus, ZIF-8, ZIF-68 and ZIF-69 were investigated [161]. Even if these three different frameworks have the same Zn-based metal node, ZIF-68 and ZIF-69 contain aromatic ring structures and hetero-linkers, which can affect the topology of the resultant carbon adsorbent. Furthermore, unlike ZIF-68, ZIF-69 exhibits chloride-based substituents on the benzimidazolate ligands. After performing a carbonization at 1273 K, the ZIF-8-derived carbon showed the highest A_{BET}, 822 m^2/g, compared to 472 m^2/g for the ZIF-68-derived carbon and to 586 m^2/g for the ZIF-69-derived carbon. The latter results evidenced that it is possible to control the A_{BET} of the resultant carbon by changing the functional group of the organic ligands. Even in that case, a further chemical activation was essential in order to enhance the porous carbon texture, allowing a 3-fold increase of the microporosity and the A_{BET}. For instance, for the ZIF-8-derived carbon, A_{BET} and V_T increased up to 2437 m^2/g and 1.266 cm^3/g, respectively, with a resultant hydrogen uptake equal to 2.59 wt% at 77 K and 0.1 MPa. Other experimental results gave hydrogen uptakes of 2.37 wt%, 2.15 wt% and 1.96 wt% measured at 77 K and 0.1 MPa with nanoporous carbons derived from ZIF-70, ZIF-68 and ZIF-69, respectively, by using furfuryl alcohol as second carbon precursor [162]. These data evidenced that similar hydrogen uptakes can be achieved by either: (i) performing a direct carbonization followed by a chemical activation of the ZIF-derived carbon; or (ii) carbonizing ZIFs impregnated with a second carbon precursor.

A study also showed the possibility of controlling the textural properties of ZIF-derived carbons by compressing them [163]. ZIF-8-derived carbons, synthesized by impregnation of the ZIF template with furfuryl alcohol followed by chemical activation with KOH, were compacted up to 370 MPa and 740 MPa. On the one hand, an improvement of the textural properties was achieved by compressing the carbons up to 370 MPa: A_{BET} increased from 3188 to 3323 m^2/g, whereas V_T increased from 1.94 to 2.32 cm^3/g. Furthermore, the most remarkable effect was the enhancement of the carbon microporosity, thus increasing the hydrogen storage capacity from 6.2 to 6.5 wt% at 77 K and 2 MPa. On the other hand, the compression up to 740 MPa had a negative effect, decreasing A_{BET} and V_T down to 1937 m^2/g and 1.11 cm^3/g, respectively. The microporosity was also reduced, with the consequent reduction of the hydrogen uptake, down to 5.7 wt%. Nevertheless, and provided that the pressure is not too high,

compression of ZIF-derived carbons was a good way to further increase their structural properties and, in turn, the hydrogen storage capacity.

Figure 9.7 shows hydrogen storage capacities obtained from templated carbons and MOFs-derived carbons reported during the past few years.

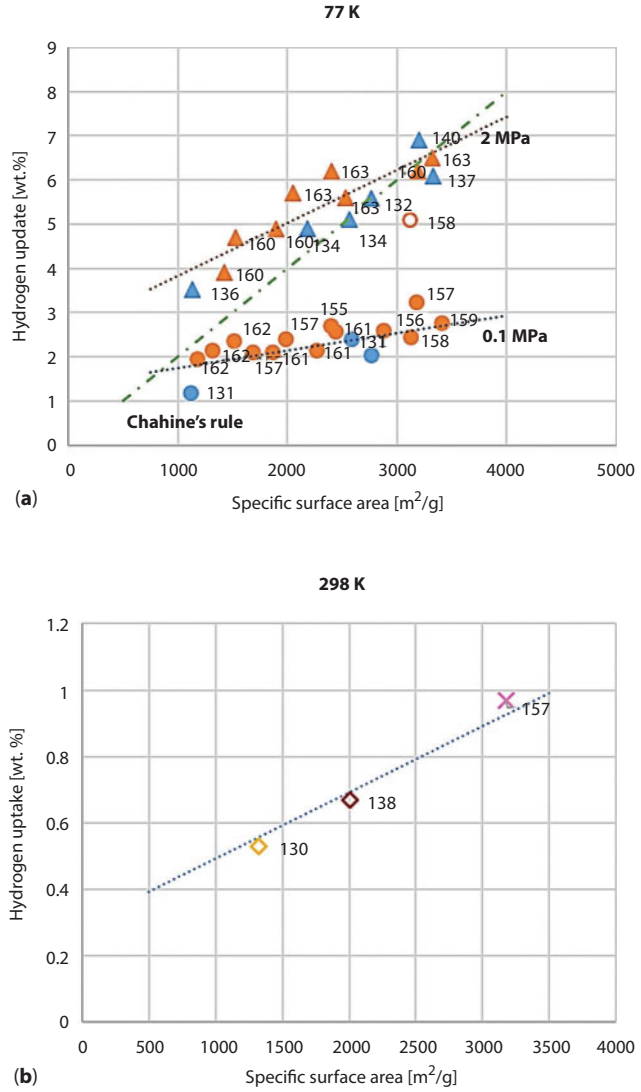

Figure 9.7 Hydrogen storage capacities of templated carbons and MOFs-derived carbons reported in recent works at: (a) 77 K, and (b) 298 K. The labels indicate the corresponding reference (• Zeolite-carbons 0.1 MPa, • MOF-carbons 0.1 MPa, ▲ Zeolite-carbons 2 MPa, ▲ MOF-carbons 2 MPa, ○ MOF-carbons 4 MPa, ◊ Silica-carbons 7-8 MPa, ◊ Silica-carbons 2 MPa, **X** MOF-carbons 10 MPa).

Figure 9.7a shows that hydrogen uptakes at both 0.1 MPa and 2 MPa follow a clear linear trend at 77 K, regardless of the precursor (zeolite or MOF). Furthermore, data at 2 MPa slightly agree with Chahine's rule. Obviously, the higher the pressure, the more the hydrogen uptake increases with the surface area. Figure 9.7b shows the low hydrogen adsorption uptake (< 1 wt%) of templated carbons and MOFs-derived carbons at 298 K compared to other carbon materials. Only a few data of hydrogen uptakes at 298 K were reported in the literature.

9.2.4 Other Carbon Materials

9.2.4.1 Carbide-Derived Carbons

Carbide-derived carbons are also promising materials for hydrogen storage. Carbide-derived carbons can be produced by removing metal ions from metallic carbides through chlorination, leading to carbonaceous structures with a very narrow pore size distribution (PSD). The advantages of using such materials are related to the possibility of tuning their textural properties by changing the chlorination temperature as well as the nature of the starting carbide. One of the first experimental works using carbide-derived carbons achieved a hydrogen uptake of 3.0 wt% at 77 K and 0.1 MPa [164]. Furthermore, an enhancement of the A_{BET}, as well as of the pore volume, can be achieved by physical or chemical activation of the carbide-derived carbon. Activation with carbon dioxide was an efficient way to enhance the microporosity [165]. Several combinations of activation temperature and dwell time were investigated [166], leading to carbon structures with A_{BET} up to 3000 m^2/g and excess hydrogen capacities up to 4.62 wt% at 77 K and 6 MPa. On the other hand, chemical activation of carbide-derived carbons with KOH also produced a significant enhancement of hydrogen storage capacity, leading to uptakes equal to 6.2 wt% at 77 K and 2 MPa (gravimetric measurement) [167]. These results highlight that carbide-derived carbons are not too far from zeolite- and MOFs-derived carbons in terms of hydrogen storage capacity [168].

9.2.4.2 Hybrid Carbon-MOF Materials

In addition to MOF carbonization as an effective way to produce carbon materials with an enhanced hydrogen storage capacity, MOFs can be used together with carbon-based materials such as ACs or zeolite-templated carbons (ZTCs), forming hybrid adsorbents with improved properties. An outstanding excess hydrogen uptake up to 13.5 wt% was reached at

77 K and 10 MPa by using a hybrid material prepared by introducing an activated carbon (NORIT-RB3) in the solution for the synthesis of MIL-101(Cr) [169]. The synthesis was carried out under mild conditions, avoiding the use of highly toxic reagents. An A_{BET} up to 3542 m^2/g and a V_T of 2.65 cm^3/g were reported, being among the highest values ever reached by a carbon material. These results clearly showed that the AC addition to a MOF structure can be beneficial for achieving an enhanced hydrogen storage capacity: in fact, by using the pristine MIL-101(Cr), an excess hydrogen capacity equal to 8.2 wt% was obtained under the same conditions. The hybrid adsorbent material MIL-101(Cr)/NORIT-RB3 was also tested for hydrogen storage at room temperature. In order to enhance the physisorption process, an aluminium-doped composite was produced by nanoconfining aluminium hydride (alane) into the hybrid material through a solution impregnation method [170]. On the one hand, the AC addition to the MOF increased the A_{BET} from 3148 to 3458 m^2/g and the hydrogen storage capacity from 0.55 to 0.69 wt% at 298 K and 10 MPa. On the other hand, the Al-doping allowed almost doubling the resultant hydrogen storage capacity from 0.69 to 1.2 wt% at room temperature and 10 MPa, even if both A_{BET} and V_T decreased in comparison to the non-doped sample.

Another hybrid material consisting of MIL-53(Cr) and a Pd-doped AC was investigated for hydrogen storage at room temperature [171]. The modification of the pristine MOF with the Pd-loaded AC resulted in the enhancement of the hydrogen uptake due to spillover, facilitating the dissociation of hydrogen molecules into atoms, followed by the migration of the latter into the MOF pores. Thus, an increase of absolute hydrogen adsorption from 0.46 to 0.80 wt% at 298 K and 6 MPa was obtained. Hybrid materials were produced by using both MIL-101(Cr)- and zeolite-templated carbons (ZTCs), exhibiting hydrogen uptakes up to 2.55 wt% at 77 K and 0.1 MPa [172]. The latter value is not too far from those commonly obtained by using only ZTCs, but is higher than that obtained by using the pristine MIL-101(Cr): 1.91 wt%.

A hydrogen storage of 0.32 wt% at 298 K and 2.65 MPa was achieved by using a hybrid material produced from natural halloysite and Al-based MOF [173]. The as-synthesized composite material was carbonized and doped with Pd nanoparticles in order to enhance both the microporosity and the spillover phenomenon, thus leading to a ternary compound designed for hydrogen adsorption. In fact, natural halloysite exhibits very high A_{BET} and porosity, well-suited for hydrogen storage, but not enough for being used alone. Hence, halloysites were investigated in combination with carbon nanotubes, as they display a cylindrical hollow tubular structure like CNTs. A hydrogen uptake as high as 0.48 wt% at room temperature

and 2.65 MPa was obtained, and even higher values, ranging from 0.50 to 0.63 wt% under the same conditions, were reached by doping the hybrid material with Pd nanoparticles [174].

9.2.4.3 Hyper-Cross-Linked Polymers–Derived Carbons

Carbon materials with high A_{BET} and well-developed microporosity were produced by carbonization of hyper-cross-linked polymers (HCPs). These materials consist of cheap cross-linked monomers exhibiting an enhanced porosity as well as a good stability. A one-step Friedel-Crafts alkylation between an external cross-linker, like formaldehyde dimethyl acetal (FDA), and several aromatic monomers is the cost-effective method nowadays adopted for the synthesis of such precursors [175]. Carbons produced by pyrolysis of HCPs synthesized from FDA and phenyltrimethylsilane are very good candidates for hydrogen storage [176]. Thus, a carbon material with an A_{BET} of 3101 m^2/g and a V_T of 1.84 cm^3/g was produced. After carbonization, the hydrogen uptake increased from 1.50 to 3.25 wt% at 77 K and 0.1 MPa. This outstanding improvement is attributed to the significant microporosity development due to carbonization, whose fraction increased from 37% to 76%.

Even better results were obtained by using benzene, thiophene and pyrrole as monomers of the HCP [177]. In particular, a pyrrole-derived carbon, chemically activated with KOH at 1073 K, led to an A_{BET} as high as 4334 m^2/g, a V_T of 3.14 cm^3/g, and a hydrogen uptake of 3.6 wt% at 77 K and 0.1 MPa. Good results were also reported for a benzene-HCP-derived carbon: a hydrogen storage up to 3 wt% at 77 K and 0.1 MPa was achieved with a carbon material exhibiting an A_{BET} of 3105 m^2/g and a V_T of 1.58 cm^3/g. The possibility of producing a countless number of HCPs simply by changing the starting monomers makes it likely that new carbon materials, with enhanced textural properties and hydrogen uptakes, will be produced.

9.2.4.4 Carbon Nanorods, Nanohorns and Nanospheres

In addition to carbon nanotubes and nanofibers, other carbon materials with a peculiar morphology can be synthesized, and might possibly be suitable for hydrogen storage, see Figure 9.8. Carbon nanorods are generally the by-product of carbon nanotubes preparation and separation, displaying an elongated shape ranging from 10 to 120 nm [178]. Alternatively, they can be directly produced through arc discharge between two graphite rods. Their shape, as well as their reduced dimension, makes possible the development of complex structures, for example by packing them with

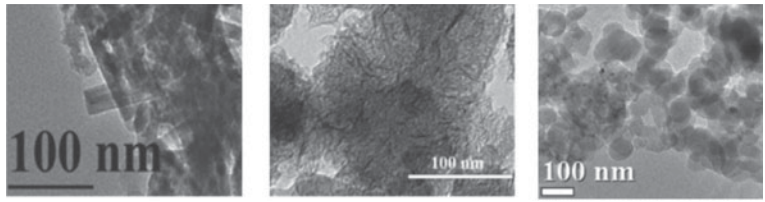

(**a**) (**b**) (**c**)

Figure 9.8 SEM images of: (a) carbon nanorods, (b) carbon nanohorns and (c) carbon nanospheres. (Adapted from (a) [179], (b) [185] and (c) [186] with permission of Elsevier).

different orientations of the tube axes, thus giving intersected structures. Hydrogen can be adsorbed especially at the points at which the single nanorods touch each other: a hydrogen storage capacity of 0.14 wt% was detected in carbon nanorods through TPR measurements, whose maximum peak was observed at 1148 K. [179].

Carbon nanohorns are other members belonging to the family of carbon nanomaterials, exhibiting a conical cap at one end, unlike CNTs. Nanohorns have typical lengths of 30–50 nm, with diameters ranging from 2 to 5 nm. Even if carbon nanohorns exhibit a developed porosity, several modifications were carried out in order to improve their textural properties. Oxidation allowed increasing their A_{BET}, whereas thermal treatment as well as metal doping enhanced the hydrogen uptake because of the spillover effect. Nevertheless, despite the additional treatments cited above, some studies reported hydrogen storage capacities below 0.20 wt% at room temperature and 2 MPa, leading to the conclusion that carbon nanohorns are not at all suitable for performing hydrogen storage [180].

Carbon nanospheres have also received great attention because of their high surface-to-volume ratio, good structural stability and large void space for encapsulating nanoparticles for doping [181, 182]. Starch-derived carbon nanospheres were investigated for hydrogen storage [183]. In order to enhance their A_{BET}, physical activation with CO_2 was carried out. This solution is environment-friendly, moreover, no chemical activation was performed, preventing the use of KOH. Despite that, remarkable results were obtained. Carbon spheres with A_{BET} as high as 3350 m^2/g and V_T of 1.75 cm^3/g were synthesized, reaching a hydrogen uptake of 6.4 wt% at 77 K and 2 MPa, measured by gravimetry. This value is comparable to the hydrogen uptakes commonly obtained with chemically activated ACs or with ZTCs. Good results were also obtained at higher temperature: a hydrogen storage capacity up to 0.51 wt% was achieved at 313 K and 3.5 MPa

by using carbon nanospheres doped with Pd nanoparticles [184]. From these results, it is clear that carbon nanospheres can be good candidates for hydrogen storage in the near future.

9.2.4.5 Carbon Nitrides

Graphitic carbon nitrides (g-C_3N_4) are bi-dimensional (graphene-like) carbonaceous materials, exhibiting light weight, developed porosity and high surface-to-volume ratios. These properties make them applicable to hydrogen storage. The hydrogen adsorption capacity of g-C_3N_4 was particularly enhanced when the latter was doped with metal nanoparticles. Furthermore, the clustering problem commonly occurring when performing decoration of graphene was prevented [187]. In this context, DFT calculations carried out on Li-decorated carbon nitride showed that each lithium atom can adsorb up to five hydrogen molecules, leading to a potential hydrogen uptake of 9.2 wt% [188]. Furthermore, graphitic carbon nitride nanosheets allowed an efficient electrocatalytic capture of molecular hydrogen [189]. Another advantage exhibited by carbon nitrides is that no templates were needed for obtaining materials with a highly porous network. For instance, hexamethylenetetramine was used as both carbon and nitrogen precursor, and ammonium chloride as blowing agent, to produce a foam-like material to be used for hydrogen storage [190]. The as-produced carbon nitride was then chemically activated by KOH, in order to enhance its textural properties. A carbonaceous material exhibiting an A_{BET} up to 1730 m^2/g and a V_T of 0.78 cm^3/g was obtained, able to ensure a hydrogen uptake up to 1.94 wt% at 77 K and 0.1 MPa. This value is still lower than those obtained for other carbon materials, but the simple, scalable and effective synthesis approach, based on a template-free procedure, might make graphitic carbon nitrides competitive with zeolite- or MOFs-derived carbons.

9.2.4.6 Carbon Aerogels

A new emerging class of carbon materials proven to ensure good hydrogen uptakes is represented by carbon aerogels [191–193]. Carbon aerogels have received great attention because of their advanced textural properties, exhibiting an enhanced ultra-microporosity ideal for hydrogen storage. Conventionally, carbon aerogels are obtained by carbonizing, at temperatures above 873 K, resorcinol-formaldehyde aerogels, themselves obtained by supercritical CO_2 drying of resorcinol-formaldehyde hydrogels. The liquid inside is exchanged by an organic solvent, itself replaced by gas to leave

intact the solid nanostructure, without pore collapse [194]. A hydrogen storage capacity up to 5.65 wt% at 77 K and 2.2 MPa was reached by a carbon aerogel having an A_{BET} of only 379 m^2/g and a V_T of 0.209 cm^3/g [193]. The micropore fraction of such material was 88% of the whole total porosity, explaining in part the high hydrogen uptake achieved. Furthermore, it is believed that pores with a very small size could not be detected at all because of the limit of nitrogen adsorption, leading to the conclusion that a higher ultra-microporosity might be involved. It is even likely that in such materials hydrogen adsorption may occur through a volume process, which may lead to condensation rather than to a surface coverage mechanism. The high microporosity was also confirmed by the decrease of performances obtained at room temperatures after Pt doping: because of the pore blocking due to metal nanoparticles, a decrease of hydrogen uptake of more than 30% was in fact observed.

9.2.4.7 Other Exotic Carbon Materials

Investigations of hydrogen storage in carbon materials have also been carried out with unconventional precursors, sometimes leading to noteworthy results. Graphenylene, a 2D-sp^2 carbon membrane, might thus be a promising material for hydrogen storage if functionalized with alkali and alkaline-earth metals. DFT calculations showed that a maximum of 20 molecules of hydrogen can be adsorbed on a graphenylene sheet functionalized with metal nanoparticles of Li, Na, K, Mg and Ca, leading to potential storage hydrogen capacities ranging from 4.9 to 6.14 wt% [195].

A remarkable hydrogen adsorption potential has been exhibited by nanocomposite materials consisting of mesoporous carbons and TiO_2. Nanometric carbon CMK-3 modified with TiO_2 in anatase form showed a hydrogen uptake as high as 2.9 wt% at 77 K and 1 MPa, with an A_{BET} of 706 m^2/g and a V_T of 0.69 cm^3/g [196]. The textural properties of the nanocomposite material were lower than those exhibited by the pristine CMK-3, having A_{BET} of 1323 m^2/g and V_T of 1.01 cm^3/g, but despite that, the achieved hydrogen uptake was increased by 30%. The combination TiO_2 anatase–CMK-3 allowed hydrogen molecules to spill over onto the carbon micropores and get adsorbed on anatase clusters. The presence of anatase clusters in CMK-3 promoted the formation of a localized distribution of electrons at the surface of TiO2-CMK-3 composite, thereby facilitating hydrogen adsorption.

Other noteworthy hydrogen uptakes came from carbons obtained by cyclotrimerization of aromatic tetranitriles [197]. Cyclotrimerization of nitriles in zinc chloride at 673 K produced polymers with high

microporosity. The hydrogen adsorption capacities increased after carbonization at temperatures higher than 873 K, even if the mesoporosity also increased concurrently [198]. A hydrogen uptake up to 2.34 wt% at 77 K and 0.1 MPa was achieved on a carbon material exhibiting A_{BET} of 1250 m^2/g and V_T of 1.45 cm^3/g [197].

Figure 9.9 shows hydrogen uptakes of various exotic carbon materials obtained until now. Figure 9.9a shows trends between A_{BET} and hydrogen uptake at 0.1 or 1 MPa and 77K, regardless of the nature of the materials. A value of around 6 wt% was obtained for carbon nanospheres and carbon aerogels at 2 MPa. The hydrogen uptake of carbon aerogel is worth mentioning as it was reached with a material having a low A_{BET} (193 m^2/g). However, the very narrow pores in such carbon aerogel make difficult the accurate measurement of A_{BET}, which might be undervalued. An outstanding hydrogen excess uptake of 13 wt% reached by the hybrid material MIL-101(Cr)/NORIT-RB3 [169] is among the highest ever reached for a carbon material. The authors justified so high a value by the introduction of AC into the MOF structure, which significantly influenced the crystallite sizes and the overall morphology. As a result, a highly defective material was obtained, exhibiting very high A_{BET} and pore volume. However, this result is highly doubtful and could never be reproduced, and hence it was not included in Figure 9.9a. Figure 9.9b shows that hydrogen adsorption capacities below 1 wt% were achieved at 298 K.

9.3 Conclusion

Nanotextured carbon materials are potentially suitable adsorbents for hydrogen storage, especially at low temperature. All the data commented on in this review have been gathered as supplementary information in the tables shown in the Appendix of this chapter, where the details about precursors, surface areas, pore volumes, hydrogen storage capacities and measurement methods are given. As can be seen, many published papers did not specify whether the uptakes were excess, absolute or total, but we tried to deduce this information as much as we could in this paper. Most of the time, and regardless of the nature of the carbon, a clear linear trend between the A_{BET} and the hydrogen uptake was found at 77 K. Another usual finding is that, at a fixed A_{BET}, higher hydrogen uptake was measured at 4 MPa than at 0.1 MPa.

Only a few exceptions do not follow this trend, due to either unconventional materials like exfoliated carbon nanofibers and hyper-cross-linked polymers-derived carbons, or to the underestimation of A_{BET} because of the

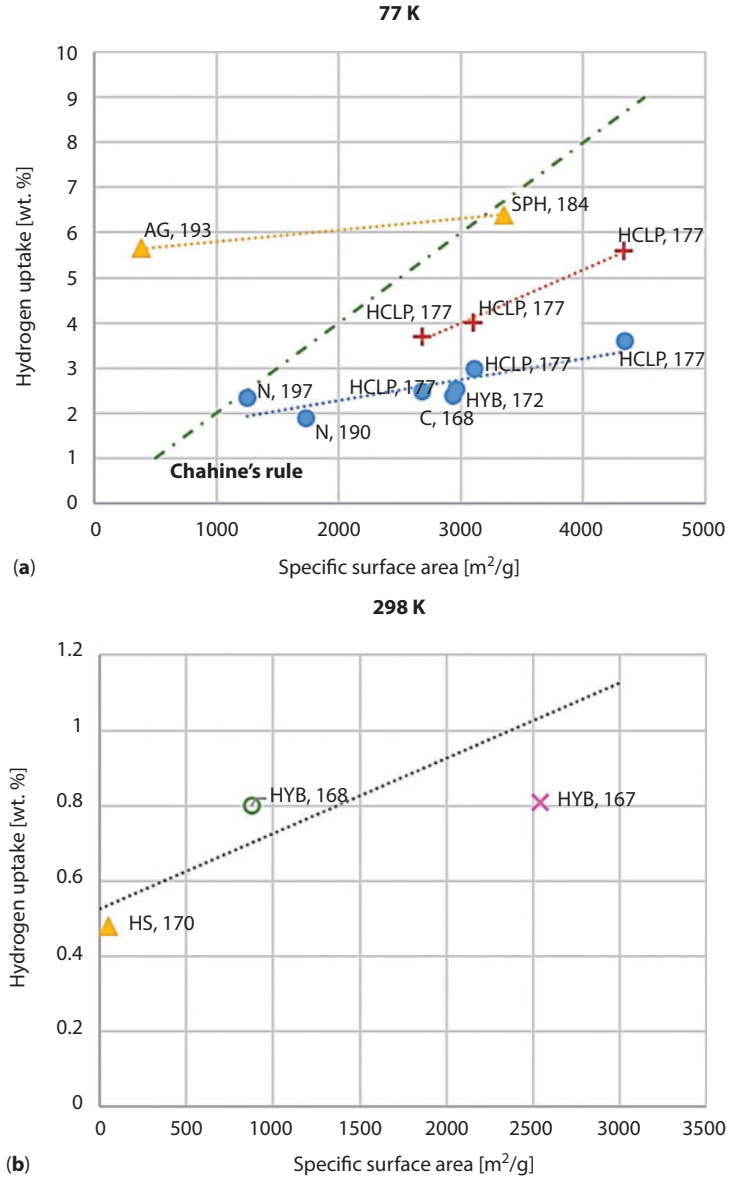

Figure 9.9 Hydrogen storage capacities on exotic carbons reported by recent works at: (a) 77 K, and (b) 298 K. The labels indicate both the typology of carbon (C=carbides; HYB=hybrid carbons; HCLP=hyper-cross-linked polymers-derived carbons; N=carbon nitrides; SPH=carbon nanospheres; AG=carbon aerogels) and the corresponding references (• 0.1 MPa, + 1 MPa, ▲2 MPa, **O** 6 MPa, × 10 MPa).

limitation of nitrogen as probe molecule for characterizing carbonaceous materials having very narrow pores. Discarding all irreproducible data that have been reported in the literature, a maximum hydrogen uptake of 7 wt% was achieved. As one may expect, the hydrogen uptake strictly depends on the textural properties of the carbons at 77 K. On the other hand, hydrogen uptake values of 1 wt%, on average, were found at 298 K for different carbon sorbents. Graphene appeared to be an exception, ensuring hydrogen uptakes even higher than 2 wt% at room temperature and moderate pressures.

Acknowledgments

This study was partly supported by the French PIA project "Lorraine Université d'Excellence," reference ANR-15-IDEX-04-LUE.

References

1. Sircar, S., Golden, T.C., Rao, M.B., Activated carbon for gas separation and storage. *Carbon* 34(1), 1–12, 1996.
2. Züttel, A., Hydrogen storage methods. *Naturwissenschaften* 91(4), 157–172, 2004.
3. de la Casa-Lillo, M.A., Lamari-Darkrim, F., Cazorla-Amorós, D., Linares-Solano, A., Hydrogen storage in activated carbons and activated carbon fibers. *J. Phys. Chem. B* 106(42), 10930–10934, 2002.
4. Fierro, V., Zhao, W., Izquierdo, M.T., Aylon, E., Celzard, A., Adsorption and compression contributions to hydrogen storage in activated anthracites. *Int. J. Hydrog. Energy* 35(17), 9038–9045, 2010.
5. Berry, G.D., Aceves, S.M., Onboard storage alternatives for hydrogen vehicles. *Energy Fuels* 12(1), 49–55, 1998.
6. Noh, J.S., Agarwal, R.K., Schwarz, J.A., Hydrogen storage systems using activated carbon. *Int. J. Hydrog. Energy* 12(10), 693–700, 1987.
7. Titirici, M.-M., *et al.*, Sustainable carbon materials. *Chem. Soc. Rev.* 44(1), 250–290, 2014.
8. Kojima, Y., *et al.*, Hydrogen adsorption and desorption by carbon materials. *J. Alloys Compd.* 421(1), 204–208, 2006.
9. Thommes, M., Cychosz, K.A., Physical adsorption characterization of nanoporous materials: Progress and challenges. *Adsorption* 20(2–3), 233–250, 2014.
10. Kayiran, S.B., Lamari, F.D., Levesque, D., Adsorption Properties and structural characterization of activated carbons and nanocarbons. *J. Phys. Chem. B* 108(39), 15211–15215, 2004.

11. Bhatia, S.K., Myers, A.L., Optimum conditions for adsorptive storage. *Langmuir* 22(4), 1688–1700, 2006.
12. Züttel, A., Materials for hydrogen storage. *Mater. Today* 6(9), 24–33, 2003.
13. Panella, B., Hirscher, M., Roth, S., Hydrogen adsorption in different carbon nanostructures. *Carbon* 43(10), 2209–2214, 2005.
14. Newns, D.M., Self-consistent model of hydrogen chemisorption. *Phys. Rev.* 178(3), 1123–1135, 1969.
15. Geusic, M.E., Morse, M.D., Smalley, R.E., Hydrogen chemisorption on transition metal clusters. *J. Chem. Phys.* 82(1), 590–591, 1985.
16. Challet, S., Azaïs, P., Pellenq, R.J.-M., Isnard, O., Soubeyroux, J.-L., Duclaux, L., Hydrogen adsorption in microporous alkali-doped carbons (activated carbon and single wall nanotubes). *J. Phys. Chem. Solids* 65(2), 541–544, 2004.
17. Bulyarskiy, S., Saurov, A. (Eds.), *Doping of Carbon Nanotubes*, Springer, 2017.
18. Cheng, H.-M., Yang, Q.-H., Liu, C., Hydrogen storage in carbon nanotubes. *Carbon* 39(10), 1447–1454, 2001.
19. Fierro, V., Bosch, G., Siperstein, F.R., Pore size distribution in microporous carbons obtained from molecular modeling and density functional theory. *Stud. Surf. Sci. Catal.* 160, 519–526, 2007.
20. Sing, K.S.W., *et al.*, Reporting physisorption data for gas/solid systems with special reference to the determination of surface area and porosity. *Pure Appl. Chem.* 57(4), 603–619, 2009.
21. Wang, Q., Johnson, J.K., Molecular simulation of hydrogen adsorption in single-walled carbon nanotubes and idealized carbon slit pores. *J. Chem. Phys.* 110(1), 577–586, 1998.
22. Jagiello, J., Thommes, M., Linares-Solano, A., Cazorla-Amorós, D., Lozano-Castelló, D., *Characterization of Carbon Micro and Ultramicropores Using Adsorption of Hydrogen and Other Simple Gases*, vol. 4. 2004.
23. Ohta, T. (Ed.), *Energy Carriers and Conversion Systems with Emphasis on Hydrogen*, vol. 2, EOLSS Publications, 2009.
24. Rzepka, M., Lamp, P., de la Casa-Lillo, M.A., Physisorption of hydrogen on microporous carbon and carbon nanotubes, *J. Phys. Chem. B* 102(52), 10894–10898, 1998.
25. Gadiou, R., Saadallah, S., Piquero, T., David, P., Parmentier, J., Vix-Guterl, C., The influence of textural properties on the adsorption of hydrogen on ordered nanostructured carbons. *Mic. Mes. Mater.* 79, 121–128, 2005.
26. Poirier, E., Chahine, R., Bose, T.K., Hydrogen adsorption in carbon nanostructures. *Int. J. Hydrog. Energy* 26(8), 831–835, 2001.
27. Brunauer, S., Emmett, P.H., Teller, E., Adsorption of gases in multimolecular layers. *J. Am. Chem. Soc.* 60(2), 309–319, 1938.
28. Walton, K.S., Snurr, R.Q., Applicability of the BET method for determining surface areas of microporous metal–organic frameworks. *J. Am. Chem. Soc.* 129(27), 8552–8556, 2007.
29. Adamson, A.W., Gast, A.P., *Physical Chemistry of Surfaces,* 6th ed., Wiley, 1997.

30. Olivier, J.P., The surface heterogeneity of carbon and its assessment, in: *Adsorption by Carbons*, Bottani, E., Tascón, J. (Ed.), 7, pp. 147–166, Amsterdam: Elsevier, 2008,.
31. Zhao, D., Wan, Y., Zhou, W., *Ordered Mesoporous Materials*, John Wiley & Sons, 2012.
32. Lozano-Castelló, D., Cazorla-Amorós, D., Linares-Solano, A., Usefulness of CO_2 adsorption at 273 K for the characterization of porous carbons. *Carbon* 42(7), 1233–1242, 2004.
33. Jagiello, J., Olivier, J.P., 2D-NLDFT adsorption models for carbon slit-shaped pores with surface energetical heterogeneity and geometrical corrugation. *Carbon* 55(Suppl C), 70–80, 2013.
34. Voskuilen, T., Zheng, Y., Pourpoint, T., Development of a Sievert apparatus for characterization of high pressure hydrogen sorption materials. *Int. J. Hydrog. Energy* 35(19), 10387–10395, 2010.
35. Blackman, J.M., Patrick, J.W., Snape, C.E., An accurate volumetric differential pressure method for the determination of hydrogen storage capacity at high pressures in carbon materials. *Carbon* 44(5), 918–927, 2006.
36. Belmabkhout, Y., Frère, M., and Weireld, G.D., High-pressure adsorption measurements. A comparative study of the volumetric and gravimetric methods. *Meas. Sci. Technol.* 15(5), 848, 2004.
37. Dreisbach, F., Seif A.H., R., Lösch, H.W., Gravimetric measurement of adsorption equilibria of gas mixture CO/H2 with a magnetic suspension balance. *Chem. Eng. Technol.* 25(11), 1060–1065, 2002.
38. Poirier, E., Chahine, R., Tessier, A., Bose, T.K., Gravimetric and volumetric approaches adapted for hydrogen sorption measurements with *in situ* conditioning on small sorbent samples. *Rev. Sci. Instrum.* 76(5), 055101, 2005.
39. Tascón, J.M.D. (Ed.), *Novel Carbon Adsorbents*, Elsevier, 2012.
40. Rakić V., Damjanović, L., Temperature-programmed desorption (TPD) methods, in: *Calorimetry and Thermal Methods in Catalysis*, Auroux, A. (Ed.), pp. 131–174, Springer: Berlin Heidelberg, 2013.
41. Miller, J.T., Meyers, B.L., Modica, F.S., Lane, G.S., Vaarkamp, M., Koningsberger, D.C., Hydrogen temperature-programmed desorption (H2 TPD) of supported platinum catalysts. *J. Catal.* 143(2), 395–408, 1993.
42. Bénard, P., Chahine, R., Storage of hydrogen by physisorption on carbon and nanostructured materials. *Scr. Mater.* 56(10), 803–808, 2007.
43. Dreisbach, F., Lösch, H.W., Harting, P., Highest pressure adsorption equilibria data: measurement with magnetic suspension balance and analysis with a new adsorbent/adsorbate-volume. *Adsorption* 8(2), 95–109, 2002.
44. Richard, M.-A., Benard, P., Chahine, R., Gas adsorption process in activated carbon over a wide temperature range above the critical point. Part 1: modified Dubinin-Astakhov model. *Adsorpt. - J. Int. Adsorpt. Soc.* 15(1), 43–51, 2009.
45. Richard, M.-A., Benard, P., Chahine, R., Gas adsorption process in activated carbon over a wide temperature range above the critical point. Part 2: conservation of mass and energy. *Adsorpt. - J. Int. Adsorpt. Soc.* 15(1), 53–63, 2009.

46. Farrusseng, D. (Ed.), *Metal-Organic Frameworks: Applications from Catalysis to Gas Storage*, John Wiley & Sons, 2011.
47. Hirscher, M. (Ed.), *Handbook of Hydrogen Storage: New Materials for Future Energy Storage*, John Wiley & Sons, 2010.
48. Vivo-Vilches, J.F., *et al.*, Biogas upgrading by selective adsorption onto CO2 activated carbon from wood pellets. *J. Environ. Chem. Eng.* 5(2), 1386–1393, 2017.
49. Yahya, M.A., Al-Qodah, Z., Ngah, C.W.Z., Agricultural bio-waste materials as potential sustainable precursors used for activated carbon production: A review. *Renew. Sustain. Energy Rev.* 46, 218–235, 2015.
50. Loloie, Z., Mozaffarian, M., Soleimani, M., Asassian, N., Carbonization and CO2 activation of scrap tires: Optimization of specific surface area by the Taguchi method. *Korean J. Chem. Eng.* 2(34), 366–375, 2016.
51. Duranoğlu, D., Beker, Ü., Steam and KOH activated carbons from peach stones. *Energy Sourc. A, Recovery Util. Environ. Effects* 34(11), 1004–1015, 2012.
52. Williams P.T., Reed, A.R., Development of activated carbon pore structure via physical and chemical activation of biomass fibre waste. *Biomass Bioenergy* 30(2), 144–152, 2006.
53. Ahmadpour, A., Do, D.D., The preparation of active carbons from coal by chemical and physical activation. *Carbon* 34(4), 471–479, 1996.
54. Schaefer, S., Fierro, V., Izquierdo, M.T., Celzard, A., Assessment of hydrogen storage in activated carbons produced from hydrothermally treated organic materials. *Int. J. Hydrog. Energy* 41(28), 12146–12156, 2016.
55. Sevilla, M., Fuertes, A.B., Mokaya, R., High density hydrogen storage in superactivated carbons from hydrothermally carbonized renewable organic materials. *Energy Environ. Sci.* 4(4), 1400–1410, 2011.
56. Fierro, V., *et al.*, Experimental evidence of an upper limit for hydrogen storage at 77 K on activated carbons. *Carbon* 48(7), 1902–1911, 2010.
57. Wang, H., Gao, Q., Hu, J., High hydrogen storage capacity of porous carbons prepared by using activated carbon. *J. Am. Chem. Soc.* 131(20), 7016–7022, 2009.
58. Melouki, R., Llewellyn, P.L., Tazibet, S., Boucheffa, Y., Hydrogen adsorption on activated carbons prepared from olive waste: effect of activation conditions on uptakes and adsorption energies. *J. Porous Mater.* 24(1), 1–11, 2017.
59. Bader, N., Ouederni, A., Optimization of biomass-based carbon materials for hydrogen storage. *J. Energy Storage* 5, 77–84, 2016.
60. Zhao, W., Luo, L., Wang, H., Fan, M., Synthesis of bamboo-based activated carbons with super-high specific surface area for hydrogen storage. *BioResources* 12(1), 1246–1262, 2017.
61. Ramesh, T., Rajalakshmi, N., Dhathathreyan, K.S., Activated carbons derived from tamarind seeds for hydrogen storage. *J. Energy Storage* 4, 89–95, 2015.

62. Zhao, W., *et al.*, Activated carbons doped with Pd nanoparticles for hydrogen storage. *Int. J. Hydrog. Energy* 37(6), 5072–5080, 2012.
63. Zhao, W., Fierro, V., Fernández-Huerta, N., Izquierdo, M.T., Celzard, A., Hydrogen uptake of high surface area-activated carbons doped with nitrogen. *Int. J. Hydrog. Energy* 38(25), 10453–10460, 2013.
64. Kopac, T., Kırca, Y., Toprak, A., Synthesis and characterization of KOH/boron modified activated carbons from coal and their hydrogen sorption characteristics. *Int. J. Hydrog. Energy*. 42(37), 23606–23616, 2017.
65. Cheng, H., Chen, L., Cooper, A.C., Sha, X., Pez, G.P., Hydrogen spillover in the context of hydrogen storage using solid-state materials. *Energy Environ. Sci.* 1(3), 338–354, 2008.
66. Pyle, D.S., Gray, E.M., Webb, C.J., Hydrogen storage in carbon nanostructures via spillover. *Int. J. Hydrog. Energy* 41(42), 19098–19113, 2016.
67. Wang, L., Yang, R.T., Hydrogen storage properties of carbons doped with ruthenium, platinum, and nickel nanoparticles. *J. Phys. Chem. C* 112(32), 12486–12494, 2008.
68. Schaefer, S., Fierro, V., Szczurek, A., Izquierdo, M.T., Celzard, A., Physisorption, chemisorption and spill-over contributions to hydrogen storage. *Int. J. Hydrog. Energy* 41(39), 17442–17452, 2016.
69. Ye, M., Zhang, Z., Zhao, Y., Qu, L., Graphene platforms for smart energy generation and storage. *Joule* 2(2), 245–268, 2018.
70. Ren, H., Cui, C., Li, X., Liu, Y., A DFT study of the hydrogen storage potentials and properties of Na- and Li-doped fullerenes. *Int. J. Hydrog. Energy* 42(1), 312–321, 2017.
71. Luo, Z., Fan, X., Pan, R., An, Y., A first-principles study of Sc-decorated graphene with pyridinic-N defects for hydrogen storage. *Int. J. Hydrog. Energy* 42(5), 3106–3113, 2017.
72. Zhai, W., Srikanth, N., Kong, L.B., Zhou, K., Carbon nanomaterials in tribology. *Carbon* 119, 150–171, 2017.
73. Granja-DelRio, A., Alonso, J.A., Lopez, M.J., Competition between palladium clusters and hydrogen to saturate graphene vacancies. *J. Phys. Chem. C* 121(20), 10843–10850, 2017.
74. Jahromi, M.P., Moradi, S.E., Nasrollahpour, A., Moradi, S.M.J., FePt/reduced graphene oxide composites for high capacity hydrogen storage. *Fuller. Nanotub. Carbon Nanostructures* 25(5), 295–300, 2017.
75. Szczesniak, B., Choma, J., Jaroniec, M., Gas adsorption properties of graphene-based materials. *Adv. Colloid Interface Sci.* 243, 46–59, 2017.
76. Faye, O., Szpunar, J.A., Szpunar, B., Beye, A.C., Hydrogen adsorption and storage on Palladium-functionalized graphene with NH-dopant: A first principles calculation. *Appl. Surf. Sci.* 392, 362–374, 2017.
77. Darkrim Lamari, F., Levesque, D., Hydrogen adsorption on functionalized graphene. *Carbon* 49(15), 5196–5200, 2011.
78. Shiraz, H.G., Tavakoli, O., Investigation of graphene-based systems for hydrogen storage. *Renew. Sustain. Energy Rev.* 74, 104–109, 2017.

79. Elyassi, M., Rashidi, A., Hantehzadeha, M.R., Elahia, S.M., Preparation of different graphene nanostructures for hydrogen adsorption. *Surf. Interface Anal.* 49(4), 230–237, 2017.
80. Tascón, J.M.D., Overview of carbon materials in relation to adsorption, in: *Adsorption by Carbons*, Bottani E., Tascón, J. (Eds.), chap. 2, pp. 15–49, Amsterdam: Elsevier, 2008.
81. Javan, M.B., Shirdel-Havar, A.H., Soltani, A., Pourarian, F., Adsorption and dissociation of H-2 on Pd doped graphene-like SiC sheet. *Int. J. Hydrog. Energy* 41(48), 22886–22898, 2016.
82. Bénard, P., *et al.*, Comparison of hydrogen adsorption on nanoporous materials. *J. Alloys Compd.* 446, 380–384, 2007.
83. Tozzini, V., Pellegrini, V., Prospects for hydrogen storage in graphene. *Phys. Chem. Chem. Phys.* 15(1), 80–89, 2012.
84. Ariharan, A., Viswanathan, B., Nandhakumar, V., Nitrogen doped graphene as potential material for hydrogen storage. *Graphene* 06(02), 41, 2017.
85. Klechikov, A., Sun, J., Hu, G., Zheng, M., Wågberg, T., Talyzin, A.V., Graphene decorated with metal nanoparticles: Hydrogen sorption and related artefacts. *Microporous Mesoporous Mater.* 250, 27–34, 2017.
86. Ramos-Castillo, C.M., Reveles, J.U., Cifuentes-Quintal, M.E., Zope, R.R., de Coss, R., Ti-4- and Ni-4-doped defective graphene nanoplatelets as efficient materials for hydrogen storage," *J. Phys. Chem. C* 120(9), 5001–5009, 2016.
87. Klechikov, A., Mercier, G., Sharifi, T., Baburin, I.A., Seifert, G., Talyzin, A.V., Hydrogen storage in high surface area graphene scaffolds. *Chem. Commun.* 51(83), 15280–15283, 2015.
88. Yuan, W., Li, B., Li, L., A green synthetic approach to graphene nanosheets for hydrogen adsorption. *Appl. Surf. Sci.* 257(23), 10183–10187, 2011.
89. Zhou, C., Szpunar, J.A., Hydrogen storage performance in Pd/graphene nanocomposites. *ACS Appl. Mater. Interfaces* 8(39), 25933–25940, 2016.
90. Ströbel, R., Garche, J., Moseley, P.T., Jörissen, L., Wolf, G., Hydrogen storage by carbon materials. *J. Power Sources* 159(2), 781–801, 2006.
91. Yoon, M., Yang, S., Wang, E., Zhang, Z., Charged fullerenes as high-capacity hydrogen storage media. *Nano Lett.* 7(9), 2578–2583, 2007.
92. Pupysheva, O.V., Farajian, A.A., Yakobson, B.I., Fullerene nanocage capacity for hydrogen storage. *Nano Lett.* 8(3), 767–774, 2008.
93. Liu, P., Zhang, H., Cheng, X., Tang, Y., Transition metal atom Fe, Co, Ni decorated B38 fullerene: Potential material for hydrogen storage. *Int. J. Hydrog. Energy* 42(22), 15256–15261, 2017.
94. Kaiser, A., *et al.*, On enhanced hydrogen adsorption on alkali (cesium) doped C60 and effects of the quantum nature of the H2 molecule on physisorption energies. *Int. J. Hydrog. Energy* 42(5), 3078–3086, 2017.
95. Liu, P., Zhang, H., Cheng, X., Tang, Y., Ti-decorated B38 fullerene: A high capacity hydrogen storage material. *Int. J. Hydrog. Energy* 41(42), 19123–19128, 2016.

96. Tang, C., Zhang, X., The hydrogen storage capacity of Sc atoms decorated porous boron fullerene B40: A DFT study. *Int. J. Hydrog. Energy* 41(38), 16992–16999, 2016.
97. Darkrim, F.L., Malbrunot, P., Tartaglia, G.P., Review of hydrogen storage by adsorption in carbon nanotubes. *Int. J. Hydrog. Energy* 27(2), 193–202, 2002.
98. Dillon, A.C., Jones, K.M., Bekkedahl, T.A., Kiang, C.H., Bethune, D.S., Heben, M.J., Storage of hydrogen in single-walled carbon nanotubes. *Nature* 386(6623), 377–379, 1997.
99. Chen, P., Wu, X., Lin, J., Tan, K.L., High H2 uptake by alkali-doped carbon nanotubes under ambient pressure and moderate temperatures. *Science* 285(5424), 91–93, 1999.
100. Yang, R.T., Hydrogen storage by alkali-doped carbon nanotubes-revisited. *Carbon* 38(4), 623–626, 2000.
101. Yürüm, Y., Taralp, A., Veziroglu, T.N., Storage of hydrogen in nanostructured carbon materials. *Int. J. Hydrog. Energy* 34(9), 3784–3798, 2009.
102. Rather, S.U., Trimetallic catalyst synthesized multi-walled carbon nanotubes and their application for hydrogen storage. *Korean J. Chem. Eng.* 33(5), 1551–1556, 2016.
103. Cassell, A.M., Raymakers, J.A., Kong, J., Dai, H., Large scale CVD synthesis of single-walled carbon nanotubes. *J. Phys. Chem. B* 103(31), 6484–6492, 1999.
104. Zhao, T., Ji, X., Jin, W., Yang, W., Li, T., Hydrogen storage capacity of single-walled carbon nanotube prepared by a modified arc discharge. *Fuller. Nanotub. Carbon Nanostructures* 25(6), 355–358, 2017.
105. Liu, C., Chen, Y., Wu, C.-Z., Xu, S.-T., Cheng, H.-M., Hydrogen storage in carbon nanotubes revisited. *Carbon* 48(2), 452–455, 2010.
106. Ghosh, S., Padmanabhan, V., Hydrogen storage capacity of bundles of single-walled carbon nanotubes with defects. *Int. J. Energy Res.* 41(8), 1108–1117, 2017.
107. Saito, Y., Yoshikawa, T., Bandow, S., Tomita, M., Hayashi, T., Interlayer spacings in carbon nanotubes. *Phys. Rev. B* 48(3), 1907–1909, 1993.
108. Wan, Q., *et al.*, Toward the development of versatile functionalized carbon nanotubes. *RSC Adv.* 5(48), 38316–38323, 2015.
109. Sharma, A., Dasgupta, K., Banerjee, S., Patwardhan, A., Srivastava, D., Joshi, J.B., *In-situ* nitrogen doping in carbon nanotubes using a fluidized bed reactor and hydrogen storage behavior of the doped nanotubes. *Int. J. Hydrog. Energy* 42(15), 10047–10056, 2017.
110. Konni, M., Dadhich, A.S., Babu Mukkamala, S., Impact of surface modifications on hydrogen uptake by Fe@f-MWCNTs and Cu@f-MWCNTs at non-cryogenic temperatures. *Int. J. Hydrog. Energy* 42(2), 953–959, 2017.
111. Elyassi, M., Rashidi, A., Hantehzadeh, M.R., Elahi, S.M., Hydrogen storage behaviors by adsorption on multi-walled carbon nanotubes. *J. Inorg. Organomet. Polym. Mater.*, 27(1), 285–295, 2017.

112. Rather, S.U., Hwang, S.-W., Comparative hydrogen uptake study on titanium-MWCNTs composite prepared by two different methods. *Int. J. Hydrog. Energy* 41(40), 18114–18120, 2016.
113. Han, Y.-J., Park, S.-J., Influence of nickel nanoparticles on hydrogen storage behaviors of MWCNTs. *Appl. Surf. Sci.* 415, 85–89, 2017.
114. Rather, S., Mehraj-ud-din, N., Zacharia, R., Hwang, S.W., Kim, A.R., Nahm, K.S., Hydrogen storage of nanostructured TiO2-impregnated carbon nanotubes. *Int. J. Hydrog. Energy* 34(2), 961–966, 2009.
115. Rather, S.U., Hydrogen uptake of cobalt and copper oxide-multiwalled carbon nanotube composites. *Int. J. Hydrog. Energy* 42(16), 11553–11559, 2017.
116. Jong, K.P.D., Geus, J.W., Carbon nanofibers: catalytic synthesis and applications. *Catal. Rev.* 42(4), 481–510, 2000.
117. Chambers, A., Park, C., Baker, R.T.K., Rodriguez, N.M., Hydrogen storage in graphite nanofibers. *J. Phys. Chem. B* 102(22), 4253–4256, 1998.
118. Rzepka, M., *et al.*, Hydrogen storage capacity of catalytically grown carbon nanofibers. *J. Phys. Chem. B* 109(31), 14979–14989, 2005.
119. Hwang, J.Y., Lee, S.H., Sim, K.S., Kim, J.W., Synthesis and hydrogen storage of carbon nanofibers. *Synth. Met.* 126(1), 81–85, 2002.
120. Jaybhaye, S., Sharon, M., Sharon, M., Sathiyamoorthy, D., Dasgupta, K., Semiconducting carbon nanofibers and hydrogen storage. *Synth. React. Inorg. Met.-Org. Nano-Met. Chem.* 37(6), 473–476, 2007.
121. Kim, B.-J., Lee, Y.-S., Park, S.-J., A study on the hydrogen storage capacity of Ni-plated porous carbon nanofibers. *Int. J. Hydrog. Energy* 33(15), 4112–4115, 2008.
122. Yadav, A., Faisal, M., Subramaniam, A., Verma, N., Nickel nanoparticle-doped and steam-modified multiscale structure of carbon micro-nanofibers for hydrogen storage: Effects of metal, surface texture and operating conditions. *Int. J. Hydrog. Energy* 42(9), 6104–6117, 2017.
123. Wu, H.-C., Li, Y.-Y., Sakoda, A., Synthesis and hydrogen storage capacity of exfoliated turbostratic carbon nanofibers. *Int. J. Hydrog. Energy* 35(9), 4123–4130, 2010.
124. Hwang, S.-H., Choi, W.M., Lim, S.K., Hydrogen storage characteristics of carbon fibers derived from rice straw and paper mulberry. *Mater. Lett.* 167, 18–21, 2016.
125. Sun, J.-K., Xu, Q., Functional materials derived from open framework templates/precursors: synthesis and applications. *Energy Environ. Sci.* 7(7), 2071–2100, 2014.
126. He, X., *et al.*, Fabrication and Characterization of nanotemplated carbon monolithic material. *Acs Appl. Mater. Interfaces* 5(17), 8572–8580, 2013.
127. Konwar, R.J., De, M., Effects of synthesis parameters on zeolite templated carbon for hydrogen storage application. *Microporous Mesoporous Mater.* 175, 16–24, 2013.
128. Attia, N.F., Lee, S.M., Kim, H.J., Geckeler, K.E., Nanoporous carbon-templated silica nanoparticles: Preparation, effect of different carbon precursors,

and their hydrogen storage adsorption. *Microporous Mesoporous Mater.* 173, 139–146, 2013.
129. Konwar, R.J., De, M., Synthesis of high surface area silica gel templated carbon for hydrogen storage application. *J. Anal. Appl. Pyrolysis* 107, 224–232, 2014.
130. Shi, J., Li, W., Li, D., Synthesis, nickel decoration, and hydrogen adsorption of silica-templated mesoporous carbon material with high surface area. *J. Phys. Chem. C* 119(41), 23430–23435, 2015.
131. Musyoka, N.M., Ren, J., Langmi, H.W., North, B.C., Mathe, M., A comparison of hydrogen storage capacity of commercial and fly ash-derived zeolite X together with their respective templated carbon derivatives. *Int. J. Hydrog. Energy* 40(37), 12705–12712, 2015.
132. Xia, Y., Yang, Z., Gou, X., Zhu, Y., A simple method for the production of highly ordered porous carbon materials with increased hydrogen uptake capacities. *Int. J. Hydrog. Energy* 38(12), 5039–5052, 2013.
133. Yang, Z., Xiong, W., Wang, J., Zhu, Y., Xia, Y., A systematic study on the preparation and hydrogen storage of zeolite 13X-templated microporous carbons. *Eur. J. Inorg. Chem.*, 2016(13–14), 2152–2158, 2016.
134. Stojmenovic, M., *et al.*, Complex investigation of charge storage behavior of microporous carbon synthesized by zeolite template. *Microporous Mesoporous Mater.* 228, 94–106, 2016.
135. Konwar, R.J., De, M., Development of templated carbon by carbonisation of sucrose-zeolite composite for hydrogen storage. *Int. J. Energy Res.* 39(2), 223–233, 2015.
136. Cai, J., Yang, M., Xing, Y., Zhao, X., Large surface area sucrose-based carbons via template-assisted routes: Preparation, microstructure, and hydrogen adsorption properties. *Colloids Surf. -Physicochem. Eng. Asp.* 444, 240–245, 2014.
137. Cai, J., Li, L., Lv, X., Yang, C., Zhao, X., Large surface area ordered porous carbons via nanocasting zeolite 10X and high performance for hydrogen storage application. *Acs Appl. Mater. Interfaces* 6(1), 167–175, 2014.
138. Masika, E., Mokaya, R., Preparation of ultrahigh surface area porous carbons templated using zeolite 13X for enhanced hydrogen storage. *Prog. Nat. Sci. Mater. Int.* 23(3), 308–316, 2013.
139. Kruk, M., Jaroniec, M., Ryoo, R., Joo, S.H., Characterization of ordered mesoporous carbons synthesized using MCM-48 silicas as templates. *J. Phys. Chem. B* 104(33), 7960–7968, 2000.
140. Yang, Z., Xia, Y., Mokaya, R., Enhanced hydrogen storage capacity of high surface area zeolite-like carbon materials. *J. Am. Chem. Soc.* 129(6), 1673–1679, 2007.
141. Xia, K., Gao, Q., Jiang, J., Wang, H., An unusual method to prepare a highly microporous carbon for hydrogen storage application. *Mater. Lett.* 100, 227–229, 2013.
142. Nishihara, H., *et al.*, Experimental and theoretical studies of hydrogen/deuterium spillover on Pt-loaded zeolite-templated carbon. *J. Phys. Chem. C* 118(18), 9551–9559, 2014.

143. Pei, X., *et al.*, Metal-organic frameworks derived porous carbons: Syntheses, porosity and gas sorption properties. *Chin. J. Chem.* 34(2), 157–174, 2016.
144. Suh, M.P., Park, H.J., Prasad, T.K., Lim, D.-W., Hydrogen storage in metal-organic frameworks. *Chem. Rev.* 112(2), 782–835, 2012.
145. Furukawa, H., Cordova, K.E., O'Keeffe, M., Yaghi, O.M., The chemistry and applications of metal-organic frameworks. *Science* 341(6149), 1230444-1/1230444-12, 2013.
146. Bobbitt, N.S., Chen, J., Snurr, R.Q., High-throughput screening of metal-organic frameworks for hydrogen storage at cryogenic temperature. *J. Phys. Chem. C* 120(48), 27328–27341, 2016.
147. Noguera-Diaz, A., Bimbo, N., Holyfield, L.T., Ahmet, I.Y., Ting, V.P., Mays, T.J., Structure-property relationships in metal-organic frameworks for hydrogen storage. *Colloids Surf. -Physicochem. Eng. Asp.* 496, 77–85, 2016.
148. Aiyappa, H.B., Pachfule, P., Banerjee, R., Kurungot, S., Porous carbons from nonporous MOFs: Influence of ligand characteristics on intrinsic properties of end carbon. *Cryst. Growth Des.* 13(10), 4195–4199, 2013.
149. Malgras, V., *et al.*, Templated synthesis for nanoarchitectured porous materials. *Bull. Chem. Soc. Jpn.* 88(9), 1171–1200, 2015.
150. Kaneti, Y.V., *et al.*, Nanoarchitectured design of porous materials and nanocomposites from metal-organic frameworks. *Adv. Mater.* 29(12), 1604898, 2017.
151. Zhao, Y., Liu, Y., Kang, H., Cao, K., Wang, Y., Jiao, L., Nitrogen-doped hierarchically porous carbon derived from ZIF-8 and its improved effect on the dehydrogenation of LiBH4. *Int. J. Hydrog. Energy* 41(39), 17175–17182, 2016.
152. Aijaz, A., Fujiwara, N., Xu, Q., From metal-organic framework to nitrogen-decorated nanoporous carbons: High CO2 uptake and efficient catalytic oxygen reduction. *J. Am. Chem. Soc.* 136(19), 6790–6793, 2014.
153. Chaikittisilp, W., Ariga, K., Yamauchi, Y., A new family of carbon materials: Synthesis of MOF-derived nanoporous carbons and their promising applications. *J. Mater. Chem. A* 1(1), 14–19, 2013.
154. Lim, S., *et al.*, Porous carbon materials with a controllable surface area synthesized from metal-organic frameworks. *Chem. Commun.* 48(60), 7447–7449, 2012.
155. Segakweng, T., Musyoka, N.M., Ren, J., Crouse, P., Langmi, H.W., Comparison of MOF-5-and Cr-MOF-derived carbons for hydrogen storage application. *Res. Chem. Intermed.* 42(5), 4951–4961, 2016.
156. Liu, B., Shioyama, H., Akita, T., Xu, Q., Metal-organic framework as a template for porous carbon synthesis. *J. Am. Chem. Soc.* 130(16), 5390–5391, 2008.
157. Yang, S.J., *et al.*, MOF-derived hierarchically porous carbon with exceptional porosity and hydrogen storage capacity. *Chem. Mater.* 24(3), 464–470, 2012.
158. Jayaramulu, K., Datta, K.K.R., Shiva, K., Bhattacharyya, A.J., Eswaramoorthy, M., Maji, T.K., Controlled synthesis of tunable nanoporous carbons for gas

storage and supercapacitor application. *Microporous Mesoporous Mater.* 206, 127–135, 2015.
159. Jiang, H.-L., *et al.*, From metal–organic framework to nanoporous carbon: Toward a very high surface area and hydrogen uptake. *J. Am. Chem. Soc.* 133(31), 11854–11857, 2011.
160. Almasoudi, A., Mokaya, R., Preparation and hydrogen storage capacity of templated and activated carbons nanocast from commercially available zeolitic imidazolate framework. *J. Mater. Chem.* 22(1), 146–152, 2011.
161. Wang, Q., Xia, W., Guo, W., An, L., Xia, D., Zou, R., Functional zeolitic-imidazolate-framework-templated porous carbon materials for CO2 capture and enhanced capacitors. *Chem.- Asian J.* 8(8), 1879–1885, 2013.
162. Pachfule, P., Biswal, B.P., Banerjee, R., Control of porosity by using isoreticular zeolitic imidazolate frameworks (IRZIFs) as a template for porous carbon synthesis. *Chem.- Eur. J.* 18(36), 11399–11408, 2012.
163. Almasoudi, A., Mokaya, R., Porosity modulation of activated ZIF-templated carbons via compaction for hydrogen and CO2 storage applications. *J. Mater. Chem. A* 2(28), 10960–10968, 2014.
164. Yushin, G., Dash, R., Jagiello, J., Fischer, J.E., Gogotsi, Y., Carbide-derived carbons: Effect of pore size on hydrogen uptake and heat of adsorption. *Adv. Funct. Mater.* 16(17), 2288–2293, 2006.
165. Schmirler, M., Glenk, F., Etzold, B.J.M., *In-situ* thermal activation of carbide-derived carbon. *Carbon* 49(11), 3679–3686, 2011.
166. Gogotsi, Y., *et al.*, Importance of pore size in high-pressure hydrogen storage by porous carbons. *Int. J. Hydrog. Energy* 34(15), 6314–6319, 2009.
167. Sevilla, M., Foulston, R., Mokaya, R., Superactivated carbide-derived carbons with high hydrogen storage capacity. *Energy Environ. Sci.* 3(2), 223–227, 2010.
168. Wang, J., *et al.*, Synthesis, characterization, and hydrogen storage capacities of hierarchical porous carbide derived carbon monolith. *J. Mater. Chem.* 22(45), 23893–23899, 2012.
169. Yu, Z., Deschamps, J., Hamon, L., Prabhakaran, P.K., Pre, P., Hydrogen adsorption and kinetics in MIL-101(Cr) and hybrid activated carbon-MIL-101(Cr) materials. *Int. J. Hydrog. Energy* 42(12), 8021–8031, 2017.
170. Prabhakaran, P.K., Catoire, L., Deschamps, J., Aluminium doping composite metal-organic framework by alane nanoconfinement: Impact on the room temperature hydrogen uptake. *Microporous Mesoporous Mater.* 243, 214–220, 2017.
171. Adhikari, A.K., Lin, K.-S., Tu, M.-T., Hydrogen storage capacity enhancement of MIL-53(Cr) by Pd loaded activated carbon doping. *J. Taiwan Inst. Chem. Eng.* 63, 463–472, 2016.
172. Musyoka, N.M., *et al.*, Synthesis of a hybrid MIL-101(Cr)/ZTC composite for hydrogen storage applications. *Res. Chem. Intermed.* 42(6), 5299–5307, 2016.

173. Jin, J., Ouyang, J., Yang, H., Pd nanoparticles and MOFs synergistically hybridized halloysite nanotubes for hydrogen storage, *Nanoscale Res. Lett.* 12, 240, 2017.
174. Jin, J., Fu, L., Yang, H., Ouyang, J., Carbon hybridized halloysite nanotubes for high-performance hydrogen storage capacities. *Sci. Rep.* 5, 12429, 2015.
175. Li, B., *et al.*, A new strategy to microporous polymers: Knitting rigid aromatic building blocks by external cross-linker. *Macromolecules* 44(8), 2410–2414, 2011.
176. Zhang, C., *et al.*, Porous carbons derived from hyper-cross-linked porous polymers for gas adsorption and energy storage. *Carbon* 114, 608–618, 2017.
177. Lee, J.-S.M., Briggs, M.E., Hasell, T., Cooper, A.I., Hyperporous carbons from hyper-cross-linked polymers. *Adv. Mater.* 28(44), 9804–9810, 2016.
178. Liu, Y., *et al.*, Carbon nanorods. *Chem. Phys. Lett.* 331(1), 31–34, 2000.
179. Abdulkreem-Alsultan, G., Islam, A., Janaun, J., Mastuli, M.S., Taufiq-Yap, Y.-H., Synthesis of structured carbon nanorods for efficient hydrogen storage. *Mater. Lett.* 179, 57–60, 2016.
180. Giasafaki, D., *et al.*, Hydrogen storage properties of Pd-doped thermally oxidized single wall carbon nanohorns. *J. Alloys Compd.* 645, S485–S489, 2015.
181. Moreno-Castilla, C., Colloidal and micro-carbon spheres derived from low-temperature polymerization reactions. *Adv. Colloid Interface Sci.* 236, 113–141, 2016.
182. Li, S., Pasc, A., Fierro, V., Celzard, A., Hollow carbon spheres, synthesis and applications – A review. *J. Mater. Chem. A* 4(33), 12686–12713, 2016.
183. Li, Y., Li, D., Rao, Y., Zhao, X., Wu, M., Superior CO2, CH4, and H-2 uptakes over ultrahigh-surface-area carbon spheres prepared from sustainable biomass-derived char by CO2 activation. *Carbon* 105, 454–462, 2016.
184. Zielinska, B., Michalkiewicz, B., Chen, X., Mijowska, E., Kalenczuk, R.J., Pd supported ordered mesoporous hollow carbon spheres (OMHCS) for hydrogen storage. *Chem. Phys. Lett.* 647, 14–19, 2016.
185. Nan, Y., Li, B., Zhang, P., Shen, S., Song, X., Positive pressure assisted-arc discharge synthesis of single-walled carbon nanohorns. *Mater. Lett.* 180, 313–316, 2016.
186. Khan, I.A., Badshah, A., Khan, I., Zhao, D., Nadeem, M.A., Soft-template carbonization approach of MOF-5 to mesoporous carbon nanospheres as excellent electrode materials for supercapacitor. *Microporous Mesoporous Mater.* 253, 169–176, 2017.
187. Zhang, W., Zhang, Z., Zhang, F., Yang, W., Ti-decorated graphitic-C3N4 monolayer: A promising material for hydrogen storage. *Appl. Surf. Sci.* 386, 247–254, 2016.
188. Wei, J., Huang, C., Wu, H., Kan, E., High-capacity hydrogen storage in Li-adsorbed g-C3N4. *Mater. Chem. Phys.* 180, 440–444, 2016.

189. Tan, X., Kou, L., Tahini, H.A., Smith, S.C., Charge modulation in graphitic carbon nitride as a switchable approach to high-capacity hydrogen storage. *ChemSusChem* 8(21), 3626–3631, 2015.
190. Talapaneni, S.N., *et al.*, Chemical blowing approach for ultramicroporous carbon nitride frameworks and their applications in gas and energy storage. *Adv. Funct. Mater.* 27(1), 1604658, 2017.
191. Tian, H.Y., Buckley, C.E., Sheppard, D.A., Paskevicius, M., Hanna, N., A synthesis method for cobalt doped carbon aerogels with high surface area and their hydrogen storage properties. *Int. J. Hydrog. Energy* 35(24), 13242–13246, 2010.
192. Zhong, M., *et al.*, A solution-phase synthesis method to prepare Pd-doped carbon aerogels for hydrogen storage. *RSC Adv.* 5(27), 20966–20971, 2015.
193. Singh, S., *et al.*, Synthesis, characterization and hydrogen storage characteristics of ambient pressure dried carbon aerogel. *Int. J. Hydrog. Energy* 41(5), 3561–3570, 2016.
194. Zuo, L., Zhang, Y., Zhang, L., Miao, Y.-E., Fan, W., Liu, T., Polymer/carbon-based hybrid aerogels: Preparation, properties and applications. *Materials* 8(10), 6806–6848, 2015.
195. Hussain, T., Hankel, M., Searles, D.J., Graphenylene monolayers doped with alkali or alkaline earth metals: Promising materials for clean energy storage. *J. Phys. Chem. C* 121(27), 14393–14400, 2017.
196. Gomez Costa, M.B., Juarez, J.M., Pecchi, G., Anunziata, O.A., Anatase-CMK-3 nanocomposite development for hydrogen uptake and storage. *Bull. Mater. Sci.* 40(2), 271–280, 2017.
197. Hu, X.-M., Chen, Q., Zhao, Y.-C., Laursen, B.W., Han, B.-H., Facile synthesis of hierarchical triazine-based porous carbons for hydrogen storage. *Microporous Mesoporous Mater.* 224, 129–134, 2016.
198. Kuhn, P., Forget, A., Su, D., Thomas, A., Antonietti, M., From microporous regular frameworks to mesoporous materials with ultrahigh surface area: dynamic reorganization of porous polymer networks. *J. Am. Chem. Soc.* 130(40), 13333–13337, 2008.
199. Gao, J., Xie, J., Liu, X., Hu, H., Preparation and evaluation of modified cyanobacteria-derived activated carbon for H-2 adsorption. *Rsc Adv.* 7(33), 20412–20421, 2017.
200. Sethia, G., Sayari, A., Activated carbon with optimum pore size distribution for hydrogen storage. *Carbon* 99, 289–294, 2016.
201. Zhao, W., Luo, L., Fan, M., Preparation and characterization of nitrogen-containing cellular activated carbon for CO2 and H-2 adsorption. *Nano* 12(1), 1750007, 2017.
202. Ramesh, T., Rajalakshmi, N., Dhathathreyan, K.S., Synthesis and characterization of activated carbon from jute fibers for hydrogen storage. *Renew. Energy Environ. Sustain.* 2, 4, 2017.

203. Schaefer, S., *et al.*, Rice straw-based activated carbons doped with SiC for enhanced hydrogen adsorption. *Int. J. Hydrog. Energy*, 42(16), 11534–11540, 2017.
204. Md. Arshad, S.H., Ngadi, N., Aziz, A.A., Amin, N.S., Jusoh, M., Wong, S., Preparation of activated carbon from empty fruit bunch for hydrogen storage. *J. Energy Storage* 8, 257–261, 2016.
205. Li, G., *et al.*, Preparation and characterization of the hydrogen storage activated carbon from coffee shell by microwave irradiation and KOH activation. *Int. Biodeterior. Biodegrad.* 113, 386–390, 2016.
206. Wang, Z., *et al.*, Nitrogen-doped porous carbons with high performance for hydrogen storage. *Int. J. Hydrog. Energy* 41(20), 8489–8497, 2016.
207. Wróbel-Iwaniec, I., Díez, N., Gryglewicz, G., Chitosan-based highly activated carbons for hydrogen storage. *Int. J. Hydrog. Energy* 40(17), 5788–5796, 2015.
208. Heo, Y.-J., Park, S.-J., Synthesis of activated carbon derived from rice husks for improving hydrogen storage capacity. *J. Ind. Eng. Chem.* 31, 330–334, 2015.
209. Choi, Y.-K., Park, S.-J., Preparation and characterization of sucrose-based microporous carbons for increasing hydrogen storage. *J. Ind. Eng. Chem.* 28, 32–36, 2015.
210. Pei, P., Whitwick, M.B., Sun, W.L., Quan, G., Cannon, M., Kjeang, E., Enhanced hydrogen adsorption on graphene by manganese and manganese vanadium alloy decoration. *Nanoscale* 9(12), 4143–4153, 2017.
211. Hosseini, A., Ghoreyshi, A.A., Pirzadeh, K., Mohammadi, M., Enhancement of hydrogen storage on multi-walled carbon nanotube through KOH activation and nickel nanoparticle deposition. *Sci. Iran.* 24(3), 1230–1240, 2017.

Appendix

Details about precursors, surface areas, pore volumes, hydrogen storage capacities and measurement methods referred to in the chapter.

n.s. not specified

List of acronyms used:

A_{BET}: BET area; V_T: total pore volume; NLDFT: nonlocal density function theory; GO: graphene oxide; rGO: reduced graphene oxide; f-MWCNTs: functionalized multi-walled carbon nanotube; ACF: activated carbon fiber; CNF: carbon nanofiber; CVD: chemical vapor deposition; FA: furfuryl alcohol; IRMOF: Iso Reticular Metal Organic Framework; ZIF: Zeolitic Imidazolate Frameworks; HCP: hyper-cross-linked polymer; FDA: formaldehyde dimethyl acetal.

Table 9.1

AC - ACTIVATED CARBONS									
Typology of carbon	**H_2 Uptake (wt.%)**	**T (K)**	**P (MPa)**	**Method**	**Quantity measured**	**A_{BET} (m^2/g)**	**V_T (cm^3/g)**	**Info**	**Reference**
AX21	5.3	77	4	gravimetric	*excess*	2772	1.1	-	[56]
	1	298	20	volumetric	*excess*				
	4.8	77	3	volumetric	*excess*	2451	1.14	no doped	[62]
	3.8	77	2	volumetric	*excess*	2023	0.93	Pd doped	
	6.5	77	8	gravimetric	*n.s.*	2527	1.10	non-doped	[63]
	5.4	77	8	gravimetric	*n.s.*	2082	0.89	N-doped	
	0.6	298	10	volumetric	*n.s.*	2850	1.40	non-doped	[67]
	1.30	298	10	volumetric	*n.s.*	2538	1.26	Ru-doped	
	1.22	298	10	volumetric	*n.s.*	2545	1.28	Pt-doped	
	1.02	298	10	volumetric	*n.s.*	2570	1.30	Ni-doped	
commercial activated carbon	7.08	77	2	gravimetric	*n.s.*	3190	1.69	KOH activation	[57]
	4	77	2	gravimetric	*n.s.*	1308	1.10	CO_2 activation	
olive stones-derived	5	77	1.2	volumetric	*n.s.*	1170	0.61	H_3PO_4 activation	[58]
	5	77	1.2	volumetric	*n.s.*	1533	0.76	$ZnCl_2$ activation	
	3.6	77	10	volumetric	*excess*	1269	0.61	KOH activation	[59]
	6.11	77	20	volumetric	*absolute*				
	1.22	298	20	volumetric	*excess*				
moso bamboo-derived	6.6	77	4	gravimetric	*n.s.*	3208	1.75	KOH activation	[60]
	2.74	77	0.1	volumetric	*n.s.*				
cyanobacteria-derived	2.52	77	0.1	volumetric	*n.s.*	1901	1.026	P-doped	[199]

(*Continued*)

Table 9.1 Cont.

AC - ACTIVATED CARBONS									
Typology of carbon	**H_2 Uptake (wt.%)**	**T (K)**	**P (MPa)**	**Method**	**Quantity measured**	**A_{BET} (m^2/g)**	**V_T (cm^3/g)**	**Info**	**Reference**
trimethylsilyl imidazole + chloroacetonitrile (synthetic)	2.96	77	0.1	volumetric	*n.s.*	1317	0.64	synthetic/ KOH activation	[200]
phenol-urea-formaldehyde-derived	1.9	77	0.1	volumetric	*n.s.*	1674	0.86	-	[201]
jute fibers-derived	1.2	308	4	volumetric	*n.s.*	1224	0.74	high-temperature measurements	[202]
rice straw-derived	0.65	298	10	volumetric	*excess*	2100 NLDFT	0.95 NLDFT	NLDFT method	[203]
sucrose-derived	0.59	298	10	volumetric	*excess*	2242 NLDFT	0.8 NLDFT	NLDFT method	[54]
empty fruit bunch-derived	1.97	77	0.1	volumetric	*excess*	687	0.362	-	[204]
coffee shell-derived	2.14	77	2	volumetric	*excess*	3149	1.67	microwave treated sample	[205]
chitosan-derived	2.71	77	0.1	volumetric	*n.s.*	2919	1.425	Ni-doped	[206]
	6.77	77	2	volumetric	*n.s.*				
	2.95	77	0.1	volumetric	*n.s.*	3066	1.38	-	[207]
	5.61	77	4	volumetric	*n.s.*				
rice husks-derived	2.85	77	0.1	volumetric	*n.s.*	2682	1.963	-	[208]
tamarind seeds-derived	4.73	298	4	volumetric	*n.s.*	1785	0.94	microwave treated + KOH activation	[61]
sucrose-derived	2.5	77	0.1	volumetric	*n.s.*	1552	1.124	-	[209]

Table 9.2

GRAPHENE - FULLERENES									
Type	**H_2 Uptake (wt.%)**	**T (K)**	**P (MPa)**	**Method**	**Quantity measured**	**A_{BET} (m^2/g)**	**V_T (cm^3/g)**	**Info**	**Reference**
nanoporous graphene	2.56	298	3.4	volumetric	*n.s.*	850	2.11	-	[79]
graphene produced from rGO	7.04	77	6	volumetric	*excess*	3230	2.22	reduced graphene oxide	[87]
graphene produced from rGO	2.7	298	2.5	gravimetric	*n.s.*	1206	-	reduced graphene oxide	[88]
Pd-decorated graphene	4.83	298	4	gravimetric	*n.s.*	-	-	doped	[89]
graphene produced from rGO	2.7	77	0.1	volumetric	*n.s.*	1018.7	-	reduced graphene oxide	[74]
graphene produced from rGO	1.5	298	9	volumetric	*excess*	580	-	doped - reduced graphene oxide	[84]
Mn-doped graphene	0.36	298	4	volumetric	*n.s.*	401	3.67	Mn-doped	[210]
Mn-V- doped graphene	1.81	298	4	volumetric	*n.s.*	326	1.79	Mn-V-doped	[210]

Table 9.3

CARBON NANOTUBES - CNTs									
Type	**H_2 Uptake (wt.%)**	**T (K)**	**P (MPa)**	**Method**	**Quantity measured**	**A_{BET} (m^2/g)**	**V_T (cm^3/g)**	**Info**	**Reference**
CNT from modified arc-discharge	1.73	77	10	volumetric	*n.s.*	-	-	modified arc-discharge	[104]
CNT from modified arc-discharge	0.67	303	10	volumetric	*n.s.*	-	-	modified arc-discharge	[104]
CNT activated with KOH	1.24	298	3.4	volumetric	*n.s.*	994	1.14	KOH activation	[111]
Fe-doped@f-MWNTs	0.39	298	7	volumetric	*n.s.*	206	-	Fe-doped	[110]
Cu-doped@f-MWNT	0.50	298	7	volumetric	*n.s.*	226	-	Cu-doped	[110]
Ni-decorated CNT	0.87	298	10	volumetric	*n.s.*	211	2.12	Ni-doped	[113]
Ni-decorated CNT	1	298	4.5	volumetric	*n.s.*	-	-	Ni-doped	[211]
Ti-decorated CNT	2	298	1.6	volumetric	*n.s.*	-	-	Ti-doped	[112]
Co-oxide/MWCNT	0.8	298	2.3	volumetric	*n.s.*	147	-	Co intercalation	[115]
Cu-oxide/MWCNT	0.9	298	2.3	volumetric	*n.s.*	237	-	Cu intercalation	[115]

Table 9.4

CARBON NANOFIBERS – CNFs									
Type	**H_2 Uptake (wt.%)**	**T (K)**	**P (MPa)**	**Method**	**Quantity measured**	**A_{BET} (m^2/g)**	**V_T (cm^3/g)**	**Info**	**Reference**
rice straw/mulberry-derived	4.35	77	2	gravimetric	*n.s.*	2260	-	-	[124]
Ni-ACF/CNFs	2.5	77	2	volumetric	*n.s*	774	-	Ni-doped	[122]
Ni-ACF/CNFs	0.75	298	5	volumetric	*n.s*	774	-	Ni-doped	[122]
CNF	1.4	298	12	volumetric	*n.s*	140	-	-	[119]
acetylene-derived	0.51	298	1	volumetric	*n.s*	357	-	CVD + activation	[120]
ethanol-derived	0.42	298	1	volumetric	*n.s*	307	-	CVD + activation	[120]
cotton-derived	0.65	298	1	volumetric	*n.s*	395	-	CVD + activation	[120]
Ni-doped CNF	2.2	298	10	volumetric	*n.s*	1310	-	Ni-doped	[121]
exfoliated CNF	5	77	1	volumetric	*n.s*	226.6	0.516	exfoliation	[123]

Table 9.5

TEMPLATED CARBONS									
Source materials	**H_2 Uptake (wt.%)**	**T (K)**	**P (MPa)**	**Method**	**Quantity measured**	**A_{BET} (m^2/g)**	**V_T (cm^3/g)**	**Info**	**Reference**
zeolite β + acetonitrile	6.9	77	2	gravimetric	*n.s.*	3200	2.41	CVD	[140]
zeolite X	2.4	77	0.1	volumetric	*n.s.*	2578	1.44	-	[131]
fly ash	1.2	77	0.1	volumetric	*n.s.*	1112	0.48	-	
EMC-2+acetonitrile	2.04	77	0.1	gravimetric	*n.s.*	2762	1.41	CVD + heat pre-treat	[132]
EMC-2+acetonitrile	5.6	77	2	gravimetric					
13X+FA+ethylene	5.11	77	2	gravimetric	*n.s.*	2568	1.41	CVD and heat treatment	[133]
13X+FA+acetonitrile	4.9	77	2	gravimetric	*n.s.*	2174	1.13	CVD and heat treatment	
silica+sucrose	0.67	298	8	gravimetric	*n.s.*	2008	1.21	CO_2 activation	[141]
10X+FA+ethylene	6.09	77	2	gravimetric	*n.s.*	3331	1.94	CVD and heat treatment	[137]
USY zeolite+sucrose	3.52	77	2	gravimetric	*n.s.*	1127	0.817	sucrose as second precursor	[136]
rice husks silica+glycerol	2.41	77	7.3	volumetric	*excess*	749	1.44	glycerol as second precursor	[128]
rice husks silica+glycerol	5.7	77	7.3	volumetric	*total*				[128]
13X+FA+ethylene	6.2	77	2	gravimetric	*excess*	3332	1.66	CVD and heat treatment	[138]
13X+FA+ethylene	7.3	77	2	gravimetric	*total*				[138]
silica+resol	0.53	298	2	volumetric	*n.s.*	1326	0.73	silica, Ni	[130]

Table 9.6

MOF-DERIVED CARBONS									
Source materials	**H_2 Uptake (wt.%)**	**T (K)**	**P (MPa)**	**Method**	**Quantity measured**	**A_{BET} (m^2/g)**	**V_T (cm^3/g)**	**Info**	**Reference**
MOF-5+FA	2.6	77	0.1	n.s.	*n.s.*	2872	2.06	FA as second precursor	[156]
MOF-5 1000°C	2.7	77	0.1	volumetric	*n.s.*	2393	1.13	Direct carbonization	[155]
ZIF-8+FA	2.77	77	0.1	volumetric	*n.s.*	3405	2.58	FA as second precursor	[159]
IRMOF-1	0.97	298	10	gravimetric	*n.s.*	3174	4.06	direct carbonization	[157]
IRMOF-1	3.25	77	0.1	volumetric	*n.s.*	3174	4.06	direct carbonization	[157]
IRMOF-3	2.1	77	0.1	volumetric	*n.s.*	1678	2.01	direct carbonization	[157]
IRMOF-8	2.41	77	0.1	volumetric	*n.s.*	1978	1.92	direct carbonization	[157]
IRMOF-3 + sucrose	2.45	77	0.1	volumetric	*n.s.*	3120	1.93	300 mg sucrose as second precursor	[158]
IRMOF-3 + sucrose	5.1	77	4	volumetric	*n.s.*				[158]
ZIF-8	2.59	77	0.1	volumetric	*n.s.*	2437	1.266	KOH activation	[161]
ZIF-68	2.11	77	0.1	volumetric	*n.s.*	1861	1.086	KOH activation	[161]
ZIF-69	2.16	77	0.1	volumetric	*n.s.*	2264	1.184	KOH activation	[161]
ZIF-68 + FA	2.15	77	0.1	volumetric	*n.s.*	1311	1.381	FA as second precursor	[162]
ZIF-69 + FA	1.96	77	0.1	volumetric	*n.s.*	1171	0.725	FA as second precursor	[162]
ZIF-70 + FA	2.37	77	0.1	volumetric	*n.s.*	1510	1.749	FA as second precursor	[162]
ZIF-8 + FA + KOH 900	6.2	77	2	gravimetric	*n.s.*	3188	1.94	FA + KOH activation	[160]

(*Continued*)

Table 9.6 Cont.

MOF-DERIVED CARBONS									
Source materials	**H_2 Uptake (wt.%)**	**T (K)**	**P (MPa)**	**Method**	**Quantity measured**	**A_{BET} (m^2/g)**	**V_T (cm^3/g)**	**Info**	**Reference**
ZIF-8 + FA + KOH 1000	4.9	77	2	gravimetric	*n.s.*	1893	1.13	FA + KOH activation	[160]
ZIF-8 + FA + KOH 1050	3.9	77	2	gravimetric	*n.s.*	1425	0.91	FA + KOH activation	[160]
ZIF-8 + FA + KOH 1100	4.7	77	2	gravimetric	*n.s.*	1523	0.95	FA + KOH activation	[160]
ZIF-8 + FA + KOH 900 + compaction at 370 MPa	6.5	77	2	gravimetric	*n.s.*	3323	2.32	compaction at 370 MPa	[163]
ZIF-8 + FA + KOH 900 + compaction at 740 MPa	5.7	77	2	gravimetric	*n.s.*	2045	1.25	compaction at 740 MPa	[163]
ZIF-8 + FA + CVD + KOH	6.2	77	2	gravimetric	*n.s.*	2399	1.60	-	[163]
ZIF-8 + FA + CVD + KOH + compaction at 370 MPa	5.6	77	2	gravimetric	*n.s.*	2534	1.77	compaction at 370 MPa	[163]
ZIF-8 + FA + CVD + KOH + compaction at 740 MPa	4.9	77	2	gravimetric	*n.s.*	1937	1.11	compaction at 740 MPa	[163]

Table 9.7

EXOTIC CARBON MATERIALS									
Typology of carbon	**H_2 Uptake (wt.%)**	**T (K)**	**P (MPa)**	**Method**	**Quantity measured**	**A_{BET} (m^2/g)**	**V_T (cm^3/g)**	**Info**	**Reference**
TiC	3	77	0.1	volumetric	*n.s.*	-	-	carbide	[164]
TiC	4.62	77	6	volumetric	*excess*	2643	1.05	carbide	[166]
ZrC	6.2	77	2	gravimetric	*n.s.*	2770	1.47	carbide	[167]
SiC	2.4	77	0.1	volumetric	*excess*	2933	2.1	carbide	[168]
SiC	4.4	77	3.6	volumetric	*excess*	2933	2.1	carbide	[168]
MIL-53(Cr) + Pd/ACs	1.92	77	6	gravimetric	*n.s.*	876	0.045 (BJH)	MOF + doped AC	[171, p. 53]
MIL-53(Cr) + Pd/ACs	0.8	298	6	gravimetric	*n.s.*	876	0.045 (BJH)	MOF + doped AC	[171, p. 53]
MIL-101 + Norit RB3	13.5	77	10	volumetric	*excess*	3542	2.65	MOF + AC	[169]
MIL-101 + Norit RB3 + alane	1.2	298	10	gravimetric	*n.s.*	2870	1.83	MOF + ACs + alane	[170]
MIL-101 + ZTC	2.55	77	0.1	volumetric	*n.s.*	2957	-	MOF + ZTC	[172]
Pd-C-Halloysite/ MOFs	0.32	298	2.65	volumetric	*n.s.*	-	-	halloysite + MOF carbonized	[173]
C-Halloysite	0.48	298	2.65	volumetric	*n.s.*	47.14	0.146	CNTs/halloysite Nanotubes	[174]

(*Continued*)

Table 9.7 Cont.

EXOTIC CARBON MATERIALS									
Typology of carbon	**H_2 Uptake (wt.%)**	**T (K)**	**P (MPa)**	**Method**	**Quantity measured**	**A_{BET} (m^2/g)**	**V_T (cm^3/g)**	**Info**	**Reference**
pyrrole (HCP)-derived	3.6	77	0.1	volumetric	*n.s.*	4334	3.14	hyper-cross-linked	[177]
pyrrole (HCP)-derived	5.6	77	1	volumetric	*n.s.*	4334	3.14	hyper-cross-linked	[177]
benzene (HCP) -derived	3	77	0.1	volumetric	*n.s.*	3105	1.58	hyper-cross-linked	[177]
benzene (HCP) -derived	4	77	1	volumetric	*n.s.*	3105	1.58	hyper-cross-linked	[177]
thyophene (HCP) -derived	2.5	77	0.1	volumetric	*n.s.*	2682	1.51	hyper-cross-linked	[177]
thyophene (HCP) -derived	3.7	77	1	volumetric	*n.s.*	2682	1.51	hyper-cross-linked	[177]
FDA + phenyltrimethylsi-lane-derived	3.25	77	0.1	volumetric	*n.s.*	3101	1.84	hyper-cross-linked	[176]
starch-derived carbon nanospheres	6.4	77	2	gravimetric	*n.s.*	3350	1.75	CO_2 act.	[183]
chemically blowing carbon nitride	1.9	77	0.1	volumetric	*n.s.*	1730	0.78	C_3N_4	[190]
triazine-based carbon	2.34	77	0.1	volumetric	*n.s.*	1250	1.45	triazine	[197]
Anatase-CMK3	2.9	77	1	volumetric	*n.s.*	706	0.67		[196]
Carbon aerogel	5.65	77	2.2	volumetric	*n.s.*	379	0.209	aerogel	[193]

Index

Mehmet Sankir and Nurdan Demirci Sankir (eds.) Hydrogen Storage Technologies, (321–324) © 2018 Scrivener Publishing LLC